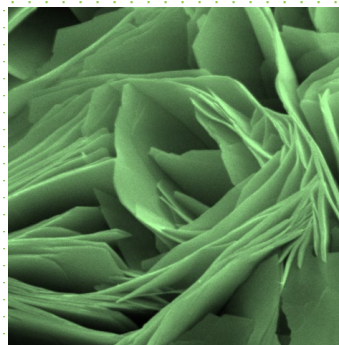
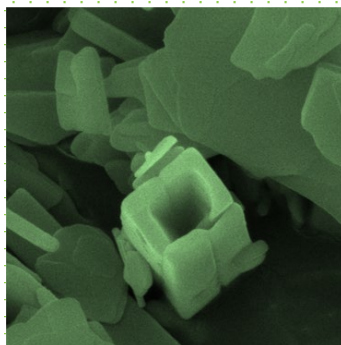




PROCEEDING

8th International Symposium on
Advanced Materials & Nanotechnology

8 – 9 October 2024



Theme:

Nanotechnology Pathway to Net-Zero Emissions by 2050

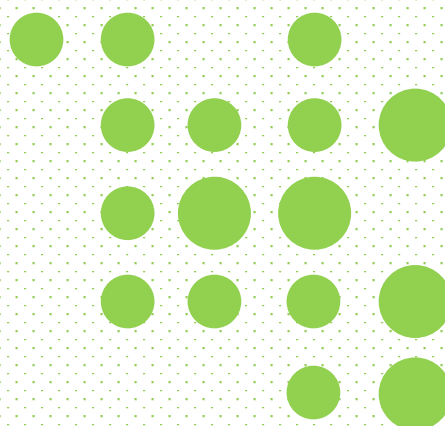


TABLE OF CONTENT

No	Paper Title / Author (s)	Pages
1.	Passive RFID Tag Antenna on Kapton Substrate for IoT Applications <i>Tark D Farnana</i>	4
2	Determination Of Tramadol and Codeine Using a Paper Screen Printed Electrode Coupled Colorimetric Device <i>Salamatu Aliyu Hayatu</i>	10
3	Development and fabrication of metal-oxide frameworks (MOFs) Nanohybrids for photocatalytic dye degradation of wastewater treatment application <i>Suriati Paiman</i>	17
4	Optimizing Bead Free PVDF Nonwoven Nanomembrane for Waste Cooking Oil (WCO) removal in wastewater <i>Yogapria Sathianathan</i>	23
5	Synthesis, Optimization, And Characterization of Biogenic Copper Oxide Nanoparticles (CuONPs) For Potential Depollution Application <i>Mhd Hazli Rosli</i>	36
6	Enhancing Enzymatic Performance with Hydroxyapatite-Biomedica for Sustainable Environmental Remediation <i>Mohamad Tajuddin Sabri</i>	45
7	Synergistic Enhancement of Mechanical Properties in Banana Fiber-Graphite Hybrid Composites with Epoxy Matrix: A Novel Approach to Sustainable High-Performance Materials <i>Senthil Kannan Nachappan</i>	57
8	Performance of Nanocellulose Fibre Reinforced Starch Biopolymer Composites <i>Muhammad Firdaus Bin Abdul Halim</i>	68
9	Cellulose Electrospun Nanofibers: Bridging Sustainability and Electronic <i>Nik Nurshakirah Farhana Binti Norazlin</i>	76
10	A Short Review on PLA Biodegradable Green Packaging Reinforced Nano Filler <i>Harshaan Arumugam</i>	87

No	Paper Title / Author (s)	Pages
11	Quality Attributes of Fresh Poultry Meat Wrapped in Corn starch-based Films Incorporated with Nanocellulose Fiber and Thymol <i>Norhazirah Nordin</i>	94
12	Preparation and Photoluminescence (PL) Characterisation of Carbon Quantum Dots (CQDs) With Different Solutions and Concentrations <i>Mhammed Ali Khalifa Mhammed Ali Alnigomi</i>	101
13	Synthesis of hydrochar-based acid catalyst for efficient esterification of palm fatty acid distillate <i>Muhammad Aliyu</i>	111
14	Synthesis of Hydroxyapatite from Polymesoda expansa Mollusk Shell Using Room Temperature and Hydrothermal Methods <i>Rosnah Nawang</i>	118
15	Thermogravimetric Analysis (TGA) of Biochar and the Paste Made from Prosopis Africana Biomass Material <i>Suleiman Babani</i>	128
16	One-Pot Functionalisation of Hydrothermally Reduced Graphene Oxide using Garcinia mangostana Peel Extract for Supercapacitors <i>Mohamad Aliff bin Ali Rahman</i>	134
17	Radiation Protection Aspect in Nuclear Power Plants Design- A Preliminary Review <i>Arunagiri Szeyuan Lam</i>	142
18	Shape Stable Phase Change Material for Thermal Energy Storage Applications <i>Anas Islam</i>	156
19	Spinodal Transformations in Thin Films <i>Rahul Basu</i>	164
20	Heat transfer and crust formation of Japanese glutinous rice during deep-frying process <i>Mohd. Nazli Naim</i>	172
21	Silicon carbide-doped halogen groups: A case for applying DFT <i>Thanh Tung Nguyen</i>	180

No	Paper Title / Author (s)	Pages
22	Review on Synthesis and Evaluation Performance of AP Based Solid Composite Propellants with GO and CNT as Burning Catalyst <i>Muhammad Faizridhwan Ramle</i>	188
23	Steel Slag as a Carbon Sequestration Agent: Potential and Mechanisms <i>Umi Rukiah Abdullah</i>	202
24	Elution of Calcium from Marble Waste as a Preparatory Step for Indirect Aqueous Mineral Carbonation for Carbon Capture and Storage <i>Muhammad Hameer Soomro</i>	209
25	Antibacterial Activity of Biosynthesized Silver Nanoparticles using Clitoria ternatea against Cutibacterium acnes <i>Khor Zhi Xin</i>	216
26	Development of Cellulose Nanospheres to Enhance the Antibacterial Activity of Lysozyme <i>Nur Khairun Atiyah Sagee Ahmad</i>	223
27	Crafting and Analyzing Magnetite Nanoparticles: A Comparative Study of Chemical and Green Synthesis with Brine Shrimp Toxicity Assessment for Biomedical Applications <i>Romesa Soomro</i>	228
28	Optimization, Characterization and Toxicity Studies of Gold Nanoparticles as Potential Biocompatible Carrier for Colon Cancer Treatment <i>Siti Nadiah Zulkifli</i>	239

NANOSENSOR AND NANO ELECTRICS

Passive RFID Tag Antenna on Kapton Substrate for IoT Applications

Tark D. Farnana^{1*}, Intan H. Hassan¹, Mohd Nizar Hamidon^{1,2}, Aduwati Sali², Maryam Md. Isa²

¹*Electrical and Electronic Engineering, Institute of Nanoscience and Nanotechnology, UPM
Serdang, Malaysia*

²*Electrical and Electronic Engineering, Faculty of Engineering, UPM
Serdang, Malaysia*

**Corresponding author's E-mail: tarkfarnana@gmail.com*

Abstract: RFID is a key technology for realizing the Internet of Things (IoT). These applications require flexible tags that can maintain communication over greater distances between the reader and the tag. In this article, we propose two designs of UHF RFID tag zigzag dipole antennas on a Kapton substrate: the first zigzag with a bending angle of 90° and the second at 45° . The two antennas oscillate at 920 MHz – the center frequency of the Malaysian band for UHF RFID. The main goal of this work is to reduce the antenna size while keeping the gain as high as possible to achieve a long reading distance. The two antennas were matched to the NXP UCODE G2iL chip using a modified inductively coupled loop. The antennas were designed and optimized using CST software. The overall size of the first antenna is 108.6×17.2 mm and achieves a gain of 2.21 dBi. The second antenna had a size of 84.10×20 mm and the maximum gain achieved was 1.89 dBi.

Keywords: flexible electronics; passive UHF RFID; zigzag dipole; tag antenna; inductively coupled loop

INTRODUCTION

The Internet of Things (IoT) is a rapidly developing technology used in various areas such as wireless sensor networks (WSN), environmental monitoring, agriculture, smart cities, smart grid, construction industry, healthcare applications, and intelligent industries. The IoT connects various devices to the Internet, enabling real-time communication and data exchange [1], [2].

Radio frequency identification (RFID) is a key to realizing IoT. RFID enables sight-free and cost-effective communication [3]. The RFID system consists of a tag and a reader, usually connected to a computer. Depending on the power source, there are two types of tags: active, passive, and semi-passive. Although passive tags have a shorter read range than active tags, they are preferred over active and semi-passive tags in many applications because they are battery-free, making them more cost-effective, reliable, and long-lasting. Passive tags consist of an antenna and an Application Specific Integrated Circuit (ASIC) or simply called an RFID chip [4]. The tag uses the energy radiated by the reader to power the chip and then communicates with the reader via wireless backscatter communication [5].

Several frequency bands have been assigned for RFID systems: Low Frequency (LF), High Frequency (HF), and Ultra High Frequency (UHF). LF and HF typically use coils to communicate with the reader via inductive coupling using magnetic flux. It is unlikely that UHF tags are intended for far-field communications and use antennas that allow longer reading distances [6].

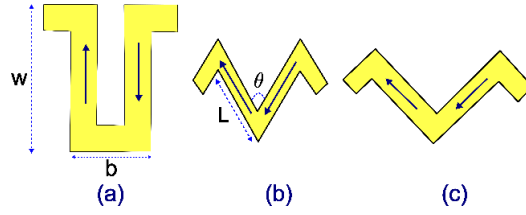


Fig. 1: Current flow in (a) mander line (b) zigzag line with bend angle $< 90^\circ$ (c) zigzag line with $\theta = 90^\circ$.

Several requirements must be met for the tag to be suitable for IoT applications: It must be flexible, small, inconspicuous, and enable a long reading distance. These requirements present challenges in the design and manufacturing phases [7].

Since the tag antenna needs to be small, various methods exist to reduce its size. A common problem is that the antenna gain decreases as the antenna size decreases, resulting in a lower reading distance, which is considered the most important factor of RFID tags.

The aim of this work is to increase the communication distance between the tag and the reader. This can be achieved by increasing the antenna gain, keeping the antenna size small, and powering the ASIC chip using an inductively coupled loop.

ANTENNA DESIGN

The communication distance, d , between the tag and the reader can be estimated using the Friis formula (1), where $EIRP$ is the effective isotropic radiated power. G_t represents the tag antenna gain, P_{th} is the chip sensitivity, ρ is the polarization mismatch, and τ is the power transmission coefficient. This coefficient indicates the degree of agreement between the antennas and the chip and can be calculated using the formula (2), where $Z_a = R_a + jX_a$ and $Z_c = R_c + jX_c$ are the antenna and chip impedances, respectively [6].

$$d = \frac{\lambda}{4\pi} \sqrt{\frac{EIRP * G_t \tau \rho}{P_{th}}} \quad (1)$$

$$\tau = \frac{4R_a R_c}{|Z_a + Z_c|^2}, \quad 0 \leq \tau \leq 1 \quad (2)$$

Malaysian Communications and Multimedia Commission (MCMC) assigned the maximum permitted EIRP value to be 4 watts [8]. The polarization mismatch is 0.5 for a linearly polarized antenna receiving a circularly polarized wave [9]. The chip sensitivity P_{th} is a chip specification given by the manufacturer. From (1) and (2), two parameters can be modified during the design phase of the tag antenna to increase the reading distance: the tag gain G_t and the transmission power coefficient τ .

Tag Antenna

Table 1: the dimensions of the 90° zigzag antenna structure.

Parameter	Value (mm)
a	4.3
b	4.3
w	1
Lc	14
Wc	7
Lx	108.6
Lp	8
Ls	120
Ws	27.5
d	3.25

Although different types of antennas can be used for RFID tags, half-wave dipole antennas are commonly used. They are highly customizable and can be bent, folded, or tip-loaded.

The wavelength at the center frequency of the UHF band for RFIDs (915 MHz) is estimated to be about 328 mm in free space. Therefore, the half-wave straight dipole antenna is about 164mm, which makes the tag size impractical in many cases. The antenna length can be shortened by using meander lines, as shown in Fig. 1(a), or by using zigzag lines, as in Fig. 1(b), instead of straight lines [10]. Both meander and zigzag antennas are highly customizable. Meander dipoles are modified by their width and pitch length, while zigzag antennas are modified by their segment length and bending angle, as shown in Fig. 1(a) and (b). The main disadvantage of the meander antenna is that the radiation from adjacent segments carrying opposite currents, as seen in Fig. 1(a), will cancel each other out, reducing efficiency. A similar scenario occurs with zigzag antennas. There is a trade-off between the shortening ratio and the radiation efficiency. For instance, the shortening ratio of a zigzag antenna increases as its bending angle increases, but its efficiency will reduce accordingly and vice versa. By making the bending angle 90° , each adjacent segment conducts orthogonal currents, resulting in orthogonal fields that do not cancel each other and provide the highest efficiency but give a low shortening ratio.

This article presents two designs of UHF RFID zigzag dipole antennas with different bending angles: 90° and 45° . The length of the two antennas was further reduced by adding capacitive tip-loading. Fig. 2 shows the 90° zigzag, and its dimensions are listed in Table. 1.

The substrate used for the two antennas is Kapton. Kapton is a polyimide film with a relative permittivity $\epsilon_r = 3.4$, tangent loss $\delta = 0.002$, and a thickness of $125 \mu\text{m}$.

RFID Chip

The sensitivity of the chip is an important parameter for long-range applications. For this reason, the NXP UCODE G2iL chip was chosen for its high sensitivity of -18 dBm . The chip impedance is $23 - j224 \Omega$ at 915 MHz is modeled by a 0.77 pF capacitor connected in parallel with a 2200Ω resistor [11].

Matching Circuit

The matching to the chip is achieved by an inductively coupled loop. The matching loop acts as an impedance transformer and the input impedance seen at the loop terminals is given by

$$Z_{in}=Z_{loop}+\frac{(2\pi fM)^2}{Z_a} \quad (3)$$

Where M is the mutual inductance of the transformer, and Z_a is the antenna impedance [7]. Z_{loop} is the impedance of the matching loop given by (4), whereas L_{loop} is the self-inductance of the loop given by

$$Z_{loop}=j2\pi fL_{loop} \quad (4)$$

The loop also includes a zigzag line to reduce its size. Additionally, this makes the antenna more intertwined with the loop, resulting in a stronger coupling.

$$Z_{loop}=j2\pi fL_{loop} \quad (4)$$

The loop also includes a zigzag line to reduce its size. Additionally, this makes the antenna more intertwined with the loop, resulting in a stronger coupling.

RESULTS AND DISCUSSION

The two antennas were simulated using the CST Microwave Studio software. First, the 90° zigzag antenna was simulated and matched to the chip. The input impedance at the loop terminals where the chip is attached is shown in Fig. 3. It is clear that an excellent match to the chip has been achieved. The power transmission coefficient τ was calculated to be 0.9991. The 3D radiation pattern is shown in Fig. 3. It is similar to traditional dipole antennas, with a slight shift caused by the matching loop.

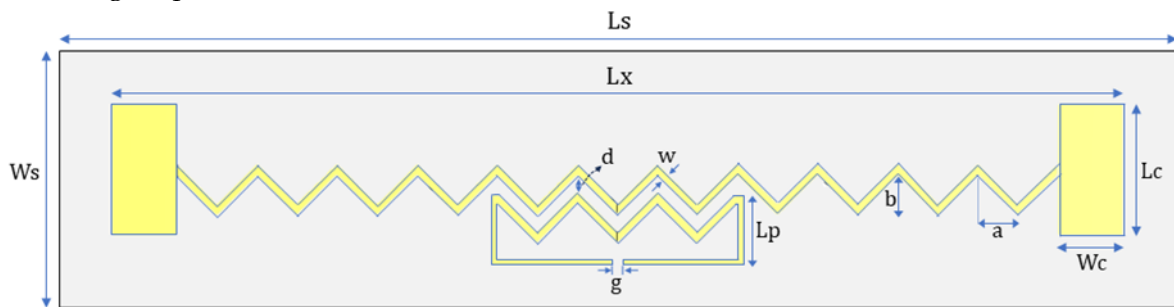


Fig 1: The geometry of the designed 90° zigzag RFID tag antenna resonates at 920 (MHz), simulated using CST software on a Kapton substrate. The antenna material is copper, and its thickness is 35 μm . The antenna was matched to an RFID tag with a complex impedance.

The 90° zigzag antenna achieved a maximum directivity and gain of 2.33 dBi and 2.21 dBi, respectively, and a radiation efficiency of -0.1217 dB or 97%. Meanwhile, the maximum directivity and gain of 45° zigzag are 2.24 dBi and 1.89 dBi, respectively, with a radiation efficiency η_r of -0.348 dB, corresponding to 92%. Although the 90° zigzag antenna achieved a significant improvement in gain compared to the 45° zigzag antenna, it had a longer axial length, as shown in Tab. 1.

For comparison, a straight dipole on a Kapton substrate was designed and simulated to oscillate at 920 MHz. The antenna dimensions were 1 mm wide and 151.4 mm. The gain and directivity were 1.9 dBi and 1.93 dBi, respectively.

The high efficiency of the 90° zigzag is due to its orthogonal segments that radiate fields that do not cancel each other out. The two antennas were compared to previous meander and zigzag dipole RFID tag antennas. The comparison is shown in Table. 2. The table shows that meander antennas generally provide lower gain than zigzag antennas. The meander antenna in [12] has some bends and is loaded with split ring resonators SRR to achieve the required shortening, resulting in a high gain of 1.96 dBi and a radiation efficiency of -0.002138 dB and 99.95%. The 90° zigzag achieved an even higher gain of 2.21 dBi, but its axial length is the highest.

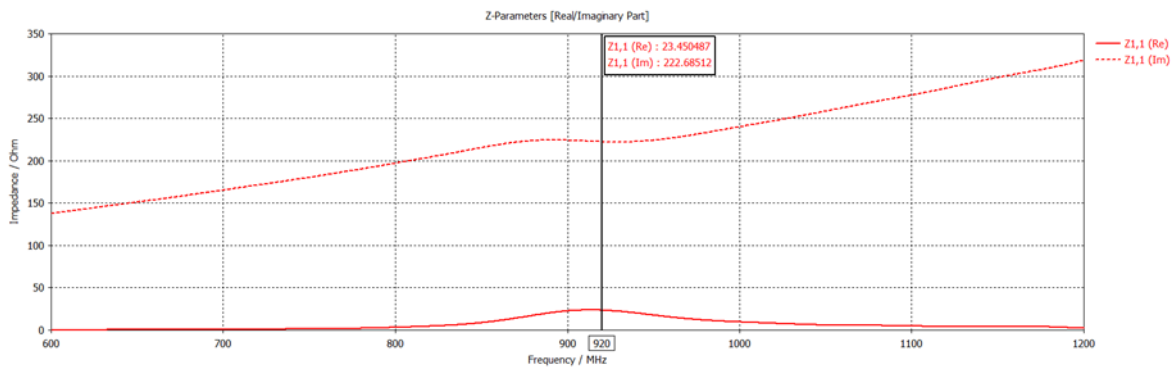


Fig. 2: The real and imaginary parts of the input impedance of the antenna after matching are approximately equal to the conjugate of the equivalent impedance of the RFID IC.

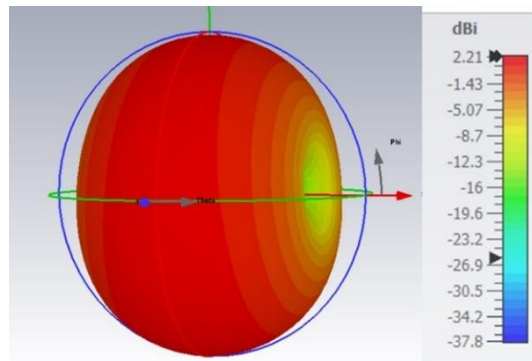


Fig. 3: 3D radiation pattern of the 90° zigzag RFID tag antenna resonates at 920 (MHz); the maximum gain is 2.21 dBi.

CONCLUSION

In this article, we presented two designs of passive RFID zigzag dipole tag antennas on a Kapton substrate, whose bending angles of the zigzag lines were 90° and 45°. Each antenna resonates in the middle of the frequency band intended for UHF RFID applications in Malaysia. The main objectives were to reduce the antenna size, maintain high gain, and ensure good matching to the RFID chip. The design and optimization of the antennas were performed using CST software. The 90° zigzag size was 108.6 × 19.7 mm and the gain was 2.21 dBi. And the 45° zigzag size was 85.5 mm and the gain was 1.89 dBi.

REFERENCES

- [1] M. Alam, K. A. Shakil, and S. Khan, Eds., *Internet of Things (IoT): concepts and applications*. Cham, Switzerland: Springer, 2020.
- [2] Y. B. Zikria, R. Ali, M. K. Afzal, and S. W. Kim, 'Next-Generation Internet of Things (IoT): Opportunities, Challenges, and Solutions', *Sensors*, vol. 21, no. 4, p. 1174, Feb. 2021.
- [3] Čolaković and M. Hadžialić, 'Internet of Things (IoT): A review of enabling technologies, challenges, and open research issues', *Computer Networks*, vol. 144, pp. 17–39, Oct. 2018.
- [4] Ahmadihaji, R. Izquierdo, and A. Shih, 'From Chip-Based to Chipless RFID Sensors: A Review', *IEEE Sensors J.*, vol. 23, no. 11, pp. 11356–11373, Jun. 2023.
- [5] H. Stockman, 'Communication by Means of Reflected Power', *Proc. IRE*, vol. 36, no. 10, pp. 1196–1204, Oct. 1948.
- [6] G. Marrocco, 'The Art of UHF RFID Antenna Design: Impedance-Matching and Size-Reduction Techniques', *IEEE Antennas Propag. Mag.*, vol. 50, no. 1, pp. 66–79, Feb. 2008.
- [7] K. V. S. Rao, P. V. Nikitin, and S. F. Lam, 'Antenna Design for UHF RFID Tags: A Review and a Practical Application', *IEEE Trans. Antennas Propag.*, vol. 53, no. 12, pp. 3870–3876, Dec. 2005.
- [8] 'Malaysian Communications And Multimedia Commission (MCMC) | Suruhanjaya Komunikasi dan Multimedia Malaysia (SKMM) - Home'. Accessed: May 14, 2023. [Online]. Available: <https://www.mcmc.gov.my/skmmgovmy/files/attachments/SRSP530RFID.pdf>
- [9] C. A. Balanis, *Antenna theory: analysis and design*, Fourth edition. Hoboken, New Jersey: Wiley, 2016
- [10] H. Nakano, H. Tagami, A. Yoshizawa, and J. Yamauchi, 'Shortening Ratios of Modified Dipole Antennas', *IEEE Trans. Antennas Propag.*, vol. 32, no. 4, pp. 385–386, Apr. 1984.
- [11] NXP Semiconductors, 'NXP UCODE G2iL'. Accessed: Aug. 15, 2024. [Online]. Available: https://www.nxp.com/docs/en/data-sheet/SL3S1203_1213.pdf
- [12] Aznabet, M. Ennasar, O. El Mrabet, S. Tedjini, and M. Khalladi, 'Meander-Line UHF RFID Tag Antenna Loaded with Split Ring Resonator', in *2016 5th International Conference on Multimedia Computing and Systems (ICMCS)*, Marrakech, Morocco: IEEE, Sep. 2016, pp. 757–759.
- [13] S. Bhaskar and A. K. Singh, 'A Compact Meander Line UHF RFID Antenna for Passive Tag Applications', *PIER M*, vol. 99, pp. 57–67, 2021.
- [14] D. Yu, Y. Ma, and Z. Zhang, 'UHF Band Tag Antenna Design in RFID System', in *2009 Asia Pacific Microwave Conference*, Singapore, Singapore: IEEE, Dec. 2009, pp. 512–515.
- [15] P. W. Sarr, I. Dioum, A. Diop, D. Ba, M. M. Khouma, and I. Gueye, 'A New Broadband Compact Meander Dipole Antenna for RFID Applications', in *2022 International Conference on Electrical, Computer and Energy Technologies (ICECET)*, Prague, Czech Republic: IEEE, Jul. 2022, pp. 1–6.
- [16] N. M. Faudzi, M. T. Ali, I. Ismail, H. Jumaat, and N. H. M. Sukaimi, 'A Compact Dipole UHF-RFID Tag Antenna', in *2013 IEEE International RF and Microwave Conference (RFM)*, Penang, Malaysia: IEEE, Dec. 2013, pp. 314–317.
- [17] S. Bhaskar and A. K. Singh, 'Meander Line Tag Antenna with Inductively Coupled Parasitic Element and T-Loop Feed', in *2017 International Symposium on Antennas and Propagation (ISAP)*, Phuket: IEEE, Oct. 2017, pp. 1–2.
- [18] S. Wickramasinghe, J. Jayasinghe, and M. Senadeera, 'A Miniaturized Printed Dipole with Non-Uniform Meander Lines for Ultra High Frequency – Radio Frequency Identification Passive Tags', in *2022 International Research Conference on Smart Computing and Systems Engineering (SCSE)*, Colombo, Sri Lanka: IEEE, Sep. 2022, pp. 262–267.
- [19] Yejun He and Bing Zhao, 'A novel UHF RFID dual-band tag antenna with inductively coupled feed structure', in *2013 IEEE Wireless Communications and Networking Conference (WCNC)*, Shanghai, Shanghai, China: IEEE, Apr. 2013, pp. 2739–2743.
- [20] V. H. Nguyen et al., 'Improving Radiation Characteristics of UHF RFID Antennas by Zigzag Structures', in *the 2011 International Conference on Advanced Technologies for Communications (ATC 2011)*, Da Nang, Vietnam: IEEE, Aug. 2011, pp. 102–105.

Determination of Tramadol and Codeine Using a Paper Screen Printed Electrode Coupled Colorimetric Device

Salamatu Hayatu^{1,2*}, Abdulrahman A Audu², Maryam D. Mahmud¹

¹Department of Pure and Applied Chemistry, Faculty of Science, Kaduna State University, Kaduna
P.M.B 2339, Nigeria

²Department of Pure and Industrial Chemistry, Faculty of Science, Bayero University, Kano P.M.B 3011, Nigeria

*Corresponding author's E-mail: salamatu.hayat@kasu.edu.ng

Abstract: We present a paper-based screen- printed electrode coupled colorimetric device for the presumptive and confirmatory analysis of tramadol and codeine. In this study, we utilized AuNPs (gold nanoparticles) to serve both as a colorimetric probe and as modifier on the paper electrode in other to enhance the sensitivity in voltametric detection. Tramadol and codeine were successfully detected in acetate buffer under optimized pH conditions, using differential pulse voltammetry (DPV) and cyclic voltammetry (CV), respectively. The colorimetric analysis produced a positive color change, while the voltametric analysis exhibited a good linear range between 0.04 to 0.4 mM, which gave $R^2=0.9018$ and $R^2=0.9725$ with a detection limit of 2.3 mM and 0.2 mM for tramadol and codeine respectively. The sensor demonstrated good reproducibility and was evaluated using urine samples from addicts.

Keywords— colorimetry, screen printed electrode, tramadol, codeine.

INTRODUCTION

Illicit or hard drugs are illegal substances that are highly addictive and pose serious risks to both people and the environment [1]. Opioids, known for their effective pain-relieving effects, are often prescribed to manage severe pain. However, frequent or excessive use of these substances can lead to a strong physical dependence that may develop into addiction [2]. Drug abuse is the misuse and addiction to medicinal opioid products. It is associated with a myriad of medical, social, and legal problems. Unfortunately, the widespread increase is evident [3]. The abuse of these drugs poses a global challenge, addressing this issue necessitates an interdisciplinary approach. The discovery, production, trafficking, and consumption of illicit drugs have been constantly growing, leading to heavy consequences for environment, human health, and society in general [4]. Research shows the prevalence of any drug use in Nigeria was estimated at 14.4 per cent or 14.3 million people aged between 15 and 64 years. The extent of drug use in Nigeria was comparatively high when compared with the 2016 global annual prevalence of any drug use of 5.6 per cent among the adult population. Cannabis was the most commonly used drug followed by opioids, mainly the non-medical use of prescription opioids and cough syrup [5].

THEORY/LITERATURE REVIEW

Detection of these drugs usually involves a two-step method [4, 6-7]. Initially, a quick presumptive test, such as color/spot tests, microcrystalline tests, ultraviolet spectroscopy, thin-layer chromatography (TLC), immunoassays, or urine dipstick tests, is conducted for screening. Subsequently, a more precise confirmatory step is performed. Presumptive testing is generally more cost effective and allows on-site measurements by untrained personnel, whereas

conventional/confirmatory methods (e.g., high-performance liquid chromatography (HPLC), portable Raman spectroscopy, liquid chromatography-mass spectroscopy (LC-MS) or gas chromatography-mass spectroscopy (GC-MS), fluorescence spectroscopy [3, 6-9] are expensive, require skilled personnel, involve complex analytical methods, and are unsuitable for on-site analysis. Colorimetry is commonly used in microfluidic paper-based devices, but combining it with electrochemical sensors provides increased sensitivity and selectivity. The need for rapid screening system necessitates the development of simple and portable/inexpensive platforms for the detection of abuse drugs [10-13]. As such, we propose a paper colorimetric sensor coupled with voltametric detection for both presumptive and confirmatory tests, respectively. Gold nanoparticles (AuNPs) are highly stable metal nanoparticles with several outstanding features, including facile synthesis and surface modification, excellent biocompatibility, and strong surface plasmon resonance in the visible region of the spectrum, making them ideal for naked-eye detection of analytes [3]. They exhibit unique optical and electrochemical properties and are widely used for sensing various analytes [14]. AuNPs was used on this sensor as modifiers to enhance the sensitivity of the sensor device. Various sensors have been applied in the voltametric detection of codeine [15-18] and tramadol [19-21], but none have reported this current method.

MATERIALS

All chemicals used were of analytical grade. Chloro auric acid (HAuCl₄), and silver conductive ink from Sigma Aldrich (USA), sodium citrate dihydrate, sodium acetate, and acetic acid from Kermel chemicals (China), potassium ferricyanide, and potassium chloride from Harris reagent (England), KCl.Ag from Radiometer analytical (France), lead (II) chloride, L(-)-Ascorbic acid, and urea from HmbG chemicals, uric acid, and HCl from Sigma Aldrich (Germany), sodium chloride, glucose, and citric acid from R&M chemicals (UK), phosphate buffer from Bendosen laboratory chemicals (Malaysia), pure tramadol powder and codeine syrup was obtained from NDLEA (national drug law enforcement agency), metallic gold card obtained from supplier.

EXPERIMENTAL

Field emission scanning electron microscopy-Energy dispersive x-ray spectroscopy (FESEM-EDX) was used to examine the morphology and elemental spectra (constituents) of the AuNPs. Transmission electron microscopy (TEM) was used to examine the shape and sizes of AuNPs. UV-Vis spectrophotometer (Lambda 35 UV-Vis spectrometer, Perkin Elmer USA) was used to analyze the changes in absorbance corresponding to the presence of the drugs. DropSens potentiostat (United Kingdom) and Autolab potentiostat controlled by Nova software 2.1.4 were used for the electroanalytical measurement (differential pulse voltammetry and cyclic voltammetry), by coupling to a computer and the sensor strip, which has three electrodes: a working electrode, a counter electrode, and a reference electrode.

Device Fabrication

Two distinct patterns were created in Corel Draw. The first pattern, which consist of circles with a diameter of 1.6 cm, was printed on a gold card using a printer. The second pattern, representing the electrode layout (comprising the working electrode (WE), reference electrode (RE), and counter electrode (CE)), was printed on an A4 laser sheet using a HP LaserJet 5100M printer. The electrode layout design on the laser sheet was exposed to a mesh, which was then used for screen printing silver ink onto the gold card [22]. The card was cured for 30 minutes at 120°C, after which individual electrochemical cells or sensor strips were cut out. The working electrode was modified with gold nanoparticles as shown in fig 1. For the screen-printed paper electrode, the working electrode was drop-coated with 10 µL of AuNPs, and the solution was allowed to dry at room temperature [23].

The reference electrode was modified with 5 μL PbCl_2 and 10 μL KCl . Ag to form the Ag/AgCl reference electrode. The Au-modified screen-printed electrode (AuMSPE) was then used for electrochemical analysis. For the colorimetric test, 10 μL of AuNPs was drop-coated onto separate working electrodes. Upon subsequent addition of 10 μL of 100 μM tramadol and 100 μM codeine, a change in colour was observed.

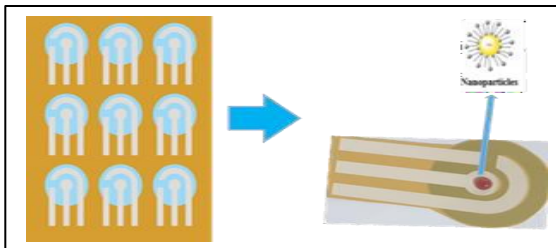


Fig. 1: Image of SPE

Synthesis of Gold Nanoparticles

In 200 mL of deionized water, 7.0 mg of HAuCl_4 was dissolved to create a pale-yellow solution. 50 mL of the solution was allowed to boil under vigorously stirred, and 5 mL of 40 mM sodium citrate was added dropwise, until a steady deep red color was obtained after 15 minutes of continuous heating and stirring [24]. The solution was kept at or below 7°C .

Colorimetric Analysis

The drug samples (codeine sulfate, and tramadol) were prepared by first creating a 1 mmol L^{-1} stock solution of each drug in water. Working standard solutions of different analyte concentrations were then prepared by diluting the stock solutions with double- distilled water [25]. To conduct the experiment, a solution of AuNPs was first dropped onto the working electrode, followed by the addition of the drug solutions. A colour change was observed, indicating the interaction between the drugs and the modified electrode.

RESULTS AND DISCUSSION

Field Emission Scanning Electron Microscopy-Energy Dispersive X-ray Spectroscopy

Fig. 2A provide the FESEM image of Ag ink SPE, showing an image saturated with Ag particles, which are not in nano size. Fig. 2C gives the EDX spectral image of Ag SPE. From the spectral image, there is one sharp peak of Ag with some small peaks of C and O. The dominant peak shows the high amount of Ag present. Fig. 2B shows small, tiny deposits of AuNPs on the surface of Ag ink SPE. The AuNPs are widely dispersed. Fig. 2D provides the EDX spectral image of AuNPs. The spectral images show sharp peak of Au with smaller peaks of O and C, which is attributed to the carbon based. These results indicate AuNPs dominates the surface and is widely distributed. It also validates the method used for synthesizing AuNPs and the purity of the AuNPs.

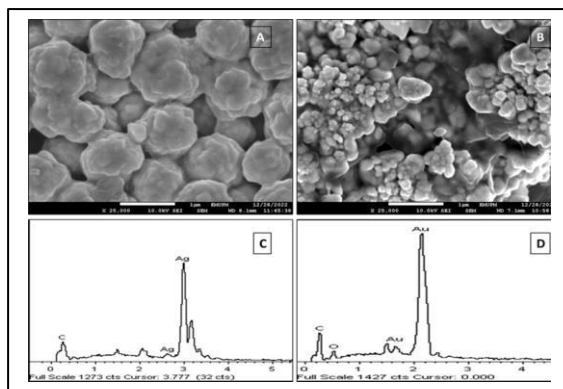


Fig. 2: FESEM-EDX image of (A and C) AgSPE (B and D) AuMSPE

Transmission Electron Microscopy

Fig. 3 illustrates the shape of AuNPs, which is assumed to be spherical. AuNPs are typically known to exhibit triangular, spherical, and hexagonal shapes. Particle sizes obtained from TEM analysis are within the nano size range, ranging from 15 nm to 40 nm. The TEM analysis further confirms that the size of AuNPs falls within the nano size range.

Colorimetry and UV-Vis Spectroscopy

Colorimetric studies were conducted for naked-eye discrimination without the use of sophisticated equipment. Figure 4A shows an image captured with a phone camera with a resolution of 1440 x 3200 pixels. Different responses were observed for each drug, indicating a unique fingerprint for each drug. Upon addition of 20 μ l of tramadol and codeine to AuNPs, the deep red color of the AuNPs changed to purple (lilac) and a much lighter purple, respectively. These results are consistent with those reported in the literature [14]. Figure 4B shows the UV-Vis absorption spectra of tramadol, codeine, and AuNPs. Tramadol gave broad overlapping peaks between 206.36nm to 263.06nm, and codeine gave a sharp broad peak at 261.13 nm. These peaks correspond to σ - σ^* bonding interactions. A broad absorption band was observed at 526.32 nm for AuNPs, which is attributed to σ - π bonding interaction, but due to the wide wavelength range of 200 to 600nm used for all the substances, including AuNPs, the band for AuNPs suppresses to a very low intensity, which makes the peak invisible when plotted with other substances. AuNPs with tramadol gave broad overlapping peaks at 210.05nm, 232.94nm, 374.59nm and a broad band at 536.16nm. AuNPs with codeine gave sharp absorption peak at 211.70nm, while the peaks at 237.26nm and 560.26nm suppresses. In summary the observed peaks are attributed to absorption of codeine and tramadol, the surface plasmon resonance of AuNPs and the potential formation due to the interactions between AuNPs with codeine and tramadol. The shift in the peak positions and the appearance of additional peaks suggest that the interaction between AuNPs with codeine and tramadol has influenced the optical properties.

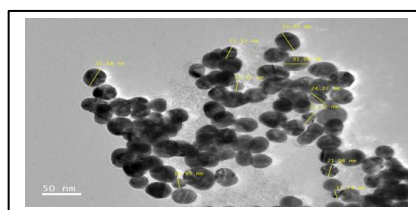


Fig. 3: TEM image of AuNPs

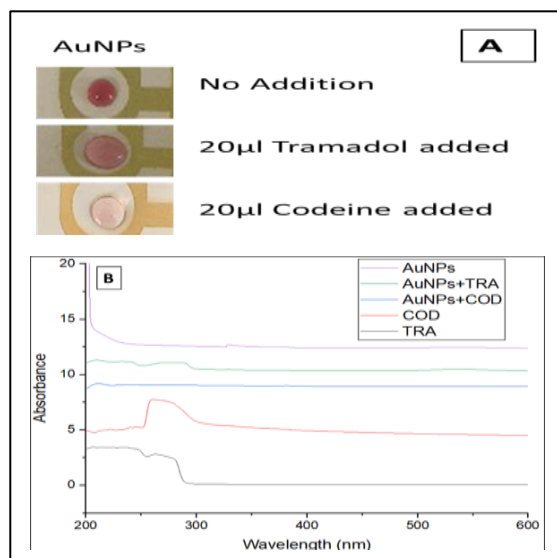


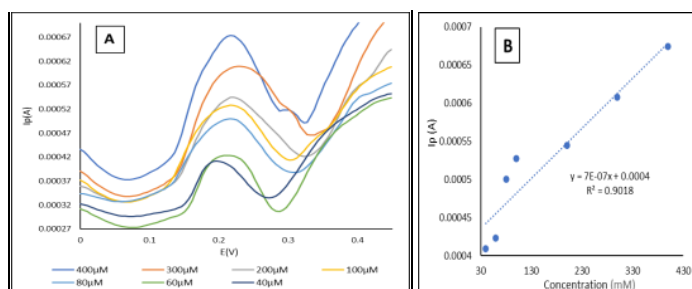
Fig. 4: (A) Colorimetric study (B) UV-Vis spectra

Cyclic and Differential Pulse Voltammetric Study of tramadol and Codeine

The sensitivity of detection was assessed by conducting a DPV and CV scan for different concentrations of tramadol and codeine ranging from 0.01 mM to 0.4 mM and 0.04 mM to 0.24 mM respectively using AuMSPE. There was no leaching of AuNPs during experiment, as AuNPs was strongly attached onto the surface of Ag SPE, also reported by [24]. Figures 5A and 5B demonstrate that the peak current increases as the concentration of tramadol increases, showing a proportional relationship between the peak current and the concentration of tramadol. The calibration plots showed good linear regression values ($R^2=0.9018$) and ($R^2=0.9725$) for tramadol and codeine respectively. The limit of detection (LOD) was calculated as 2.3 mM and 0.2 mM for both tramadol and codeine respectively.

Validation and Real Sample Application

The applicability of the proposed method was evaluated by analysis of codeine and tramadol in urine samples. The result obtained for the original samples and for samples spiked with codeine and tramadol was validated with GC-MS analysis, and the data obtained in Table 1 and 2 shows good correlation between the developed method and the standard method.



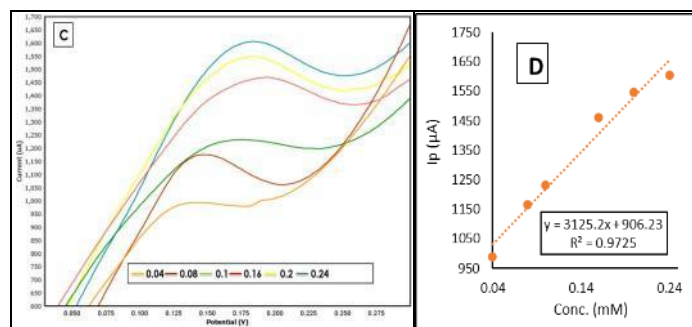


Fig. 5: (A and B) DPV and calibration plot for 0.04 to 0.4mM tramadol (C and D) CV and calibration plot for 0.04 to 0.24mM codeine

Table 1: Determination of Tramadol in real sample

Sensor	Tramad ol Added (mM)	Tramad ol Found (mM)	% Recovery
AuMSP E	Tramado l	2.3 mM (LOD)	
	0.03	0.033	110
GC-MS	0.2	0.16	80
	0.03	0.025	83.7
	0.2	0.17	85

Table 2: Determination of Codeine in real sample

Sensor	Codein e Added (mM)	Codein e Found (mM)	% Recover y
AuMSP E		0.2 mM (LOD)	
	0.04	0.032	80.0
GC-MS	0.3	0.283	94.3
	0.04	0.032	80.0
	0.3	0.245	81.6

CONCLUSION

The AuMSPE coupled colourimetric device was successfully fabricated and utilized for the colourimetric and voltametric detection of tramadol and codeine. The sensitivity of the sensor was enhanced by modifying it with AuNPs, which also served as a colorimetric probe for both drugs. This device represents the first reported instance of detecting tramadol and codeine using this dual method. Calibration studies for both drugs showed a good linear response, with a low limit of detection in the range of 0.2mM and 2.3mM for codeine and tramadol respectively. The sensor was successfully applied on urine samples from addicts.

REFERENCES

- [1] Sanghavi, B. J., Wolfbeis, O. S., Hirsch, T., & Swami, N. S. *Microchim Acta* (2015) 182:1–41.
- [2] De Araujo, W. R., Cardoso, T. M. G., da Rocha, R. G., Santana, M. H. P., Muñoz, R. A. A., Richter, E. M., Coltro, W. K. T. (2018). *Analytica Chimica Acta*, 1034, 1–21.
- [3] Mohseni, N., Bahram, M., & Baheri, T. (2017). *Sensors and Actuators, B: Chemical*, 250, 509–517.
- [4] Rycke, E. De, Stove, C., Dubrue, P., Saeger, S. De, & Beloglazova, N. (2020). *Biosensors and Bioelectronics*, 169, 112579.
- [5] National Bureau of Statistics. (2018). Retrieved from <https://nigerianstat.gov.ng/elibrary/read/881>.
- [6] Musile, G., Wang, L., Bottoms, J., Tagliaro, F., & McCord, B. (2015). *Analytical Methods*, 7(19), 8025–8033.
- [7] Bazyar H (2023). *Sensors* 23:5856.
- [8] Garcia-gutierrez E, Lledo-fernandez C (2013) *Chemosensors*.
- [9] Ali EMA, Edwards HGM (2016). *Drug Test Anal*.
- [10] Coltro, T., Cheng, C., Carrilho, E., & Jesus, D. P. De. (2014). *Electrophoresis*, 00, 1–16.
- [11] Toniolo, R., Pizzariello, A., Impellizzieri, F., Piccin, E., & Bontempelli, G. (2013). *Electrophoresis*, 34, 1–7.
- [12] Schmidt-Speicher, L. M., & Länge, K. (2021). *Current Opinion in Electrochemistry*, 29, 100755.
- [13] Nesakumar, N., Kesavan, S., Li, C. Z., & Alwarappan, S. (2019). *Journal of Analysis and Testing*, 3(1), 3–18.
- [14] Lodha, A., Pandya, A., Sutariya, P. G., & Menon, S. K. (2014). *RSC Advances*, 4(92), 50443–50448.
- [15] Habibi B, Abazari M, Pournaghi- Azar MH (2014) *Colloids SurfB* 114: 89–95.
- [16] Afkhami, A., Khoshshafar, H., Bagheri, H., & Madrakian, T. (2014). *Sensors & Actuators: B. Chemical*, 203, 909–918.
- [17] Hossein, M., & Rasouli, F. (2014). *Electroanalysis*, 2033–2042.
- [18] Li, Y., Li, K., Song, G., Liu, J., Zhang, K., & Ye, B. (2013). *Sensors & Actuators: B. Chemical*, 182, 401–407.
- [19] Zhao, J., Kan, Y., Chen, Z., Li, H., & Zhang, W. (2023). *Biosensors* 2023, 13(2), 284.
- [20] Mousaabadi, K.Z.; Ensafi, A.A.; Rezaei, B. *Chemosphere* 2022, 303,135149.
- [21] Aflatoonian, M. R., Tajik, S., Aflatoonian, B., & Beitollahi, H. (2020). *Frontiers in Chemistry*, 8(November), 1–8.
- [22] De Araujo, W. R., & Paixão, W. R. (2014). *Analyst*, 139(11), 2742–2747.
- [23] Hayatu, S., Audu, A. A., Ladan, M., Yusof, N. A., (2023). *MJAS*, 27(5), 993–1002.
- [24] Tukur, S., Azah Yusof, N., & Hajian, reza. (2014). *IEEE Sensors Journal*, (II), 1–1.
- [25] Adkins, J., Boehle, K., & Henry, C. (2015). *Electrophoresis*, 1–33.

ENVIRONMENTAL MONITORING AND REMEDIATIONS

Synthesis and Optical Properties of Metal-Oxide Frameworks (MOFs) Nanohybrids for Photocatalytic Dye Degradation of Wastewater Treatment Application

Suriati Paiman^{1,2*}, Che Syazana Che Ab Razak¹, Suresh Sagadevan³, Erum Pervaiz⁴

¹ Department of Physics, Faculty of Science, Universiti Putra Malaysia, 43400 UPM Serdang, Selangor, Malaysia

² Functional Nanotechnology Devices Laboratory (FNDL), Institute of Nanoscience and Nanotechnology, Universiti Putra Malaysia, 43400 UPM Serdang, Selangor, Malaysia

³ Nanotechnology and Catalysis Research Centre (NANOCAT), University of Malaya, 50630 Kuala Lumpur, Malaysia

⁴ Department of Chemical Engineering, School of Chemical & Materials Engineering, National University of Sciences and Technology, Islamabad, Pakistan

*Corresponding author's phone: +603-9769 6661 E-mail: suriati@upm.edu.my

Abstract: In this work, we synthesized and characterized metal-organic frameworks (MOFs) UiO-66, ZIF-67, graphitic carbon nitride (g-C₃N₄), and nanohybrids. After synthesising pristine materials (g-C₃N₄, UiO-66, and ZIF-67), nanohybrids (CZ, and CU) were formed. The materials were characterised using XRD, UV-Vis, Zeta potential, and dynamic light scattering (DLS). X-ray diffraction (XRD) analysis confirmed MOF formation, and optical property analysis revealed their light-related behaviour. Initial photocatalytic degradation experiments on methylene blue (MB) need further testing to confirm their accuracy. This study suggests ways to develop nanohybrids for sustainable applications.

Keywords: MOFs, g-C₃N₄, Nanohybrids, Zeta Potential, Photocatalytic Degradation and Optical Properties.

INTRODUCTION

Novel materials that support sustainable technologies are needed to reach net-zero emissions by 2050. Due to their structural and electrical properties, metal-organic frameworks (MOFs) as UiO-66 and ZIF-67 and graphitic carbon nitride (g-C₃N₄) are attractive materials (4). MOFs are useful for catalysis and environmental remediation due to their high surface area, tunable porosity, and chemical flexibility. Due to its photocatalytic capabilities with visible light, g-C₃N₄, a semiconductor without metal components, is of interest (8). This is crucial for energy and environmental applications. Hybrids of g-C₃N₄ and MOFs can improve stability, electronic interactions, and photocatalytic performance. This study strategically combines g-C₃N₄ with UiO-66 and ZIF-67, a combination that has yet to be reported.

LITERATURE REVIEW

Recent studies have explored novel photocatalytic systems combining MOFs and other nanomaterials for enhanced performance. A dual Z-scheme heterojunction of UiO-66(Zr)/MIL-125(Ti)-NH₂/g-C₃N₄ demonstrated improved photocatalytic activity for C-C bond

formation under visible light (1). Another study reported a g-C₃N₄@ZIF-67/NiS_x composite with 8.32 times higher hydrogen production than pure g-C₃N₄ (2). Coordination bond-connected UiO-66-NH₂(Zr/Ti)/ carboxyl-functionalized MXene heterostructures showed exceptional hydrogen evolution rates of 2187 $\mu\text{mol g}^{-1} \text{h}^{-1}$, surpassing most MOF-based photocatalysts (3). Additionally, g-C₃N₄/ZIF-67 nanocomposites exhibited improved photocatalytic dye degradation and hydrogen production, with 3.84 times greater H₂ production than bare g-C₃N₄ (4). These studies highlight the potential of combining MOFs, g-C₃N₄, and other nanomaterials for enhanced photocatalytic applications in various reactions.

MATERIALS

Reagents and chemicals of analytical grade were used to synthesize all the samples. The study used melamine with a 99% purity to synthesize pure g-C₃N₄, 1,4-benzenedicarboxylic acid (HBDC/BDC) with a 98% purity, zirconium (IV) chloride (ZrCl₄) with a 99.5% purity, N, N-dimethylformamide (DMF) with a 99.8% purity, and acetic acid with a 99% purity. The synthesis of ZIF-67 involved cobalt nitrate hexahydrate, 2-methylimidazole (2-MIM), and methanol.

EXPERIMENTAL

Synthesis of materials

(i) Synthesis of g-C₃N₄

The synthesis of graphitic carbon nitride (g-C₃N₄) begins with the preparation of melamine, which is heated to 550°C in a muffle furnace for 6 hours. The temperature is then maintained at 550°C for an additional 5 hours using a Carbolite furnace. After cooling, the resulting powder is ground to a fine texture, completing the synthesis of g-C₃N₄.

(ii) Synthesis of UiO-66

UiO-66 is synthesized by dissolving 150 mg of zirconium tetrachloride in 30 ml of dimethylformamide, followed by the addition of 115 mg of 1,4-benzene dicarboxylic acid and acetic acid. The solution is then transferred to a Teflon-lined autoclave for hydrothermal treatment. Afterward, the resulting precipitates were collected and separated, followed by multiple washings with distilled water and ethanol.

(iii) Synthesis of ZIF-67

To prepare ZIF-67, cobalt nitrate hexahydrate is dissolved in methanol, while 2-methylimidazole was dissolved in a separate beaker. The mixtures were then gradually combined, stirred, and aged for three days. The resulting solution was filtered using a nylon filter membrane to collect the purple ZIF-67 precipitate, which was subsequently washed with methanol and dried below the decomposition temperature of 60 °C until completely dry.

(iv) Synthesis of g-C₃N₄/ZIF-67 nanohybrid (CZ)

The ZIF-67/g-C₃N₄ nanohybrid (CZ) is synthesized by first preparing g-C₃N₄. A fresh ZIF-67 solution is then prepared following the pure ZIF-67 synthesis method. Once the ZIF-67 solution was ready, g-C₃N₄ was added and thoroughly mixed. The ZIF-67/g-C₃N₄ nanohybrid forms after a three-day reaction at room temperature. The same method is used to prepare the CU hybrid sample (5).

Characterisation Techniques

The formed catalyst underwent compositional analysis and phase investigation using a powder X-ray diffractometer (RIGAKU Miniflex600c). The test used Cu-K α radiation with 2θ between 5° and 70°. The optical properties of all samples were obtained from UV-Vis- Nir Spectrophotometer UV3600 Shimadzu. The Zeta potential and dynamic light scattering (DLS) were measured using Nano Series from Malvern Tech. The study tested CZ, and CU nanohybrids for photocatalytic activity and adsorption using 40 mgL⁻¹ of MB at room temperature. The solution was darkened for 30 minutes, and the degradation experiment lasted 120 minutes. Samples were taken every 15 minutes, and UV-visible spectrophotometers (Perkin Elmer Lambda 35) measured MB solution degradation.

RESULTS AND DISCUSSION

The XRD pattern of the MOFs matched the simulated structure of ZIF-67 and UiO-66 from the Cambridge Structural Data file (CCDC 1429244 and 2054314). XRD examination validated the synthesis of all pure materials, including g-C₃N₄, ZIF-67, and UiO-66. Fig. 1(a) and 1(b) illustrate the XRD patterns for these materials. The distinctive peaks for g-C₃N₄ were at 12.97° and 27.57°, corresponding to the (100) and (002) planes. UiO-66 showed distinct peaks at 2θ values corresponding to planes (111), (200), (400), (600), and (731), while ZIF-67 peaks corresponding to planes (011), (002), (112), (022), (013), and (222). The XRD peaks match the literature (6), verifying the materials' formation and phases.

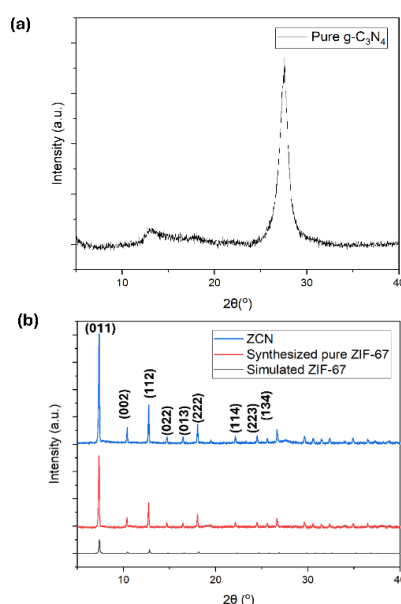


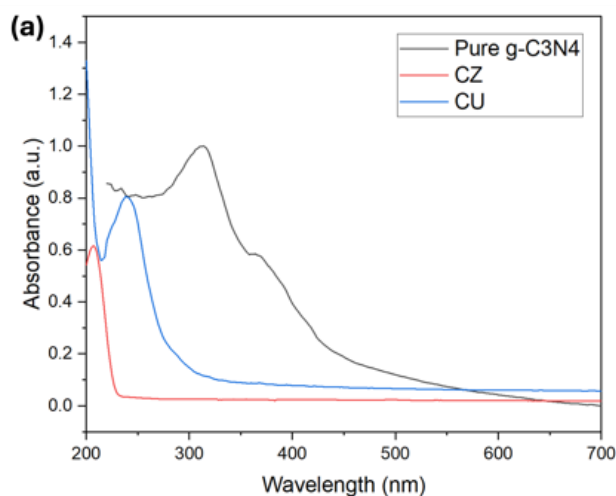
Fig. 1. XRD patterns of g-C₃N₄, ZIF-67 and CZ hybrid

Table 1 lists all pure and hybrid sample peaks. The CZ and CU hybrid samples showed distinct XRD peaks of pure ZIF-67 and UiO-66 from g-C₃N₄ peaks. MOF materials have distinctive crystalline structures, functionalization processes, and chemical compositions, which may explain the hybrid material's prominent ZIF-67 or UiO-66 peaks in the XRD pattern.

TABLE 1. XRD peak position of all samples

Sample	Peak positions
g-C ₃ N ₄	12.97°, 27.57°
ZIF-67	7.34°, 10.37°, 12.72°, 14.67°, 16.41°, 18.02°
UiO-66	7.35°, 8.49°, 11.98°, 17.04°, 25.67°, 30.7°
CZ	7.35°, 10.38°, 12.73°, 14.7°, 16.45°, 18.03°, 22.14°, 24.5°, 25.56°, 26.65°
CU	7.4°, 8.63°, 12.12°, 25.79°

The optical properties of pure and synthesized hybrids were studied using a UV-Vis spectrophotometer. The band gaps were estimated using the Taut plot (Fig. 3). This study found that the calculated bandgap values for all synthesised samples, including g-C₃N₄, ZIF-67, UiO-66, and their hybrids (CZ of 5.38 eV and CU of 4.27 eV), match the observed absorption edges and literature (7). This consistency confirms the accuracy of the synthesis and characterisation methods and the bandgap measurements in confirming the materials' electronic properties. The absorption edge and bandgap show that the electronic transitions responsible for absorption match the calculated energy gaps. Despite the hybrids' low g-C₃N₄, their bandgap values are consistent with expectations, suggesting that the g-C₃N₄ could improve their optical properties.



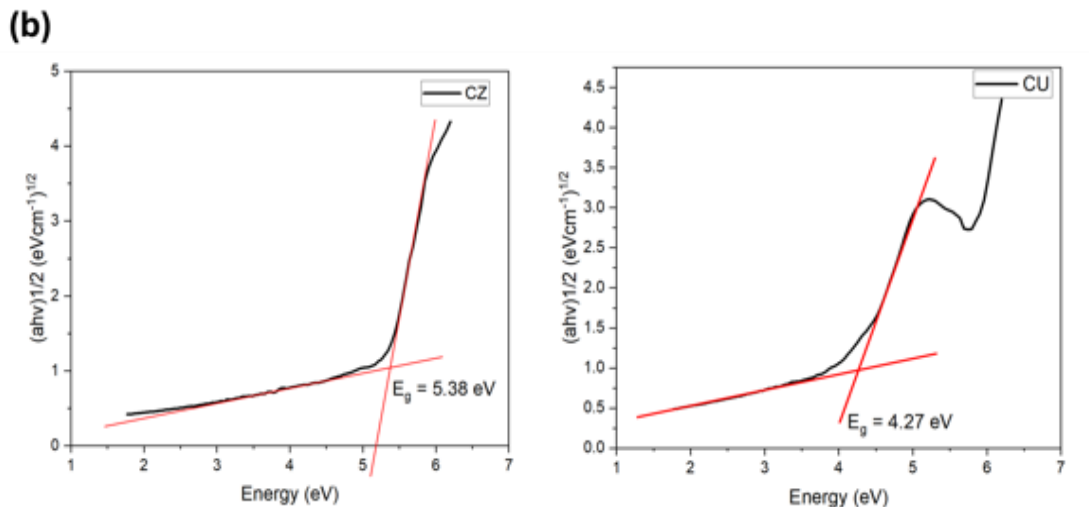
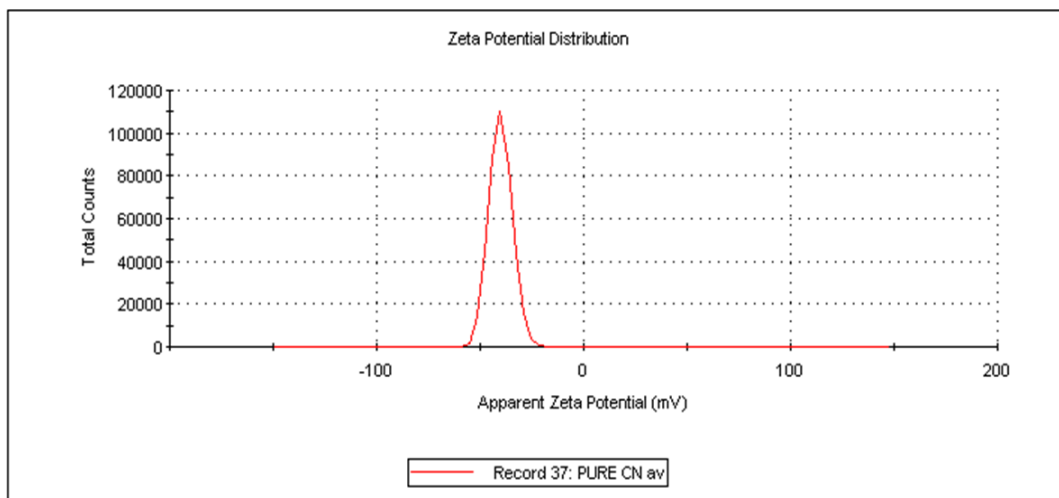


Fig. 2. (a) UV-visible absorbance spectra, (b) Tauc plots for CZ and CU.

Zeta potential and DLS analyses assessed charge stability and particle dispersion in synthesised materials. Pure g- C_3N_4 had the highest stability of the pure samples, with a zeta potential of -40.5 mV (Fig. 3), indicating well-dispersed particles and a uniform size distribution, indicating small. Pure UiO-66 and ZIF-67 showed moderate stability (-21.8 and -24.5 mV, respectively), indicating particle aggregation but overall stability. CZ hybrid showed low stability, with significant particle aggregation and a broad size distribution, which could affect performance. Unlike the CZ hybrid, the CU hybrid had moderate stability, like pure UiO-66, with some particle aggregation but better stability. These findings show that pure and hybrid materials have different particle dispersion and stability, which are important for photocatalytic applications.

Fig. 3. Zeta Potential Distribution for pure g- C_3N_4



CONCLUSION

In conclusion, g- C_3N_4 , UiO-66, and ZIF-67 and their composites have been successfully synthesised and have promising uses in photocatalysis. The successful formation of the pure and hybrid materials, containing g- C_3N_4 and MOFs, was confirmed through X-ray diffraction analysis. The UV-Vis spectroscopy results displayed absorption properties similar to the expected band edges and photon energies. Also, the limited amount of g- C_3N_4 in MOF hybrids hindered substantial

bandgap modification. This indicates that additional improvements in the synthesis process may be necessary to enhance the integration and interaction between g-C₃N₄ and MOFs.

ACKNOWLEDGEMENTS: This research was funded by the Ministry of Higher Education Malaysia under the Fundamental Research Grant Scheme (FRGS/1/2023/STG05/UPM/02/11).

REFERENCES

- [1] H. Sepehrmansourie, H. Alamgholiloo H, M.A. Zolfigol, N.N. Pesyan, M.M. Rasooli, "Nanoarchitecting a Dual Z- Scheme Zr-MOF/Ti-MOF/g-C₃N₄ Heterojunction for Boosting Gomberg– Buchmann–Hey Reactions under Visible Light Conditions," ACS Sustain Chem Eng., vol 11, no 8, pp. 3182–93, 2023.
- [2] Y. Zhang, Z. Jin, Boosting Photocatalytic Hydrogen Evolution Achieved by NiS_x Coupled with g-C₃N₄@ZIF-67 Heterojunction. The Journal of Physical Chemistry C. 2019.
- [3] L. Shi, C. Wu, Y. Wang, Y. Dou, D. Yuan, H. Li et al. Rational Design of Coordination Bond Connected Metal- Organic Frameworks/MXene Hybrids for Efficient Solar Water Splitting. Adv Funct Mater. 32, 2022.
- [4] K.C. Devarayapalli, S.P. Vattikuti, T.V.M Sreekanth, K.S. Yoo, P.C. Nagajyothi, J. Shim. Hydrogen production and photocatalytic activity of g-C₃N₄/Co-MOF(ZIF-67) nanocomposite under visible light irradiation. Applied Organometallic Chemistry, 34(3), 2020.
- [5] S. Shah, I. Mubeen, E. Pervaiz, H. Nasir, Facile and efficient synthesis of carboxylic terminated Ti₃C₂T_x nanosheets using citric acid, FlatChem, 41, pp100544, 2023.
- [6] S. Sunasee, K. H. Leong, K. T. Wong, G. Lee, S. Pichiah, I. Nah, B. Jeon, Y. Yoon & M. Jang, Sonophotocatalytic degradation of bisphenol A and its intermediates with graphitic carbon nitride. Environmental Science and Pollution Research., 26(2), pp 1082-1093, 2019.
- [7] S. Minallah, E. Pervaiz, M. U. Yousaf, M. B. K. Niazi, L. Honghong &M. Yang, Ternary adsorbent photocatalyst hybrid (APH) nanomaterials for improved abstraction of tetracycline from water. Separation Science and Technology., 55(15), pp 2623-2641, 2020.
- [8] A. Alaghmandfard, K.A Ghandi, Comprehensive Review of Graphitic Carbon Nitride (g-C₃N₄)–Metal Oxide- Based Nanocomposites: Potential for Photocatalysis and Sensing. Nanomaterials., 12(2), 2022.

Optimizing Bead Free PVDF Nonwoven Nanomembrane for Waste Cooking Oil (WCO) Removal in Wastewater

Yogapria **Sathianathan**¹, Amalina Binti Muhammad **Afifi**², Nor Ishida Binti Zainal Abidin³

¹*Department of Mechanical Engineering, University of Malaya, Kuala Lumpur 50603, Malaysia.*

²*Department of Mechanical Engineering, University of Malaya, Kuala Lumpur 50603, Malaysia.*

³*Department of Mechanical Engineering, University of Malaya, Kuala Lumpur 50603, Malaysia.*

**Corresponding author's phone: +603-79675385*

E-mail: yogapria@um.edu.my / amalina@um.edu.my

Abstract: The efficient separation capabilities of nonwoven nanomembranes have led to their increasing use in the treatment of wastewater, there also many research has been published in past studies for the nanomembrane usage for the treatment[39- 41]. The aim of this work is to create poly(vinylidene) fluoride (PVDF) nanomembranes with bead free and high surface porosity by electrospinning methods, which will aid in the adsorption of used cooking oil by providing more binding site for the contaminant. Nanofibers without beads were produced by fabricating PVDF membranes with polymer concentrations between 16 and 25 weight percent in a 7:3 solvent mixture of DMF and Acetone. Prior to and following adsorption, the membranes were evaluated using SEM. For effective oil adsorption, high porosity and homogeneous fiber shape were validated by the characterisation. The results showed that PVDF nanomembranes with greater polymer concentrations (25 wt%) had greater porosity and oil adsorption capacity with 70% of WCO removal from the oily wastewater. SEM analyse revealed uniform nanofiber structures with increased surface roughness post-adsorption. These findings support the effectiveness of PVDF nonwoven nanomembranes in oily water treatment, making them promising solution for wastewater management and environmental protection.

Keywords: PVDF,electrospinning, nanofiber, chitosan, waste cooking oil

INTRODUCTION

The significant amount of hazardous pollutants, including heavy metals, organic compounds, bacteria, oily molecules, and minerals, present a major risk to the environment and public health in untreated oily wastewater. It is projected by the World Health Organization (WHO, 2020) that two billion people worldwide have probably consumed water tainted with excrement, which can result in illnesses like cholera, typhoid, dysentery, and polio. In order to provide consumers with clean water, drastic measures were needed to preserve sustainable water management techniques and mitigate the effects of rising water pollution [1].

Oily wastewater has grown to be a significant environmental issue, mostly coming from home sources and the food and beverage sectors[2]. Domestic wastewater often contains oils and greases from household cleaning and cooking, which increase the overall pollutant load in municipal wastewater systems [3]. Moreover the food and beverage industry, known for its high-water usage and organic waste production, generates substantial amounts of wastewater containing fats, oils, and greases (FOGs) [4]. Traditional wastewater treatment facilities often struggle to separate oil and water emulsions, leading to secondary pollutants during preliminary treatment.

Improper management of oily wastewater disposal has led to environmental issues such as clogged sewage systems, disrupted biological treatment processes, and oil slicks on water surfaces that harm aquatic life [5]. The increasing volume of oily wastewater generated by industrial activity and population growth underscores the need for efficient treatment techniques. In 2019, approximately 209 million metric tons of edible oils were produced worldwide, with a significant portion used in homes and the food industry[6].

Traditional methods of treating oily wastewater have included physical techniques such as skimming and gravity separation, which utilize the different densities of oil and water to separate free oils [7]. However, these methods are often insufficient for dissolved or emulsified oils, necessitating more advanced treatment procedures. Furthermore, the chemical treatment method like chemical oxidation, flocculation, and coagulation have been conducted to remove oil but this step can generate secondary pollutants that require further treatment [8]. Biological treatment using activated sludge and biofiltration have proven in breaking down organic contaminants, including oils successfully although this method often require long retention periods and are sensitive to even the slightest environmental changes [9].

In addition, membrane technology has gained attention for its effectiveness in treating various contaminants present in wastewater recently from previous research. Membrane filtration such as microfiltration, ultrafiltration, nanofiltration, and reverse osmosis, are proven to offers higher removal efficiency, compact design, and the ability to handle a broad spectrum of pollutants. This processes use semi-permeable membranes to separate water and contaminants from oil based by focusing on factors like hydrophobicity, charge interaction, and size exclusion [10].Based on past research, microfiltration and ultrafiltration membranes are proven effective in separating emulsified oils and suspended particles from wastewater, hence making them ideal for large-scale applications due to their high permeate flux and low-pressure operation[11].

Despite its advantages, membrane technology faces challenges such as membrane fouling, which reduces permeability ,increases operating costs to treat the membrane for increasing the reusability [12]. Research to mitigate fouling and improve membrane performance include membrane modification, regular cleaning, and the application of anti-fouling coatings have to be further conducted to improvised the membrane technology in the remediation studies

Polyvinylidene fluoride (PVDF) membranes have emerged as a highly viable solution for oil-water separation due to their strong mechanical strength, chemical resistance, thermal stability, and durability [13]. PVDF's hydrophobic properties facilitate the removal of oils from water, while its high porosity and pore size distribution enhance filtration efficiency. The mechanical strength of PVDF membranes allows them to withstand physical damage and pressure changes typical in wastewater treatment applications [14]. Additionally, PVDF membranes offer design flexibility, as they can be produced in various forms, such as hollow fiber and flat sheet membranes, requiring less maintenance and replacement due to their chemical resistance [15].

The study focuses on the potential of PVDF membranes, particularly in separating waste cooking oil made from palm oil, to improve oil-water separation efficiency. The results aim to address rising concerns about water pollution and the global need for clean water resources by advancing sustainable and effective wastewater treatment technology.

LITERATURE REVIEW

Polyvinylidene fluoride (PVDF) is a semicrystalline polymer distinguished by its repeating unit $-(CH_2CF_2)_n-$, which provides great mechanical strength, strong chemical resistance, thermal stability, and aging resistance. These qualities are critical for their use in separation membranes

[16]. PVDF can additionally be processed easily into tubular, hollow fiber, and flat sheet membranes. PVDF dissolves in solvents such as DMAc, DMF, acetone, and NMP, making it easier to electrospun due to its exceptional mechanical, chemical resistance, hydrolytic stability, and thermal stability [17]. In particular, water purification has been the focus of recent research on PVDF membrane development and applications.

The β -phase exhibits remarkable ferroelectric and piezoelectric capabilities whereas the α -phase, with its trans-planar conformation, confers substantial mechanical strength and thermal stability [18]. For the polymer to be used in harsh filtering settings, its strong mechanical qualities are crucial. PVDF's composition has some of the strongest carbon-fluorine bonds in organic chemistry, giving it outstanding resistance to a wide range of solvents, acids, and base. Because of its chemical stability, PVDF can be used in harsh environments without affecting membrane dependability or long-term sustainability [19]. The low surface energy of the polymer contributes to its hydrophobic qualities, which renders it advantageous in numerous separation scenarios. PVDF fibrous membranes are typically made by phase inversion or electrospinning.

Phase inversion is another widely used method. It involves first dissolving PVDF in a solvent and then precipitating the polymer using a non-solvent medium [20]. This method produces a porous membrane structure with varied pore size and distribution. Both methods enable you to tailor membrane properties such as fiber diameter, pore size, and surface roughness, which is crucial for optimizing filtration performance. Electrospinning pulls a polymer solution into fine fibers, which are then collected on a collector to form a nonwoven mat [21]. This method yields membranes with large surface areas and porosity by creating fibers with sizes ranging from nanometres to micrometres.

A fabrication technology known for its ease of use and adaptability in creating nanofibers with unique morphologies is called electrospinning, and it was first used in 1993 [22]. The manufacturing of nanofibers from a wide range of materials, including polymers, ceramics, metals, and their mixtures, is made possible by this process, which constantly draws nanofibers from a viscoelastic fluid through the electrostatic repulsion between surface charges. Both before and after the electrospinning process, the surfaces of the nanofibers generated by this method can be functionalized or changed with molecular species or nanoparticles [23]. These nanofibers can display a variety of secondary morphologies, including porous, hollow, or core-sheath structures.

Electrospun nanofibers are created by applying electric force to melts or charged threads of polymer solutions to create fibers with nanometer-sized diameters [24]. These nanofibers' sizes and physical characteristics are greatly influenced by the kind of material and manufacturing process utilized to create them. Generally speaking, electrospinning produces a nonwoven fibrous mesh with pore diameters between three and five μm . High porosity are advantageous for applications including air filtration, microfiltration, and cell infiltration barriers, while smaller pores are required for broader applications [25]. The polymer that is employed has a significant impact on the electrospun membrane's pore size.

The limits of varying pore size using electrospinning parameters have been addressed by a number of different ways. These comprise the use of spacers that are transitory, adjustments made after electrospinning, and control over the distribution of fiber. To make electrospun nanofiber membranes with variable fiber diameters, porosities, and thicknesses, for example, a hot-pressing technique has been used consistently. The rejection fraction of particles for 0.2 μm particles can increase from 0% to almost 100% using this technique, which can considerably lower membrane porosity from about 86% to as low as 34% [26]. Particles as small as 0.1 μm can be rejected by some membranes made of small diameter nanofibers when they are hot-pressed

under high pressure. These membranes show less fouling and greater flow values without sacrificing particle rejection as compared to traditional microfiltration media.

The conductivity and viscosity of the polymer solution, the applied voltage, the needle tip-collector distance, and the ambient temperature and humidity all have an impact on the electrospinning process [27]. These parameters control both the extrinsic and intrinsic features of nanofibers. Due to their high surface area, light weight, and interconnected porous structure, electrospun polymeric nanofibers are particularly useful as membrane materials for environmental remediation. The distinct characteristics of these materials have prompted scholars and businesses to investigate their possibilities across several domains, such as serving as reinforcing fillers for advanced polymer composites.

A wide range of nanofibrous materials can be produced by varying the electrospinning parameters and the surrounding environment. An intricate yet crucial part of electrospinning is surface modification of nanofibers to improve their characteristics. Depending on the intended purpose, this method may entail the employment of different agents to obtain particular qualities, such as hydrophilicity or hydrophobicity. Modifications to the surface of electrospun polymeric nanofibrous membranes, for instance, have been demonstrated to greatly improve their effectiveness in water treatment, an area of extensive research.

The high porosity, microscale interstitial space, connectedness, and huge surface-to- volume ratio of nonwoven electrospun nanofiber meshes make them very useful for membrane fabrication [28]. The significance of electrospun materials in scientific and industrial breakthroughs is cemented by these features, which make them extremely promising for a variety of applications.

A significant advancement in the fabrication of PVDF nonwoven nanomembranes for the treatment of oily wastewater is the electrospinning method. Electrospinning facilitates the construction of efficient separation membranes by yielding nanofibers with specific properties. The method is especially well- suited to tackle the problems related to treating oily wastewater because of its capacity to alter surfaces and regulate fiber characteristics. Electrospinning's flexibility and adaptability enable the production of PVDF membranes with exceptional efficiency and performance. To further increase membrane efficacy, more study in this area should concentrate on adjusting electrospinning conditions and investigating creative improvements. To fully realize the potential of electrospinning in environmental applications— particularly in the sustainable treatment of oily wastewater and further research is necessary.

MATERIALS

Poly(vinylidene fluoride) (PVDF) was purchased from Thermo Scientific (United States of America). N,N- Dimethylformamide (DMF) and Acetone (Analytical Reagent) were purchased from R&M Chemicals (Selangor, Malaysia)

EXPERIMENTAL

This experiment include 3 phase including preparation of PVDF membrane, preparation of Simulated Oily Wastewater (SOW) and the characterization of the membrane.

Preparation of PVDF membrane.

Waste cooking oil was dissolved in 50 mg/L of water to produce a mixture that mimics WCO was stirred for three hours at room temperature at a speed of 150 rpm in order to ensure complete mixing and emulsion formation. The resulting SOW was then used for subsequent experiments.

The filtration process was done using a magnetic flow meter, which allowed for precise monitoring and control of the flow rate during the filtration process, ensuring consistent and accurate measurements. The membrane used was dried overnight at 70°C.

Preparation of Simulated Oilywastewater (SOW)

Waste cooking oil was dissolved in 50 mg/L of water to produce a mixture that mimics WCO was stirred for three hours at room temperature at a speed of 150 rpm in order to ensure complete mixing and emulsion formation. The resulting SOW was then used for subsequent experiments. The filtration process was done using a magnetic flow meter, which allowed for precise monitoring and control of the flow rate during the filtration process, ensuring consistent and accurate measurements. The membrane used was dried overnight at 70°C.

Characterization using Scanning Electron Microscope (SEM)

The morphology of the PVDF membrane was examined using SEM (Model: TM 3030, Hitachi). The membrane samples were mounted on carbon-tape aluminum holders and coated with a thin layer of platinum under vacuum to enhance conductivity and image quality. SEM images were taken at various magnifications to observe the surface structure and porosity of the membrane, providing detailed insights into its morphological characteristics.

RESULTS AND DISCUSSION

Performance in separation and filtration applications is greatly influenced by the structure of PVDF (Polyvinylidene Fluoride) membranes, especially those with a higher polymer content [29]. Higher pore diameters and a fibrous, net-like structure are seen in the SEM pictures of a PVDF membrane with a 25wt% concentration, as shown in Figure 3. These features are essential for effective separation procedures. The structural arrangement of these membranes is vital for their effective use in oil-water separation, industrial wastewater treatment, and even air filtration technologies.

Extensive study has been undertaken to determine the association between membrane morphology and functional efficacy. The permeability and selectivity of a membrane can be significantly impacted by its pore size and porosity [30]. The PVDF-25 membrane's larger pore sizes promote high permeability, which is necessary for operations without compromising the quality of separation. Furthermore, a major factor in the membrane's capacity to avoid fouling, a prevalent issue in membrane-based filtering systems, is the interconnectivity and pore size in the fibrous network. High porosity facilitates the easier movement of particles and fluids through the membrane, hence reducing the risk of pore blockages and surface fouling.

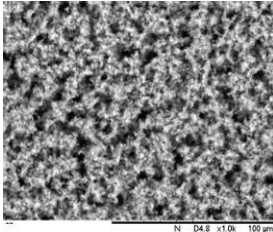
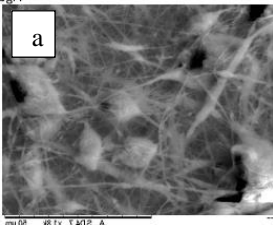
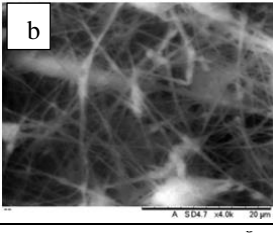
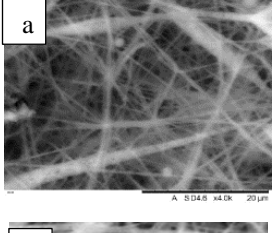
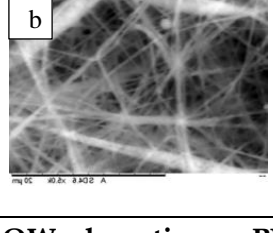
This property is especially helpful in the oil-water separation process, since the membrane needs to be able to withstand large particle loads without clogging. The final morphology of PVDF membranes is also influenced by the fabrication factors, which include solvent type, polymer concentration, and electrospinning settings. Variations in these characteristics might be fine-tuned to produce membranes with the desired pore structures and surfaces. The observed fibrous, net-like morphology during electrospinning is probably the consequence of improved phase separation brought about by the use of a 25wt% PVDF concentration.

According to previous research, which examined the mechanical characteristics of PVDF membranes under various fabrication circumstances, the PVDF-25 membrane's increased surface area brought about by its fibrous structure also enhances its mechanical strength and thermal stability [31]. Based to their research, a greater polymer concentration influences pore

size as well as the membrane's general resilience, which qualifies it for use in industrial settings with tough environmental conditions.

Furthermore, PVDF-25 membranes' higher surface roughness and a porous pore structure can improve a membrane's adsorption capacity, which in turn strengthens the membrane's ability to withstand oil fouling by encouraging water to pass through it [32]. However, the other membrane that fabricated has shown beaded membrane, membrane non uniform fibres formed with bigger lumps of polymer in between the fibre strands and also irregular pore size with beaded surface along with bigger size of lumps due the low concentration of PVDF and voltage in Figure 1, high voltage supply fore Figure 2 and large amount of polymer used in Figure 4. Thus, the optimum polymer formulation for PVDF to produce bead free membrane was 25 wt% at 21Kv with 6ml/he feed rate at the distance between the needle and collector at constant 9cm.

Table 1. PVDF membrane electrospun in different concentration.

PVDF nonwoven membrane	
SEM image	Parameters
	PVDF concentration :18wt% DMF: Acetone: 7:3 Voltage:18kV Feed rate: 6.0 ml/hr Collector distance: 7 cm Figure 1: PVDF membrane electrospun has visible droplets pattern on it with tiny pores on the membrane which magnifies the pore size at 100 µm.
 	PVDF concentration: 25 wt% DMF: Acetone: 7:3 Voltage:23kV Feed rate: 9.0 ml/hr Collector distance: 7 cm Figure 2 :(a) and (b) was PVDF fabricated with 25 wt% that shows visible lumps on the membrane.
 	PVDF concentration: 25 wt% DMF: Acetone: 7:3 Voltage:22kV Feed rate: 9.0 ml/hr Collector distance: 7 cm Figure 3: (a) & (b) shows the complex crosslinked fiber net that was fabricated with bigger pore size that will be suitable separation of oil molecule from the wastewater.

SOW adsorption on PVDF membrane

The main objective of this experiment is to determine how effectively PVDF membranes operate when treating two different types of simulated oily wastewater (SOW). The SOW 1 was prepared as emulsion of water and WCO that represents large oil particles on the wastewater's surface. Where else SOW 2 is made by waste cooking oil that has been emulsified with dishwashing soap and water to create a more complex and cloudy emulsion.

PVDF membranes that are widely recognized for their hydrophobic properties, has high thermal stability, and mechanical strength, making them suitable for oil-water separation processes [33]. The performance of these membranes in treating SOW 1 and SOW 2 was evaluated under controlled laboratory conditions. SOW 1 is an emulsion that mimics the contents of large oil particles that appear on the surface of the wastewater, often known as oil slick. In contrast, SOW 2 is an emulsion consisting of waste cooking oil and water, bound together with dishwashing soap as a binding agent, forming a much more complex and thicker emulsion. Both types of SOWs represent typical wastewater discharged from household kitchens.

In the experiment, the PVDF membrane was subjected to SOW 1 at a vacuum pressure of 100 rpm. Before the drying process, slick oil patches were observed on the surface of the membrane, indicating the presence of oil particles. The volumetric analysis before and after filtration revealed a 60% successful adsorption rate, demonstrating the membrane's capacity to filter the oil particles from the surface of SOW 1. Interestingly, after the oven drying process, the membrane did not exhibit any oil patches and appeared as a new membrane, suggesting that it can be reused for further filtration processes. This finding aligns with previous studies highlighting the reusability and efficiency of PVDF membranes in oil-water separation applications [34].

For SOW 2, the filtration process did not result in visible oil slicks on the membrane surface, even after overnight drying. This could be attributed to the more complex nature of the emulsion, where the binding agent (dishwashing soap) facilitated the formation of smaller oil particles, enhancing the adsorption process. The adsorption rate for SOW 2 was recorded at 70%, surpassing the performance observed with SOW 1. The constant vacuum pressure of 100 rpm applied during the filtration of SOW 2 further underscores the membrane's capability to handle varying emulsion complexities without compromising efficiency.

The superior performance of the PVDF membrane in treating SOW 2 can be linked to its intrinsic properties and the nature of the emulsion. PVDF's hydrophobic surface interacts more effectively with the smaller oil droplets present in SOW 2, allowing for better adsorption and separation. Studies have demonstrated that the hydrophobic interactions between PVDF membranes and oil particles play a crucial role in enhancing oil retention and minimizing fouling [35].

Moreover, the absence of visible oil patches on the membrane post-drying in the case of SOW 2 suggests that the smaller oil particles were more uniformly distributed and adsorbed onto the membrane surface. This uniform adsorption of WCO through pressure supplied in the magnetic flow meter is beneficial for maintaining the membrane's integrity and reusability. Previous research supports the notion that PVDF membranes can be effectively regenerated and reused multiple times without significant loss in performance [36].

The PVDF membrane demonstrated significant potential for treating household oily wastewater, with varying efficacy depending on the emulsion type. SOW 1, with its larger oil particles, showed a 60% adsorption rate, while SOW 2, with its smaller and more complex oil droplets, achieved a 70% adsorption rate. The membrane's reusability post-drying further enhances its

appeal for sustainable wastewater management. These findings are consistent with past research, which highlights the robustness and efficiency of PVDF membranes in oil-water separation processes. Future studies could explore optimizing the membrane's surface properties to further improve adsorption rates and extend the lifespan of the membranes in practical applications.



Figure 5: (a) shows the oil droplets on the membrane from SOW 1 and (b&c) represent oil patches on the membrane from SOW 2, both membranes are before the drying process

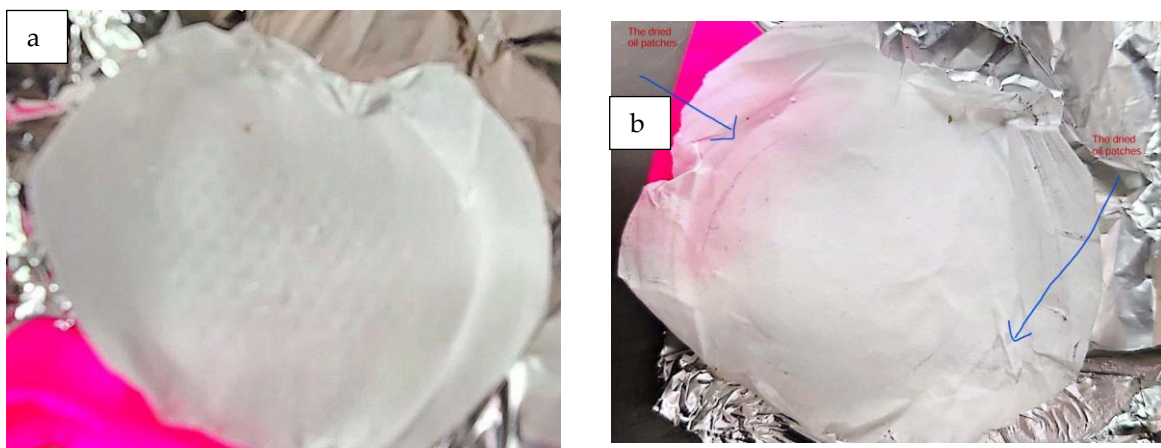


Figure 6: PVDF membrane (a) & (b) are after over drying overnight at 70 °C. Oil patches mark is spotted on the membrane surface of (b). However not patches spotted on membrane (a).

SEM analysis after WCO adsorption on the PVDF membrane.

The SEM picture shows the surface morphology of post WCO adsorption of the PVDF membrane in Figure (a). The surface morphology of the membrane in detail and was obtained at an 800x magnification with a 100 μm scale bar. The membrane surface displays a blurry oil slick, which is a sign of the WCO's oil particles coating spreading over the surface. This finding implies that a thin layer of WCO has adsorbed on top of the membrane, influencing both its surface texture as well as its porosity.

The Figure 7 (a) exhibits the presence of oil particles adsorbed onto the membrane. These particles are irregularly scattered across the membrane surface, bringing attention to the places where the oil droplets have attached themselves more securely. The hydrophobic properties of PVDF facilitate the interaction between the hydrophobic oil molecules and the membrane surface, hence enhancing the adsorption of oil particles onto the membrane. Understanding this relationship is critical to comprehending PVDF membranes' efficacy and adsorption capacity in the treatment of oil- contaminated water.

In the adsorption process, hydrophobic interactions are crucial. The continuous oil film forms as a result of the hydrophobic PVDF surface's propensity to draw and retain oil molecules. Given that it reduces permeability and clogs pores, this coating could negatively impact the membrane's performance. The WCO have distributed to form a thin, homogeneous layer as indicated by the oil slick's hazy appearance in the SEM image. This could have an impact on the membrane's overall filtration effectiveness.

The SEM image of a nonwoven nanomembrane following WCO adsorption is shown in Figure 7 (b), which was likewise taken at a 800x magnification with a 100 μm scale bar. The adsorption behavior of the nonwoven nanomembrane is different from that of the PVDF membrane depicted in Figure 7 (a). In contrast to the PVDF membrane, the image demonstrates that the majority of the oil particles are adsorbed onto the nanomembrane, with fewer occurrences of a continuous oil slick.

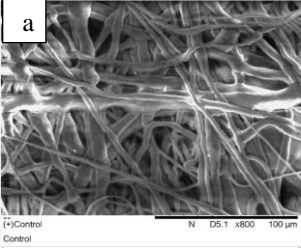
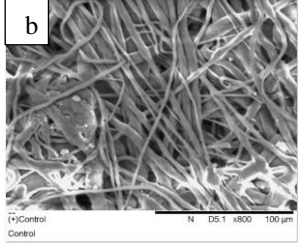
More oil particles can be absorbed because of the nanomembrane's nonwoven structure, which offers a large surface area for adsorption. This due the SOW that break into smaller molecules when react with dishwashing soap. The nonwoven membrane's fibers form a network that adsorbed oil droplets, increasing the effectiveness of adsorption. Applications requiring a high oil removal capacity will benefit most from this feature.

The SEM pictures shown in Figures 7(a) and (b) provide important information about the ways in which type of WCO molecules adsorbs on PVDF membrane. Due to its hydrophobic surface, the PVDF membrane often forms a thin oil film that clogs the pores and reduces filtration efficiency. Previous research has demonstrated that hydrophobic membranes have a propensity to absorb oil more readily because of their attraction for hydrophobic molecules, which supports this occurrence [37]. It is mainly the size of the oil molecule present during the process that causes the differences in adsorption performances between the two membranes.

The electrospun nonwoven nanomembrane in this study demonstrates higher effectiveness in WCO adsorption compared to the PVDF membrane used in previous research. The PVDF membrane often forms a continuous oil film that clogs its pores, reducing overall filtration efficiency. Conversely, the nonwoven nanomembrane, with its larger surface area and fibrous structure, allows for more efficient oil adsorption and fewer occurrences of oil slicks[38]. This structural advantage enables greater oil removal capacity, making the nonwoven

nanomembrane more effective for applications in treating oil-contaminated water. Its enhanced adsorption capacity makes it highly suitable for oil removal processes.

Table 2. PVDF membrane after adsorption study.

PVDF nonwoven membrane	
SEM image	After adsorption
<div><div>a</div></div> <div><div>b</div></div>	Figure 7: (a) & (b) show the SEM imaging after adsorption in SOW 1 and SOW 2 respectively.

b

CONCLUSION

The study conclusively confirms the superior efficacy of PVDF membranes, particularly those with a 25wt% polymer concentration, in treating simulated oily wastewater. The membranes demonstrated their potential in real-world applications with their remarkable adsorption rates of 60% for SOW 1 and 70% for SOW 2. The PVDF-25 membranes' net-like, fibrous structure greatly improves their permeability, mechanical strength, and fouling resistance, guaranteeing optimal performance and reusability. The results of post-filtration study showed that these membranes could potentially be efficiently regenerated, retaining their effectiveness throughout time. The study's conclusions, which emphasize the resilience and effectiveness of PVDF membranes in oil- water separation procedures, are in line with previous studies. It is recommended that future studies concentrate on surface alterations to improve PVDF membrane hydrophilicity and lessen oil fouling.

ACKNOWLEDGEMENTS: This work is supported by Ministry of Higher Education under Fundamental Research Grant scheme with grant number FRGS/1/2022/TK09/UM/02/22.

REFERENCES

- [1] Obaideen, K., Shehata, N., Sayed, E. T., Abdelkareem, M. A., Mahmoud, M. S., & Olabi, A. G. (2022). The role of wastewater treatment in achieving sustainable development goals (SDGs) and sustainability guideline. *Energy Nexus*, 7, 100112.
- [2] Kaya, D., & Hung, Y. T. (2021). Advances in treatment of vegetable oil refining wastes. *Environmental and natural resources engineering*, 325-375.
- [3] Widyarani, Wulan, D. R., Hamidah, U., Komarulzaman, A., Rosmalina, R. T., & Sintawardani, N. (2022). Domestic wastewater in Indonesia: Generation, characteristics and treatment. *Environmental Science and Pollution Research*, 29(22), 32397-32414
- [4] Sultana, N., Roddick, F. A., & Pramanik, B. K. (2024). Fat, oil and grease wastewater and dishwashers: Uncovering the link to FOG deposition. *Science of the Total Environment*, 907, 168032.
- [5] Elbehiry, F., Alshaal, T., Elhawat, N., & Elbasiouny, H. (2021). Environmental- friendly and cost-effective agricultural wastes for heavy metals and toxicants removal from wastewater. In *Cost- efficient Wastewater Treatment Technologies: Natural Systems* (pp. 107-127). Cham: Springer International Publishing.
- [6] Smeu, I., Dobre, A. A., Cucu, E. M., Mustăţea, G., Belc, N., & Ungureanu, E.
- [7] (2022). Byproducts from the vegetable oil industry: The challenges of safety and sustainability. *Sustainability*, 14(4), 2039. Erfani, H., Madhu, N. R., Khodayari, S., Qureshi, M. A., Swetanshu, Singh, P., & Jadoun, S. (2024). Separation and removal of oil from water/wastewater in the oil industry: a review. *Environmental Technology Reviews*, 13(1), 325-343.
- [8] Zhao, C., Zhou, J., Yan, Y., Yang, L., Xing, G., Li, H., ... & Zheng, H. (2021). Application of coagulation/flocculation in oily wastewater treatment: A review. *Science of The Total Environment*, 765, 142795.
- [9] Tian, Y., Zhou, J., He, C., He, L., Li, X., & Sui, H. (2022). The formation, stabilization and separation of oil–water emulsions: a review. *Processes*, 10(4), 738.
- [10] Ahmed, S. F., Mofijur, M., Nuzhat, S., Chowdhury, A. T., Rafa, N., Uddin, M. A., ... & Show, P. L. (2021). Recent developments in physical, biological, chemical, and hybrid treatment techniques for removing emerging contaminants from wastewater. *Journal of hazardous materials*, 416, 125912.
- [11] Zhang, K., Wu, H. H., Huo, H. Q., Ji, Y.L., Zhou, Y., & Gao, C. J. (2022). Recent advances in nanofiltration, reverse osmosis membranes and their applications in biomedical separation field. *Chinese Journal of Chemical Engineering*, 49, 76-99.
- [12] Baig, N., Salhi, B., Sajid, M., & Aljundi, I. H. (2022). Recent progress in microfiltration/ultrafiltration membranes for separation of oil and water emulsions. *The Chemical Record*, 22(7), e202100320.
- [13] Patel, H. K., Kalaria, R. K., Jokhakar, P. H., Patel, C. R., & Patel, B. Y. (2022). Removal of emerging contaminants in water treatment by an application of nanofiltration and reverse osmosis. In *Development in wastewater treatment research and processes* (pp. 385-400). Elsevier.
- [14] Lai, C. Y., Groth, A., Gray, S., & Duke, M. (2014). Nanocomposites for improved physical durability of porous PVDF membranes. *Membranes*, 4(1), 55-78.
- [15] Meng, L., Lv, Y., Deng, P., Li, N., Huang, M., Mansouri, J., & Chen, V. (2021). Novel PVDF membrane with sandwich structure for enhanced membrane distillation. *Chemical Engineering Journal*, 415, 128960.
- [16] Gergeous, G. M. B., Hassanin, A., & Shehata, N. PvdF Nanostructures Characterizations and Techniques for Enhanced Piezoelectric Response: A Review.
- [17] Saxena, P., & Shukla, P. (2021). A comprehensive review on fundamental properties and applications of poly (vinylidene fluoride) (PVDF). *Advanced Composites and Hybrid*

Materials, 4, 8-26.

- [18] Dai, J., Shao, J., Zhang, Y., Hang, R., Yao, X., Bai, L., & Hang, R. (2024). Piezoelectric dressings for advanced wound healing. *Journal of Materials Chemistry B*, 12(8), 1973-1990.
- [19] Saxena, P., & Shukla, P. (2022). A comparative analysis of the basic properties and applications of poly (vinylidene fluoride) (PVDF) and poly (methyl methacrylate) (PMMA). *Polymer Bulletin*, 79(8), 5635-5665.
- [20] Duraikkannu, S. L., Castro-Muñoz, R., & Figoli, A. (2021). A review on phase- inversion technique-based polymer microsphere fabrication. *Colloid and Interface Science Communications*, 40, 100329.
- [21] Li, Y., Zhu, J., Cheng, H., Li, G., Cho, H., Jiang, M., ... & Zhang, X. (2021). Developments of advanced electrospinning techniques: A critical review. *Advanced Materials Technologies*, 6(11), 2100410.
- [22] Bölgen, N., Demir, D., Aşık, M., Sakım, B., & Vaseashta, A. (2022). Introduction and fundamentals of electrospinning. In *Electrospun Nanofibers: Principles, Technology and Novel Applications* (pp. 3-34). Cham: Springer International Publishing.
- [23] Chen, H., Huang, M., Liu, Y., Meng, L., & Ma, M. (2020). Functionalized electrospun nanofiber membranes for water treatment: A review. *Science of the Total Environment*, 739, 139944.
- [24] Fadil, F., Affandi, N. D. N., Misnon, M. I., Bonnia, N. N., Harun, A. M., & Alam, M. K. (2021). Review on electrospun nanofiber-applied products. *Polymers*, 13(13), 2087.
- [25] Langwald, S. V., Ehrmann, A., & Sabantina, L. (2023). Measuring physical properties of electrospun nanofiber mats for different biomedical applications. *Membranes*, 13(5), 488.
- [26] Khulbe, K. C., & Matsuura, T. (2020). The advances of electrospun nanofibers in membrane technology. *Journal of Membrane Science and Research*, 6(3), 251-268.
- [27] Ibrahim, H. M., & Klingner, A. (2020). A review on electrospun polymeric nanofibers: Production parameters and potential applications. *Polymer Testing*, 90, 106647.
- [28] AlAbduljabbar, F. A. (2022). Photocatalytic Affinity Membranes for the treatment of Dyes Contaminated Wastewater. Fabrication of the photocatalytic affinity membranes, using chemical and electrohydrodynamic processes; electrospinning, and electro spraying, for the efficient removal and degradation of the dyes that are present in the contaminated water (Doctoral dissertation, University of Bradford).
- [29] Zou, D., & Lee, Y. M. (2022). Design strategy of poly (vinylidene fluoride) membranes for water treatment. *Progress in Polymer Science*, 128, 101535.
- [30] Xu, G. R., Xing, Y. L., Wang, M., An, Z. H., Zhao, H. L., Xu, K., & Liu, Q. (2022). Electrospun nanofibrous membranes as promising materials for developing high-performance desalination technologies. *Desalination*, 528, 115639.
- [31] Magdy, G., Hassanin, A. H., Kandas, I., & Shehata, N. (2024). PVDF Nanostructures Characterizations and Techniques for Enhanced Piezoelectric Response: A Review. *Materials Chemistry and Physics*, 129760.
- [32] Tanudjaja, H. J., Hejase, C. A., Tarabara, V. V., Fane, A. G., & Chew, J. W. (2019). Membrane-based separation for oily wastewater: A practical perspective. *Water research*, 156, 347-365.
- [33] Dong, W., Liu, F., Zhou, X., Wang, L., Zhao, Z., Zhou, Y., ... & Li, D. (2022). Superhydrophilic PVDF nanofibrous membranes with hierarchical structure based on solution blow spinning for oil- water separation. *Separation and Purification Technology*, 301, 121903.
- [34] Pakdel, E., Wang, J., Varley, R., & Wang, X. (2021). Recycled carbon fiber nonwoven functionalized with fluorine- free superhydrophobic PDMS/ZIF-8 coating for efficient oil-water separation. *Journal of Environmental Chemical Engineering*, 9(6), 106329.
- [35] Cao, L., Liu, H., Li, H., Lin, H., & Li, L. (2024). Dopamine co-coating with fulvic acid on PVDF membrane surface for hydrophilicity improvement and highly-efficient oily water

- purification. *Journal of Water Process Engineering*, 64, 105722.
- [36] Queirós, J. M., Salazar, H., Valverde, A., Botelho, G., de Luis, R. F., Teixeira, J., ... & Lanceros-Mendez, S. (2022). Reusable composite membranes for highly efficient chromium removal from real water matrixes. *Chemosphere*, 307, 135922.
- [37] Wang, Z., Hou, D., & Lin, S. (2016). Composite membrane with underwater- oleophobic surface for anti-oil-fouling membrane distillation. *Environmental science & technology*, 50(7), 3866-3874.
- [38] Saeed, A., Zhan, D., Nawaz, M. A. H., Hu, Q., Haider, A. A., Shareef, S., ... & Liu, J. (2024). Fabrication of superhydrophobic nonwoven fabric membrane by using a single-step facile strategy for enhanced oil-water separation. *Colloids and Surfaces A: Physicochemical and Engineering Aspects*, 695, 134242.
- [39] Obaid, M., Mohamed, H. O., Yasin, A.S., Yassin, M. A., Fadali, O. A., Kim, H., & Barakat, N. A. (2017). Under-oil superhydrophilic wetted PVDF electrospun modified membrane for continuous gravitational oil/water separation with outstanding flux. *Water research*, 123, 524-535.
- [40] Sun, F., Li, T. T., Ren, H. T., Shiu, B.C., Peng, H. K., Lin, J. H., & Lou, C. W. (2021). Dopamine-decorated lotus leaf- like PVDF/TiO₂ membrane with underwater superoleophobic for highly efficient oil-water separation. *Process Safety and Environmental Protection*, 147, 788-797.
- [41] Manakhov, A., Rybkin, I., AlGhunaimi, F. I., & Aljaryyed, N. W. (2023, March). Nanomembranes from Polymeric Waste for Produced Water Treatment. In *SPE Middle East Oil and Gas Show and Conference* (p. D032S122R001). SPE.

Synthesis, and Characterization of Biogenic Copper Oxide Nanoparticles (CuONPs) for Potential Depollution Application

Mhd Hazli Rosli^{1,2}, Abubakar Dantani Meli² and Che Azurahanim Che Abdullah*,^{1,2}

¹*Institute of Nanoscience and Nanotechnology, Universiti Putra Malaysia, 43400 Serdang, Selangor Darul Ehsan*

²*Biophysics Lab, Department of Physics, Faculty of Science, Universiti Putra Malaysia, 43400 Serdang, Selangor Darul Ehsan (empty line)*

* Corresponding Author's Email: azurahanim@upm.edu.my

Abstract: The increased interest in biosynthesis of nanoparticles has been fueled by the need for clean, nontoxic, chemicals, low-cost approaches, environmentally friendly solvents, and renewable materials. The method used to synthesize Copper Oxide Nanoparticles (CuONPs) ensures the use of non-toxic materials, the absence of toxic by-products, and the rapid production of CuONPs. The first green synthesis of CuONPs using *Hibiscus sabdariffa* which is commonly known as roselle is described in this study. CuONPs in the sample were synthesized using a modified sol-gel method. FTIR, DLS, UV Vis and XRD characterization methods of the CuONPs samples were all meaningful. The present study synthesizes CuONPs using roselle extract. According to the peaks identified in FTIR chemical fingerprint studies CuONPs were formed and stabilized in the presence of the extract's primary compound. DLS revealed the size of CuONPs in solution and UV-vis UV-visible spectra of CuONPs indicated the absorption spectrum tends to increase as even the intensity of absorption increases. The band stabilizes ranging between 211 - 214 nm, attributed to the formation of CuONPs. In addition, a broad plasmonic band was observed, indicating that the CuONPs are spherical in shape. The crystalline nature was revealed by XRD analysis. The study concludes that the bio-profile of the plant influences the nanoparticles' properties. Thus, plant extracts can alter the properties of synthetic NPs. These findings may aid in our understanding of how plants produce nanoparticles for industrial applications. This study primarily focuses on the synthesis of CuONPs via the sol-gel method and their surface characterization as photocatalysts using XRD, FT-IR, and UV-Vis spectroscopic techniques to examine the photodegradation of MB dyes under UV-vis light irradiation (Krishna et al., 2023). Additionally, the influence of variables such as reaction time, catalyst type, and initial dye concentration on the photodegradation process of the model dye has been investigated, with a degradation mechanism proposed. Overall, a novel approach has been developed that holds potential for the treatment of wastewater containing cationic dyes (Groeneveld et al., 2023). Additional research in this area may aid researchers in understanding how the NPs are shaped by the plant's biochemistry.

Keywords: *Hibiscus sabdariffa*; Roselle; copper oxide; nanoparticles; green synthesis

INTRODUCTION

Nanoparticles (NPs) have caught the attention of scientists due to various applications that NPs can provide. For example, biosensors to detect and trace for electrochemical analysis (Fu et al., 2024). Besides that, NPs play a big role as antimicrobials, water purification, and removal of pollutants due to their unique physiochemical and photocatalytic properties (Tripathy et al., 2024). From size perspective, NPs range from 2nm-100nm depending on the type of NPs that been produced as well as the process that would be involved during the synthesis. Metal NPs including gold, silver, platinum, palladium, copper, magnesium, zinc, and copper have garnered a lot of interest for usage in a range of applications (Singh et al., 2020). Because of their optical, catalytic, and electrical properties, copper oxide (CuO) is among the most well-known and has

been applied more frequently in a range of sectors. CuO is one of the most famous metal oxide NPs around the world due to its photocatalytic properties. In this research we utilized roselle (*hibiscus sabdariffa*), one of the plants that can easily be found around Malaysia. The cost for this herb plant is inexpensive and available everywhere in Malaysia (Naz et al., 2023). There are many functional groups that can act as reducing agents. Due to these properties and not only as an antimicrobial behavior, roselle had been chosen to be reducing agent to produce green CuONPs (Wacharanad et al., 2021).

MATERIALS

To prepare plant extracts, Roselle flowers were purchased from a local market in Malaysia. The compound Copper II Chloride-dihydrate ($\text{CuCl}_2 \cdot 2\text{H}_2\text{O}$) was obtained from the supplier SYSTEM, Malaysia. Sodium hydroxide (NaOH) was obtained from the supplier R&M in London, UK. The chemical C1011 Acetone QP was purchased from HmbG chemicals. Methylene blue (MB), a compound with the chemical formula $\text{C}_{16}\text{H}_{18}\text{ClN}_3\text{S}$ and a molar mass of 319.86 g/mol, was obtained from Merck for the purpose of depollution.

EXPERIMENTAL

Preparation of Roselle flower extract

The acquired roselle flowers were meticulously cleansed using flowing tap water to eliminate any dust particles, and subsequently dried under direct sunlight to eliminate any remaining moisture. The preparation of roselle leaf extract involved placing 5g of finely cut dried flowers in a 500ml glass beaker, and adding 400ml of sterile distilled water (Juhari et al., 2021). The mixture was subsequently heated to its boiling point for a duration of 5 minutes, during which the colour of the aqueous solution transitioned from clear to a shade of brown-yellow. Subsequently, the mixture was allowed to cool to the ambient temperature and underwent filtration using Whatman No. 1 filter paper. The extract was stored at ambient temperature to facilitate its utilisation in subsequent experiments (Baliyan et al., 2022).

Preparation of biogenic CuONPs

In order to produce green CuONPs using the sol-gel method, copper chloride was introduced into a beaker containing distilled water, following a previously established procedure by Santhosh Kumar and his team, with minor adjustments. The beaker was positioned on a magnetic stirrer and agitated at a specific speed of 200 revolutions per minute (RPM) for a duration of two minutes (Sadiq et al., 2023). Subsequently, roselle extract was precisely added to the beaker using a dropper, drop by drop. While stirring, the bluish solution underwent a transformation into a black precipitate, indicating the formation of CuONPs. The agitation persisted at a speed of 200 RPM for a duration of 4 hours at a temperature of 80°C. The substance was subjected to centrifugation at a speed of 6000 RPM for a duration of 15 minutes. It was then washed with distilled water and dried in an oven maintained at a temperature of 90°C (Amaliyah et al., 2020a). The precipitate was separated by passing it through filter paper with a pore size of 0.1 micrometres. Subsequently, the precipitate that had undergone filtration was subjected to a drying process in an oven set at a temperature of 100°C for a duration of 24 hours. Finally, the desiccated black precipitate was ground and stored in vials (Altay Benetti et al., 2021).

Characterization of CuONPs

The synthesized CuONPs were characterized using various techniques XRD Ringaku X-ray diffractometer (UPM, Serdang, Malaysia), FTIR (FTIR-spectrum 400, Perkin Elmer, USA), DLS (Malvern Zetasizer USA) and UV-Vis (Jenway 7315, Staffordshire, UK) to determine their structural, optical, and morphological properties.

Photocatalysis

A solution of MB was prepared by dissolving 10 mg of MB in 1000 mL of distilled water. For the experimental treatment, 10 mg of CuO NPs were introduced into 100 mL of the MB dye solution. In the control experiment, no CuO NPs were added to the dye solution. A 10-watt UV lamp emitting at a wavelength of 254 nm was submerged in the 100 mL dye solution. The entire experimental setup was conducted within a custom-designed enclosure.

RESULTS AND DISCUSSION

Structural analysis

The X-Ray diffraction analysis reveals the structural characteristics of the powder material, as depicted in Figure 1. The XRD results were compared to the JCPDS card (Pookmanee et al., 2004). Figure 1 displays the two main peaks of 2θ , with assigned values of 35.50, 38.72, 42.46, 48.81, 53.57, 61.65, 66.13, and 74.30° corresponding to the crystallographic planes (002), (200), (111), (-202), (002), (202), (113), (311), and (220). These values provide evidence that the CuONPs possess a monoclinic structure, which matches the JCPDS card no.450937. No additional diffraction peaks corresponding to a supplementary phase have been observed. The prominent and distinct peaks indicate that the products obtained have a high degree of crystallisation. The size of the crystallite has been determined by utilising the 2θ and FWHM values of the (h k l) peaks, employing Scherrer's equation: $D = k\lambda / \beta \cos \theta$, (1) The average crystallite size (D) is measured in Ångstroms (Å). The shape factor (k) is a constant value of 0.9. The wavelength of X-ray (λ) is 1.5406 Ångstroms. The Bragg angle (θ) is used in the calculation. The exacted line broadening of the samples is represented by the variable (β). By utilising Scherrer's formula, the monoclinic (200) diffraction peak was analysed to determine certain characteristics. The materials used in this analysis, as well as their source, are described in adequate length in the work by Nasiri et al. (2023).

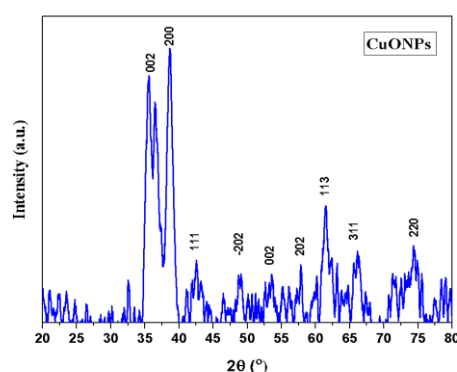


Fig.1. XRD Pattern of CuONPs synthesized from roselle.

Fourier Transform Infrared (FT-IR) spectroscopy was used to verify the successful production of CuONPs and to detect any functional groups on the surface of the nanoparticles created using

roselle. The FT-IR spectrum of roselle displayed distinct absorption peaks at 3348, 3186, 2918, 1857, 1614, 1414, 1217, 613, and 501 cm^{-1} , as depicted in Figure 2. These peaks represent functional groups including hydroxyl (-OH), vinyl (-CH-), ether (-C-O-), alkoxy (-O-CH), alkyl (-C-H), and ester (-C-O) groups, respectively. The presence of these functional groups signifies the presence of phenolic compounds, such as flavanols like catechins and procyanidins (Almisbah et al., 2023). These compounds are acknowledged for their function as reductive agents and stabilisers in the production of CuONPs. Furthermore, the absorption peak detected at 1016 cm^{-1} is typically associated with C-O stretching vibrations, which could arise from functional groups like alcohols, ethers, or esters (Amaliyah et al., 2020b).

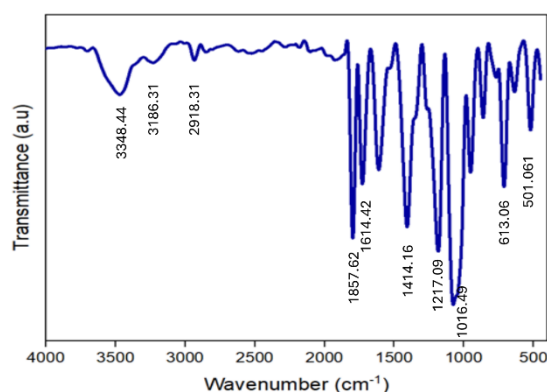


Fig. 2. FTIR Spectra of CuONPs synthesized *roselle*

The CuONPs had an average particle size of 291.4 nm, when the roselle concentration was 25 mM, as demonstrated by DLS and summarised in Table 1. The nanoparticles demonstrated a monodisperse distribution, as evidenced by a polydispersity index (PDI) of 0.236 and inline with previous study by Kim and colleagues (2019) where the PDI value is 0.193.

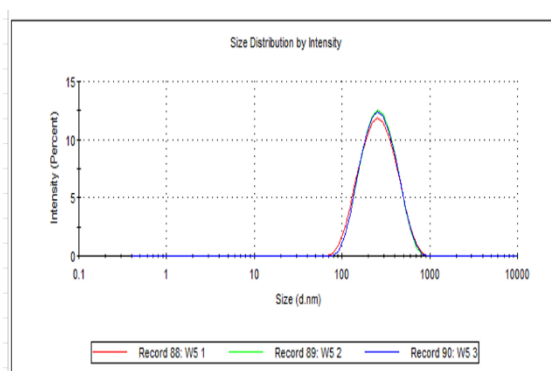


Fig. 3. DLS of CuONPs synthesized from *roselle*.

Table 1. DLS of CuONPs

Sample	Z- Average diameter of CuONPs (d.nm)	Average PDI
CuONPs 25 mM	291.4	0.236

The UV-vis spectrum of the CuONPs, as shown in Fig. 4, displays a maximum absorption peak at 270 nm. This peak is attributed to the surface plasmon resonance of the metal oxide. In metal oxide NPs, surface plasmon resonance arises from the collective oscillation of free electrons in the conduction band when excited by incident electromagnetic radiation. This phenomenon occurs when the wavelength of the incident light exceeds the particle diameter. The appearance of a surface plasmon absorption band with a maximum at 270 nm confirms the successful formation of CuONPs (Fouda et al., 2023).

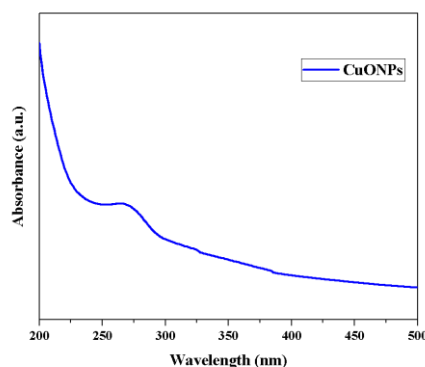


Fig. 4. UV-vis spectra of absorbance CuO NPs synthesized *roselle*

PHOTOCATALYSIS

Photocatalysis has been suggested as an effective method for reducing environmental pollution and has been effectively implemented for this objective (Pavel et al., 2023). Under ambient conditions and atmospheric pressure, this technique is regarded as one of the most efficacious methods for the degradation of a broad spectrum of environmental pollutants. Additionally, it is renowned for its exceptional efficiency, affordability, and eco-friendliness (Panda et al., 2021; Sharma et al., 2020). According to Dianey et al. (2021), photocatalytic reactions consist of three main phases: (1) absorption of light, (2) separation and transfer of photogenerated electrons (e^-) and holes (h^+), and (3) redox reactions taking place on the photocatalyst's surface (Huang et al., 2020).

This study utilised CuONPs as photocatalysts to degrade a commercial dye solution by harnessing UV light as the energy source. CuONPs are widely recognised as p-type semiconductors due to their narrow band gap of 1.2 electron volts (eV) (Ramesh, 2021). Fig. 5 demonstrates that the decomposition of methylene blue (MB) dye only achieved 81% after 160 minutes of exposure to ultraviolet (UV) light. In addition, the absorbance of MB increased as the exposure time was extended, as shown in the graphs presented in Fig 5.

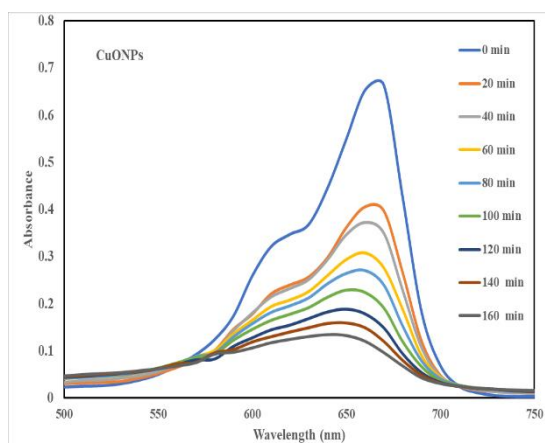


Fig. 5. photocatalytic degradation mechanism of MB synthesized from roselle

At zero minutes, CuONPs showed very little initial degradation efficiency on methylene blue (MB) dye. The effect of different irradiation durations on the degradation of MB dye was assessed within a time range of 20 to 160 minutes. The dye concentration was kept constant at 10 mg/L, while the catalyst load varied. This information is presented in Figure 5. The most rapid degradation rate of the MB dye was observed after 160 minutes of exposure to UV light. The accelerated deterioration is attributed to the swift absorption rate prior to achieving balance, which is facilitated by the heightened presence of active surfaces on CuONPs. During equilibrium, the process of adsorption, which is regulated by attachment, is anticipated to occur because there are sorption sites available as reported by (Bahramian et al., 2023).

CONCLUSION

The Sol-gel technique was employed to create ecofriendly CuONPs photocatalysts utilizing roselle flower extract with the aim of photodegrading MB. To ascertain the crystalline size, functional group, and surface composition of CuONPs, the photocatalysts were synthesised and characterised using X-ray diffraction (XRD), Fourier-transform infrared spectroscopy (FTIR), and ultraviolet-visible spectroscopy (UV-vis).

A decision was made to initiate an investigation to examine the influence of various time periods on the degradation of MB. As a result, the catalyst exhibited the greatest ability to break down substances, and the most effective degradation occurred after 160 minutes. According to the findings, the degradation efficiency of MB dye was determined to be 77.18%. CuONPs have demonstrated remarkable photocatalytic abilities when exposed to UV-visible light, rendering them highly suitable and desirable for the elimination of environmentally harmful substances, especially organic dyes.

REFERENCES

- [1] Almisbah, S. R. E., Mohammed, A. M. A., Elgamouz, A., Bihi, A., & Kawde, A. (2023). Green synthesis of CuO nanoparticles using *Hibiscus sabdariffa* L. extract to treat wastewater in Soba Sewage Treatment Plant, Sudan. *Water Science & Technology*, 87(12), 3059–3071. <https://doi.org/10.2166/wst.2023.153>
- [2] Altay Benetti, A., Bianchera, A., Buttini, F., Bertocchi, L., & Bettini, R. (2021). Mannitol Polymorphs as Carrier in DPIs Formulations: Isolation Characterization and Performance. *Pharmaceutics*, 13(8), 1113. <https://doi.org/10.3390/pharmaceutics13081113>
- [3] Amaliyah, S., Pangesti, D. P., Masruri, M., Sabarudin, A., & Sumitro, S. B. (2020a). Green synthesis and characterization of copper nanoparticles using Piper retrofractum Vahl extract as bioreductor and capping agent. *Heliyon*, 6(8), e04636. <https://doi.org/10.1016/j.heliyon.2020.e04636>
- [4] Amaliyah, S., Pangesti, D. P., Masruri, M., Sabarudin, A., & Sumitro, S. B. (2020b). Green synthesis and characterization of copper nanoparticles using Piper retrofractum Vahl extract as bioreductor and capping agent. *Heliyon*, 6(8), e04636. <https://doi.org/10.1016/j.heliyon.2020.e04636>
- [5] Bahramian, H., Fattah-alhosseini, A., & Karbasi, M. (2023). Development of porous ceramic coatings via the PEO process: The key role of CuO nanoparticles in methylene blue photodegradation under visible light illumination. *Applied Surface Science Advances*, 18, 100511. <https://doi.org/10.1016/j.apsadv.2023.100511>
- [6] Baliyan, S., Mukherjee, R., Priyadarshini, A., Vibhuti, A., Gupta, A., Pandey, R. P., & Chang, C.-M. (2022). Determination of Antioxidants by DPPH Radical Scavenging Activity and Quantitative Phytochemical Analysis of Ficus religiosa. *Molecules*, 27(4), 1326. <https://doi.org/10.3390/molecules27041326>
- [7] Fouda, A., Saied, E., Eid, A. M., Kouadri, F., Alemam, A. M., Hamza, M. F., Alharbi, M., Elkelish, A., & Hassan, S. E.-D. (2023). Green Synthesis of Zinc Oxide Nanoparticles Using an Aqueous Extract of Punica granatum for Antimicrobial and Catalytic Activity. *Journal of Functional Biomaterials*, 14(4), 205. <https://doi.org/10.3390/jfb14040205>
- [8] Fu, Y., Liu, T., Wang, H., Wang, Z., Hou, L., Jiang, J., & Xu, T. (2024). Applications of nanomaterial technology in biosensing. *Journal of Science: Advanced Materials and Devices*, 9(2), 100694. <https://doi.org/10.1016/j.jsamd.2024.100694>
- [9] Groeneveld, I., Kanelli, M., Ariese, F., & van Bommel, M. R. (2023). Parameters that affect the photodegradation of dyes and pigments in solution and on substrate – An overview. *Dyes and Pigments*, 210, 110999. <https://doi.org/10.1016/j.dyepig.2022.110999>
- [10] Huang, C.-W., Nguyen, B.-S., Wu, J. C.-S., & Nguyen, V.-H. (2020). A current perspective for photocatalysis towards the hydrogen production from biomass-derived organic substances and water. *International Journal of Hydrogen Energy*, 45(36), 18144–18159. <https://doi.org/10.1016/j.ijhydene.2019.08.121>
- [11] Juhari, N. H., Martens, H. J., & Petersen, M. A. (2021). Changes in Physicochemical Properties and Volatile Compounds of Roselle (*Hibiscus sabdariffa* L.) Calyx during

- Different Drying Methods. *Molecules*, 26(20), 6260. <https://doi.org/10.3390/molecules26206260>
- [12] Kim, A., Ng, W. B., Bernt, W., & Cho, N.-J. (2019). Validation of Size Estimation of Nanoparticle Tracking Analysis on Polydisperse Macromolecule Assembly. *Scientific Reports*, 9(1), 2639. <https://doi.org/10.1038/s41598-019-38915-x>
- [13] Krishna, M. G., Murthy, M. N., Sreelatha, C. J., Kumar, K. R., & G. Chandrakala. (2023). SOL-GEL SYNTHESIZED COPPER OXIDE (CuO) NANOPARTICLES AND THEIR PHOTOCATALYSTS AND ANTIBACTERIAL APPLICATIONS. *RASAYAN Journal of Chemistry*, 16(04), 2256–2260. <https://doi.org/10.31788/RJC.2023.1618663>
- [14] Nasiri, S., Rabiei, M., Palevicius, A., Janusas, G., Vilkauskas, A., Nutalapati, V., & Monshi, A. (2023). Modified Scherrer equation to calculate crystal size by XRD with high accuracy, examples Fe₂O₃, TiO₂ and V₂O₅. *Nano Trends*, 3, 100015. <https://doi.org/10.1016/j.nwnano.2023.100015>
- [15] Naz, S., Gul, A., Zia, M., & Javed, R. (2023). Synthesis, biomedical applications, and toxicity of CuO nanoparticles. *Applied Microbiology and Biotechnology*, 107(4), 1039–1061. <https://doi.org/10.1007/s00253-023-12364-z>
- [16] Panda, S. K., Aggarwal, I., Kumar, H., Prasad, L., Kumar, A., Sharma, A., Vo, D.-V. N., Van Thuan, D., & Mishra, V. (2021). Magnetite nanoparticles as sorbents for dye removal: a review. *Environmental Chemistry Letters*, 19(3), 2487–2525. <https://doi.org/10.1007/s10311-020-01173-9>
- [17] Pavel, M., Anastasescu, C., State, R.-N., Vasile, A., Papa, F., & Balint, I. (2023). Photocatalytic Degradation of Organic and Inorganic Pollutants to Harmless End Products: Assessment of Practical Application Potential for Water and Air Cleaning. *Catalysts*, 13(2), 380. <https://doi.org/10.3390/catal13020380>
- [18] Pookmanee, P., Rujijanagul, G., Ananta, S., Heimann, R. B., & Phanichphant, S. (2004). Effect of sintering temperature on microstructure of hydrothermally prepared bismuth sodium titanate ceramics. *Journal of the European Ceramic Society*, 24(2), 517–520. [https://doi.org/10.1016/S0955-2219\(03\)00197-3](https://doi.org/10.1016/S0955-2219(03)00197-3)
- [19] Ramesh, M. (2021). CuO as efficient photo catalyst for photocatalytic decoloration of wastewater containing Azo dyes. *Water Practice and Technology*, 16(4), 1078–1090. <https://doi.org/10.2166/wpt.2021.067>
- [20] Sadiq, M. U., Shah, A., Haleem, A., Shah, S. M., & Shah, I. (2023). Eucalyptus globulus Mediated Green Synthesis of Environmentally Benign Metal Based Nanostructures: A Review. *Nanomaterials*, 13(13), 2019. <https://doi.org/10.3390/nano13132019>
- [21] Sharma, A., Erdenedelger, G., Mo Jeong, H., & Lee, B.-K. (2020). Controlled oxygen functional groups on reduced graphene using rate of temperature for advanced sorption process. *Journal of Environmental Chemical Engineering*, 8(3), 103749. <https://doi.org/10.1016/j.jece.2020.103749>
- [22] Singh, A., Gautam, P. K., Verma, A., Singh, V., Shivapriya, P. M., Shivalkar, S., Sahoo, A. K., & Samanta, S. K. (2020). Green synthesis of metallic nanoparticles as effective alternatives to treat antibiotics resistant bacterial infections: A review. *Biotechnology Reports*, 25, e00427. <https://doi.org/10.1016/j.btre.2020.e00427>

- [23] Tripathy, J., Mishra, A., Pandey, M., Thakur, R. R., Chand, S., Rout, P. R., & Shahid, M. K. (2024). Advances in Nanoparticles and Nanocomposites for Water and Wastewater Treatment: A Review. *Water*, 16(11), 1481. <https://doi.org/10.3390/w16111481>
- [24] Wacharanad, S., Thatree, P., Yiemwattana, P., Paoprajak, P., Ngamsangiam, P., Valyanont, M., & Yiemwattana, I. (2021). Antimicrobial Activity of Roselle-capped Silver Nanochip on *Aggregatibacter actinomycetemcomitans*. *European Journal of Dentistry*, 15(03), 574–578. <https://doi.org/10.1055/s-0041-1725574>

Production of Eco-Enzymes Immobilized on Hydroxyapatite-Biomedica for Sustainable Environmental Remediation

Mohamad Tajuddin **Sabri**¹, Norhafizah **Abdullah**², Mohamad Syazarudin Md **Said**², Nur Syakina **Jamali**^{1,*}

¹*Institute of Nanoscience and Nanotechnology, Universiti Putra Malaysia, 43400 Seri Kembangan, Malaysia*

²*Department of Chemical and Environmental Engineering, Faculty of Engineering, Universiti Putra Malaysia, 43400 Seri Kembangan, Malaysia*

**Corresponding author's phone: +603-97694464*

E-mail: syakina@upm.edu.my

Abstract: Eco-enzymes, derived from fruit, vegetable wastes, and other kitchen waste, are a sustainable alternative to produce beneficial detergents and soap from the wastes through a catalytic reaction. In general, there is a lack of studies that have been published to utilize the fruit wastes by using the eco enzyme mechanisms with addition of any biomedica implementation for the efficiency towards modifying the biomedica concentration in the system. It has been demonstrated that adding hydroxyapatite nanoparticles to the biomedica could increase the enzymatic yield. Thus, this study investigates the enhancement of enzymatic yield in eco-enzymes by adding hydroxyapatite nanomaterials. The research focuses on the effects of these nanomaterials on pH value, total solids (TS), total suspended solids (TSS), volatile suspended solids (VSS), and chemical oxygen demand (COD) in the characterization of eco-enzymes derived from apple, pineapple, and citrus peels. Fruit wastes were used to create eco-enzymes in a conventional ratio of 1:3:10 with sugar, water, and fruit wastes. Clay-hydroxyapatite (CHAP) nanomaterials were introduced to the fermentation process with different dosage concentrations from 0%, 2.5%, 5.0%, 10.0%, 15.0%, and 20.0%. Based on the pH value, total solids, total suspended solids, volatile suspended solids, and COD, the enzymatic yield was examined. Using Fourier Transform Infrared (FTIR) and CHN, eco-enzymes with hydroxyapatite were characterized. The appropriate conditions for the dosage concentration of hydroxyapatite in boosting the enzymatic yield of the eco enzyme will be determined by the correlation between the various reactions.

Keywords: eco-enzyme; clay hydroxyapatite; nanomaterial biomedica

INTRODUCTION

Eco-enzyme is one of the mechanisms widely used to produce beneficial products including multipurpose cleaners, wastewater treatment, and plant enhancers. The substrate of eco-enzyme can be any biodegradable organic matter including kitchen waste which nowadays has grown in popularity. Eco-enzyme consists of several enzymes which are protease, amylase, and lipase all of these enzymes could be employed in different uses (Bharvi S. Patel et al., 2021[1]). In 1980, Rosukan Poompanvong from Thailand discovered how simple it was to make eco-enzyme. Brown sugar, kitchen trash, and water were the only three basic elements needed for the enzyme's fermentation, and their ratio was 1:3:10. The fermentation process of eco-enzyme making takes three months to degrade into beneficial products (Hanasah et al., 2020[2]).

The 3 months product of fermentation is brownish generally depending on the type of waste used. It contains organic acids, carbon dioxide, and ethanol which come from the chemical process involving the breakdown of large complex molecules into smaller molecules. The bacteria which naturally in wastes help in converting the complex sugar into simpler ones (Siddiqui et al., 2023[3]). In general, there were a variety of substrates that have been utilized for producing the eco-enzymes through 3 months of fermentation. These substrates come from different sources of kitchen waste including vegetables, fruit wastes, fruit peels, and other food

wastes. All of the wastes that contain high amounts of nutrients will influence the mechanisms of eco-enzyme production through the breakdown of the organic matter (Rosnina et al., 2023[4]). In this study, aimed to produce hydroxyapatite clay as an enzyme immobilizer for eco-enzyme applications while addressing existing gaps in enzyme characterization by examining how varying dosages of the immobilizer impact enzyme activity and stability, thus contributing to improved eco-enzyme effectiveness and broader applications in sustainable processes.

The efficacy of eco-enzymes studied following the incorporation of hydroxyapatite during their manufacturing process provides significant insights into their potential for environmentally sustainable remediation. Hydroxyapatite, a stable and biocompatible material, is crucial for enhancing the properties of eco-enzymes (Mysore et al., 2024[5]). By integrating hydroxyapatite into the enzyme production process, researchers can evaluate changes in enzyme stability, activity, and interactions with contaminants. Characterization techniques such as spectroscopic analysis and enzyme kinetics are commonly employed to assess the influence of hydroxyapatite on the structural and functional characteristics of eco-enzymes, offering a deeper understanding of their catalytic efficiency in degrading pollutants.

Characterization studies conducted on hydroxyapatite have yielded promising results for the application of eco-enzymes in bioremediation. Beyond stabilizing the enzymes, hydroxyapatite may also alter their conformational dynamics, leading to increased substrate affinity and reaction rates. Research indicates that these modified eco-enzymes demonstrate improved performance in degrading a variety of contaminants, including heavy metals and organic compounds. Thus, incorporating hydroxyapatite into the production of eco-enzymes marks a significant advancement in developing more effective biocatalysts for environmental cleanup, promoting sustainable practices, and supporting ecosystem health.

MATERIALS

The materials and chemicals used in the methodology include pineapple waste, apple waste, citrus waste, eggshells, brown sugar, distilled water, silica gel, 1M acetic acid, phosphoric acid (H_3PO_4), sodium bentonite clay, granular activated carbon (GAC), iron powder, sodium alginate, calcium chloride (CaCl_2), 0.1N sodium hydroxide (NaOH), phenolphthalein indicator, potassium dichromate ($\text{K}_2\text{Cr}_2\text{O}_7$), silver nitrate (AgNO_3), sulfuric acid (H_2SO_4), deionized water, KBr powder, and aluminum foil.

EXPERIMENTAL

Sample collection

The fruit wastes, pineapple, apple, and citrus were collected at Whole Foods Express Sri Serdang to make the eco enzyme. The eggshell sample was collected at the UNITEN cafeteria. The eggshell samples were washed and directly sun-dried for 1 hour.

Sample preparation

The fruit wastes and eggshells were first ground to make them finer. After that, it was autoclaved at 121° C for 15 minutes. Sterilized eggshells were packed in individual plastic bags containing silica gel to avoid contamination and absorb moisture while the sterilized fruit wastes were directly put inside the fermentation container for the fermentation process. About 600 g of sterile fruit wastes were measured and added into the fermentation container together with 200g of brown sugar and 2L of distilled water.

Clay Hydroxyapatite production

The hydroxyapatite should be prepared by raw materials which consist high amount of calcium. Eggshells were used to take the calcium components from it. The pretreatment of eggshells was done by leaching eggshells with 1M acetic acids for 60 min to remove the eggshell membranes. The eggshells are ground and then incinerated for two hours at 950°C. The extracted calcium was then mixed with the H₃PO₄ phosphoric acid to produce the desired hydroxyapatite HAP. (Mohd Pu'ad et al., 2019[5]).

The mixed solution was incinerated again to make the HAP powder. The clay hydroxyapatite was prepared by using the pulverized HAP powder and mix with 3 metal clays which are iron mix powder, sodium bentonite clay, and GAC with the weight by part 15.5 HAP, 16.5 sodium bentonite clay, 2 GAC, and 5 iron powder and made in 100g. the mixture was then calcinate from 100 to 1050°C with different increasing periods. Sodium alginate was prepared to mix with the CHAP mixture. About 2% of CaCl₂ was prepared in 5 L to be soaked with the CHAP for the hardening process and dried overnight. (Mo et al., 2022[6]).

Eco enzyme production

The preparation of eco-enzymes started with the grinding of fruit wastes and their peels into smaller pieces. Weighted the 600 g of the fruit wastes and put into 6 different fermenter bottles of 2 L of distilled water and varying the concentration of clay-hydroxyapatite CHAP which were utilized as the raw ingredients in this research. The CHAP was introduced with different concentrations from 2.5%, 5.0%, 10.0%, 15.0, and 20.0% w/v which indicates to 5 g with 200 g of brown sugar. An airtight container was filled with 200 g of brown sugar, 600 g of peels, and 2 L of water. The fermenter tank lid was perforated with one hole to connect with 5.0 ml of syringe for weekly sampling and gas releasing. The fermenter tank is fully covered with aluminum foil to make the system in dark fermentation. Following three months of fermentation, the fruit waste that had dropped to the bottom is combined, filtered, and then poured back up to eliminate any remaining clear solution that contains carbon dioxide, ethanol, and organic acids. (Fadlilla et al., 2023[7]).

Sample analysis

pH

A pH value and temperature test are to determine the acidity of the eco-enzyme throughout the fermentation process weekly. The sampling was taken weekly at about 50 ml for sample analysis and soaked with the pH probe to analyze the value of pH.

TS, TDS, and TSS value

A sample was divided into two, 10 ml for TS and another 10 ml for TDS. Both analyses are to determine the amount of solids and dissolved solids present in the eco-enzyme fermentation process. The drying at 105°C in the oven removes all the water content in the sample which is high enough to evaporate the free water molecule and leave the solid component sample only. The calculation for TS and TDS is as below:

$$TS \left(\frac{mg}{L} \right) = \left(\frac{W2 - W1}{Volume\ of\ Sample\ (mL)} \right) \times 100$$

$$TDS \left(\frac{mg}{L} \right) = \left(\frac{W2 - W3}{Volume\ of\ Sample\ (mL)} \right) \times 100$$

where:

W3 : Final weight (after furnace)
 W2 : Final weight (after drying)
 W1 : Initial weight

COD value

The efficiency of substrate breakdown was determined using COD analysis. In a 15 mL falcon tube, a total mass of one gram of sample was diluted with 20x dilution of deionized water. A syringe filter was then used to filter the sample. A total of two mL of filtrate was added to COD vials containing a solution of premixed chemicals (K₂Cr₂O₇, AgNO₃, and H₂SO₄). Following two hours of digestion at 150 °C (Lovibond Thermoreactor, RD125), the filtrate-containing COD vials were cooled to room temperature (27 °C). Following technique COD 8000, the COD values of the digested samples were read using UV-Vis DR 2800.

Acetic acid content

Acetic acid content is to determine the presence of acetic acid content in the eco-enzyme as there is production of organic acids throughout the fermentation. The acetic acid was measured by using the titration method with a dilution factor of 5 mixing 2 ml of eco-enzyme with 8 ml of distilled water. Two to three drops of phenolphthalein indicator were added into the mixing solution to indicate the pink colour once titrated with 0.1N of NaOH. After the titration, the volume of NaOH was determined to calculate the acetic acid content by using the formula below:

$$Acetic\ acid\ content \left(\frac{g}{L} \right) = (V_{NaOH} \times N_{NaOH} \times Mr_{NaOH} \times Dilution\ Factor) / (V_{sample})$$

Where:

V_{NaOH} = Volume of sodium hydroxide
 N_{NaOH} = Normal sodium hydroxide
 Mr Acetic Acid =Molecular weight acetic acid
 V_{Sample} = Volume sample
 Dilution Factor = 5

FTIR

About 1 ml of eco enzyme solution sample was weighed with the addition of 0.1 g KBr powder and should not exceed 0.5 and above. The mixture of the two samples was blended by using the pestle mortar. Once the sample was already mixed up, the sample was put inside the dry pellet pressing die and pressed to flatten the sample and was crushed. The standard of the sample was obtained by clicking the BKG button on the monitor. Once the standard of the sample was obtained, the FTIR analysis was run, and the results of the desired compound and bonds present in the sample were shown in the FTIR graph based on peak values.

RESULTS AND DISCUSSION

Characterization of eco-enzyme and CHAP.

CHAP characterization.

Table 5.1 Analysis of CHAP before and after the fermentation.

Analysis	CHAP (Before Fermentation)	CHAP (After Fermentation)
Carbon	3.155	7.998
Hydrogen	0.4101	1.438
Nitrogen	-0.0767	0.0762
Sulphur	0.018	0.011

Based on Table 5.1, carbon showed the highest composition among the four macronutrients both before and after fermentation, at 3.155%, followed by hydrogen at 0.4101%, sulfur at 0.018%, and nitrogen at -0.0767%. After fermentation, the composition of CHN macronutrients increased, with carbon at 7.998%, hydrogen at 1.438%, and nitrogen at 0.0762%. However, the sulfur composition decreased to 0.011%. This situation happened as a result of fruit wastes deteriorating during the fermenting process. The increase in carbon by approximately 4.843% after fermentation is attributed to biofilm formation, which accumulates organic acids and other carbon-rich components. This indicates the efficiency of the process in incorporating organic compounds into the CHAP structure, where a higher carbon content correlates with the higher production of bioactive compounds essential to the functionality and effectiveness of the eco-enzyme (Dhakal et al., 2024[8]). The rise in hydrogen content from 0.4101% to 1.438% suggests the formation of organic compounds, such as organic acids and alcohols, which likely contribute to the eco-enzyme's reactivity, enhancing its ability to break down complex matter.

The negative nitrogen content before fermentation, which is negligible, reflects the low nitrogen levels in CHAP. However, after fermentation, the increase in nitrogen indicates the assimilation of nitrogenous compounds like proteins and amino acids, which are introduced during fermentation. This presence of nitrogen after fermentation suggests that enzymatic reactions have occurred, supporting microbial growth and improving the efficiency of the eco-enzyme products. Conversely, the slight decrease in sulfur content from 0.018% to 0.011% suggests that some sulfur was utilized during the fermentation process for the synthesis of amino acids.

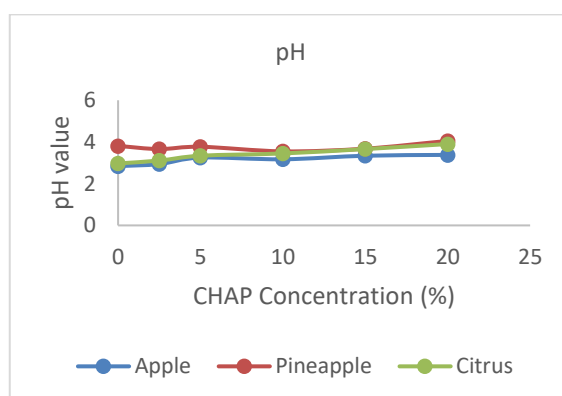


Fig. 1: Graph of pH against different CHAP concentration.

Table 5.2 Analysis of eco-enzyme with different concentration of CHAP and different type of eco-enzyme fruits.

CHAP Concentration (%)	Analysis	Apple	Pineapple	Citrus
0	pH	2.84	3.81	2.97
2.5		2.94	3.66	3.11
5		3.25	3.77	3.34
10		3.17	3.55	3.45
15		3.34	3.68	3.66
20		3.38	4.05	3.9
0	Total Solid (ppm)	828.40	695.50	896.97
2.5		790.90	721.10	905.66
5		780.70	724.30	772.66
10		821.70	612.00	701.65
15		778.00	743.80	777.84
20		770.80	784.70	748.47
0	Total Dissolved Solid (ppm)	506.83	333.98	686.12
2.5		601.53	508.05	694.81
5		475.78	320.68	415.83
10		185.99	410.02	423.80
15		437.17	393.92	566.83
20		271.86	245.15	465.23
0	COD Removal (%)	32.72	4.35	12.95
2.5		13.33	23.93	4.23
5		4.64	7.03	23.23
10		33.12	5.46	2.26
15		12.49	23.88	22.58
20		22.45	20.80	12.53
0	Acetic Acid Content (g/L)	142.62	7.51	69.06
2.5		127.61	12.01	36.03
5		73.56	18.02	69.06
10		120.10	16.51	84.07
15		93.08	27.02	61.55
20		109.59	27.02	66.06

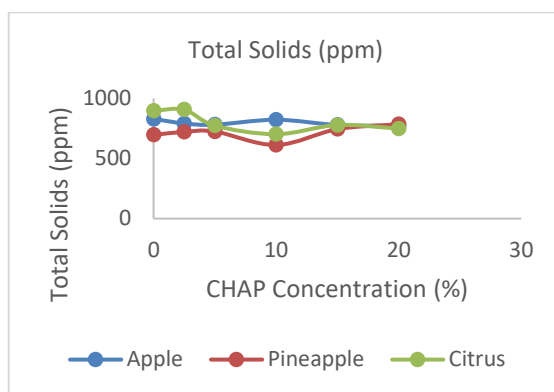


Fig. 2: Graph of total solids against different CHAP concentration.

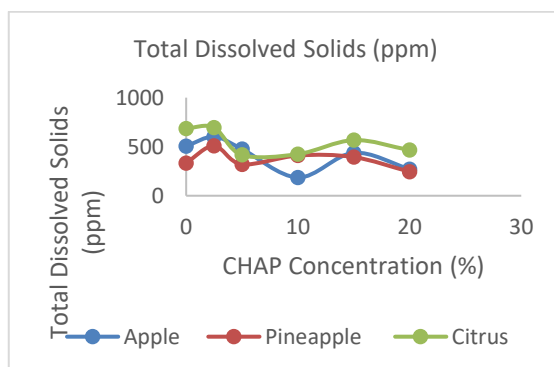


Fig. 3: Graph of total dissolved solids against different CHAP concentration.

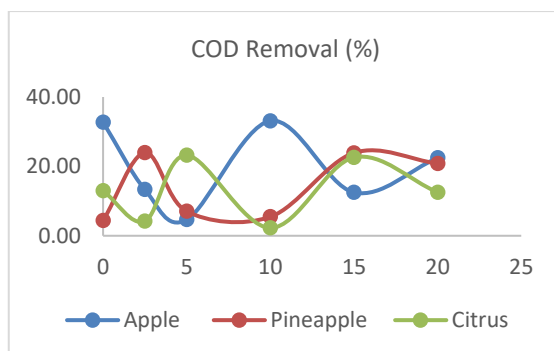


Fig. 4: Graph of COD removal against different CHAP concentration.

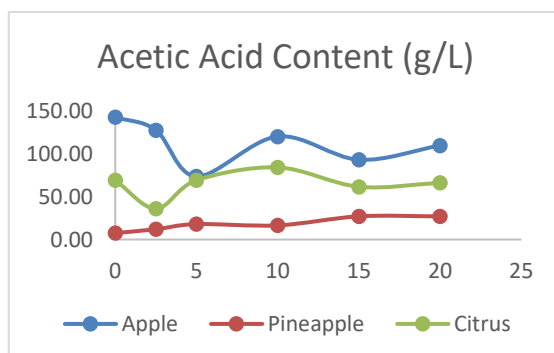


Fig. 5: Graph of acetic acid content against different CHAP concentration.

From Table 5.2 and Fig. 1, the pH value for apple increases from 2.84 to 3.38, for pineapple from 3.81 to 4.05, and for citrus from 2.97 to 3.9. The pH values for all three fruits generally show an increasing trend with the rise in CHAP concentrations. Specifically, higher CHAP concentrations tend to increase the pH level of all fruit types in the eco-enzyme, indicating a possible buffering effect of CHAP during the fermentation process.

For total solids in Fig.2, there are fluctuations across different CHAP concentrations. In apples, total solids decrease with increasing CHAP concentration, except at 10% CHAP, where there is a slight increase. However, for pineapple, there is no clear trend, with only slight fluctuations observed. For citrus, total solids decrease with increasing CHAP concentration, with a significant drop at 5% CHAP due to CHAP's functionality in reducing solid content during fermentation, potentially leading to clearer eco-enzyme solutions.

Regarding COD removal in Fig 4, for all fruit types, COD removal tends to increase with rising CHAP concentration. For apple, COD removal significantly increases from 32.72% to 22.45% at 20% CHAP. For pineapple, COD removal slightly increases but drops at higher CHAP concentrations. For citrus, COD removal generally increases but also shows some fluctuations. Overall, COD removal efficiency improves with higher CHAP concentrations, enhancing the breakdown of organic matter in all fruit types.

For acetic acid content in Fig 5, the acid content generally increases with rising CHAP concentration. In apples, the content increases from 142.62 g/L to 109.59 g/L, while in citrus, it increases from 69.06 g/L to 66.06 g/L. However, the acetic acid content in pineapple shows only minimal increases with some fluctuations. The fluctuations in pineapple's results when varying CHAP concentrations are likely due to the complex interplay of factors, including pineapple's high sugar and enzyme content and the variable interactions between the organic materials in pineapple and CHAP (Maghraby et al., 2023[9]).

Pineapples are naturally high in sugars such as glucose and sucrose, which are primary substrates in the fermentation process that produce acetic acid and other byproducts (Rasit & Chee Kuan, 2018[10]). The fluctuating levels of acetic acid and COD removal may result from variations in how these sugars are fermented under different CHAP concentrations, where some CHAP concentrations might facilitate more efficient fermentation, while others might inhibit certain microbial activities, leading to inconsistent results. Moreover, pineapple contains natural enzymes like bromelain, which might interact differently with CHAP. These enzymes could either enhance or disrupt the fermentation process, leading to variability in the breakdown of solids and the production of acetic acid.

CHAP might interact differently with various organic compounds in pineapple. The adsorption of organic molecules onto the surface of CHAP particles might vary depending on the concentration, leading to inconsistent removal of total solids and production of acetic acid. (Aina et al., 2022[11]).

Table 5.3 Analysis of FTIR for 20% of eco-enzyme for all fruit types.

CHAP Concentration (%)	Absorbance peak	Functional group	Compound
Apple 20.0%	3312.25	O-H stretch	Alcohols, phenols
	2112.84	C≡C stretch (Alkyne)	Alkynes
	1639.13	C=C stretch (Alkene)	Alkenes
	1402.13	C-H bend (Methyl group)	Alkanes
	1280.60	C-O stretch	Esters, ethers, carboxylic acids
	1041.75	C-O stretch	Alcohols, ethers, esters
Pineapple 20.0%	3310.46	O-H stretch	Alcohols, phenols
	2123.66	C≡N stretch (Nitrile)	Nitriles
	1639.32	C=C stretch (Alkene)	Alkenes
	1043.56	C-O stretch	Alcohols, ethers, esters
	599.26	C-Cl stretch	Chlorinated organic compounds
Citrus 20.0%	3309.76	O-H stretch	Alcohols, phenols
	2118.23	C≡C stretch (Alkyne)	Alkynes
	1637.90	C=C stretch (Alkene)	Alkenes
	1415.71	C-H bend (Methyl group)	Alkanes
	1042.32	C-O stretch	Alcohols, ethers, esters
	602.05	C-Cl stretch	Chlorinated organic compounds

Table 5.3 presents the Fourier Transform Infrared (FTIR) analysis, indicating the peak absorbance of the control eco-enzyme from different fruit types after three months of fermentation. By identifying the bond areas for single, double, and triple bonds, and the fingerprint region, it becomes easier to separate and identify bonds at different locations.

For single bonds, the wide absorption band at the range 3200-3550 cm⁻¹ indicates the presence of hydroxide compounds, confirming the presence of hydroxyl (OH) groups, which are typical for alcohols or carboxylic acids. This peak represents the bonds present in the eco-enzyme, which are broken down through enzymatic reactions during the degradation of organic materials, functioning as natural cleaning agents. Hydroxyisourate hydrolase and vicianin hydrolase enzymes catalyze the breaking of these bonds by reacting with water, which breaks the bonds linking the composition of the substrate itself. The natural function of most hydrolases is digestion, breaking down the components and nutrients of the eco-enzyme into smaller units.

During the complex degradation of eco-enzymes, the presence of alkynes or nitriles is observed at the range 2100-2260 cm^{-1} for alkynes and 2200-2260 cm^{-1} for nitriles. Although these are less common in natural fermentation products apples and citrus show predominantly alkynes while pineapple retains nitriles which indicates that the CHAP concentration may influence the type of triple-bonded compounds that

persist during the fermentation. The presence of nitriles in pineapple shows that it consists of a unique biochemical reaction between the natural enzymes and their chemical composition. At a range of 1620-1680 cm^{-1} and 1670-1820 cm^{-1} , there is the presence of C=O stretching and C=C in the CHAP-enriched sample rather than the control sample due to higher presence of unsaturated hydrocarbons which facilitates the formation of different organic compounds during fermentation. The peaks at range 1000-1300 cm^{-1} and 1350-1470 cm^{-1} which are related to C-H and C-O stretching, represent the presence of esters or alcohols, which are common in bioactive compounds. Additionally, C-Cl is stretching at 599.54 cm^{-1} , possibly from chlorinated organic compounds, which might originate from environmental contamination or additives. The higher the peak absorbance, the greater the number of bonds present in the eco-enzyme, as this is linked to the composition structure. Peak intensity usually correlates with an increase in the number of functional groups (per unit volume) associated with a molecular bond, and a shift in peak position typically indicates a change in the electron distribution of the molecular bond (Mohamed, 2017[12]).

For the three different fruit-based eco-enzymes with and without CHAP, the FTIR analysis shows the presence of functional groups representing organic acids such as acetic acid, alcohol, and some esters. These compounds are known for their antimicrobial properties, which can influence enzymatic activity. The presence of organic acids in the eco-enzymes naturally contributes to pH reduction, potentially enhancing the effectiveness of organic fruit waste degradation into beneficial natural products throughout the fermentation process. Alcohols and ethers, which are byproducts of fermentation, function in solubilizing dissolved oils present in fruits along with other hydrophobic substances. Moreover, esters might be more prominently present in apple-based eco-enzymes due to the chemical composition of apples, which naturally contain high sugar content and acids. This could lead to the production of specific secondary metabolites that, along with fermentation conditions, favour ester formation, making them more prominent in the FTIR analysis compared to pineapple and citrus eco-enzymes. This FTIR analysis indicates the main functional groups which remain stable across both eco-enzyme control and without CHAP and the CHAP show their influences types and abundances of certain organic compounds to modify the fermentation process which might lead to a more effective product. The eco-enzyme with CHAP shows a promising shift towards the bioactive compounds which could enhance the eco-enzyme's performance.

CONCLUSION

Based on the experimental study, it shows that the enhancement of enzyme in eco-enzymes through the addition of hydroxyapatite nanomaterials throughout the fermentation process is successful. By systematically varying the concentration of hydroxyapatite, the research showed significant improvements in key parameters such as the pH value, total solids, total dissolved solids, and chemical oxygen demands (COD) removal. The introduction of hydroxyapatite not only enhanced the production of bioactive compounds in the production process but also

influenced a more efficient breakdown of organic matter particularly in eco-enzymes derived from different types of fruits, apple, pineapple, and citrus.

ACKNOWLEDGEMENTS: In the name of Allah, The Most Gracious and The Most Merciful. Praise to Allah the almighty for his goodness and mercy and his blessing to keep me and strengthen my soul to complete my final year project successfully. First and foremost, I would like to express my gratitude and special thanks to my parents, Mr. Sabri bin Abd Rahman and Mrs. Rozita binti Wabong, for being incredibly supportive and encouraging. They never passed judgment on me and always lent an ear, listening to all of my complaints.

Beforehand, I would like to express my deepest gratitude and appreciation to my supervisor, Dr Nur Syakina Jamali for giving me a great chance and his guidance to complete my project. It is always a pleasure to remind all of his guidance as he worked tirelessly to provide good instrumentations and knowledges throughout my master journey.

REFERENCES

- [1] Bharvi S. Patel, Bhanu R. Solanki, & Archana U. Mankad. (2021). Effect of eco-enzymes prepared from selected organic waste on domestic waste water treatment. *World Journal of Advanced Research and Reviews*, 10(1), 323–333.
- [2] Y. Hasanah, L. Mawarni, and H. Hanum, “Eco Enzyme and Its Benefits for Organic Rice Production and Disinfectant,” *J. Saintech Transf.*, vol. 3, no. 2, hal. 119–128, 2020.
- [3] Siddiqui SA, Erol Z, Rugji J, Taşçı F, Kahraman HA, Toppi V, Musa L, Di Giacinto G, Bahmid NA, Mehdizadeh M, Castro-Muñoz R. An overview of fermentation in the food industry - looking back from a new perspective. *Bioresour Bioprocess*. 2023 Nov 28;10(1):85.
- [4] A.G, Rosnina & Wirda, Zurrahmi & Hafizh, M.. (2023). The Important Roles of Ecomychorizae to Increase Growth Rate of Sacha Inchi (*Plukenetia volubilis* L.) that Potentially as Raw Material of Biofuel. *Proceedings of Malikussaleh International Conference on Multidisciplinary Studies (MICOMS)*. 3. 00058.
- [5] Mohd Pu’ad, N. A. S., Alipal, J., Abdullah, H. Z., Idris, M. I., & Lee, T. C. (2019). Synthesis of eggshell derived hydroxyapatite via chemical precipitation and calcination method. *Materials Today: Proceedings*, 42, 172–177.
- [6] Mo, H., Wang, N., Ma, Z., Zhang, J., Zhang, J., Wang, L., Dong, W., & Zang, L. (2022). Hydroxyapatite Fabrication for Enhancing Biohydrogen Production from Glucose Dark Fermentation. *ACS Omega*, 7(12), 10550–10558.
- [7] Fadlilla, T., Budiastuti, Mt. S., & Rosariastuti, M. R. (2023). Potential of Fruit and Vegetable Waste as Eco-enzyme Fertilizer for Plants. *Jurnal Penelitian Pendidikan IPA*, 9(4), 2191–2200.
- [8] Dhakal, Milan & Ghimire, Saphal & Karki, Geeta & Deokar, Gitanjali & Al-Asmari, Fahad & Nirmal, Nilesh. (2024). Fruit Waste: Potential Bio-Resource for Extraction of Nutraceuticals and Bioactive Compounds.

- [9] Maghraby, Y. R., El-Shabasy, R. M., Ibrahim, A. H., & Azzazy, H. M. E. S. (2023). Enzyme Immobilization Technologies and Industrial Applications. In ACS Omega (Vol. 8, Issue 6, pp. 5184–5196). American Chemical Society.
- [10] Rasit, N., & Chee Kuan, O. (2018). Investigation on the Influence of Bio-catalytic Enzyme Produced from Fruit and Vegetable Waste on Palm Oil Mill Effluent. IOP Conference Series: Earth and Environmental Science, 140(1).
- [11] Aina, S., Du Plessis, B., Mjimba, V., & Brink, H. (2022). Eggshell valorization: Membrane removal, calcium oxide synthesis, and biochemical compound recovery towards cleaner productions. Biointerface Research in Applied Chemistry, 12(5), 5870–5883.
- [12] Mohamed, Mohamad & Jaafar, Juhana & Ismail, Ahmad & Othman, Mohd Hafiz & Rahman, Mukhlis. (2017). Fourier Transform Infrared (FTIR) Spectroscopy.

GREEN MATERIALS AND PRODUCTS

Synergistic Enhancement of Mechanical Properties in Banana Fiber-Graphite Hybrid Composites with Epoxy Matrix: A Novel Approach to Sustainable High-Performance Materials

Senthil Kannan N^{1*}, Omprakasam S² and Raghu R³

^{1,2,3} Department of Mechanical Engineering, Sri Ramakrishna Engineering College,
Coimbatore, India

*Corresponding author's E-mail: nsk@srec.ac.in/ senthilphd18@gmail.com

Abstract: Composite materials have gained significant attention due to their exceptional mechanical properties and diverse applications in various industries. In this study, the potential of utilizing banana fiber as a reinforcement material in combination with graphite for the development of composite materials is explored. Banana fiber, sourced from agricultural waste, offers an eco-friendly alternative to conventional reinforcement materials, while graphite contributes to enhancing electrical conductivity and mechanical strength. Various weight percentages of banana fiber (10%, 20% and 30% by weight) and graphite (10%, 20% and 30% by weight) in epoxy were utilized for the development of the composites. Results revealed that the combination of the graphite (10 wt. %)/banana fiber (30%) has the higher tensile strength of 1.580 kN, the graphite (30 wt. %)/banana fiber (10%) has the higher compressive strength of 0.480 kN, among the various combinations of the graphite and banana fiber composites.

Keywords—composite materials; Banana fiber; Graphite; Mechanical properties; Experimental analysis.

INTRODUCTION

Composite materials have garnered immense interest in recent years due to their versatility, offering tailored properties that outperform traditional materials in various applications [1]. Among the array of composite constituents, natural fibers have emerged as promising alternatives to synthetic reinforcements, owing to their renewable nature and relatively low cost [2]. Banana fiber, derived from the stem of the banana plant, is one such natural fiber gaining attention for its remarkable mechanical properties and abundance in tropical regions. Concurrently, graphite, with its excellent electrical conductivity and mechanical strength, presents an intriguing option for enhancing the performance of composite materials [1]. This study endeavors to explore the synergistic effects of combining banana fiber and graphite as constituents in composite materials. The recent researchers has not explored on approaching combination of banana and graphite composite materials as they have different characteristic when they are mixed in different combination and can be used for different applications. The banana fiber carries the ability to withstand more tensile force and graphite carries the ability to withstand more compressive force [2]. For the following uses, these developed natural fiber composites can be a highly economical material: The building and construction industry: false ceiling and partition panels, partition boards, wall, floor, window, and door frames, roof tiles, and pre-fabricated or movable buildings that may be employed in the event of natural disasters like earthquakes, cyclones, or floods, among others [1].

The following are the primary goals of the current research work: Assess the mechanical properties of banana fiber and graphite composites, specifically focusing on tensile and compressive strengths. Determine the optimal ratio of banana fiber to graphite in the composite by testing various weight percentages (10%, 20%, and 30%) of banana fiber and (10%, 20%, and 30%) graphite in an epoxy matrix.

THEORY/LITERATURE REVIEW

Natural fiber-reinforced polymer composites have garnered significant attention in recent years due to their sustainability, eco-friendliness, and cost-effectiveness. Banana fiber, in particular, has been extensively studied for its potential to enhance mechanical properties of biocomposites [2]. Bharath et al. [3] examined the effect of compression molding parameters on natural fiber composites. They found that compression pressure had the most significant influence on tensile and bending strength, followed by mold temperature and pressure application time. A hybrid composite with 0.8% nano-filler addition exhibited enhanced tensile strength (183 MPa), bending strength (158.3 MPa), and hardness (23.8 HV). Ibrahim et al. [4] studied the effect of graphite microparticles on epoxy matrix composites. They reported a significant decrease in tensile strength (over 50%) with 1 wt% graphite loading, while flexural strength initially increased with 0.1 wt% graphite before decreasing at higher concentrations. Wear rate was found to decrease sharply with increasing graphite content due to the formation of a lubricating layer at the contact surface. Nguyen and Nguyen [5] investigated the mechanical properties of banana fiber-reinforced poly(lactic acid) (PLA) composites. They found that treating banana fibers with 5% NaOH improved fiber-matrix compatibility. Composites with 20 wt% banana fiber exhibited optimal mechanical properties, including tensile strength of 52.57 MPa, flexural strength of 70.35 MPa, impact strength of 155.45 J/m, and hardness of 23.8 Hv. Ramesh et al. [6] investigated the abrasive water jet machining of banana fiber-reinforced polyester composites. They observed that standoff distance had the greatest impact on surface roughness (60.63%) and kerf angle (74.80%). Ku et al. [7] reviewed the tensile properties of natural fiber-reinforced polymer composites. They found that the rule of mixture (ROM) accurately predicted tensile strengths for various natural fiber-reinforced HDPE composites, while the Halpin-Tsai equation was most suitable for predicting the Young's modulus of multi-fiber composites. In another study, Nguyen and Nguyen [8] explored banana fiber-reinforced epoxy composites. They reported that composites with up to 20 wt% banana fiber showed improved tensile, compressive, and impact strengths compared to neat epoxy. The 20 wt% banana fiber composite demonstrated a limiting oxygen index of 20.8% and satisfactory thermal stability. Ahmed et al. [9] reviewed the properties of graphite nanoparticles (GNP) and their industrial applications. They noted that GNPs exhibit significantly different properties at the nanoscale compared to their bulk form, and even low concentrations of GNPs can substantially alter fluid properties when used as additives. This literature review demonstrates the growing interest in natural fiber-reinforced composites, particularly those utilizing banana fibers, and highlights the potential for enhancing mechanical and thermal properties through various treatment methods and processing techniques. Additionally, the incorporation of graphite and graphite-based nanocomposites offers promising avenues for further improving composite performance in various applications.

MATERIALS

The properties of banana fiber and graphite is shown in Table 1. The Cellulose, Hemi Cellulose, and Lignin content are measured using chemical analysis methods such as Van Soest method. Moisture content is determined through oven-drying methods, measuring weight loss. The Pectin content is analyzed through extraction and colorimetric methods. Density is measured through the pycnometry method. The fibers were extracted from the pseudostem of the nendran banana plant which was planted in Sri Ramakrishna Engineering College premises in Coimbatore.

Table 1: Properties of the banana fiber and graphite

Banana fiber		
Sl No.	Property	Range
1	Cellulose (%)	60-64
2	Hemi Cellulose (%)	6-19
3	Lignin (%)	5-10
4	Moisture (%)	11
5	Pectin (%)	3-5
6	Density (g/cm ³)	1-1.5
7	Elongation at breaking (%)	4-6.5
8	Young's Modulus (GPa)	20
Graphite		
1	Density (g/cm ³)	2.09-2.23
2	Porosity (%)	0.7-53
3	Compressive Strength (MPa)	20-200
4	Tensile Strength (MPa)	8-70
5	Young's Modulus (GPa)	8-15

The basic properties of epoxy and hardener are shown in Table 2, which is used as received from Araldite.

Table 2: Basic properties of Epoxy and Hardener

Properties	Epoxy LY556	Hardener HY951
Visual appearance	Medium viscosity, colorless clear liquid	Brownish yellow color liquid
Viscosity at room temperature	9000–12000 MPa	500–1000 MPa
Density at room temperature	1.13–1.16 gm/cc	0.946 gm/cc

EXPERIMENTAL

The experimental procedure begins with the preparation of banana fibers, which are cleaned, cut to a uniform length of approximately 30 mm, and treated with 5% NaOH solution for 2 hours to remove impurities and enhance fiber-matrix adhesion. The treated fibers are then washed thoroughly with distilled water and dried in an oven at 80°C for 24 hours. Next, the epoxy matrix is prepared by mixing the resin and hardener according to the manufacturer's recommended ratio. The composite fabrication process involves weighing appropriate amounts of banana fibers, graphite powder, and epoxy matrix for each composition (10%, 20%, and 30% by weight for both banana fiber and graphite). The graphite powder is first mixed with the epoxy matrix using a mechanical stirrer for 10 minutes to ensure uniform dispersion. Treated banana fibers are then gradually added to this mixture, stirring continuously to achieve uniform distribution. The resulting mixture is poured into a pre-treated mold and cured in a hot press at 80°C and 5 MPa pressure for 2 hours. After cooling to room temperature, the composite is removed from the mold and post-cured in an oven at 100°C for 2 hours to enhance cross-linking and improve mechanical properties. Finally, the fabricated composite is cut into appropriate sizes for tensile and compressive testing according to ASTM standards, cleaned with acetone, and dried before testing. Tensile and compressive tests are conducted using a universal testing machine, and the maximum load at failure is recorded for each sample to calculate the tensile and compressive strengths for different compositions. The composite is fabricated and the XRD analysis, SEM examination, FTIR analysis, tensile testing and compression testing is carried out to study its behavior. Each technique offers unique insights into the chemical composition, structural properties, and microstructural features of the composite.

RESULTS AND DISCUSSION

The fracture specimens after the test are shown in Fig. 1.



Fig. 1: Fractured test specimens

Fig. 2, 3 and 4 shows the tension test results for all the composites. This composition achieved the highest tensile strength of 1.580 kN among the various combinations tested. Fig. 5,6 and 7 presents the compression test results for the composition with 30% graphite and 10% banana fiber. This combination demonstrated the highest compressive strength of 0.480 kN among all tested compositions. Higher banana fiber content (30%) contributes to improved tensile strength, likely due to the fiber's ability to resist tensile loads. Higher graphite content (30%) enhances compressive strength, possibly because graphite particles can effectively distribute compressive loads throughout the matrix.

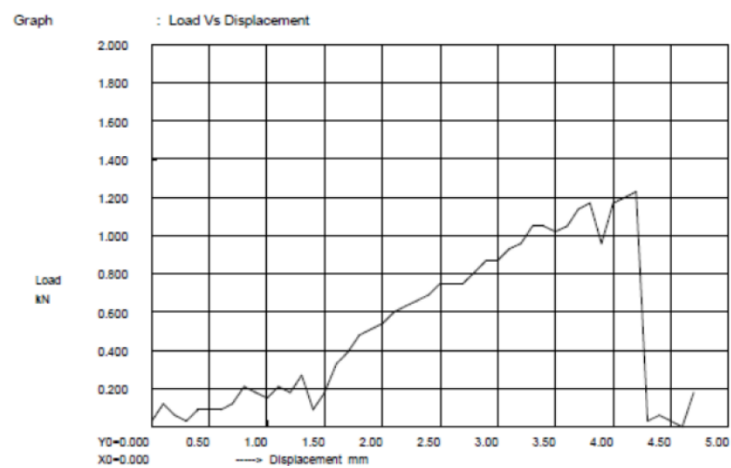


Fig. 2: Tension test results for 30% graphite and 10% banana fiber composition

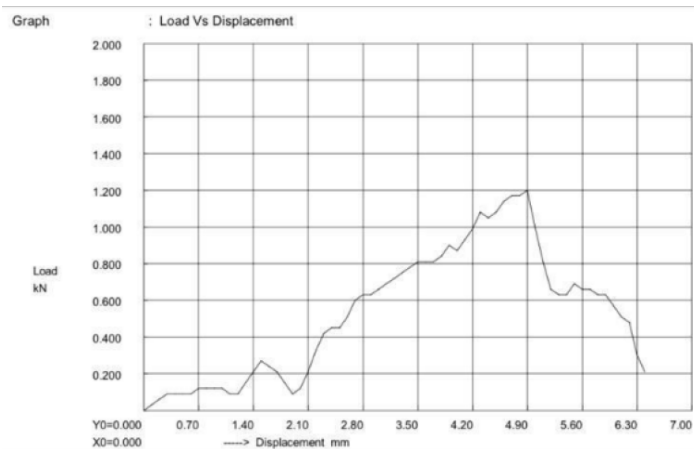


Fig. 3: Tension test results for 20% graphite and 20% banana fiber composition

Test Certificate	
Date : 13-12-2023	
OMEGA INSPECTION AND ANALYTICAL LABORATORY,	
Sample Identification : 10% GRAPHITE, 30% BANANA FIBER	
Machine : Universal Testing Machine, 600 kN	
Input Data	File Name : 23-1319-T1 Sample Type : Rectangular Bar Width : 7.6 mm Gauge Length : 0 mm
Record No. : 1	Area : 48.980 mm ² Thickness : 6.2 mm
Results of Tension Test Maximum Force (Fm) : 1.560 kN	
Graph : Load Vs Displacement	
Y0=0.000 X0=0.000 Displacement mm	
TESTED BY	INSPECTED BY
WITNESSED BY	

Fig. 4: Tension test results for 10% graphite and 30% banana fiber composition

The tension test report for 10% graphite and 30% banana fiber composition is 1.580 kN and the compression test reports that 30% graphite and 10% banana fiber composition is 0.480 kN.

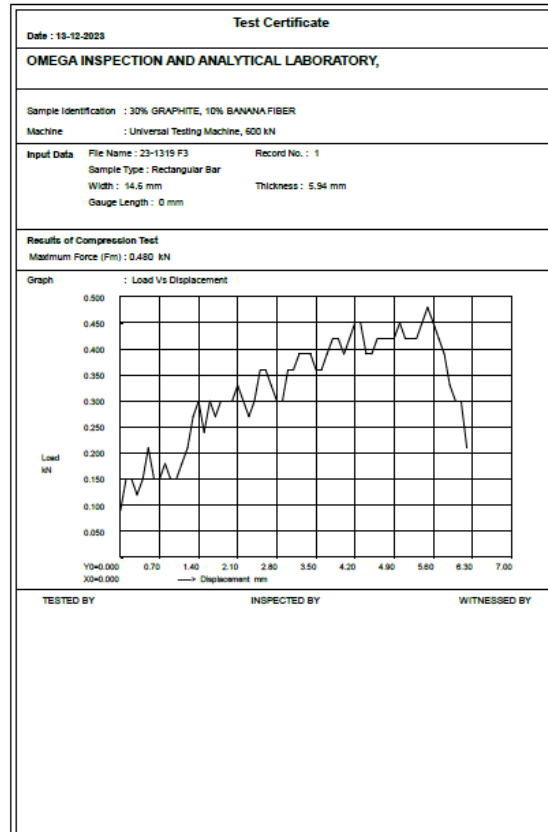


Fig. 5: Compression test results for 30% graphite and 10% banana fiber composition

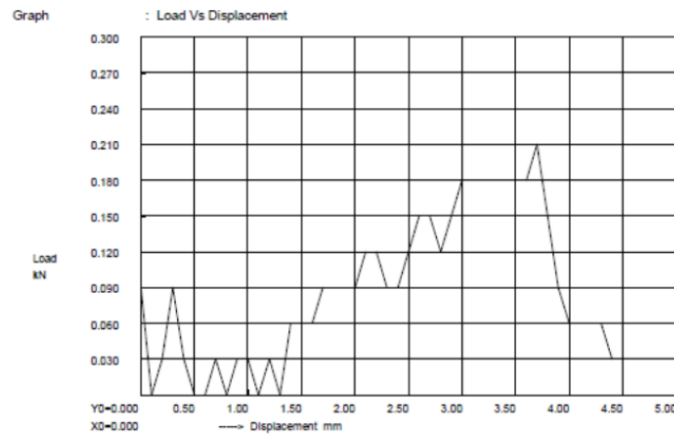


Fig. 6: Compression test results for 20% graphite and 20% banana fiber composition

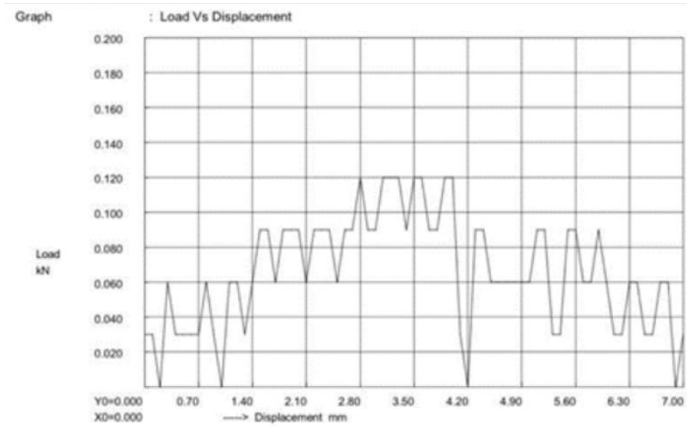


Fig. 7: Compression test results for 10% graphite and 30% banana fiber composition

Figs. 8,9 and 10 show the Fourier Transform Infrared (FTIR) spectroscopy results for the banana fiber/graphite composites. FTIR helps identify the chemical bonds and functional groups present in the composite.

- Peaks around 3300-3500 cm^{-1} , indicating O-H stretching from cellulose in banana fibers
- Peaks around 2800-3000 cm^{-1} , representing C-H stretching from both fibers and epoxy matrix
- Peaks around 1000-1200 cm^{-1} , showing C-O stretching from cellulose and epoxy
- Peaks specific to graphite, typically around 1580 cm^{-1} and 1360 cm^{-1}

The presence and intensity of these peaks can confirm the successful incorporation of banana fibers and graphite into the epoxy matrix.

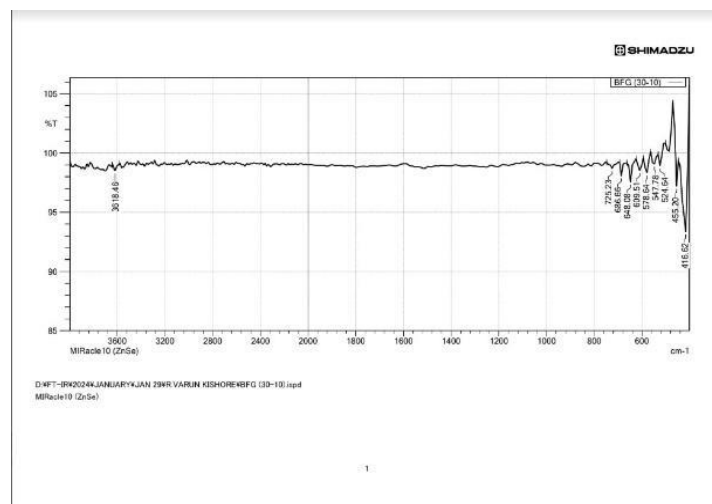


Fig. 8: FTIR examination of the 30 % banana fiber/10 % graphite composite

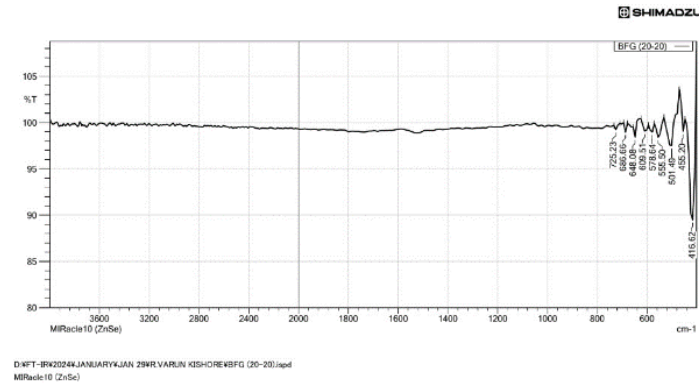


Fig. 9: FTIR examination of the 20 % banana fiber/20 % graphite composite

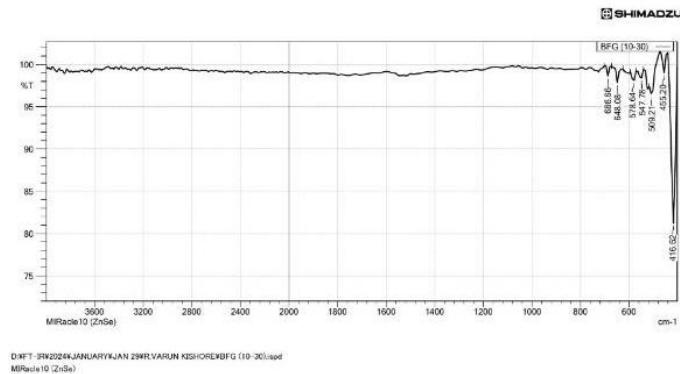


Fig. 10: FTIR examination of the 10 % banana fiber/30 % graphite composite

Figs. 11,12 and 13 present the X-Ray Diffraction (XRD) results for the banana fiber/graphite composite. XRD analysis helps identify the crystalline structures present in the material. Broad peaks around $15-17^\circ$ and $22-23^\circ$ 2θ would indicate cellulose from banana fibers. A sharp peak around $26-27^\circ$ 2θ would represent graphite. The absence of sharp peaks in other regions would suggest the amorphous nature of the epoxy matrix. The relative intensities of these peaks can provide information about the proportions of crystalline components in the composite.

Fig. 14 shows the Scanning Electron Microscopy (SEM) examination of the banana fiber/graphite composite. SEM provides information about the surface morphology and fiber distribution within the composite. SEM results for such composites revealed the distribution and orientation of banana fibers within the matrix, the interface between fibers and the epoxy matrix, indicating the quality of adhesion, the dispersion of graphite particles throughout the composite and any voids or defects in the material.

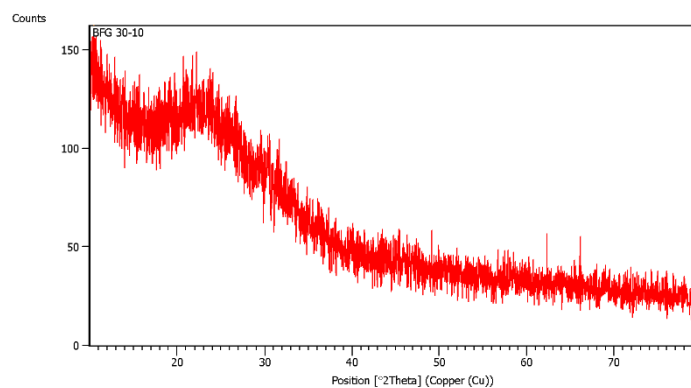


Fig. 11: XRD examination of the 30 % banana fiber/ 10 % graphite composite.

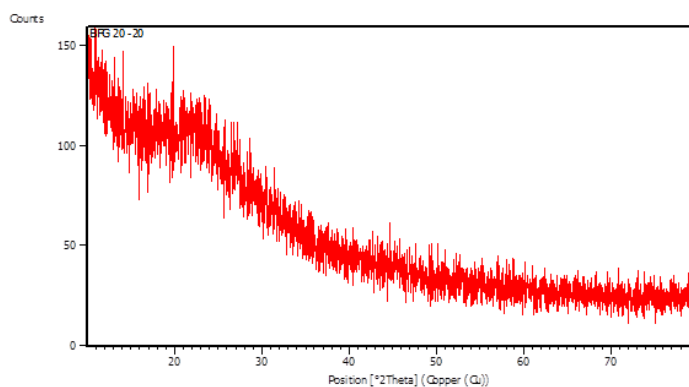


Fig. 12: XRD examination of the 20 % banana fiber/ 20 % graphite composite

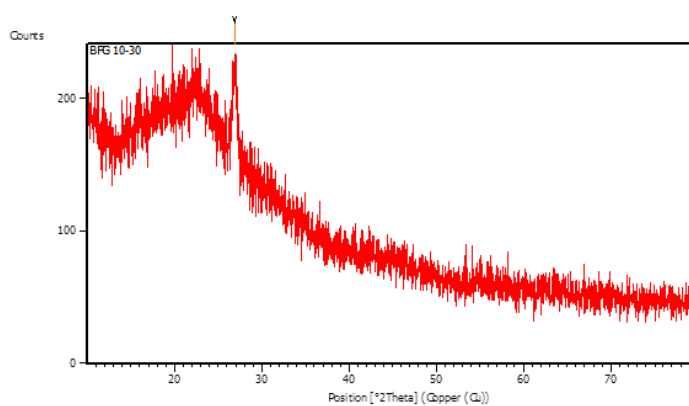


Fig. 13: XRD examination of the 10 % banana fiber/ 30 % graphite composite

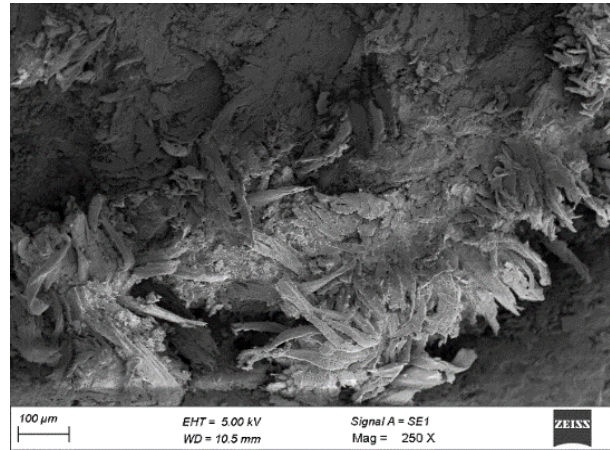


Fig. 14: SEM examination of the banana fiber/graphite composite

CONCLUSIONS

This study has successfully demonstrated the potential of utilizing banana fiber and graphite as reinforcement materials in the development of eco-friendly composite materials with enhanced mechanical properties. The investigation of various weight percentages of banana fiber and graphite in epoxy matrix has yielded valuable insights into the performance of these novel composites. The results clearly indicate that the composition of the composite significantly influences its mechanical properties. Notably, the combination of 10 wt% graphite and 30 wt% banana fiber exhibited the highest tensile strength of 1.580 kN. This suggests that a higher content of banana fiber contributes to improved tensile properties, likely due to the fiber's ability to effectively distribute tensile loads throughout the matrix. Conversely, the composite with 30 wt% graphite and 10 wt% banana fiber demonstrated the highest compressive strength of 0.480 kN. This finding indicates that a higher graphite content enhances the composite's resistance to compressive forces, possibly due to the graphite particles' capacity to distribute compressive loads more efficiently within the matrix. These results highlight the complementary roles of banana fiber and graphite in enhancing different aspects of the composite's mechanical performance. The ability to tailor the composition to achieve desired properties makes these composites highly versatile for various applications. Furthermore, the use of banana fiber, an agricultural waste product, as a reinforcement material offers an environmentally friendly alternative to conventional synthetic fibers. This aligns with the growing demand for sustainable materials in industry.

ACKNOWLEDGMENT

The authors are grateful to Department of Mechanical Engineering for providing access to the facilities for carrying out the experiments at Centre for Research, Sri Ramakrishna Engineering College, Coimbatore.

REFERENCES

- [1] Senthilkannan, N., Ganesh kishore, S., Hariharasudhan, T., Kishore, S.: An investigation on mechanical Properties of banana coir fibre reinforced composites. *International Journal of Advanced Research in Engineering and Technology* 12(3), 604-612 (2021)
- [2] Senthil Kannan, N., Nagabhooshanam, N., Kumar, A., Rao, P.K.V., Patil, P.P., Bharathi, B.V.V.L.K.: Preparation and characterization of opuntia-cladode fiber and citron peel biochar toughened epoxy biocomposite. *Polymer Composites* 43(9), 6571-6577 (2022)
- [3] Bharath, K.N., Basavarajappa, S.: Applications of biocomposite materials based on natural fibers from renewable resources: a review. *Science and Engineering of Composite Materials* 23(2), 123-133 (2016)
- [4] Ibrahim, M.M., El-Tayeb, N.S.M., Shazly, M., El-Sayed Seleman, M.M.: An experimental study on the effect of graphite microparticles on the mechanical and tribological properties of epoxy matrix composites. *Functional Composite Materials* 5(1), 2 (2024)
- [5] Nguyen, T.A., Nguyen, T.H.: Study on mechanical properties of banana fiber-reinforced materials poly (lactic acid) composites. *International Journal of Chemical Engineering* (2022)
- [6] Ramesh, M.J.P.I.M.S.: Flax (*Linum usitatissimum* L.) fibre reinforced polymer composite materials: A review on preparation, properties and prospects. *Progress in Materials Science* 102, 109-166 (2019)
- [7] Mohammed, A.A., Bachtar, D., Rejab, M.R.M., Siregar, J.P.: Effect of microwave treatment on tensile properties of sugar palm fibre reinforced thermoplastic polyurethane composites. *Defence Technology* 14(4), 287-290 (2018)
- [8] Nguyen, T.A., Nguyen, T.H.: Banana fiber-reinforced epoxy composites: mechanical properties and fire retardancy. *International Journal of Chemical Engineering* 2021, 1-9 (2021)
- [9] Ahmed, M., Ahmed, H., Adebayo, P., Carter, R., Khanal, L.: Mechanical Properties and Application of Graphite and Graphite-based Nanocomposite: A Review. (2023)

Performance of Nanocellulose Fibre Reinforced Starch Biopolymer Composites

A.H.M. Firdaus¹, M.F.M.I. Hafiz² S.M. Sapuan^{1,2} and E.S. Zainudin²

¹ Advanced Engineering Materials and Science (AEMC), University Putra Malaysia, Serdang, Malaysia

² Department of Mechanical Engineering, Faculty of Engineering, Universiti Putra Malaysia, Serdang, Malaysia

*Corresponding author's E-mail: gs69785@student.upm.edu.my

Abstract: Extensive research has been conducted on incorporating nanocellulose into its starch-based plants comprising arrowroot nanocellulose as a filler and arrowroot starch as biopolymer. The aim of this research is to investigate the mechanical and morphological properties of nanocellulose arrowroot fiber reinforced arrowroot starch biopolymer composites. The ARNCC loading ranged from 0 to 3 wt%. Solution casting method was performed to prepare the arrowroot starch (AS) biopolymer film with different Arrowroot Nanocrystalline Cellulose (ARNCC) loading (0,1 and 3%wt) utilizing a combined 30% glycerol and sorbitol as a plasticizer. The study highlights the substantial improvements in mechanical properties due to the introduction of ARNCC into AS film, notably a 173% increase in tensile strength, achieving 4.31 MPa with ARNCC3. However, the increase of ARNCC loading decreases the young's modulus of AS film which indicates that the film become lesser stiffness. Morphological studies provide valuable insights into the structure and composition of the composites, revealing a well-defined interface between the ARNCC and the AS matrix. The existence of bridge cracking on the surface of ARNCC2 and ARNCC3 improves the ability of the film to distribute the stress and improve the tensile strength of the AS film.

INTRODUCTION

Growing worldwide environmental concerns have led to an increasing demand for environmentally friendly products in the modern world. So, an alternative approach for the development of environmentally friendly products involves the utilization of bio-based materials [1]. These materials encompass a wide range of substances, including biopolymers, natural fibres and bio composites. In essence, a biopolymer composite is a material composed of a biodegradable biopolymer matrix derived from natural sources and reinforcing materials that are designed to optimize properties while maintaining environmental sustainability. Udayakumar et al. claimed that biopolymer composites are created by integrating natural fibres as fillers within biodegradable polymer matrices [2]. Recently, researchers have shown significant interest in biomaterials derived from natural sources due to their accessibility and cost-effectiveness.

The utilization of nanocellulose fibres in bio-based materials is highly significant due to their exceptional properties and diverse applications. These nano-sized cellulose fibrils or crystals are widely used as components in a variety of industries since they provide bio-based materials excellent strength, stiffness and biodegradability. Furthermore, the introduction of nanocellulose arrowroot fibre into bio-based materials enhances their flexibility, offering a wider range of

possible uses in several industrial applications. Tarique et al. claimed that arrowroot fibre has small diameter which leads to high tear resistance making it beneficial for packaging and suitable for tissue paper purposes [3].

Arrowroot starch which derived from the rhizomes of the arrowroot plant can serve as the biopolymer due its unique properties and diverse application. Arrowroot is a starch-rich rhizome that generates easily digested starch with great gelling characteristics and a high amylose content (35.20%), making it suitable for film production and having stronger mechanical and barrier properties than amylopectin [4]. Its outstanding gelling properties lead to enhanced texture and stability in food applications while the high amylose concentration which facilitates film manufacturing, offers eco-friendly packaging solutions. Therefore, in this study the effect of nanocellulose arrowroot fibre reinforcement arrowroot starch biopolymer for film production was investigated.

METHODOLOGY

There are various processes that have been done to make sure this project is a success. The process starts with purchasing the arrowroot tuber from the supplier. Then, the process continued with the extraction of the arrowroot starch (AS) and extraction of arrowroot nanocellulose crystalline (ARNCC) using acid hydrolysis method. Next, the biopolymer film was prepared using solution casting method with different ARNCC loadings (0, 1 and 3 wt%).

The extraction of arrowroot starch was carried out at the lab Advanced Engineering Materials and Composites Research Centre (AEMC), Universiti Putra Malaysia (UPM). The arrowroot extraction procedure began with the selection of arrowroot rhizomes, followed by peeling and cutting process. The cut rhizomes were then crushed in Toshiba countertop blender with distilled water in a ratio of 1:2 (m/m) of arrowroot to water for 5 minutes to form a homogeneous mass. The mass was next filtered through a double cotton cloth to separate the solid components. To guarantee complete starch removal, the mass was rinsed three times with distilled water, aiding in fibre separation. After around 12 hours of starch sedimentation, water was manually removed, and the resultant starch was dried in an air flow oven at 60 °C for four hours. Figure 1 shows the process of arrowroot starch (AS) extraction.



Fig. 1: Process of arrowroot starch (AS) extraction

Nanocrystalline cellulose (NCC) was prepared by acid hydrolysis of the cellulose as described by Sanyang et al. (2016). The acid hydrolysis was conducted using a 60 wt% H₂SO₄ solution at 45 °C. The hydrolysis time in this study was fixed at 45 minutes, which was found to be the optimum duration. The ratio of the obtained cellulose to liquor was 5:100 (wt%) (5g arrowroot cellulose to 100g H₂SO₄ solution). The hydrolysed cellulose sample was washed five times by centrifugation (6,000 rpm, 10 minutes, and 8 °C) to remove excess sulfuric acid. The suspension was then dialyzed against distilled water until a constant pH was reached. The

resulting suspension was sonicated for 30 minutes, then subjected to a freeze-drying process and stored in a cool place.

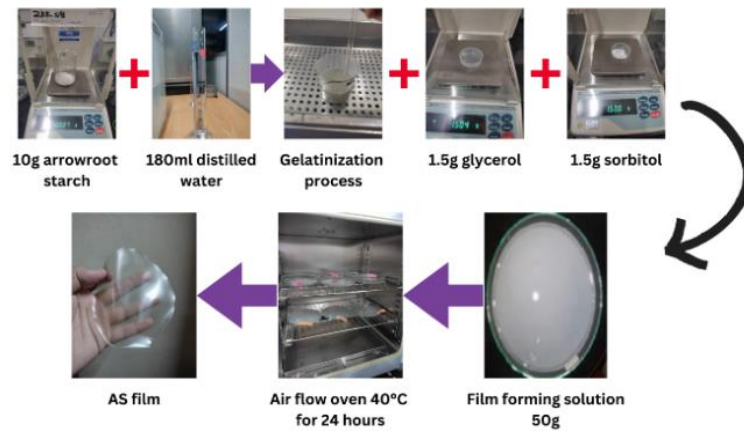


Fig. 2: The biopolymer film preparation process

The film production was carried out at the lab Advanced Engineering Materials and Composites (AEMC), University Putra Malaysia. Biopolymer nanocomposites were developed utilizing the conventional solution casting method. An aqueous suspension of arrowroot nanocellulose crystalline (ARNCC) was prepared by mixing a known concentration of ARNCC (1 to 4 wt% based on arrowroot starch) with distilled water. The arrowroot starch (AS) film-forming solution was prepared by adding 10 g of arrowroot starch to 180 mL of distilled water. Then, 30% of a combined glycerol and sorbitol plasticizer (in a 1:1 ratio) was added to the mixture under constant stirring while heating the mixture at 80 °C for 15 minutes. The film-forming suspension was allowed to cool before 50g of the suspension was poured into each petri dish (13 cm in diameter). The dishes containing the film-forming solution were placed in an oven at 40 °C for 24 hours. AS-based films prepared without ARNCC served as the control (denoted as AS films). Nanocomposite films with 0, 1 and 3wt% ARNCC were designated as Control, ARNCC1, and ARNCC3, respectively. Afterward, the dehydrated samples were conditioned at 25 °C for 24 h, detached from the plates and stored at 25 ± 3 °C and 52% relative humidity for a week before characterization. Figure 2 shows the ARNCC/AS film preparation process. Meanwhile,

The tensile behaviours of bio composite samples were tested at room temperature using an Instron 3366 tensile machine following the ASTM D882-02 standard. The test was carried out at the Strength of Material Laboratory, Universiti Putra Malaysia. The samples (70 × 10 mm²) were properly fixed between tensile clamps. For this test, 3 specimens were tested based on the different nanocellulose loading (0,1,3 wr%). Initially, the gauge length of the samples and the machine crosshead speed were set at 30 mm and 2 mm/min, respectively. Tensile strength, tensile modulus and elongation were measured for 5 replicates of each specimen. The mechanical properties were evaluated using the mean value of the measurements. Finally, the data obtained were tabulated and analyzed after the experiment was carried out. Figure 3 shows the INSTRON 3366 Tensile Machine and the measured length of biopolymer film, respectively.



Fig 3: INSTRON 3366 Tensile Machine

The SEM analysis was carried out at Institute Tropical Forestry and Forest Product, Universiti Putra Malaysia. The purpose of this analysis is to study the surface morphology of arrowroot nanocellulose reinforced arrowroot starch biopolymer film with different percentage of fibre loading (0,1,3 wt%) by setting an acceleration voltage of 5kN using Scanning electron microscope EM-30AX Plus machine. For this analysis, the fractured surface of the films resulting from the tensile test were tested to evaluate the microstructure of the films.

The resultant biopolymer films then undergo two main tests which are tensile test and surface morphology of the tensile specimen using scanning electron microscope (SEM). Figure 4 shows the flowchart process for this project.

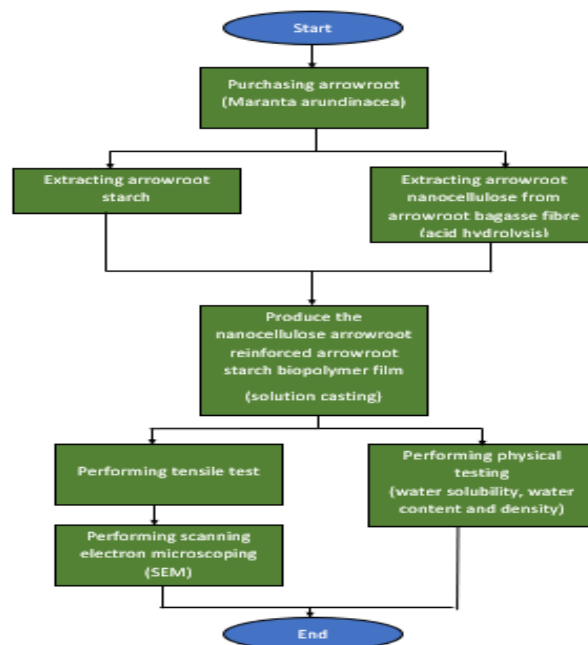


Fig. 4: The flowchart process for this research.

RESULTS AND DISCUSSIONS

Tensile Strength

The bar graph from Figure 5 presents the tensile strength of arrowroot biopolymer starch films reinforced with varying concentrations of ARNCC. The data indicates a clear positive correlation between ARNCC loading and tensile strength. At 0% nanocellulose, the tensile strength is 2.50 MPa. This value increases significantly to 3.44 MPa with 1% nanocellulose loading and reaches 4.31 MPa at 3% loading. This trend implies that adding ARNCC significantly improves the mechanical properties of the starch film. Nanocellulose functions as a reinforcing agent, increasing tensile strength due to its high aspect ratio and strong hydrogen bonding potential, which improves the interaction between ARNCC and the AS matrix. The higher tensile strength is due to better load transfer efficiency and the formation of a more rigid and cohesive network inside the film. As a result, these improvements make the film more durable and suited for applications required better mechanical performance. Figure 5 shows the graph of tensile strength of different ARNCC/AS loadings

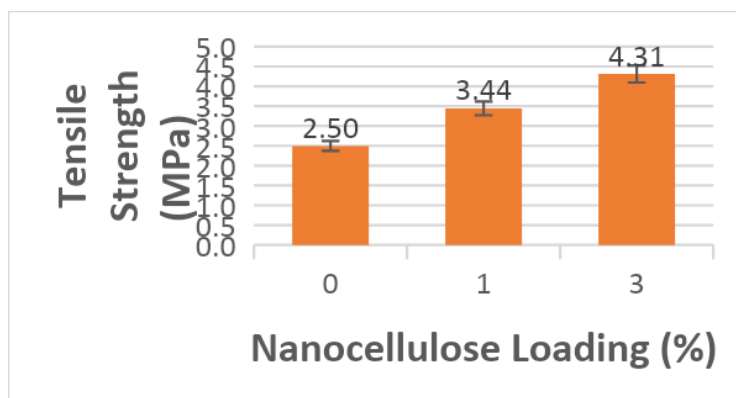


Fig. 5: Graph of tensile strength of varying ARNCC/AS loadings

Young's Modulus

The second graph from Figure 6 indicates that as the concentration of ARNCC increases, the Young's modulus decreases. The Young's modulus at 0% nanocellulose is 65.72 MPa, suggesting a rather stiff material. At 1% loading, this value decreases to 49.87 MPa, and at 3% loading, it decreases even lower to 32.45 MPa. This decline suggests that while the film becomes stronger with higher nanocellulose content, it also becomes less stiff and more flexible. The reduction in stiffness might be due to the ARNCC disrupting the rigid AS matrix, creating a more pliable network. Figure 6 shows the graph of young's modulus of different ARNCC/AS loadings.

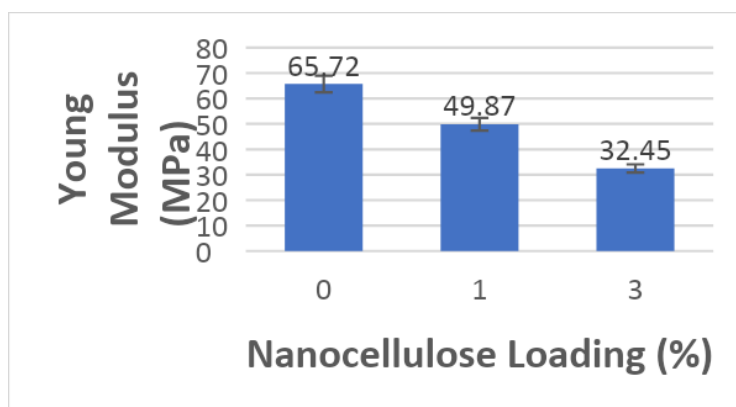


Fig. 6: Graph of young's modulus of different ARNCC/AS loadings

Elongation at Break

The third graph from Figure 7 demonstrates that increasing the loading of ARNCC results in an increase in elongation at break. The elongation at break is 13.41% at 0% ARNCC, which significantly increases to 38.85% at 1% loading and further to 44.98% at 3% loading. This implies that the film's ductility increases with the addition of ARNCC, enabling it to stretch further before breaking. The reason for the increased elongation is due to ARNCC providing the biopolymer matrix a more flexible network, which allows for more deformation while under stress. Figure 7 shows the graph of elongation at break of different ARNCC/AS loadings.

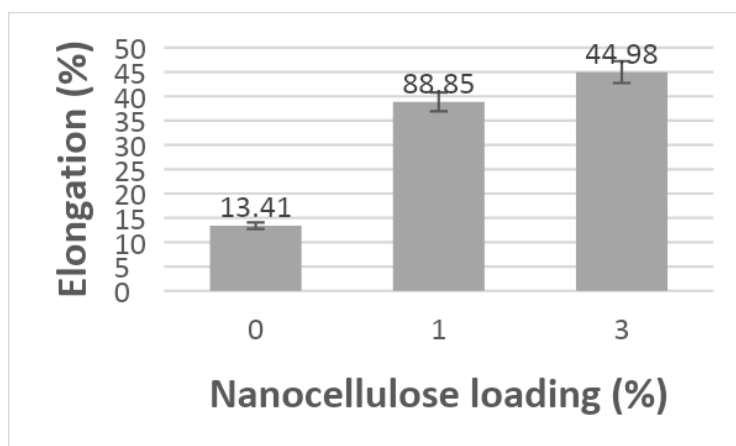


Fig. 7: Graph elongation at break of different ARNCC/AS loadings

Generally, there are various factors that can affect the mechanical properties of the nanocomposite film such as filler contents, porosity and grain size. The fractured surface of the tensile for the three different loadings of arrowroot nanocellulose reinforced arrowroot starch biopolymer films were examined using Scanning Electron Microscope (SEM) from Figure 8. Nanocellulose can be identified as white dots which correspond as cellulose nanocrystalline (CNCs).

Microstructure Analysis of biopolymer films

From the figure 5 below, the control film shows the smoothest surface compared to other films. The roughness surface of Figure 5 (b) and Figure 5 (c) may be due to the higher contents of arrowroot nanocellulose. According to Kilic et al. (2009), the surface roughness can affect the tensile strength of the sample [5]. Based on this observation, the increases of the surface

roughness could potentially increase the tensile strength of the nanocomposite film. Figure 8 shows the surface morphology of tensile fracture surface at 1000 magnificant.

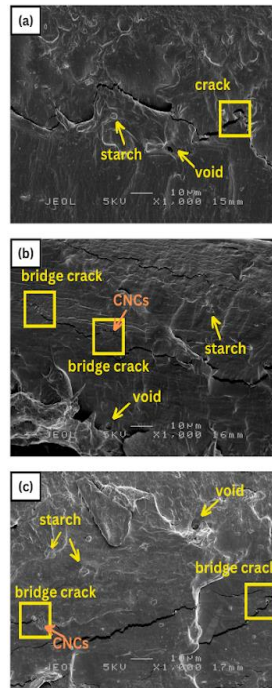


Fig. 8: Surface morphology of tensile fracture surface at 1000 of (a), Control (b) ARNCC1 and (c) ARNCC3

Furthermore, the control film shows a highly extensive fracture compared to other two films. Generally, this surface fracture can affect the mechanical properties of the film. Talebi et al. (2021) reported that the addition of CNCs improves the mechanical properties of the composite films by bridging cracks, which enhances the tensile strength and elongation [6]. Based on Figure 8 (b) and Figure 5 (c), the present of CNCs span across the cracks increase the tensile strength of the film by stretching across the opening cracks and help to reduce crack propagation.

CONCLUSION

The tensile properties of these films showed that ARNCC/AS with 3% loading showed the better tensile strength compared to other loadings. However, by increasing the ARNCC loading will decrease the young's modulus and elongation of the AS film which indicates that the film become more stiffness with increasing of ARNCC loading. Furthermore, Scanning Electron Microscope SEM analysis revealed that the influence of ARNCC content on the fracture surface morphology of ARNCC/AS films. The result showed that the increase of ARNCC loading produces the roughness surface of the film which causes the better tensile properties for the film. Besides, the existence of bridge crack on the ARNCC1 in reducing films indicates that nanocellulose plays an important role to reduce the stress and enhanced the tensile properties of the film.

ACKNOWLEDGEMENTS

This work was supported by Fundamental Research Grant Scheme (FRGS) from Kementerian Pendidikan Tinggi (KPT) that made this research possible.

REFERENCES

- [1].B. Aaliya, K. V. Sunooj, and M. Lackner, "Biopolymer composites: a review," *International Journal of Biobased Plastics*, vol. 3, no. 1, pp. 40–84, Jan. 2021, doi: 10.1080/24759651.2021.1881214.
- [2].G. P. Udayakumar *et al.*, "Ecofriendly biopolymers and composites: Preparation and their applications in water-treatment," *Biotechnol Adv*, vol. 52, p. 107815, Nov. 2021, doi: 10.1016/J.BIOTECHADV.2021.107815.
- [3].J. Tarique, S. M. Sapuan, A. Khalina, S. F. K. Sherwani, J. Yusuf, and R. A. Ilyas, "Recent developments in sustainable arrowroot (*Maranta arundinacea* Linn) starch biopolymers, fibres, biopolymer composites and their potential industrial applications: A review," *Journal of Materials Research and Technology*, vol. 13, pp. 1191–1219, Jul. 2021, doi: 10.1016/J.JMRT.2021.05.047.
- [4].J. Tarique, S. M. Sapuan, and A. Khalina, "Effect of glycerol plasticizer loading on the physical, mechanical, thermal, and barrier properties of arrowroot (*Maranta arundinacea*) starch biopolymers," *Scientific Reports 2021 11:1*, vol. 11, no. 1, pp. 1–17, Jul. 2021, doi: 10.1038/s41598-021-93094-y.
- [5].M. Kiliç, E. Burdurlu, S. Aslan, S. Altun, and Ö. Tümerdem, "The effect of surface roughness on tensile strength of the medium density fiberboard (MDF) overlaid with polyvinyl chloride (PVC)," *Mater Des*, vol. 30, no. 10, pp. 4580–4583, Dec. 2009, doi: 10.1016/J.MATDES.2009.03.029.
- [6].H. Talebi, F. A. Ghasemi, and A. Ashori, "The effect of nanocellulose on mechanical and physical properties of chitosan-based biocomposites," <https://doi.org/10.1177/00952443211017169>, vol. 54, no. 1, pp. 22–41, May 2021, doi: 10.1177/00952443211017169.

Cellulose Electrospun Nanofibers: Bridging Sustainability and Electronics

Nik Nurshakirah Farhana Binti Norazlin¹, Mohd Ali Mat Nong^{2*}, Mas Jaffri Masarudin^{1,2}, Juraina Md Yusof², Mohd Hafizuddin Ab Ghani², Ismayadi Ismail², Rosnah Nawang², Che Azurahaman Che Abdullah²,

¹*Faculty of Biotechnology and Biomolecular Sciences, Universiti Putra Malaysia, Serdang, Malaysia*

²*Institute of Nanoscience and Nanotechnology, Universiti Putra Malaysia, Serdang, Malaysia*

*Corresponding author's E-mail: mohd_alee@upm.edu.my, kirahfrhna02@gmail.com

Abstract: The pursuit of sustainable and high-performance materials has spotlighted cellulose-based electrospun nanofibers for electronic applications. Derived from the abundant biopolymer cellulose, these nanofibers combine biodegradability, renewability, and mechanical strength with the benefits of electrospinning, such as high surface area and tunable properties. This review examines the synthesis, characterization, and functionalization of cellulose nanofibers, emphasising their role in flexible electronics, energy storage, sensors, and conductive composites. Despite challenges in scalability and performance optimization, advancements show improved conductivity and mechanical properties. Future directions highlight the transformative potential of these eco-friendly materials, aiming to foster further research and development towards a sustainable and efficient electronic industry. The main aim in the future direction is to advance research and development of cellulose-based electrospun nanofibers to create sustainable and high-performance materials for electronic applications. This involves overcoming challenges in scalability and optimizing performance to enhance conductivity and mechanical properties, ultimately contributing to a more sustainable and efficient electronic industry. The focus is on harnessing the eco-friendly nature of these materials to drive innovation in flexible electronics, energy storage, sensors, and conductive composites, paving the way for greener technological solutions.

Keywords: cellulose nanofibers; electrospinning; sustainable electronics; functionalization; energy storage

INTRODUCTION

Electronics materials have undergone significant advancements in recent years, driven by the need for innovative, sustainable, and efficient solutions. Among the various materials explored, cellulose-based electrospun nanofibers have emerged as a promising candidate due to their unique combination of properties. Derived from natural sources, cellulose is the most abundant biopolymer on Earth, known for its biodegradability, renewability, and excellent mechanical strength [1]. When processed into electrospun nanofibers, cellulose exhibits remarkable characteristics such as high surface area, flexibility, and the potential for functionalization, making it an attractive material for a wide range of electronic applications.

The process of electrospinning provides an effective method for fabricating cellulose-based nanofibers with controlled morphology and properties. This technique offers significant advantages, including simplicity, and the ability to produce continuous fibers. The resulting

nanofibers can be tailored to meet specific requirements, such as enhanced conductivity, improved mechanical properties, and increased surface reactivity, through various pre-processing and post-processing treatments and incorporation of functional additives.

Electrospinning is a simple and effective technique for creating nanofiber membranes with large specific surface areas, carefully regulated fibre alignments, and porous surfaces. Because of these qualities, electrospun nanofibers may be used in a variety of fields, such as biomedical, energy, catalysis, sensors, and filtration [2]. The integration of cellulose-based electrospun nanofibers into electronic devices opens new possibilities for sustainable and high-performance materials. Moreover, their potential applications span a diverse array of fields, including flexible and wearable electronics, energy storage devices, sensors, and conductive composites. As researchers continue to explore and optimise the properties of these nanofibers, the intersection of material science, engineering, and electronics promises to yield innovative solutions that address the growing demand for environmentally friendly and efficient electronic materials.

In this paper the recent advancements in the development and application of cellulose-based electrospun nanofibers as electronic materials are discussed. This review covers the synthesis methods, structural characterization, and functionalization techniques used in current and possible future applications that enable these nanofibers to meet the stringent requirements of modern electronic devices. Furthermore, we will highlight the challenges and future directions in this rapidly evolving field, emphasizing the potential impact of cellulose-based nanofibers on the future of electronics.

SYNTHESIS METHODS

Several methods are used to synthesize cellulose nanofibers. These include electrospinning of cellulose, cellulose derivatives, and nanocellulose [3].

Electrospinning of cellulose: This process involves an electric field to draw thin fibers from a cellulose solution. It allows for the creation of continuous cellulose nanofibers with diameters typically in the nanometer range.

Electrospinning of cellulose Derivatives: Similar to the electrospinning of pure cellulose, this method involves using cellulose derivatives, such as cellulose acetate or carboxymethyl cellulose, as the starting material. These derivatives can be more easily dissolved in solvents, facilitating the electrospinning process.

Electrospinning of Nanocellulose: Nanocellulose, which includes cellulose nanocrystals (CNCs) and cellulose nanofibrils (CNFs), can also be electrospun to produce nanofibers. This technique often involves blending nanocellulose with other polymers to achieve the desired fiber characteristics and stability.

Electrospinning of cellulose involves dissolving pure cellulose in a suitable solvent system, such as a mixture of DMF and PAN, or an ionic liquid. The polymer-solvent system and the necessary fibre characteristics determine the optimal stirring time. The electrospinning process is affected differently by longer and shorter stirring durations [4]. The cellulose solution

is then loaded into a syringe equipped with a needle, connected to a high-voltage power supply. When voltage is applied, the electrostatic force creates a jet of the solution that travels towards a grounded collector. As the jet travels, the solvent evaporates, leaving behind cellulose nanofibers. This method allows for the production of continuous fibers with diameters ranging from nanometers to micrometers, with fiber morphology controlled by adjusting parameters like solution concentration, voltage, and needle-to-collector distance.

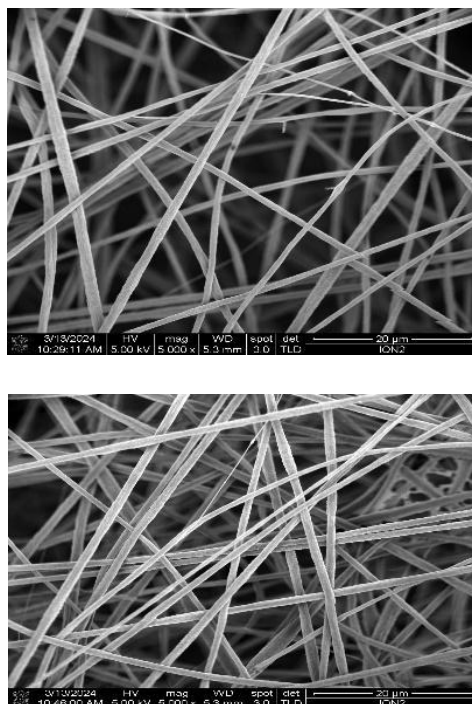


Fig.1. Shows the structure of Cellulose Acetate nanofibers

Nanofiber synthesis requires a specific electrospinning setup tailored to experimental conditions. A setup with a 25 cm gap between the needle and collecting plate, using a stainless steel No. 23 needle, is critical for optimizing fiber formation. This configuration enables proper polymer jet stretching, solidification, and solvent evaporation, producing uniform, defect-free fibers. The stainless steel needle ensures precise flow control and maintains a stable electric field, enhancing fiber consistency and quality. This setup is crucial for generating reproducible, high-quality fibers suitable for filtration, tissue engineering, and drug delivery. The solution volume was maintained at 4 mL, with a voltage range of 25–30 kV and a flow rate of 1 mL h⁻¹. The positive electrode was connected to the high-voltage needle, and the negative electrode was attached to the stainless-steel collecting plate [5].

Dissolving cellulose in conventional solvents poses challenges due to its high viscosity, necessitating specific solvent systems. Solvent systems that promote the disentanglement or decrystallization of cellulose have been identified, facilitating its dissolution process [6]

CELLULOSE ELECTROSPUN NANOFIBERS CHARACTERIZATION

Following electrospinning, cellulose nanofibers are characterized using various techniques to assess their physical, chemical, and thermal properties. The electrospun polymer fibers

demonstrate several notable attributes, including enhanced mechanical properties such as increased tensile strength and stiffness, as well as an exceptionally high surface-area-to-volume ratio, which can be up to 103 times that of the nanofiber [1]

Morphology and mechanical properties

Morphological and physical characterization of nanofibers is crucial for their classification and future development. In the case of cellulose electrospun nanofibers, properties such as solution homogeneity, fiber diameter, and bead presence can be assessed using scanning electron microscopy (SEM) and tensile strength can be measured with a universal tensile machine (UTM). The nanofiber webs, with an average diameter of 950 ± 50 nm, were found to be largely defect-free, with no significant bead formation, and were produced continuously under optimized electrospinning conditions. These findings provide a basis for future research [4].

The mechanical properties of two formulations, PAN (Polyacrylonitrile) and PAN with CA (Polyacrylonitrile with cellulose acetate), were evaluated and compared as shown in Table 1. PAN demonstrated a higher tensile strength at maximum load (8.39%) in contrast to PAN with CA, which exhibited a lower value (1.33%). This suggests that PAN can endure a greater force before failure. Conversely, PAN with CA showed a markedly higher tensile strain at break (37.09%) compared to PAN (23.79%), indicating superior elasticity and the ability to elongate more before breaking. In terms of stiffness, PAN with CA exhibited a higher modulus (19.29 MPa), reflecting greater resistance to deformation under stress, whereas PAN had a lower modulus (15.04 MPa), implying greater flexibility. Furthermore, the tensile extension at maximum load for PAN (2.60 mm) was significantly higher than that of PAN with CA (0.41 mm), reinforcing the observation that PAN possesses greater flexibility. While the flexibility of PAN was noted to be higher, no specific data on the flexibility of PAN with CA was provided. Finally, in terms of ductility, PAN with CA was reported to have a higher ductility compared to PAN, suggesting that PAN with CA is better able to undergo plastic deformation before fracture. Overall, PAN excels in strength and flexibility, while PAN with CA is characterized by enhanced elasticity, stiffness, and ductility.

Table 1. Tensile results PAN and PAN with CA

Formulation	PAN	PAN + CA
Tensile Strain at Maximum Load (%)	8.39%	1.33%
Tensile Strain at Break (%)	23.79%	37.09%
Modulus (MPa)	15.03721	19.29410
Tensile Extension at Maximum Load (mm)	2.60049	0.41208
Flexibility	more flexible	
Ductility		higher

Chemical and electrochemical properties

Fourier transform infrared (FT-IR) spectroscopy was employed to analyze the functional group content of the materials [7]. The composition of the electrospinning solution, including the

cellulose chemical formula, is critical for evaluating compatibility and functionality, as well as its influence on nanofiber characteristics. This includes the development of composite nanofibers aimed at enhancing flexibility and strength. Challenges related to the dissolution of cellulose in solvents have prompted investigations into combining cellulose with other materials to produce electrospun cellulose composite nanofibers, which are utilized across various industries [11]. Solutions lacking surfactants fail to produce fine, uniform jets due to the rapid evaporation of the solvent, unlike those with surfactants. Surface tension in these cases may lead to the formation of beads on the liquid jet [7]. Understanding the functional groups of each polymer and material in the electrospinning solution offers valuable insights for novel applications. Cellulosic materials, characterized by their 1D hierarchical structures and hydroxyl groups, have attracted considerable interest as natural bio-templates for the fabrication of lithium-ion battery (LIB) electrodes [12].

The electrochemical performance of cellulose electrospun nanofibers was assessed using a 4-point probe. A decrease in current at both peaks, indicative of reduced electrode surface conductivity, was observed when the membrane was placed onto the FTO substrate. This reduction may affect sensor sensitivity due to the insulating properties of cellulose acetate (CA) [13].

Thermal properties

The TGA curve illustrates the sample deterioration in three distinct phases. The initial phase, occurring between 30 and 50 °C, involves moisture extraction from the sample. The second phase, observed between 250 and 400 °C, is marked by significant mass loss, during which nearly the entire sample deteriorates. In the final phase, above 400 °C, complete degradation of the nanofiber occurs, leaving only a minimal residue [7]. The data plotted on the graph is derived from continuous monitoring of the sample weight, coupled with the passage of specific gases and associated degradation processes.

POTENTIAL AND APPLICATION OF CELLULOSE ELECTROSPUN NANOFIBER IN ELECTRONIC FIELD

Cellulose's sustainability, owing to its biocompatibility, biodegradability, non-toxicity, and environmental friendliness, has facilitated the development of various applications. Wearable electronic devices, which must be portable, self-powered, and highly efficient, have driven the advancement of several nanogenerator technologies, including those based on photoelectric, thermoelectric, piezoelectric, triboelectric, and moist-electric generation [14]. Recent research highlights the use of electrospun nanofibers in electrochemical devices such as solar cells, fuel cells, rechargeable batteries, supercapacitors, and hydrogen storage systems [15]. Many studies have focused on cellulose-based materials. The high surface-to-volume ratio and superior spinnability of cellulose acetate (CA) nanofibers enable the incorporation of numerous sensing elements, resulting in a rapid reaction time (30s) and high sensitivity across a concentration range from 200 ppm to 12,750 ppm. Integrating cellulose (and its derivatives) with electrospinning technology presents an effective approach for producing nanostructured porous materials with promising functionalities, flexibility, renewability, and biodegradability [16]. Notable applications of cellulose electrospun nanofibers in the electronics field include:

Bacterochromic cellulose sensor

A novel smart biochromic textile sensor was developed by immobilizing anthocyanin extract into electrospun cellulose acetate nanofibers, enabling the detection of bacteria for various

applications, including healthcare monitoring [3]. This sensor integrates cellulose acetate-based nanofibers with anthocyanin extracted from red cabbage to create a tactile-based bacterial biosensor. Upon exposure to an affected medium, the sensor exhibits colorimetric changes. The combination of low mass, high permeability, porosity, flexibility, and a broad surface area of the nanofibers facilitates effective analyte contact, resulting in an inexpensive and highly sensitive diagnostic tool.

Cellulose-curcumin composite colorimetric sensor

To monitor the real-time deterioration of raw chicken, electrospun regenerated cellulose nanofiber (RCA) composites coated with curcumin (CUR) (CUR-Cot) were developed. This novel method, particularly relevant to the food safety sector, employs cellulose-based nanofibers for sensor applications. Typically, sensing components, such as pigments or dyes, are integrated with support materials—including glass, film, nanofibers, cellulose, polyvinyl alcohol, starch, chitosan, and chitin—to create smart colorimetric sensors [2].

Mercury ions electrochemical sensor

The development of rapid technologies for mercury detection is essential due to the hazards associated with environmental mercury contamination, which necessitates stringent control of this element [11]. Accurate measurement of mercury ions (Hg^{2+}) in various matrices, including soil, water, air, and biological samples, is critical. To address this need, an environmentally friendly electrochemical sensor was developed for detecting mercury (II) ions (Hg^{2+}). This sensor utilizes electrospun cellulose acetate nanofibers modified with silver nanoparticles (AgNPs) on fluorine-doped tin oxide (FTO) glass [13].

Solar-powered interfacial evaporation

This article introduces a novel bio-based nanofibrous foam designed for solar interface evaporation with exceptional efficiency. To achieve this, an in-situ layer-by-layer self-assembly process combined with electrospinning was employed to fabricate a hybrid membrane composed of cellulose nanofibers and graphene oxide (GO). The principle of solar-driven interfacial evaporation involves using an evaporator to convert solar energy into heat, which is then concentrated at the evaporation interface to generate water vapor. Utilizing cellulose and a straightforward three-step synthesis process, a unique three-dimensional Janus-type nanofibrous foam evaporator was developed. This evaporator effectively absorbs solar energy and facilitates water pumping across various foam layers [17].

4.5 Lithium-ion battery separator

The rapid advancement in lithium-ion battery (LIB) technology has led to its widespread application in both portable electronics and large- and medium-scale energy storage systems [12]. This study presents a novel composite membrane consisting of electrospun poly(vinyl alcohol)/melamine (PVAM) nonwoven membranes sandwiched between zeolitic imidazole frameworks-67 (ZIF-67) decorated cellulose acetate nanofibers (ZIF-67@CA). The separator plays a crucial role in enhancing the lifespan of LIBs by providing ion transport pathways between the cathode and anode and preventing electrical short circuits [5]. This novel composite nonwoven membrane demonstrates potential for use in lithium-ion battery systems, offering high power and safety, making it particularly suitable for electric vehicles (EVs) [8].

Based templates for lithium-ion metal electrodes

The electrospinning method was employed to fabricate nanoscale cellulosic fiber templates, which were subsequently used to develop one-dimensional hollow TiO₂ electrodes [12]. The exceptional electrochemical performance of these electrodes is attributed to their unique hollow nanostructure and optimized phase, which contribute to a large BET surface area and enhanced ion diffusion.

Enhancement of triboelectric generator performance

The triboelectric nanogenerator (TENG) represents a promising technology for mechanical energy harvesting, characterized by its low cost, high efficiency, and straightforward production process [18]. The control of nanofiber diameter can be precisely achieved by adjusting humidity, which affects the surface morphology, roughness, and frictional contact area of triboelectric materials through the electrospinning process [19].

Moist-induced electricity generators (MEGs)

The combination of enhanced hydrophilicity increased specific surface area, and reduced pore size enabled a single MEG derived from the optimized CA membrane to achieve an output voltage of approximately 700 mV and a maximum output power density of 2.45 $\mu\text{W cm}^{-2}$ [14]. To develop an affordable, effective, and wearable MEG, a novel tree-like structure cellulose acetate (CA) nanofiber membrane was fabricated using a one-step electrospinning process involving CA solutions and organic branched salt.

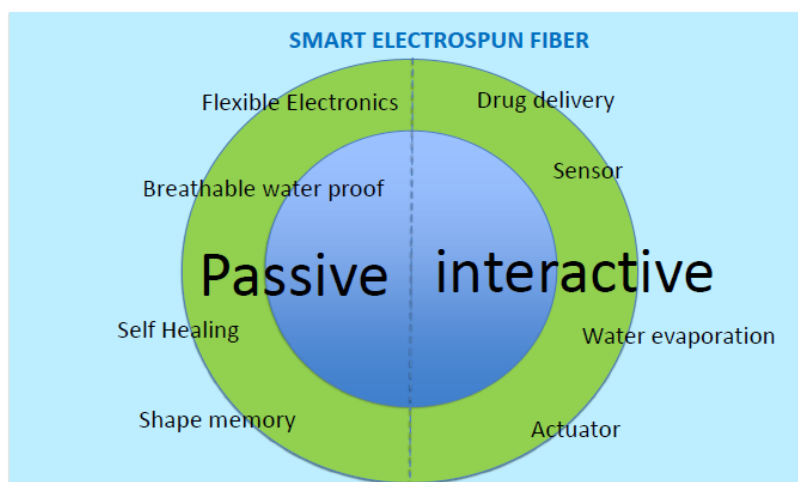


Fig. 3. The potential and application of electrospun nanofibers

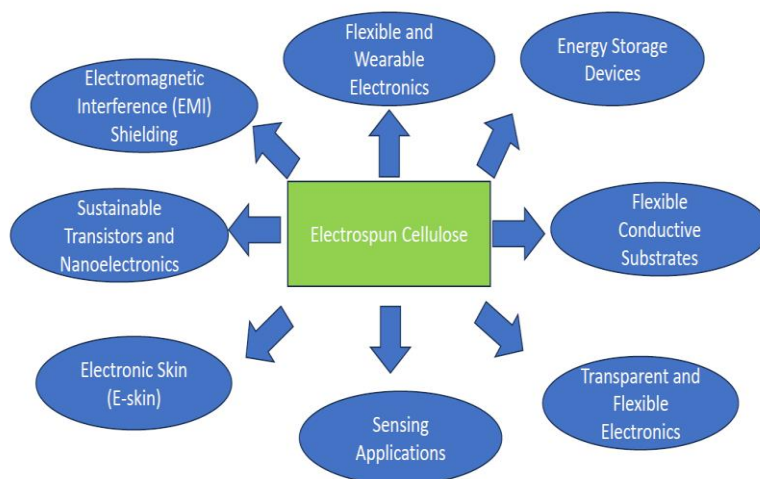


Fig. 4. The potential and application of cellulose electrospun nanofibers in the electronic field [20].

CHALLENGES

Cellulose electrospun nanofibers present several challenges in their application. Methodologically, while nanofiber-based electrodes demonstrate exceptional rate capability and cycle stability, large-scale industrial manufacturing faces significant hurdles due to the slow production rates associated with electrospun nanofibers [15]. This low productivity stems from the optimized electrospinning conditions, which involve low flow rates during spinning and generally low polymer concentrations in the spinning solutions [16]. To address these issues, new electrospinning units with advanced features have been developed. These innovations aim to overcome the challenges while capitalizing on the high porosity, low density, and large specific surface area of electrospun nanofibers, a technique that proves formidable in creating nanofiber nonwovens and sponges with a wide range of potential applications [21].

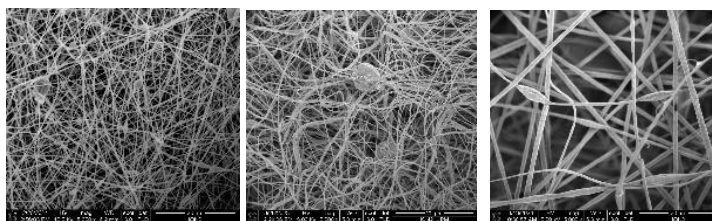


Fig. 5. Shows the different optimised nanofiber morphology of the fibres during the solidification. Fibres that are (a) PAN; (b) CA; (c) PAN with CA .

Despite the advantageous properties of cellulose nanofibers, optimization of their composition for electronics and energy-related applications remains limited. To date, no studies have systematically compared the morphological, rheological, and mechanical properties of cement composites incorporating cellulose nanofiber (CNF) suspensions from various sources, which differ in quality and uniformity, including mixtures of thick and thin fibers [23]. Cellulose derivatives, with their structural modifications, exhibit significantly higher solubility in a wide range of chemical and inorganic solvents compared to cellulose itself [16]. Therefore, to prevent

defects, as depicted in Figure 3 [22], it is crucial to optimize the electrospinning solution, methodology, and fabrication processes.

FUTURE DIRECTIONS

In the field of electronic materials for devices and technology, energy-related applications such as energy storage, energy conversion, and conductive materials are likely to attract significant attention regarding the prospects of cellulose electrospun nanofibers. Understanding the importance of a three-dimensional porous structure in flexible support materials for developing conducting electrodes, cellulose and its derivatives demonstrate great potential with the emergence of numerous electro-conductive materials [16].

Cellulose acetate has emerged as a key material for developing flexible and durable non-composite and composite conductive materials, owing to its straightforward manufacturing process via electrospinning. Its higher solubility compared to cellulose makes cellulose acetate (CA) a frequent choice in the production of electrospun nanofiber membranes [14]. While a detailed cost assessment remains necessary, electrospun webs of CA and deacetylated CA are suggested as promising electrolyte membrane materials for dye-sensitized solar cells [24]. The application of simple electrospinning techniques combined with cellulose-based materials for creating electrolyte membranes, electrodes [12, 14, 18, 19], and semi-conductive or conductive materials opens avenues for advancing knowledge and enhancing the potential of cellulose electrospinning within the electronics field.

CONCLUSION

Cellulose electrospun nanofibers exhibit considerable potential as future materials for electronics and conductivity applications, leveraging the sustainable properties of cellulose and its derivatives alongside the electrospinning technique. The methods of characterization are critical, as they impact the accuracy and ability to diagnose both successful outcomes and issues related to the developed materials. Although challenges related to scalability and material optimization for specific applications may limit short-term utilization of cellulose-based electrospun nanofibers, ongoing research and solution optimization have the potential to drive significant advancements in nanomaterials development and related industries. The advancement of electronics and energy-related technologies is increasingly vital, offering substantial benefits for current and future technological applications.

ACKNOWLEDGEMENTS

This project is supported by Universiti Putra Malaysia (UPM), Malaysia under the Geran Inisiatif Putra Muda (GP-IPM) - (GP-IPM/2022/9733300).

REFERENCES

- [1] Majumder, S., Sharif, A., & Hoque, M. E. (2020). Electrospun cellulose acetate nanofiber: characterization and applications. In Elsevier eBooks (pp. 139–155). <https://doi.org/10.1016/b978-0-12-819661-8.00009-3>
- [2] Iqbal, M. A., Gohar, S., Yabuta, Y., Fanghua, L., Ling, W., Farooq, M., Sarwar, M. N., Mayakrishnan, G., & Kim, I. S. (2024). Green extract surface-coated electrospun cellulose nanofibers as an efficient, reversible, and reusable smart colorimetric sensor for real-time monitoring of chicken freshness. *Current Research in Biotechnology*, 100192. <https://doi.org/10.1016/j.crbiot.2024.100192>
- [3] Hassan, N. F., Khattab, T. A., Fouda, M. M., Zaid, A. S. A., & Aboshanab, K. M. (2024). Electrospun cellulose nanofibers immobilized with anthocyanin extract for colorimetric determination of bacteria. *International Journal of Biological Macromolecules*, 257, 128817. <https://doi.org/10.1016/j.ijbiomac.2023.128817>
- [4] Elaissaoui, I., Sayeb, S., Ounif, I., Ferhi, M., Karima, H., & Ennigrou, D. J. (2024). Preparation and characterization of acetate cellulose electrospun nanofibers membrane: Potential application on wastewater treatment. *Heliyon*, 10(12), e32552. <https://doi.org/10.1016/j.heliyon.2024.e32552>
- [5] Song, Y., Sheng, L., Wang, L., Xu, H., & He, X. (2021). From separator to membrane: Separators can function more in lithium ion batteries. *Electrochemistry Communications*, 124, 106948. <https://doi.org/10.1016/j.elecom.2021.106948>
- [6] Ghasemi, M., Tsianou, M., & Alexandridis, P. (2017). Assessment of solvents for cellulose dissolution. *Bioresource Technology*, 228, 330–338. <https://doi.org/10.1016/j.biortech.2016.12.049>
- [7] De Almeida, D. S., Duarte, E. H., Hashimoto, E. M., Turbiani, F. R., Muniz, E. C., De Souza, P. R., Gimenes, M. L., & Martins, L. D. (2020). Development and characterization of electrospun cellulose acetate nanofibers modified by cationic surfactant. *Polymer Testing*, 81, 106206. <https://doi.org/10.1016/j.polymertesting.2019.106206>
- [8] Wu, X., Karuppiyah, C., Wu, Y., Zhang, B., Hsu, L., Shih, J., Li, Y. J., Hung, T., Ramaraj, S. K., Jose, R., & Yang, C. (2024). Unveiling high-power and high-safety lithium-ion battery separator based on interlayer of ZIF-67/cellulose nanofiber with electrospun poly(vinyl alcohol)/melamine nonwoven membranes. *Journal of Colloid and Interface Science*, 658, 699–713. <https://doi.org/10.1016/j.jcis.2023.12.098>
- [9] Demirbas, U. (2019). Cr:Colquiriite Lasers: Current status and challenges for further progress. *Progress in Quantum Electronics*, 68, 100227. <https://doi.org/10.1016/j.pquantelec.2019.100227>
- [10] El Messiry, M., & Fadel, N. (2019). The tensile properties of electrospun Poly Vinyl Chloride and Cellulose Acetate (PVC/CA) bi-component polymers nanofibers. *Alexandria Engineering Journal*, 58(3), 885–890. <https://doi.org/10.1016/j.aej.2019.08.003>
- [11] Malik, S., Khan, A., Ali, N., Ali, F., Rahdar, A., Mulla, S. I., Nguyen, T. A., & Bilal, M. (2022). Electrospun cellulose composite nanofibers and their biotechnological applications. In Elsevier eBooks (pp. 329–348). <https://doi.org/10.1016/b978-0-323-85835-9.00016-7>
- [12] Oh, S., Kim, J., Dar, M. A., & Kim, D. (2019). Synthesis and characterization of uniform hollow TiO₂ nanofibers using electrospun fibrous cellulosic templates for lithium-ion battery electrodes. *Journal of Alloys and Compounds*, 800, 483–489. <https://doi.org/10.1016/j.jallcom.2019.06.048>
- [13] Romaguera-Barcelay, Y., Gandarilla, A., Alves, J. F., Tavares, A. P., De Souza, T. C., Segala, K., Farias, T., Cunha, J., Sales, M. G. F., & Brito, W. R. (2024). Electrochemical Hg²⁺ sensor based on electrospun cellulose acetate nanofibers doped with Ag nanoparticles. *Microchemical Journal*, 111069. <https://doi.org/10.1016/j.microc.2024.111069>
- [14] Zhang, J., Hou, Y., Lei, L., & Hu, S. (2022). Moist-electric generators based on electrospun cellulose acetate nanofiber membranes with tree-like structure. *Journal of Membrane Science*, 662, 120962. <https://doi.org/10.1016/j.memsci.2022.120962>
- [15] Zhu, J., Yan, C., Li, G., Cheng, H., Li, Y., Liu, T., Mao, Q., Cho, H., Gao, Q., Gao, C., Jiang, M., Dong, X., & Zhang, X. (2024). Recent developments of electrospun nanofibers for electrochemical energy storage and conversion. *Energy Storage Materials*, 65, 103111. <https://doi.org/10.1016/j.ensm.2023.103111>

- [16] Zhang, Y., Zhang, C., & Wang, Y. (2021d). Recent progress in cellulose-based electrospun nanofibers as multifunctional materials. *Nanoscale Advances*, 3(21), 6040–6047. <https://doi.org/10.1039/d1na00508a>
- [17] Sui, Z., Xue, X., Wang, Q., Li, M., Zou, Y., Zhang, W., & Lu, C. (2024). Facile fabrication of 3D Janus foams of electrospun cellulose nanofibers/rGO for high efficiency solar interface evaporation. *Carbohydrate Polymers*, 331, 121859. <https://doi.org/10.1016/j.carbpol.2024.121859>
- [18] Zhao, L., Zheng, Q., Ouyang, H., Li, H., Yan, L., Shi, B., & Li, Z. (2016). A size-unlimited surface microstructure modification method for achieving high performance triboelectric nanogenerator. *Nano Energy*, 28, 172–178. <https://doi.org/10.1016/j.nanoen.2016.08.024>
- [19] Ishu, N., Sardana, S., & Mahajan, A. (2024). Controlling electrospun nanofibers surface morphology using relative humidity for enhancing triboelectric nanogenerator performance. *Chemical Physics Letters*, 141289. <https://doi.org/10.1016/j.cplett.2024.141289>
- [20] SAE Media Group. (2022, August 30). Electrospinning advantages for wearable technology. *Medical Design Briefs*. <https://www.medicaldesignbriefs.com/component/content/article/46454-electrospinning-advantages-for-wearable-technology>
- [21] Li, S., Duan, G., Zhang, G., Yang, H., Hou, H., Dai, Y., Sun, Y., & Jiang, S. (2024). Electrospun nanofiber nonwovens and sponges towards practical applications of waterproofing, thermal insulation, and electromagnetic shielding/absorption. *Materials Today Nano*, 25, 100452. <https://doi.org/10.1016/j.mtnano.2024.100452>
- [22] Williams, G. R., Raimi-Abraham, B. T., & Luo, C. J. (2018). Electrospinning fundamentals. In *Nanofibres in Drug Delivery* (pp. 24–59). UCL Press. <https://doi.org/10.2307/j.ctv550dd1.6>
- [23] Taheri, H., Heidari, N. A., Perrot, A., Siqueira, G., Nyström, G., & Kawashima, S. (2024). Selection of suitable cellulose nanofibers derived from eco-friendly sources for the production of lightweight cementitious composites with tuned rheological, mechanical, and microstructure properties. *Cement and Concrete Composites*, 105586. <https://doi.org/10.1016/j.cemconcomp.2024.105586>
- [24] Kaschuk, J. J., Miettunen, K., Borghei, M., Frollini, E., & Rojas, O. J. (2019). Electrolyte membranes based on ultrafine fibers of acetylated cellulose for improved and long-lasting dye-sensitized solar cells. *Cellulose*, 26(10), 6151–6163. <https://doi.org/10.1007/s10570-019-02520-y>
- [25] Angel, N., Vijayaraghavan, S. N., Yan, F., & Kong, L. (2020). Electrospun Cadmium selenide Nanoparticles-Loaded Cellulose acetate fibers for solar thermal application. *Nanomaterials*, 10(7), 1329. <https://doi.org/10.3390/nano10071329>
- [26] Tenea, A., Dinu, C., Buica, G., & Vasile, G. (2023). Electrochemical system for field control of HG²⁺ concentration in wastewater samples. *Sensors*, 23(3), 1084. <https://doi.org/10.3390/s23031084>

A Short Review on PLA Biodegradable Green Packaging Reinforced Nano Filler

Harshaan Arumugam¹, Mohd Hafizuddin Ab Ghani^{2*}, Mas Jaffri Masarudin^{1,2}, Ismayadi Ismail², Rosnah Nawang², Mohd Ali Mat Nong², Che Azurahaman Che Abdullah², Umer Rashid², Balkis Hazmi², Nishata Royan Rajendran Royan³, Wan Nazri Wan Busu⁴, Ruey Shan Chen⁵

¹*Faculty of Biotechnology and Biomolecular Sciences, Universiti Putra Malaysia, Serdang, Malaysia*

²*Institute of Nanoscience and Nanotechnology, Universiti Putra Malaysia, Serdang, Malaysia*

³*School of Engineering, UOW Malaysia KDU University College, Shah Alam, Malaysia*

⁴*Science and Food Technology Research Centre, Malaysian Agricultural Research and Development Institute, Serdang, Malaysia*

⁵*Department of Applied Physics, Faculty of Science and Technology, Universiti Kebangsaan Malaysia, Bangi Malaysia*

**Corresponding author's E-mail: m_hafizuddin@upm.edu.my*

Abstract: Polylactic acid (PLA) is gaining popularity for green packaging due to its eco-friendly nature. However, drawbacks like brittleness and low heat resistance limit its wider use. This review explores how reinforcing PLA with nanoclay fillers can improve its properties, including mechanical strength, heat tolerance, and barrier functions, while maintaining biodegradability for sustainable packaging. While these enhancements offer advantages, challenges such as dispersion of the fillers, cost factors, and safety regulations will also be addressed. Future research will focus on developing efficient techniques for using nanofillers. Overall, this review emphasises the immense potential of PLA-nanofiller composites as a promising and practical alternative for eco-friendly packaging, aligning with global efforts to reduce plastic waste and environmental damage.

Keywords: polylactic acid (PLA); nano fillers; green packaging; biodegradability

INTRODUCTION

The growing concern for environmental degradation and pollution has spurred a surge in interest for sustainable packaging solutions. These alternatives to traditional plastic packaging offer significant potential to minimise environmental impact. As environmental awareness rises, consumers increasingly demand products with reduced environmental footprints. This emphasis on sustainability is driving industries to adopt practices that reduce waste and pollution. Furthermore, consumers actively seek out products with eco-friendly packaging, recognizing the link between environmental health and human well-being. Many companies are strategically incorporating sustainability initiatives to improve their brand image and meet stakeholder expectations. Phelan and co-workers have conducted a study on companies and how they address plastic pollution and what are the sustainable packaging methods they practise [1].

Poly(lactic acid) (PLA), a biodegradable and bioactive thermoplastic derived from renewable resources like corn starch, cassava roots, or sugarcane, is emerging as a key material for sustainable green packaging. PLA is produced through polycondensation of lactic acid or ring-opening polymerization of lactide. Marek Brzeziński & Basko have stated that this structure is known as a stereocomplex, which leads to enhanced thermal stability and mechanical strength with decreased degradation time or drug release [2]. A study was conducted by Kalita and fellow researchers to determine the biodegradation and characterisation of PLA infused with algae biomass which eventually shows higher degradability [3]. Additionally, microorganisms can break down PLA back into lactic acid, a naturally occurring and non-toxic compound, further enhancing its biodegradability.

Nano fillers are microscopic particles, typically between 1 and 100 nanometers in size. These tiny particles are incorporated into polymer matrices to improve various properties of the material. They can significantly alter the physical, chemical, mechanical, and structural (morphological) properties of materials. Nano fillers can be broadly classified into two categories: organic and inorganic. Studies have been conducted by Abdul Khalil and friends between organic and inorganic nano fillers and their improvements in the basic properties of composites [4].

PLA IN GREEN PACKAGING

The range of physical, chemical and mechanical properties makes PLA a versatile biodegradable polymer that is most suitable for packaging. PLA has a transparent appearance which is similar to conventional plastics. The density of PLA is around 1.24g/cm³ making it relatively lightweight compared to other polymers [5]. The melting point ranges from 150°C to 180°C [6].

As for the chemical properties, PLA is known to have moderate chemical resistance. However, it may be degraded by strong acids or bases. In a 3D printing materials corrosion test the PLA has degraded when interacted with strong solvent [7].

PLA can be the most suitable polymer to be used in green packaging due to several factors, particularly its biodegradability. Biodegradation of PLA has been determined under composting conditions by Luo and team, proving the biodegradability nature of PLA [8]. Apart from that, PLA is derived from renewable resources such as corn starch and sugarcane. However, conventional plastic is produced from depleting non-renewable resources such as petroleum, eventually causing harm to the environment. Besides, PLA is approved for food contact uses as it has been given green light by the Food and Drug Administration (FDA) [9].

NANO FILLERS IN PLA

Nano fillers are reinforced with polymers such as PLA in order to come out with better performance in various applications. There are several types of nano fillers available that can be used to be incorporated into polymers like PLA such as nano cellulose, nano silica, graphene oxide, nano chitosan and nano silver [10]. All these types of nano fillers can be included within PLA as they tend to provide thermal and dielectric properties that can improve the nanocomposites produced as stated by Nilagiri Balasubramanian & Ramesh [11].

The very first common example of nanoclays is layered clay minerals that are used together with PLA to prepare nanocomposites. The most common type of clay mineral used with PLA is montmorillonite (MMT) which is used for packaging purposes [12]. Nanoclays are chosen to be used due to their availability and its ability to transform into nano sized particles. **Fig.1.** Shows the structure of the modified MMT studied when Nuruzzaman and his team were researching nanoclay as a carrier in a pesticide delivery system [13].

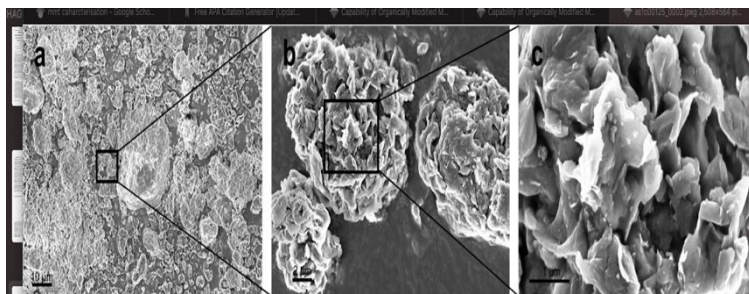


Fig.1. Morphological features of nanoclay [13].

Carbon nanotubes are cylindrical in shape and consist of a single layer of carbon atoms rolled up as sheets. This nano filler possesses limitations such as causing side effects to human health when used as a drug carrier which was studied by Zhang and his researchers [14]. **Fig.2.** Shows the applications of carbon nanotubes used in polymer composite materials as illustrated by Chen and his team [15].

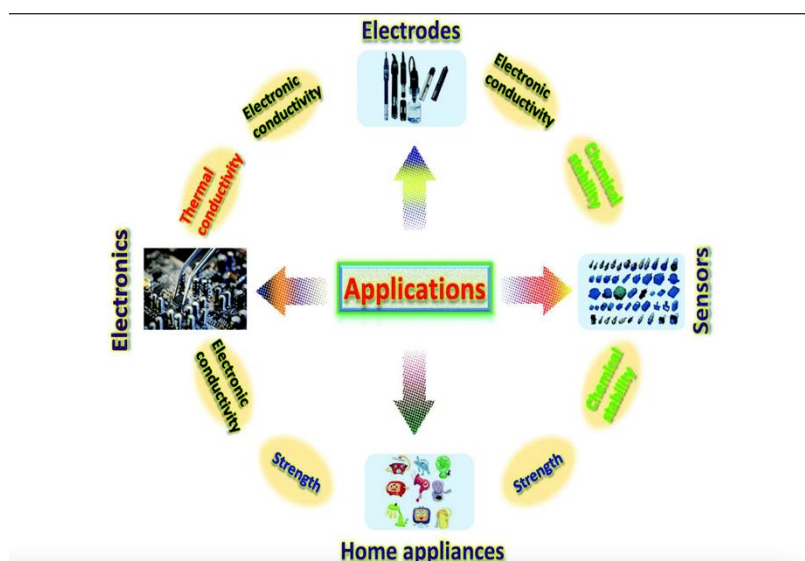


Fig.2. The broad range of carbon nanotube applications in polymer composites materials [15].

Metal oxides are also a type of common nanofiller that is reinforced with PLA. Zinc oxide (ZnO) and titanium dioxide (TiO₂) are types of metal oxides that are incorporated with PLA to produce nanocomposites. Type of nanofillers used can be varied according to the final end product that is being produced. Cellulose nanofibers and layered double hydroxides are also types of nanofillers that are being studied by researchers.

ENHANCED PROPERTIES OF PLA WITH NANO FILLERS

The incorporation of nano fillers into PLA can influence and improve various properties of the nanocomposites produced. First, the mechanical properties of the PLA will improve heavily due to the addition of nano fillers. Kiendl and Gao have said that PLA can be too brittle to stand on its own which limits its widespread application [16]. The tensile strength of PLA will increase due to the dispersion of nano fillers within the PLA matrix. Apart from tensile strength, the flexural strength of PLA will also increase when nano fillers are added to the PLA. When nano fillers are added to the PLA, the nanocomposites produced will withstand high stress without having any breakage. These statements are evident in an experiment conducted by Markos Petousis and his team with the results showing that mechanical strength which is inclusive of tensile, flexural and impact resistance of PLA nanocomposites were enhanced due to the addition of nano fillers which was Al_2O_3 [17].

Other than that, the thermal stability of the nanocomposites can be improved compared to the unmodified PLA. Neat PLA possesses 90% crystallization behaviour which heavily affects the thermal stability of the PLA [18]. The structure of PLA as a packaging will be maintained at higher temperatures, making it suitable for robust applications. **Fig.3.** shows the distribution of nano fillers with increasing percentages within the PLA matrix where it is observable that the matrix is becoming rougher from image A to E compared to the neat PLA in image A [19].

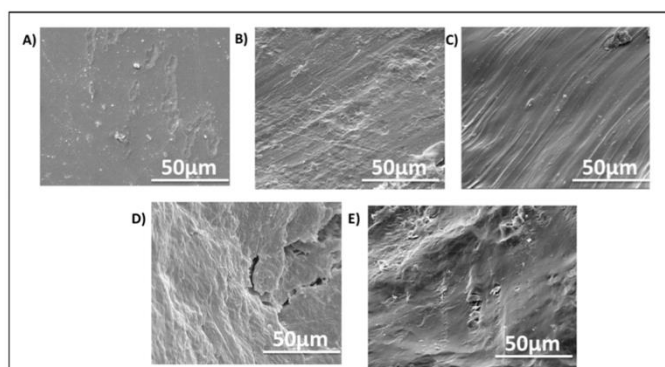


Fig.3. SEM images of PLA/MMT with increasing percentage from A to E [19].

PLA on its own has very poor barrier property. Barrier property is defined as the resistance of the material to substances such as gaseous, moisture and also ultraviolet rays. Nanofillers help to create a pathway for gas molecules which eventually decreases their rate of diffusion within the PLA matrix making PLA suitable for food packaging. Certain nanofillers do provide UV blocking-properties which is purposeful in protecting contents inside the PLA packaging.

CHALLENGES AND LIMITATIONS

Reinforcement of nano fillers in PLA to produce green packaging can pose several challenges. Agglomeration can occur within the PLA matrix where the nano fillers clump together which was evident in research by Yan and his team. This is due to the high surface area-to-volume ratio of the nano fillers that can lead to strong Van der Waals forces. Due to these interactions, nano fillers will not be dispersed uniformly within the PLA matrix, eventually reducing the performance of nanocomposites produced mechanically [20]. There are some key

factors to consider when scaling up the production of PLA as sustainable packaging. Raw materials to make the packaging should be taken into account which was evident in the study conducted by Wellenreuther and his researchers [21]. Since PLA is derived from renewable sources, the raw materials are heavily dependent on the agricultural market. There might be fluctuations in the agricultural market which can directly affect the cost PLA upscaling. Next, is the scalability which can heavily influence the cost to produce green nanocomposites. Switching from lab-scale to industrial-scale will be financially challenging due to high production costs [22].

Incorporation of nano fillers in PLA can be a difficult part which can be hazardous to the health and environment. There are cases where certain nano fillers such as CNT are found to cause respiratory problems which lead to inflammation and fibrosis [14]. Nano fillers that persist for a long time period can have significant impacts on the ecosystem harming the soil and water quality.

FUTURE PROSPECTS

PLA and nano filler technology is being explored to bring out the best of them to produce high quality functional materials. Smart and responsive composites are one of the trends that are being researched whereby the incorporation of nano fillers into PLA will make the nanocomposites respond to external stimuli such as temperature, pH or water [23].

Industrial applications are increasingly utilising PLA for food packaging due to its potential for enhanced properties without compromising biodegradability. This improved versatility, coupled with eco-friendly practices, can significantly contribute to a greener environment by promoting PLA as a sustainable alternative to conventional plastics, particularly in packaging [24].

CONCLUSION

PLA biodegradable green packaging reinforced with nano fillers has all the potential to be a substitute for conventional plastics highlighting its bio-friendly nature. There might be certain limitations such as brittleness when it comes to using PLA on its own without modifying which can be solved by the addition of nano fillers. The bigger aspect of the challenge can be presented in terms of industrial and market scale addressing issues such as cost implications and also health risks involving nanocomposites production. However, all these limitations need proper further research not only scientifically but also from a marketing perspective to promote PLA reinforced nano fillers as sustainable green nanocomposites.

ACKNOWLEDGEMENTS

This project is supported by Universiti Putra Malaysia (UPM), Malaysia under the Geran Inisiatif Putra Muda (GP-IPM) - (GP-IPM/2022/9716100).

REFERENCES

- [1] Phelan, A., Meissner, K., Humphrey, J., & Ross, H. (2022). Plastic pollution and packaging: Corporate commitments and actions from the food and beverage sector. *Journal of Cleaner Production*, 331(331), 129827.
- [2] Marek Brzeziński, & Basko, M. (2023). Polylactide-Based Materials: Synthesis and Biomedical Applications. *Molecules*, 28(3),1386–1386.
- [3] Kalita, N. K., Damare, N. A., Hazarika, D., Bhagabati, P., Kalamdhad, A., & Katiyar, V. (2021). Biodegradation and characterization study of compostable PLA bioplastic containing algae biomass as potential degradation accelerator. *Environmental Challenges*, 3, 100067.
- [4] Abdul Khalil, H. P. S., Chong, E. W. N., Owolabi, F. A. T., Asniza, M., Tye, Y. Y., Rizal, S., Nurul Fazita, M. R., Mohamad Haafiz, M. K., Nurmiati, Z., & Paridah, M. T. (2018). Enhancement of basic properties of polysaccharide-based composites with organic and inorganic fillers: A review. *Journal of Applied Polymer Science*, 136(12), 47251.
- [7].
- [5] Unionfab. (2024, April 22). *PLA Density: A Comprehensive Guide*. Unionfab.
- [6] Sreekumar, K., Bindhu, B., & Veluraja, K. (2021). Perspectives of polylactic acid from structure to applications. *Polymers from Renewable Resources*, 12(1-2), 60–74.
- [7] Ara, E. (2020, February 26). *Chemical resistance: The ultimate 3D printing materials corrosion test*. BCN3D Technologies.
- [8] Luo, Y., Lin, Z., & Guo, G. (2019). Biodegradation Assessment of Poly (Lactic Acid) Filled with Functionalized Titania Nanoparticles (PLA/TiO₂) under Compost Conditions. *Nanoscale Research Letters*, 14.
- [9] DeStefano, V., Khan, S., & Tabada, A. (2020). Applications of PLA in Modern Medicine. *Engineered Regeneration*, 1(1), 76–87.
- [10] Reshmi Olayil, V Arumugaprabu, Das, O., & Anselm, L. (2021). A Brief Review on Effect of Nano fillers on Performance of Composites. *IOP Conference Series. Materials Science and Engineering*, 1059(1), 012006–012006.
- [11] Nilagiri Balasubramanian, K. B., & Ramesh, T. (2018). Role, effect, and influences of micro and nano-fillers on various properties of polymer matrix composites for microelectronics: A review. *Polymers for Advanced Technologies*, 29(6), 1568–1585.
- [12] Vilarinho, F., Vaz, M. F., & Silva, A. S. (2020). The Use of Montmorillonite (MMT) in Food Nanocomposites: Methods of Incorporation, Characterization of MMT/Polymer Nanocomposites and Main Consequences in the Properties. *Recent Patents on Food, Nutrition & Agriculture*, 11(1), 13–26.
- [13] Nuruzzaman, M., Liu, Y., Ren, J., Rahman, M. M., Zhang, H., Hasan Johir, M. A., Shon, H. K., & Naidu, R. (2021). Capability of Organically Modified Montmorillonite Nanoclay as a Carrier for Imidacloprid Delivery. *ACS Agricultural Science & Technology*, 2(1), 57–68.
- [14] Zhang, C., Wu, L., de Perrot, M., & Zhao, X. (2021). Carbon Nanotubes: A Summary of Beneficial and Dangerous Aspects of an Increasingly Popular Group of Nanomaterials. *Frontiers in Oncology*, 11.
- [15] Chen, J., Liu, B., Gao, X., & Xu, D. (2018). A review of the interfacial characteristics of polymer nanocomposites containing carbon nanotubes. *RSC Advances*, 8(49), 28048–28085.
- [16] Kiendl, J., & Gao, C. (2020). Controlling toughness and strength of FDM 3D-printed PLA components through the raster layup. *Composites Part B: Engineering*, 180, 107562.
- [17] Markos Petousis, Nectarios Vidakis, Nikolaos Mountakis, Papadakis, V., & Lazaros Tzounis. (2022). Three-Dimensional Printed Polyamide 12 (PA12) and Polylactic Acid (PLA) Alumina (Al₂O₃) Nanocomposites with Significantly Enhanced Tensile, Flexural, and Impact Properties. *Nanomaterials*, 12(23), 4292–4292.
- [18] Ma, B., Wang, X., He, Y., Dong, Z., Zhang, X., Xiao Dong Chen, & Liu, T. (2021). *Effect of poly(lactic acid) crystallization on its mechanical and heat resistance performances*. 212, 123280–123280.
- [19] Ferreira, R. R., Farina, M. C., Maia, A., & Rondes F. S. Torin. (2023). PLA Films Containing Montmorillonite Nanoclay–Citronella Essential Oil Hybrids for Potential Active Film Formulation. *Macromol*, 3(2), 200–210.

- [20] Yan, D., Wang, Z., Guo, Z., Ma, Y., Wang, C., Tan, H., & Zhang, Y. (2020). Study on the properties of PLA/PBAT composite modified by nanohydroxyapatite. *Journal of Materials Research and Technology/Journal of Materials Research and Technology*, 9(5), 11895–11904.
- [21] Wellenreuther, C., Wolf, A., & Zander, N. (2021). Cost structure of bio-based plastics: A Monte-Carlo-analysis for PLA. *HWWI Research Papers*.
- [22] Jem, K. J., & Tan, B. (2020). The development and challenges of poly (lactic acid) and poly (glycolic acid). *Advanced Industrial and Engineering Polymer Research*, 3(2).
- [8].
- [23] Wei Chun Lin, Fang Yu Fan, Hsin Chung Cheng, Lin, Y., Yung Kang Shen, Jing Shiuan Lai, Wang, L., & Muhammad Ruslin. (2021). Optimization Shape-Memory Situations of a Stimulus Responsive Composite Material. *Polymers*, 13(5), 697–697.
- [24] Naser, A. Z., Deiab, I., & Darras, B. M. (2021). Poly(lactic acid) (PLA) and polyhydroxyalkanoates (PHAs), green alternatives to petroleum-based plastics: a review. *RSC Advances*, 11(28), 17151–17196.

Quality Attributes of Fresh Poultry Meat Wrapped in Corn starch-based Films Incorporated with Nanocellulose Fiber and Thymol for Active Packaging Application

Norhazirah Nordin¹, Siti Hajar Othman^{1,2,*}, Roseliza Kadir Basha¹, Suraya Abdul Rashid²

¹*Department of Process and Food Engineering, Faculty of Engineering, Universiti Putra Malaysia, Serdang, Malaysia*

²*Institute of Nanoscience and Nanotechnology, Universiti Putra Malaysia, Serdang, Malaysia*

**Corresponding author's E-mail: s.hajar@upm.edu.my*

Abstract: Corn starch (CS)-based films incorporated with nanocellulose fiber (CNF) and thymol (Thy) were prepared via the solution casting method. The combined effect of CNF and Thy on quality attributes of fresh chicken meat stored at 10 °C was investigated regarding visual appearance, weight loss, pH, and total viable count (TVC). In terms of visual appearance upon 7 days of storage, chicken meat samples exhibited shrinkage due to moisture loss, except for the sample wrapped in commercial film. However, the samples wrapped in CS/CNF/Thy films had better visual appearance, odor, and minimal pH change. Microbial populations were the lowest for sample wrapped in CS/CNF/Thy film compared to the CS and commercial films. In brief, the application of the active film considerably delayed the growth of microorganisms on chicken meat sample, increasing the food shelf life (<7 days) compared to control samples (<3 days) thus promising for active food packaging application.

Keywords—chicken meat; thymol; nanocellulose; starch film; quality attributes

INTRODUCTION

Fresh poultry meat, characterized by its high protein and moisture content, provides an ideal environment for microbial growth and oxidative processes, thereby being highly perishable[1]. These factors contribute to the loss of quality attributes and safety, resulting in domestic food waste, economic losses, and potential health hazards. To address these challenges, active packaging films, which incorporate active compounds such as antimicrobial agents, is a promising approach to preserving meat quality and prolonging shelf life[2]. For instance, gelatin/carrageenan-based nanocomposite films incorporated with tumeric essential oil able to reduce bacterial growth in chicken meat from 3.08 log CFU/g to 2.81 log CFU/g after 14 days of refrigerated storage[3]. Similarly, bacterial cellulose/polyvinyl alcohol films that contain Perilla essential oil emulsion displayed antimicrobial properties and mitigated the pH changes and oxidative rancidity of chilled beef, which resulted in extended shelf life[4].

Active packaging film can be designed using biopolymers such as corn starch (CS) as the base material, owing to its biodegradability, availability, and cost-effectiveness[5]. However, pure CS film often had poor mechanical and barrier properties. Thus, nanocellulose fiber (CNF) can be incorporated to overcome these limitations, while thymol (Thy) can provide additional functionalities. Thy contains a phenolic hydroxyl group which possesses significant antimicrobial and antioxidant properties[6]. The hydroxyl group of Thy and the hydrophobic character allow it to disrupt the microbial cell membrane, leading to leakage of proton flux and

intracellular constituents, and hence cell death[7]. Thy also bind with bacterial genomic DNA, disrupting protein synthesis that resulted in significant structural changes, ultimately leading to cell death[8].

Previous studies have utilized Thy in various packaging systems. In one study, Zabidi et al.[9] incorporated Thy in PLA/PBS-based films, and found that Thy at 9 wt.% loading able to show prolonged shelf life of chicken meat by having better odour and no fungal growth upon storage for 3 days at room temperature. Nonetheless, to our knowledge, there is limited research on the combined use of Thy and CNF in CS-based films for fresh poultry meat preservation. Only Othman et al.[10] have demonstrated the effectiveness of thymol in maintaining the quality of fresh beef wrapped in CS-based films, however, the study focused only on visual observation and microbial growth reduction. Thus, the present work aims to evaluate the effect of CS-based films incorporated with CNF and Thy in maintaining the quality attributes of fresh chicken meat in terms of visual appearance, weight loss, pH, and microbial growth reduction.

MATERIALS

Corn starch (33% amylose, 67% amylopectin), glycerol, thymol crystal (99%), Tween 20 (polyoxyethylene-20- sorbitan monooleate), methanol, and ethanol (99.7%) were obtained from R&M Chemicals Sdn. Bhd., Malaysia. The CNF suspension was purchased from Zoepnano Sdn. Bhd., Malaysia. Plate count agar and peptone water were obtained from Oxoid Limited, United Kingdom. The commercial plastic film and the chicken breast were purchased from a local supermarket, Hero Mart Sri Serdang, Malaysia.

EXPERIMENTAL

Preparation of films

The CS-based films (CS and CS/CNF/Thy) were prepared by solution casting method as described by Nordin et al.[11]. Briefly, CS was dispersed in distilled water (4% w/v) containing glycerol (25 wt.%) and gelatinized by heating at 90 °C for 30 min at using a hot plate stirrer (DAIHAN, Jakarta, Indonesia). Meanwhile, CNF/Thy emulsion was prepared by dispersing thymol (10 wt.% of CS) in 40 ml of distilled water containing CNF (1.5 wt.% of starch) at 50 °C. The concentration of thymol and CNF chosen in this study were based on prior studies by Othman et al.[10], where this formulation exhibited optimum overall performance including antibacterial activities. Tween 20 (fixed at 275 µL) was added as a surfactant and the emulsion was continuously stirred for 30 min at 1000 rpm. Then, the emulsion was added to the gelatinized film solution, dropwise at 50 °C with continuous stirring. Subsequently, the film solution underwent ultrasonication in ice bath (Qsonica, 500 W, 20 kHz, Newtown, CT) before casting (40 mL).

The CS film was prepared using the same procedure but without CNF and Thy. All film solution underwent drying in an air-conditioned room for 48 h and then placed in a ventilated oven (Memmert, USA) at 40 °C for 15 min. The dried films were peeled and conditioned in a desiccator containing saturated salt prior to further analysis.

Application of the films for fresh chicken meat preservation

The chicken meat was first sprayed with 75% ethanol to kill any available bacteria. Then the meat samples (3 cm x 3 cm) were enveloped in respective film (6 cm x 6 cm). In this part, a few treatments were made for comparison: samples wrapped with CS film, CS/CNF/Thy, and commercial film, individually. The samples were stored in a laboratory chiller at 10 °C for 7 days.

Evaluation of quality attributes of the chicken meat was conducted on days 0, 3, and 7, for the weight loss, pH, and total viable count (TVC). The visual appearance of the samples was photographed on each sampling day. The weight of the chicken meat samples was also determined using an analytical balance (Shimadzu, Japan). The percentage of weight loss was calculated according to equation (1).

$$\text{Weight loss (\%)} = \frac{\text{Weight}_i - \text{Weight}_t}{\text{Weight}_i} \times 100$$

where, weight_t represents weight of the sample on the sampling day and weight_i is the initial weight.

The pH changes of the chicken meat samples were determined by homogenizing 5 g of chicken meat sample in 45 mL of distilled water and macerated using probe homogenizer (DAIHAN, HG-15D, Korea) to produce a homogenized slurry[12]. Then, the pH of the homogenate was taken in triplicates by immersing a glass electrode of a pH meter (Mettler Toledo, China) in the slurry, and was averaged.

For the microbiological assessment, about 10 g of chicken meat sample was macerated in 90 mL of sterile 0.1% peptone water and then appropriate serial dilution of the homogenate was prepared. The TVC was determined using the pour plate method, using 0.1 mL of the diluent. After the molten media solidified, all plates were incubated at 37 °C for 24 h. Then, colony count was performed and expressed in log CFU/g.










Statistical analysis

Statistical analyses were conducted using Minitab software (Minitab Inc, State College, PA, USA). A p-value of <0.05 indicates a statistically significant difference between means.

RESULTS AND DISCUSSION

Based on Table 1, notable changes can be seen for samples in CS and CS/CNF/Thy films starting from day 3 onwards.

Table 1: Comparison of visual appearance of chicken meat samples over the storage time at 10 °C.

Films	Day 0	Day 3	Day 7
CS			
CS/ CNF/Thy			
Comm-ercial			

On day 3, the chicken meat sample packed in CS film exhibited notable shrinkage. The chicken meat sample in CS/CNF/Thy film exhibited similar behavior, but less pronounced than that of the CS film, indicating better film barrier against moisture loss with the presence of CNF. The presence of Thy could also have preserved the meat color better by minimizing oxidation and reducing the growth of microbes which responsible for the color changes. On day 7, the chicken samples in CS and CS/CNF/Thy films exhibited severe shrinkage and discoloration, however, CS/CNF/Thy film was slightly better at maintaining the visual appearance of the sample. Meanwhile, the chicken meat sample in commercial film remained the pinkish color and fresh look on days 3 and 7 but exhibited strong potent odor, which was linked to the presence of chicken 'juice' observed in the packaging[13]. These juices, when trapped within the commercial film packaging which has low permeability to water vapor, can provide a conducive environment for microbial growth[9,14] and the production of off-odors, contributing to the strong potent odor.

A general increasing trend in weight loss and pH was observed in all samples as the storage duration increased from day 0 to day 7 (see Fig. 1 and Fig. 2). The weight loss was mainly attributed to moisture loss whereas the pH changes were ascribed to the accumulation of alkaline substances such as amines and ammonia caused by the breakdown of proteins by the proteolytic enzymes of spoilage bacteria[15].

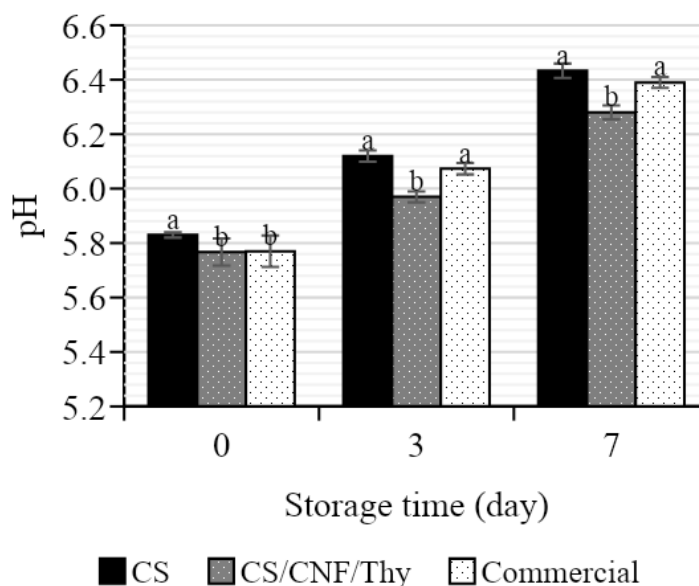


Fig 1: Comparison of pH values of chicken meat samples over the storage time at 10 °C.

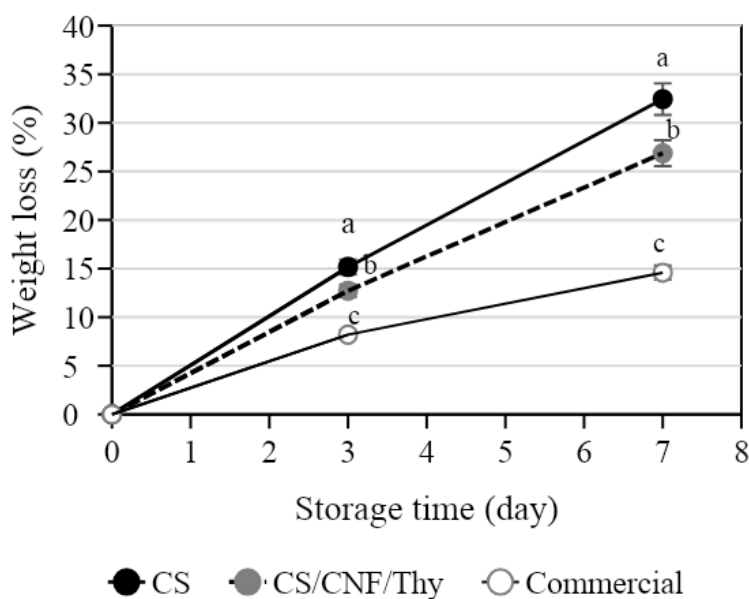


Fig 2: Comparison of percentage of weight loss of chicken meat samples over the storage time at 10 °C.

The samples in CS/CNF/Thy and commercial films had a slower increase in pH and weight loss ($p < 0.05$) compared to that of CS film which were attributed to the components present in the film formulation. In particular, the Thy possessed antibacterial activity, while the CNF and the highly branched structure of the commercial film could have induced additional barriers for moisture and gaseous exchange potentially influencing metabolic processes that impacted the pH and weight loss.

The TVC of the sample packed in CS/CNF/Thy film remained below the maximum permissible limit (7 log CFU/g)[16] up to day 3, and significantly lower than the samples in CS and LDPE films during the 7 days of storage (Fig. 3). This was attributed to the presence of Thy which possessed antibacterial activities that inhibited the growth of microbes, correlating to the results of pH. The efficiency of CS/CNF/Thy films in retarding the increase of microbial load in comparison to the CS and commercial films was also ascribed to the presence of CNF that acted as a physical barrier to provide controlled release of Thy[11]. This led to better retention of Thy, which has the potent phenolic hydroxyl group that created unfavourable conditions for microbial growth. Based on the TVC analysis, samples in CS and commercial films had a shelf life of <3 days, while it was <7 days for sample in CS/CNF/Thy film. These results proved the effectiveness of the release of Thy from the film upon contact with the chicken meat sample.

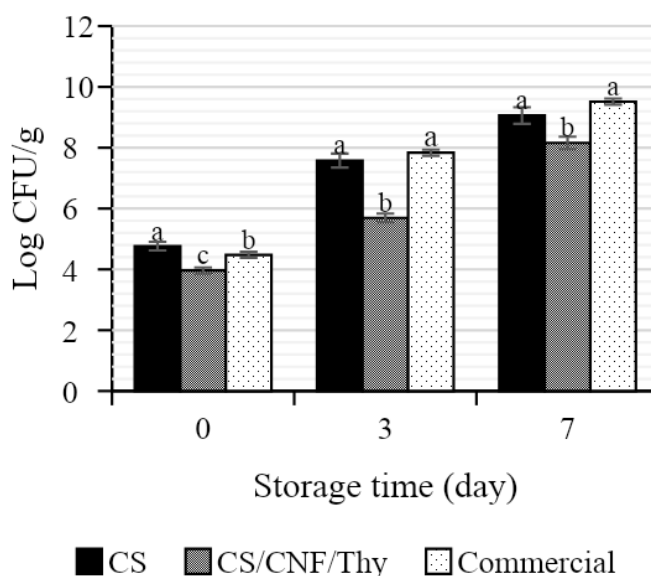


Fig 3: Comparison of TVC values of chicken meat samples over the storage time at 10 °C.

CONCLUSION

The findings proved the active functionality of CS-based film incorporated with CNF and Thy in maintaining the quality attributes of chicken meat stored at 10 °C. Such effects are influenced by the barrier properties and presence of active compounds in the film. Thus, CS/CNF/Thy film produced in this study is promising to be used as active packaging material. Future studies are necessary to explore the production of the active films in larger scale, ensuring the consistency in controlled release behaviour while maintaining cost-effectiveness.

ACKNOWLEDGEMENTS

This research was supported by the Fundamental Research Grant Scheme (FRGS), Ministry of Higher Education Malaysia (Vot no.: 5540711, Project no. FRGS/1/2024/TK05/UPM/02/9).

REFERENCES

- [1] A. Ahmadi, P. Ahmadi, A. Ehsani. Development of an active packaging system containing zinc oxide nanoparticles for the extension of chicken fillet shelf life. *Food Science & Nutrition*, 8(10), pp.5461-5473, 2020.
- [2] Y. Xu, N. Rehmani, L. Alsubaie, C. Kim, E. Sismour, A. Scales. Tapioca starch active nanocomposite films and their antimicrobial effectiveness on ready-to-eat chicken meat. *Food Packaging and Shelf Life*, 16, pp.86-91, 2018.
- [3] Ali, M. S., M. Haq, V. C. Roy, T. C. Ho, J. S. Park, J. M. Han, B. S. Chun. Development of fish gelatin/carrageenan/zein bio-nanocomposite active-films incorporated with turmeric essential oil and their application in chicken meat preservation. *Colloids and Surfaces B: Biointerfaces*, 226, 113320, 2023.
- [4] Y. Ma, Y. Cao, L. Zhang, Q. Yu. Preservation of chilled beef using active films based on bacterial cellulose and polyvinyl alcohol with the incorporation of Perilla essential oil Pickering emulsion. *International Journal of Biological Macromolecules*, 132118, 2024.
- [5] B. Wang, X. Xu, Y. Fang, S. Yan, B. Cui, A. M. Abd El-Aty. Effect of different ratios of glycerol and erythritol on properties of corn starch-based films. *Frontiers in Nutrition*, 9, p.882682, 2022.
- [6] M. J. Galotto, C. L. De Dicastillo, A. Torres, A. Guarda. Thymol: Use in antimicrobial packaging. In *Antimicrobial food packaging* (pp. 553-562). Academic Press. 2016.
- [7] E. Medina, N. Caro, L. Abugoch, A. Gamboa, M. Díaz-Dosque, C. Tapia. Chitosan thymol nanoparticles improve the antimicrobial effect and the water vapour barrier of chitosan-quinoa protein films. *Journal of Food Engineering*, 240, pp.191-198, 2019.
- [8] L. H. Wang, Z. H. Zhang, X. A. Zeng, D. M. Gong, M. S. Wang. Combination of microbiological, spectroscopic and molecular docking techniques to study the antibacterial mechanism of thymol against *Staphylococcus aureus*: membrane damage and genomic DNA binding. *Analytical and bioanalytical chemistry*, 409, pp.1615-1625, 2017.
- [9] N. N. Zainal, I. S. M. A. Tawakkal, M. S. M. Basri, S. H. Ariffin, M. N. Naim. Effect of thymol on properties of bionanocomposites from poly (lactic acid)/poly (butylene succinate)/nanofibrillated cellulose for food packaging application. *International Journal of Biological Macromolecules*, 251, 126212, 2023.
- [10] S. H. Othman, B. M. Wane, N. Nordin, N. Z. Noor Hasnan, R. A. Talib, J. N. W. Karyadi. Physical, mechanical, and water vapor barrier properties of starch/cellulose nanofiber/thymol bionanocomposite films. *Polymers*, 13(23), p.4060, 2021.
- [11] N. Nordin, S. H. Othman, R. Kadir Basha, S. Abdul Rashid. Controlled Release and Antibacterial Activity of Corn Starch-based Films Containing Nanocellulose and Thymol. *Physica Scripta*, 99, 075951, 2024.
- [12] S. M. Yimenu, J. Koo, B. S. Kim, J. H. Kim, J. Y. Kim. Freshness-based real-time shelf-life estimation of packaged chicken meat under dynamic storage conditions. *Poultry Science*, 98(12), pp.6921-6930, 2019.
- [13] N. Mohamad, M. M. Mazlan, I. S. M. A. Tawakkal, R. A. Talib, L. K. Kian, M. Jawaid. Characterization of active polybutylene succinate films filled essential oils for food packaging application. *Journal of Polymers and the Environment*, 30(2), pp.585-596, 2022.
- [14] C. Wang, A. Aji, Ethylene scavenging film based on low-density polyethylene incorporating pumice and potassium permanganate and its application to preserve avocados. *LWT*, 172, 114200, 2022.
- [15] Z. Chen, W. Tian, X. Qin, H. Wang, L. Tan, X. Liu. Chitosan/oxidized Konjac Glucomannan films incorporated with Zanthoxylum Bungeanum essential oil: A novel approach for extending the shelf life of meat. *International Journal of Biological Macromolecules*, 262, p.129683, 2024.
- [16] A. Ntzimani, A. Kalamaras, T. Tsironi, P. Taoukis. Shelf life extension of chicken cuts packed under modified atmospheres and edible antimicrobial coatings. *Applied Sciences*, 13(6), 4025, 2023.

Preparation and Photoluminescence (PL) Characterisation of Carbon Quantum Dots (CQDs) with Different Solutions and Concentrations

Mhammed Ali Khalifa Mhammed Ali Alnigomi ¹, H. Jaafar,^{1,2} S. Shafie ^{1,2}, M.A. Mustafa ¹ and M. A. Kamarudin³

¹*Department of Electrical and Electronic Engineering, Faculty of Engineering, Universiti Putra Malaysia, Serdang, Malaysia*

²*Institute of Nanotechnology and Nanoscience (ION2), Universiti Putra Malaysia, Serdang, Malaysia*

³*Department of Physics, Faculty of Science, Universiti Putra Malaysia, Serdang, Malaysia*

+60123005786

Email : jhaslina@upm.edu.my

Abstract: In this study, carbon quantum dots (CQDs) using watermelon peels were synthesized using the carbonization technique at 220°C for two hours and their optical properties were investigated through Photoluminescence (PL) measurements. The CQDs were synthesized in three different solvents: water (DI), methanol (MtOH), and ethanol (EtOH) with variety of concentration of 3, 6, and 9 mg/ml, with excitation wavelengths of 350, 375, 400, and 450 nm. It was discovered that CQD density increases with concentration for ethanol (EtOH), which allows for more dispersion of incoming light, enhancing light dispersion. Di water has the shortest PL emissions rate with concentration (6,9 mg/ml) in Ethanol and Methanol, whereas concentration 3 mg/ml is slightly higher than 3 mg/ml Ethanol and Methanol.

Keywords: CQDs, photoluminescence, dispersion, synthesis.

INTRODUCTION

In recent years, carbon quantum dots (CQDs) have garnered significant interest from researchers worldwide due to their unique properties, including small size (ideal for certain bio-applications), biocompatibility, photoluminescence (PL) properties, high-temperature stability, chemically inert structure, and ease of functionalization [1]. The discovery of CQDs can be traced back to a 2004 publication, which reported the generation of fluorescent nanoparticles from single-wall carbon nanotubes. Subsequent synthesis of CQDs with surface passivation resulted in improved fluorescence emission [2-3].

Carbon quantum dots (CQDs) can be synthesized using both bottom-up and top-down methodologies. Top-down methods include mechanical milling, laser ablation, electrochemical oxidation, chemical oxidation, and ultrasonic-assisted methods [4-9]. Bottom-up approaches involve plasma treatment, hydrothermal synthesis, pyrolysis, and microwave-assisted carbonization [10-14]. These methods often require complex procedures, expensive raw materials, and harsh conditions, limiting large-scale production.

CQDs' fluorescence requires precise modification of size and particle surface chemical groups. Various surface modification attempts using organic and inorganic methods have been made to enhance luminescence and colloidal stability, but passivation remains complex due to persistent dangling bonds. In this study, we synthesized CQDs from watermelon peels, exploring the impact of different solvents and concentrations on their optical properties using photoluminescence (PL).

METHODOLOGY

Fig. 1 shows the preparation of CQDs where watermelon peels were first cleaned and then sliced into smaller pieces. These pieces were dried in the sun for three days to remove moisture. The dried peels were carbonized in a furnace at 220°C for two hours. After carbonization, the peels were ground and sieved to obtain finer carbon powder particles.

The sieved carbon powder was then measured into three different amounts: 3 mg, 6 mg, and 9 mg, and used in three distinct solvents: deionized water (DI), methanol (MtOH), and ethanol (EtOH).

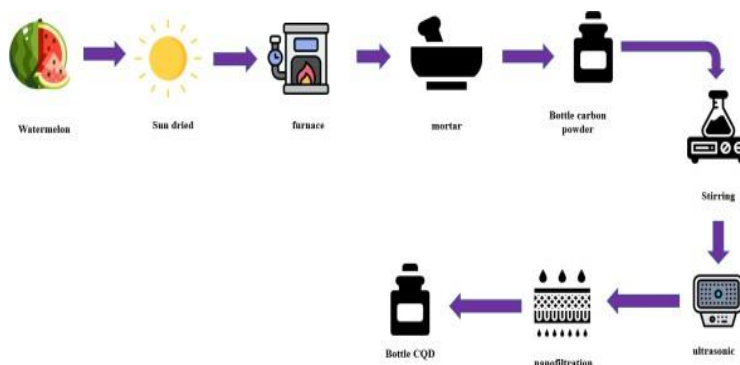


Fig 1. Step by step the process of preparing of carbon quantum dot.

RESULTS AND DISCUSSION

This detailed analysis offers significant insights into the modulation of PL behavior as a function of concentration, providing a non- destructive and sensitive approach for investigating CQD optical properties. Fig. 2 to Fig. 4 illustrate the PL spectra of CQDs in DI-water at concentrations of 3, 6, and 9 mg/ml, with excitation wavelengths of 350, 375, 400, and 450 nm, respectively. Fig. 5 illustrates the comparison of the PL spectra of CQDs in DI water at concentrations of 3, 6, and 9 mg/ml, with an excitation wavelength of 375 nm. Fig 6 to 8 demonstrates the PL spectra of CQDs Ethanol at concentrations of 3 mg/ml, 6 mg/ml, and 9 mg/ml at an excitation wavelength of 350,375,400,450 nm. Fig. 9 presents a comparative analysis of the PL spectra for CQDs in ethanol at concentrations of 3, 6, and 9 mg/ml, with an excitation wavelength of 375 nm. The PL spectra of CQDs at methanol concentrations of 3 mg/ml, 6 mg/ml, and 9 mg/ml with excitation at 350,375,400, and 450 nm are shown in Fig 10, 11, and 12. A comparison of the PL spectra of the CQDs at 3, 6.9 mg/ml of methanol with 450 nm excitation can be seen in Fig 13. Fig 14 portrays the PL spectra of CQDs/DI water/Ethanol/Methanol concentration 3 mg/ml, whereas Fig 15 illustrates the PL spectra of CQDs/DI water/Ethanol /Methanol concentration 6 mg/ml, and Figure 16 represents the PL spectra of CQDs/DInwater/Ethanol /Methanol concentration 9 mg/ml.

DI-Water

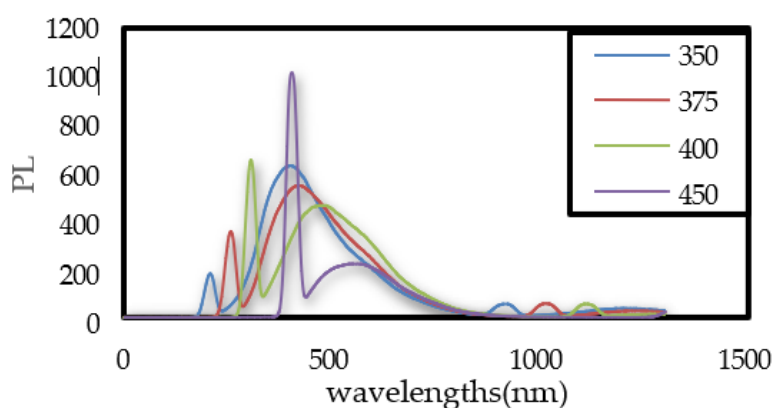


Fig 2. PL spectra of CQDs DI water concentration of 3 mg/ml with excitation of 350,375,400,450 nm.

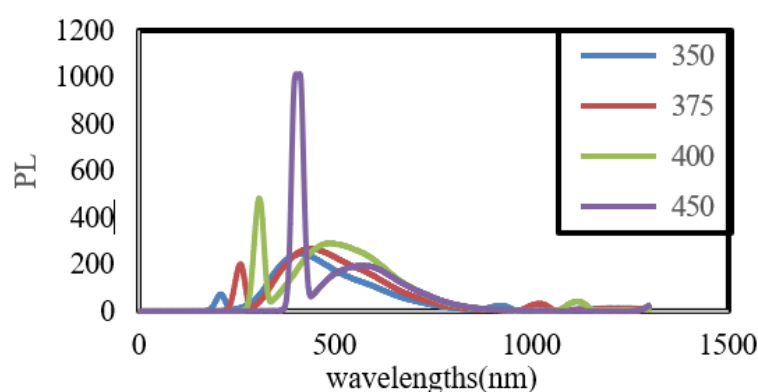


Fig 3. PL spectra of CQDs DI water concentration of 6 mg/ml with excitation of 350,375,400,450 nm.

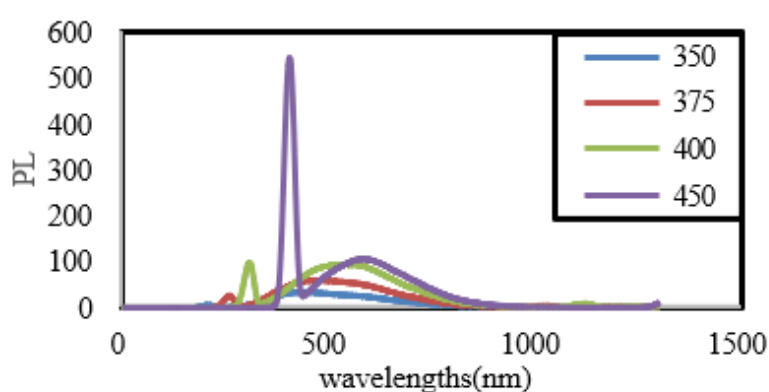


Fig 4: PL spectra of CQDs DI water concentration of 9 mg/ml with excitation of 350,375,400,450 nm.

The excitation's peak value (450 nm) within the 200–500 nm wavelength range is displayed in Fig 2. PL spectra have very narrow full-width halfway points (FWHMs). The excitation's peak value

(450 nm) in the 400–500 nm wavelength range appears in Fig. 3. The PL spectra's full width halfway point (FWHM) is extremely narrow. Moreover, it was noted that the value of PL emissions increased significantly from 3 mg/ml to 6 mg/ml in comparison to the initial concentration of 3 mg/ml. Fig 4 demonstrates that the peak value of the excitation (450) nm is in the region of (400-500) nm wavelength, and the full width halfway point (FWHM) of the PL spectra is narrow. Furthermore, when the concentration increased from 6 mg/ml to 9 mg/ml, the value of PL emissions increased in comparison to the concentration at 6 mg/ml.

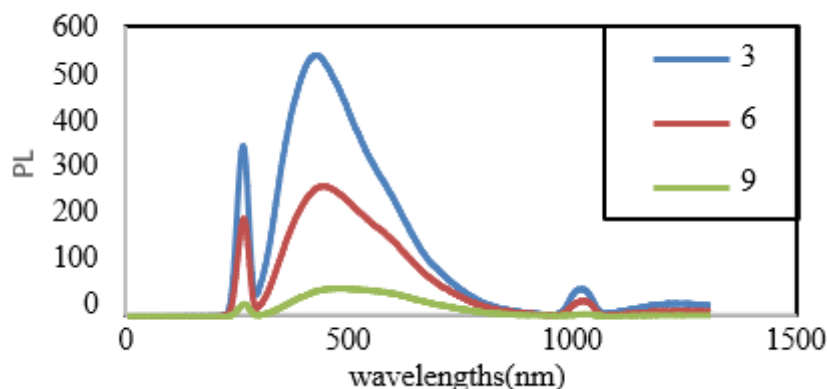


Fig 5. PL spectra of CQDs DI water Concentration of 3, 6,9 mg/ml with excitation of 375nm.

It was observed that at an excitation of 375 nm, within the wavelength range of 200 to 900 nm, the full width at half maximum (FWHM) of the PL spectra is wide. The optimal concentration for PL emissions was determined to be 3 mg/ml.

Ethanol

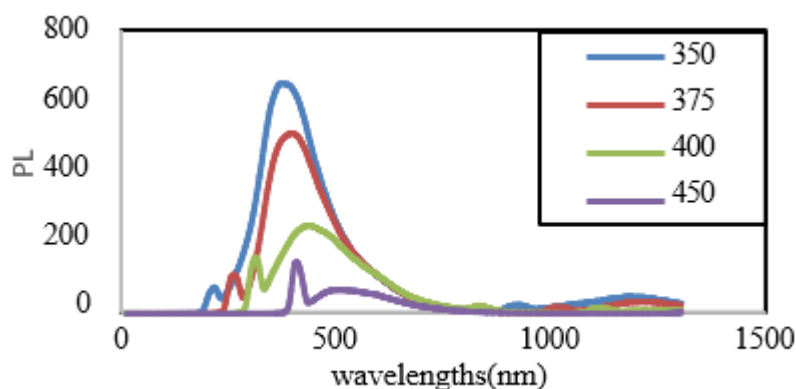


Fig 6. PL spectra of CQDs Ethanol concentration of 3 mg/ml with excitation of 350,375,400,450 nm.

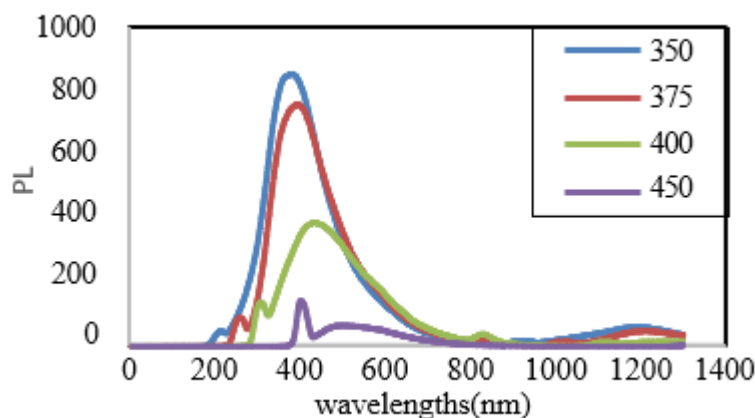


Fig 7. PL spectra of CQDs Ethanol concentration of 6 mg/ml with excitation of 350,375,400,450 nm.

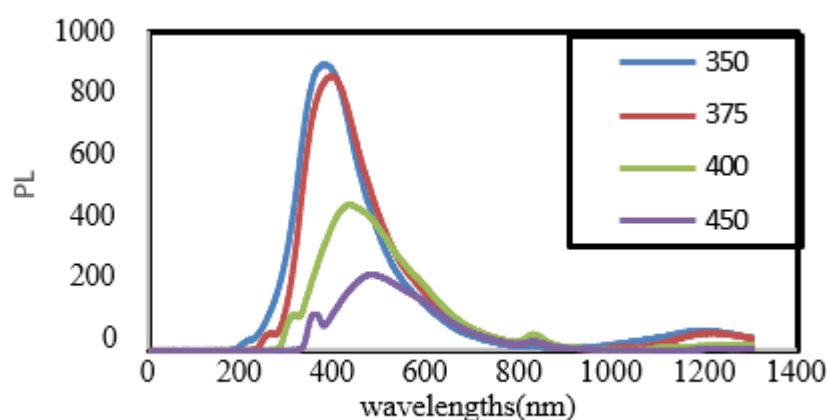


Fig 8. PL spectra of CQDs Ethanol Concentration of 9 mg/ml with excitation of 350,375,400,450 nm.

The peak value of the excitation (350) nm was detected at a wavelength range of (200 to 900) nm, and the full width halfway point (FWHM) of the PL spectra is quite broad. It is noted that as the concentration increases, so does the peak value. Fig 7 (350) nm at the range of (200 to 900) nm wavelength and Fig 8 with the peak value of the excitation (375) nm at the range of (200 to 800) nm wavelength has the same width (FWHM).

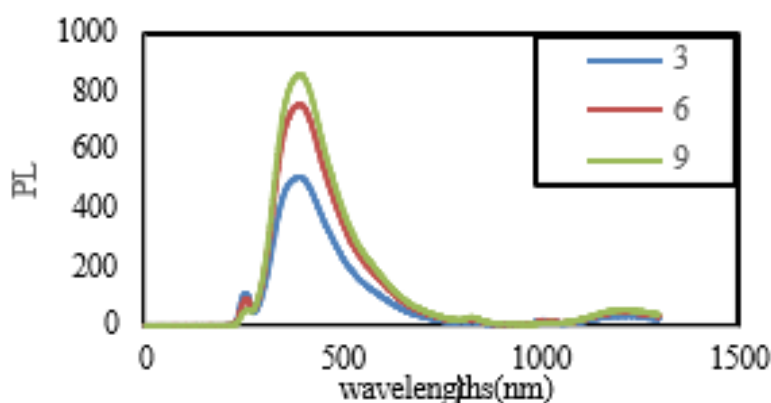


Fig 9. PL spectra of CQDs Ethanol concentration of 3,6,9 mg/ml with excitation of 375 nm.

The results indicate that the 9 mg/ml concentration yields the highest emission intensity. At an excitation wavelength of 375 nm, within the range of 200 to 900 nm, the PL spectra exhibit a wide full width at half maximum (FWHM).

Methanol

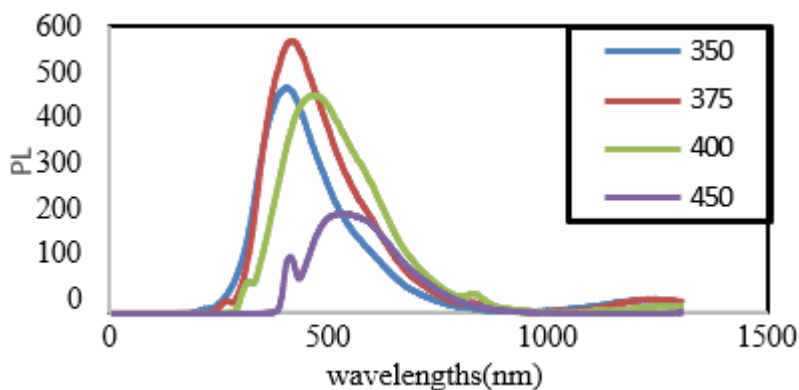


Fig 10. PL spectra of CQDs methanol concentration of 3 mg/ml with excitation of 350,375,400,450 nm.

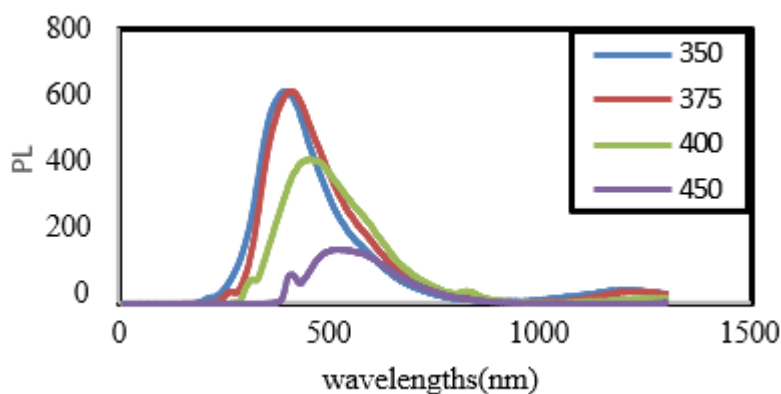


Fig 11. PL spectra of CQDs methanol concentration of 6 mg/ml with excitation of 350,375,400,450 nm.

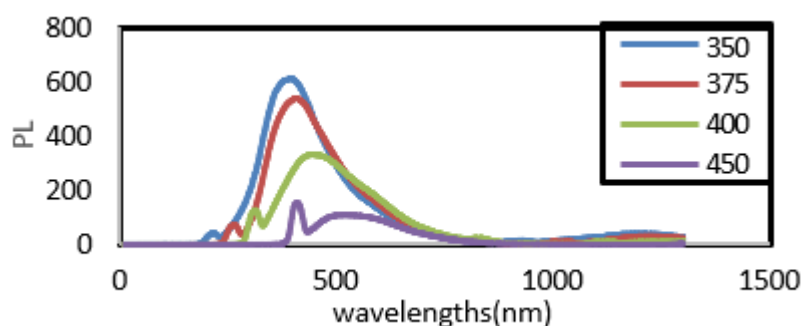


Fig 12. PL spectra of CQDs methanol concentration of 9 mg/ml with excitation of 350,375,400,450 nm.

It was noted that both had the full-width halfway point (FWHM) of the PL spectra and the peak value of the excitation (375) nm at the range of (200 to 800) nm wavelength is extremely broad. The excitation's peak value (375 nm) in the range of (200 to 800) nm is shown in Fig 11, and Fig 12's peak value (375 nm) at the same (FWHM) of PL spectra is shown in Fig 10 and 11.

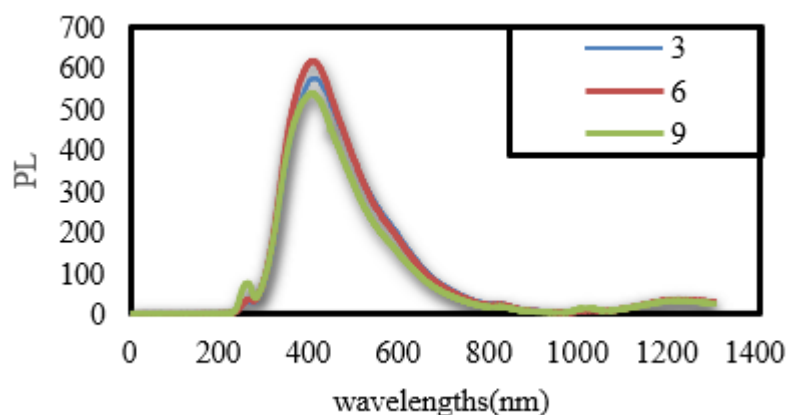


Fig 13:PL spectra of CQDs DI methanol concentration of 3, 6,9 mg/ml with excitation of 375nm.

It was observed that the peak value of the excitation (375) nm at the range off (200 to 800) nm wavelength for the three concentrations and the best value was 6 mg/ml.

CQD PL spectra showed distinct emission peaks in the visible range, with the emission wavelength dependent on the base material and CQD concentration. An insignificant redshift in the emission peak location was observed as CQD concentration increased, indicating a reduction in the bandgap of CQDs as well as the contribution that comes from CQD size. This can be observed in the normalization graph of PL spectra in Fig 14, 15, and 16 as the energy shifts from greatest to lowest concentration. The redshift can be explained by the quantum confinement effect, which states that increasing the concentration of CQDs increases the probabilities of exciton confinement, resulting in a reduction in the bandgap and a redshift in the emission wavelength [15], [16]. The analysis is further examined by identifying the full width halfway point (FWHM) of PL spectra in varied concentrations and comparing the three distinct base materials Di Water, Methanol, and Ethanol, as demonstrated in Fig 14, 15, and 16. The intensity of the PL spectra fluctuated with concentration. The PL intensity reduced at lower doses, increased at middle values, and eventually reached saturation at higher concentrations (6-9 mg/ml). This tendency may be described by the conflict between radiative and non-radiative decay processes, as well as the light scattering effect [15], [16].

At larger concentrations, the radiative decay processes dominate, resulting in a higher PL intensity. Additionally, enhanced light scattering effects can lead to higher PL intensity at higher concentrations. Light scattering happens when photons collide with particles having dimensions on the order of their wavelength, such as CQDs. The density of CQDs rises with concentration, allowing in more scattering of incoming light [15], [16]. When comparing the three base materials, as shown in Figures 14,15, and 16, Di water has the shortest PL emissions rate with concentration (6,9 mg/ml) in Ethanol and Methanol, whereas concentration 3 is slightly higher than Ethanol and in the range of Methanol.

The FWHM analysis reveals CQD homogeneity and size dispersion. A smaller FWHM may indicate high purity and homogeneity if the size distribution is tighter [15], [16]. When compared to other samples, the concentration of 9 mg/ml has the smallest FWHM linewidth spectrum, as shown in Fig 16. This demonstrates that the CQDs' size and surface characteristics are more homogenous, which leads to more consistent emission behavior.

Additionally, the intensity of the PL spectra fluctuated with concentration. The PL intensity reduced at lower doses, increased at middle values and eventually reached saturation at higher concentrations (6-9 mg/ml). This tendency may be described by the conflict between radiative and non- radiative decay processes, as well as the light scattering effect. At larger concentrations, the radiative decay processes dominate, resulting in a higher PL intensity. Additionally, enhanced light scattering effects can lead to higher PL intensity at higher concentrations. Light scattering happens when photons collide with particles having dimensions on the order of their wavelength, such as CQDs. The density of CQDs rises with concentration, allowing in more scattering of incoming light. When comparing the three base materials, as shown in Fig 14,15, and 16, Di water has the shortest PL emissions rate with concentration (6,9 mg/ml) in Ethanol and Methanol.

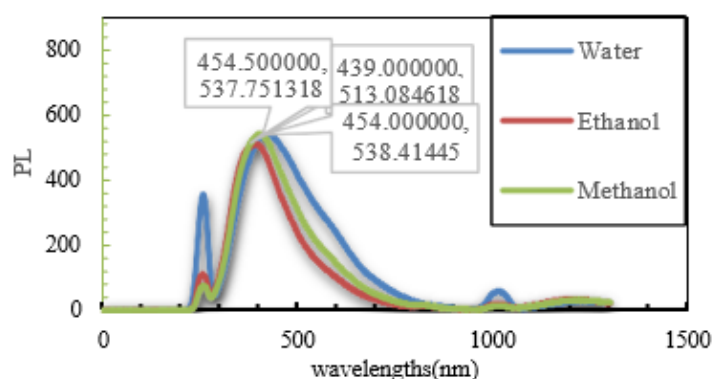


Fig 14: PL spectra of CQDs/DI water/Ethanol/Methanol Concentration 3 mg/ml.

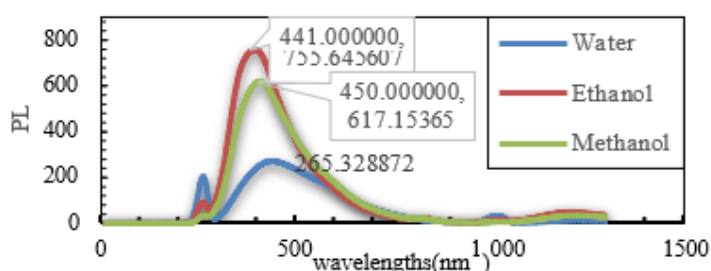


Fig 15: PL spectra of CQDs/DI water/Ethanol/Methanol Concentration 6 mg/ml.

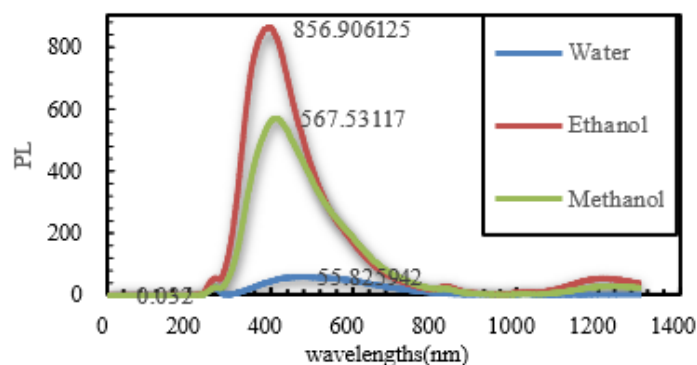


Fig 16: PL spectra of CQDs/DI water/Ethanol/Methanol Concentration 9 mg/ml.

CONCLUSION

In conclusion, CQD density increases with concentration, allowing for more dispersion of incoming light. When the three base materials are compared, as shown in Fig 14,15, and 16, DI water has the lowest PL emissions rate with concentrations (6,9 mg/ml) in Ethanol and Methanol, but concentration 3 is somewhat higher than Ethanol and in the range of Methanol. The radiative decay processes take over at greater concentrations, resulting in a higher PL intensity. Furthermore, increased light scattering effects can result in greater PL intensity at larger concentrations.

ACKNOWLEDGEMENTS: This work funded by Putra-IPS Grant/2022/9735300 under Faculty of Engineering and Institute of Nanotechnology and Nanoscience, Universiti Putra Malaysia.

REFERENCES

- [1] M. J. Molaei, "A review on nanostructured carbon quantum dots and their applications in b Times New Romanotechnology, sensors, and chemiluminescence," *Talanta*, vol. 196, no. August 2018, pp. 456–478, 2019, doi: 10.1016/j.talanta.2018.12.042.
- [2] X. Xu et al., "Electrophoretic Analysis and Purification of Fluorescent Single-Walled Carbon Nanotube Fragments," *J. Am. Chem. Soc.*, vol. 126, no. 40, pp. 12736–12737, Oct. 2004, doi: 10.1021/ja040082h.
- [3] Y.-P. Sun et al., "Quantum-Sized Carbon Dots for Bright and Colorful Photoluminescence," *J. Am. Chem. Soc.*, vol. 128, no. 24, pp. 7756–7757, Jun. 2006, doi: 10.1021/ja062677d.
- [4] W. Wu et al., "Cu-N dopants boost electron transfer and photooxidation reactions of carbon dots," *Angew. Chemie - Int. Ed.*, vol. 54, no. 22, pp. 6540–6544, 2015, doi: 10.1002/anie.201501912.
- [5] A. Singh, P. K. Mohapatra, D. Kalyanasundaram, and S. Kumar, "Self- functionalized ultrastable water suspension of luminescent carbon quantum dots," *Mater. Chem. Phys.*, vol. 225, no. October 2018, pp. 23–27, 2019, doi:10.1016/j.matchemphys.2018.12.031.
- [6] H. Li et al., "Water-soluble fluorescent carbon quantum dots and photocatalyst design," *Angew. Chemie - Int. Ed.*, vol. 49, no. 26, pp. 4430–4434, 2010, doi: 10.1002/anie.200906154.
- [7] L. Bao et al., "Electrochemical tuning of luminescent carbon nanodots: From preparation to luminescence mechanism," *Adv. Mater.*, vol. 23, no. 48, pp. 5801–5806, 2011, doi:10.1002/adma.201102866.
- [8] M. Li, C. Hu, C. Yu, S. Wang, P. Zhang, and J. Qiu, "Organic amine-grafted carbon quantum dots with tailored surface and enhanced photoluminescence properties," *Carbon N. Y.*, vol. 91, pp. 291–297, 2015, doi: 10.1016/j.carbon.2015.04.083.

- [9] H. Li et al., "One-step ultrasonic synthesis of water-soluble carbon nanoparticles with excellent photoluminescent properties," *Carbon N. Y.*, vol. 49, no. 2, pp. 605–609, 2011, doi: 10.1016/j.carbon.2010.10.004.
- [10] J. Wang, C. F. Wang, and S. Chen, "Amphiphilic egg-derived carbon dots: Rapid plasma fabrication, pyrolysis process, and multicolor printing patterns," *Angew. Chemie - Int. Ed.*, vol. 51, no. 37, pp. 9297–9301, 2012, doi: 10.1002/anie.201204381.
- [11] M. F. Gomes, Y. F. Gomes, A. Lopes- Moriyama, E. L. de Barros Neto, and C. P. de Souza, "Design of carbon quantum dots via hydrothermal carbonization synthesis from renewable precursors. *Biomass Convers. Biorefinery* 9, 689–694 (2019)." 2019.
- [12] Y. Liu et al., "Hydrothermal synthesis of nitrogen and boron co-doped carbon quantum dots for application in acetone and dopamine sensors and multicolor cellular imaging," *Sensors Actuators, B Chem.*, vol. 281, no. October 2018, pp. 34–43, 2019, doi: 10.1016/j.snb.2018.10.075.
- [13] H. Qi et al., "Biomass-derived nitrogen- doped carbon quantum dots: highly selective fluorescent probe for detecting Fe 3+ ions and tetracyclines," *J. Colloid Interface Sci.*, vol. 539, pp. 332–341, 2019, doi: 10.1016/j.jcis.2018.12.047.
- [14] J. Q. Zhang, M. H. Fan, W. Li, H. Xie, H.C. Wu, and S. P. Wang, "Fire safety of cables in power grid: Tracking combustion test standards of cables and new insights on test framework," *CIGRE Sess. 46*, vol. 2016-August, p. 3441, 2016.
- [15] X. D. Mai, Y. T. H. Phan, and V. Q. Nguyen, "Excitation-Independent Emission of Carbon Quantum Dot Solids," *Advances in Materials Science and Engineering*, vol. 2020, 2020, doi: 10.1155/2020/9643168.
- [16] H. Wang et al., "Excitation wavelength independent visible color emission of carbon dots," *Nanoscale*, vol. 9, no. 5, pp. 1909–1915, Feb. 2017, doi: 10.1039/c6nr09200d.

Synthesis of Hydrochar-Based Acid Catalyst for Efficient Esterification of Palm Fatty Acid Distillate

Muhammad Aliyu^{1,*}, Umer Rashid¹, Toshiki Tsubota², Wan Azlina Wan Ab Karim Ghani³, Muhamad Amran bin Mohd Salleh³, Duy Anh Khuongab², Ali Salisu⁴,

¹ *Institute of Nanoscience and Nanotechnology, Universiti Putra Malaysia, 43400 UPM Serdang, Selangor, Malaysia.*

² *Department of Materials Science, Faculty of Engineering, Kyushu Institute of Technology, Kitakyushu, Fukuoka 804-8550, Japan.*

³ *Department of Chemical and Environmental Engineering, Faculty of Engineering, Universiti Putra Malaysia, Serdang, Selangor, 43400, Malaysia*

⁴ *Department of Chemistry, Faculty of Natural and Applied Science, Sule Lamido University, Kafin Hausa, Jigawa state, 204, Nigeria.*

**Corresponding author's phone: +601158907635 E-mail: muhdaliyu200@gmail.com*

Abstract: Heterogeneous catalysts are attractive and sustainable and can replace homogeneous catalysts due to their reusability, low cost, and ease of access. This research utilized hydrothermal carbonization (HTC) to create hydrochar from desert date waste, and a novel catalyst (DDWAHC-S) was developed by activating the hydrochar with H₃PO₄ and impregnating it with H₂SO₄. The acid catalyst, featuring an amorphous structure, had a specific surface area of 98.47 m²/g, a pore diameter of 6.15 nm, and an acid density of 13.71 mmol/g, proving effective for PFAD esterification in biodiesel production. Under optimal conditions, it achieved a biodiesel yield of 91.56% and maintained over 85% efficiency after four cycles, highlighting its promise as a sustainable catalyst for biodiesel production from PFAD.

Keywords: Biodiesel; acid catalyst; palm fatty acid distillate; Desert date waste; Hydrochar; Hydrothermal Carbonization

INTRODUCTION

The widespread use of fossil fuels to power vehicles and generate electricity contributes to hazardous emissions that pose risks to human health and the environment [1]. Biodiesel, a renewable and sustainable alternative, has gained attention due to its minimal greenhouse gas emissions and oxygen-rich molecular structure that enhances combustion efficiency [2].

This study focuses on utilizing palm fatty acid distillate (PFAD), a by-product of palm oil refining, as a feedstock for biodiesel production. PFAD's high free fatty acid (FFA) content presents a challenge addressed by employing acid catalysts. Homogeneous acid catalysts offer good conversion efficiency but have limitations regarding recoverability and purification [3].

Heterogeneous catalysts are favoured for their reusability and simplicity in separation. The research takes advantage of palm leaf waste as a low-cost and abundant source of biomass-based catalyst support [4]. Rather than traditional drying methods, the study employs hydrothermal carbonization (HTC) to produce hydrochar (HC) from wet biomass, offering an energy-efficient alternative. HC produced using this method has various applications, including carbon support for catalysts due to its active surface sites [1].

Using desert date waste (DDW) as a carbon source for producing hydrochar-based catalysts is convenient and readily accessible, especially in regions with abundant resources, such as the Sahara and sub-Saharan areas like Nigeria [5].

The novelty of this research lies in optimizing the production of hydrochar- based catalysts and biodiesel parameters for sustainability and waste management. The main objectives are to produce HC from DDW, synthesize a heterogeneous hydrochar acid catalyst, and optimize catalytic conditions for PFAD esterification. This study explores optimizing hydrochar acid catalyst synthesis for biodiesel production, aiming to contribute to sustainable energy.

MATERIALS and METHOD

Materials

The desert date waste (DDW) was sourced from the Baturiya Game Reserve in Hadejia, Jigawa, Nigeria. The PFAD feedstock was sourced from Jomalina R&D, Sime Darby Co. Bhd. in Malaysia. Sulfuric acid (H_2SO_4) with 98% purity and phosphoric acid (H_3PO_4) with 50% purity was obtained from Merck & Co. Methanol (MeOH) with a high analytical grade purity of 99.8% was obtained from JT Baker. Hexane (90% purity) was purchased from Merck & Co., USA.

Preparation of Activated Hydrochar

The desert date waste mills were ground into smaller particles using a Fritsch Pulverized 16 cross-beater mill to enhance hydrochar formation. This ground material (5 g) was hydrothermally carbonized at 200°C for 12 hours. The mixture was filtered and rinsed with distilled water until it reached a pH of 7 at room temperature. It was then dried at 80 °C for 6 hours. The powder that was obtained was assigned as DDWHC. For the chemical activation of DDWHC, the DDWHC powder was first activated with H_3PO_4 at a 2:1 weight ratio for 12 hours at 27 °C to increase the hydrochar's porosity [1]. To eliminate any unreacted H_3PO_4 , the slurry was filtered and washed with hot distilled water at 80°C until the pH reached 7. The resulting product was dried at 80 °C for 6 hours and named DDWAHC.

Synthesis of Acid Hydrochar-based Catalyst

The DDWAHC powder was then impregnated using a reflux method with 120 mL of concentrated H_2SO_4 at 150 °C for 6 hours. The unreacted H_2SO_4 was removed through filtration, and the product was washed with hot distilled water at 80°C until the pH was neutral. Finally, the product was dried at 80 °C for 6 hours, resulting in the final product designated as DDWAHC-S.

Esterification of PFAD

The PFAD is heated for 1 hour at 70°C before being filtered to remove impurities. The filtered PFAD is used as a feedstock in biodiesel production. Batch esterification processes are performed to produce biodiesel. Methanol, PFAD, and a catalyst were placed in a three-neck flask. The mixture was heated to the temperature (°C) set by the variables and swirled at a rate of 450 rpm. The esterification process began in a reflux reactor in a silicon oil water bath. Catalyst doses ranging from 1 to 6 (wt.%), reaction temperatures ranging from 333.15 K to 383.15 K, reaction times ranging from 1 to 6 hours, and Methanol to PFAD molar ratios ranging from 9:1 to 21:1 are among the esterification process variables. After the esterification, the biodiesel product was centrifuged to separate it from the catalyst and the final product as a biodiesel. Gas chromatography was used to analyze the biodiesel yield.

Biodiesel Analysis

The biodiesel product was analyzed using a GC-FID with a BPX-70 capillary. n-hexane was the GC solvent, and methyl heptadecanoate was the internal standard. The reference standards included methyl palmitate, methyl myristate, methyl linoleate, methyl stearate, and methyl oleate at 1000 ppm each. A 1 μ m sample of the biodiesel was injected into the port, and the GC temperature ranged from 100 to 250 °C at a rate of 10 °C/min. Biodiesel yield (%) was calculated using an Eq. (1).

$$\text{Biodiesel yield (\%)} = \frac{(\sum A - A_{MH})}{A_{MH}} \times \frac{(C_{MH} \times V_{MH})}{W_t} \times 100 \quad (1)$$

Where, $\sum A$ represents the combined area of the peaks corresponding to free fatty acids (FFA), A_{MH} is the area of the peak for the internal standard, C_{MH} is the methyl heptadecanoate concentration, the methyl heptadecanoate volume used, and W_t is the mass of the biodiesel.

Catalyst Characterization

FT-IR analysis used a Perkin-Elmer Spectrum (100 FTIR) Spectrometer in the 400 - 4000 cm⁻¹. X-ray diffraction (XRD) on a Shimadzu-6000 machine assessed crystallite size and structure, employing a scanning range and rate of 4 min⁻¹ of theta (θ) from 20 to 80. FESEM (FEI, NOVA NANOSEM 230) examined surface morphology, and energy-dispersive X-ray spectroscopy (EDX) (Oxford Instruments, Model 7582) evaluated surface elemental composition. The Brunauer-Emmett-Teller (BET) technique measured specific surface area with Thermo Fisher Scientific (Sorptomatic 1990 series). Boehm titration (BT) was employed to measure catalyst acid density [4] The thermogravimetric analysis (TGA) on a Mettler Toledo 990 machine was used to determine thermal stability. CHNS analysis was used to determine sulfur leached during the usability study.

Catalyst's Reusability Evaluation

The spent DDWAHC-S catalyst, collected after biodiesel production, was purified with n-hexane and dried at 110°C to eliminate solvents and moisture, ensuring optimal performance. After drying, the catalyst can be reused, with evaluations continuing until a significant decrease in biodiesel yield is observed, indicating diminished catalytic activity. These assessments were crucial for determining the catalyst's practical applicability and sustainability in the esterification of PFAD.

RESULTS AND DISCUSSION

Characterization of the Catalyst

The FTIR spectra of DDWHC, DDWAHC, and DDWAHC-S show significant absorption bands in Fig. 1, including C=C stretching of polyaromatic carbon rings, Si-O-Si stretching from silanol groups, carbonization of hemicellulose, presence of -SO₃H groups, and -OH group vibrations from sulfonic acid moieties in DDWAHC-S. Broad peaks in DDWHC and DDWAHC correspond to C-H bond stretching, while absent in DDWAHC-S, suggesting substantial hydrogen removal due to chemical treatment.

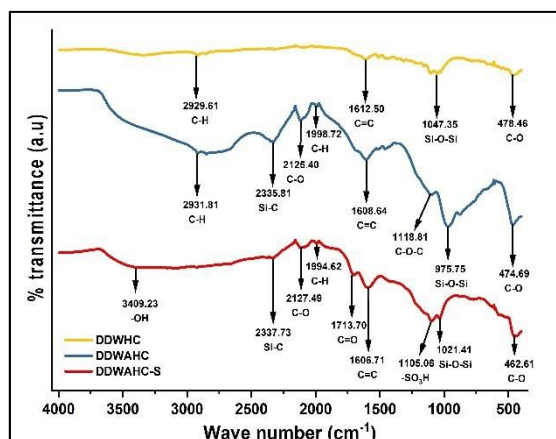


Fig. 1: FT-IR results of DDWHC, DDWAHC and DDWAHC-S

Boehm's method confirmed the presence of acidic groups on DDWAHC-S surfaces. NaOH titration was used to determine the acidic group concentration in the catalyst. PLAHC-S had an acid content of 13.71 mmol/g, higher than Aliyu et al. [1]. Other weak acidic functional groups, such as carboxylic acids, also contribute to PFAD esterification. Low-acidity sites corresponded to the peak band of -OH functional groups in the FTIR spectrum.

The XRD analysis of DDWHC, DDWAHC, and DDWAHC-S revealed amorphous phases in Fig. 2. DDWHC contained graphitic structures at 23° and 30°, corresponding to carbon planes. DDWAHC and DDWAHC-S were primarily amorphous, with a broad peak representing amorphous polycyclic aromatic carbon rings. Due to activation and sulfonation, the impurity peak at 15° in DDWHC disappeared from the spectra of DDWAHC and DDWAHC-S.

The surface morphologies of DDWHC, DDWAHC, and DDWAHC-S were examined using FESEM at 25,000x magnification. Figs. 3b, c, and d reveal an irregular, undulating structure. DDWAHC displayed a cracked porous layer, likely due to activation with phosphoric acid, resulting in high porosity and surface area. DDWAHC-S showed agglomerated small and large particles due to sulfonation.

EDX analysis confirmed the elemental compositions: DDWHC had 76.41 wt.% carbon, 22.90 wt.% oxygen, and 0.69 wt.% silicon; DDWAHC had 58.38 wt.% carbon, 38.14 wt.% oxygen, 0.73 wt.% silicon, and 8.75 wt.% phosphorus; DDWAHC-S had 69.28 wt.% carbon, 24.98 wt.% oxygen, 0.60 wt.% silicon, and 5.13 wt.% sulfur. High oxygen content indicated covalent bonds, primarily oxygen atoms bonded to silicon (S-O-Si).

The BET analysis revealed that DDHC, DDWAHC, and DDWAHC-S had mesoporous structures with surface areas 48.55 m²/g, 105.23 m²/g, and 91.5647 m²/g, respectively. These structures facilitated esterification by enhancing fatty acid diffusion.

Fig. 3a shows the TGA of DDWHC, DDWAHC, and DDWAHC-S. All three materials showed similar initial weight losses of 14.88% from 302.86 °C to 424.09 °C due to moisture and volatile components. A subsequent 9.08% weight loss between 456.27 °C and 584.04 °C was due to hemicellulose. The final significant weight loss of 42.83% between 580.45 °C and 1000 °C were attributed to lignin decomposition. These findings suggest that DDWAHC-S has sufficient thermal stability for esterification reactions.

Optimization of Esterification of PFAD using Acid Catalyst

The study focuses on biodiesel production's economic viability and commercial feasibility, highlighting DDWAHC-S as the most efficient catalyst. The one variable at a time (OVAT) method was used to optimize critical variables influencing PFAD esterification reaction.

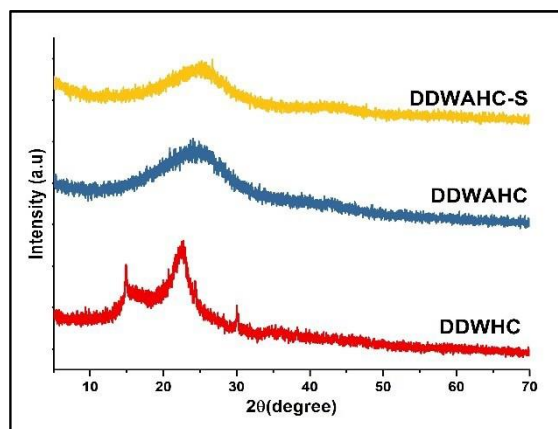


Fig. 2: XRD results of DDWHC, DDWAHC and DDWAHC-S

Catalyst Dosage.

The impact of catalyst dosage on biodiesel yield was examined with a 3-hour reaction time, a 15:1 methanol to PFAD ratio, and a 353.15 K temperature, depicted in Fig 4a. Higher catalyst doses increased active sites, enhancing esterification interactions and biodiesel yield. Increasing the catalyst dosage from 1 to 4 wt.% led to biodiesel yield rising from 52.89% to 82.45%. However, a further increase from 5 to 6 wt.% reduced biodiesel yield from 81.34% to 81.22%, attributed to mass transfer challenges [2]. The optimal dosage was 4 wt.% for maximum biodiesel yield, balancing active site availability and mass transfer efficiency.

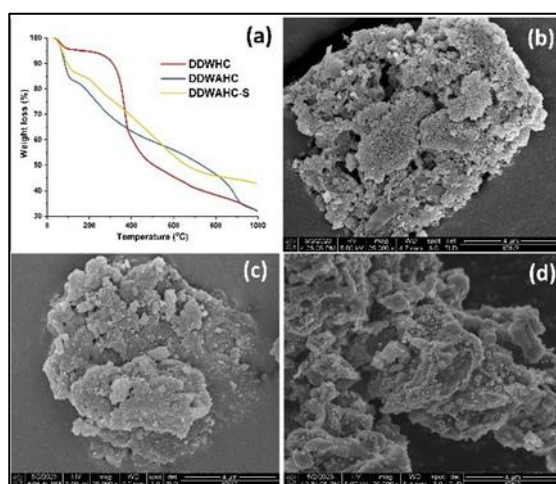


Fig. 3: The result of (a) TGA and FESEM images of (b) DDWHC, (c) DDWAHC, & (d) DDWAHC-S.

Reaction Temperature

The impact of reaction temperature on biodiesel yield was studied between 333.15 K to 383.15 K and is depicted in Fig. 4b. Increasing temperature from 333.15 K to 353.15 K enhanced biodiesel yields from 61.34% to 84.34% due to the energy required for solid-to-liquid transformation and improved methanol homogeneity. Beyond this range, at 363.15 K to 383.15 K, biodiesel yields decreased from 81.23% to 75.34% due to the vaporization of methanol, leading to reduced esterification efficiency [1]. The optimal temperature for maximum biodiesel yield was 353.15 K.

Reaction Time

The impact of reaction time on biodiesel yield using DDWAHC-S catalyst, with a catalyst dose of 4 wt.%, methanol: PFAD molar ratio of 15:1, and a reaction temperature of 353.15 K is depicted in Fig. 4c. As reaction time increased from 1 to 4 h, biodiesel yield rose significantly, from 59.55% to 89.56%, due to enhanced collisions on active sites, promoting adsorption and desorption processes [1]. No notable improvement was observed after 4 hours. This suggests 4 hours is the optimum reaction time for the highest biodiesel yield.

Molar ratio of Methanol to PFAD.

The methanol to PFAD molar ratio was evaluated from 9:1 to 21:1 while keeping the temperature at 353.15 K, reaction time at 4 hours, and catalyst loading at 4 wt.%. As shown in Fig. 4b, the biodiesel yield increased from 60.45% at a 9:1 ratio to 91.56% at an 18:1 ratio due to better methoxy species presence on the DDWAHC-S surface, enhancing PFAD conversion [5]. However, at a 21:1 ratio, yield decreased due to diluted PFAD and saturated catalyst sites. Further, increasing the molar ratio did not significantly improve yield due to reaction reversibility and product formation. The optimal methanol to PFAD molar ratio was 18:1.

Reusability of Catalyst

Heterogeneous acid catalysts are favoured for their reusability, as depicted in Fig 5. In six consecutive reaction runs, the catalyst maintained over 85% biodiesel yield for the four cycles. According to the CHNS analysis of biodiesel, the fourth reusability study revealed a 1.2% reduction in sulphur species, implying that -SO₃H groups are removed from the surface of DDWAHC-S during the reaction. Eliminating -SO₃H from the DDWAHC-S surface may result in the loss of very acidic active sites and reduced esterification activity.

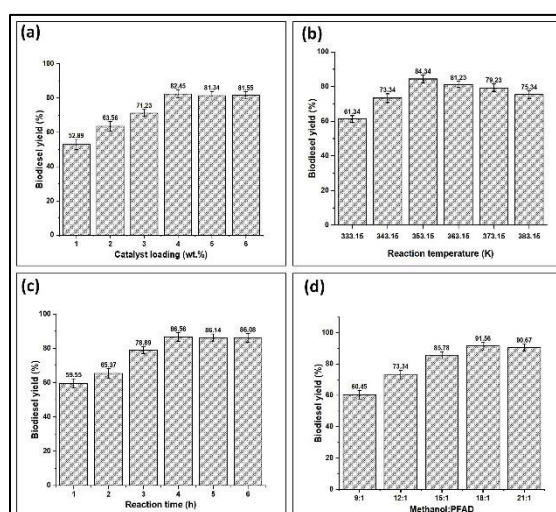


Fig. 4: Catalytic optimization variables: (a) catalyst dosage, (b) reaction temperature, (c) reaction time, and (d) methanol: PFAD molar ratio.

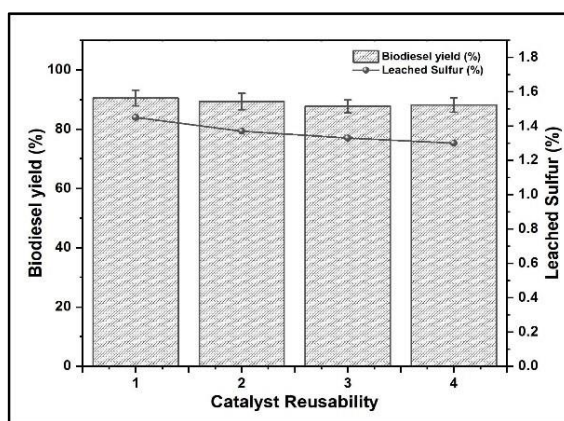


Fig. 5: Reusability test and Sulfur leached determination

CONCLUSION

This study explored using desert date waste to synthesize a heterogeneous acid catalyst for esterifying PFAD into biodiesel. Techniques included HTC, activation with H₃PO₄, and functionalization with H₂SO₄. HTC preserved active polar species, H₃PO₄ activation increased catalyst porosity, and H₂SO₄ treatment enhanced acidic sites by adding -SO₃H groups, resulting in a 91.56% biodiesel yield under optimal conditions. The catalyst showed good reusability, retaining 85% yield after four uses. Overall, HTC-based catalyst preparation is a cost-effective and energy-efficient alternative to conventional methods for biodiesel production.

ACKNOWLEDGEMENTS: The authors thank the Researchers Supporting Project (Project No. 9765000) at Universiti Putra Malaysia.

REFERENCES

- [1] Aliyu, M., Moser, B.R., Alharthi, F.A., Rashid, U.: Efficient production of biodiesel from palm fatty acid distillate using a novel hydrochar-based solid acid catalyst derived from palm leaf waste. *Process Safety and Environmental Protection*. 187, 1126–1139 (2024).
- [2] Akinfalabi, S.I., Rashid, U., Ngamcharussrivichai, C., Nehdi, I.A.: Synthesis of reusable biobased nano-catalyst from waste sugarcane bagasse for biodiesel production. *Environ Technol Innov.* 18, (2020).
- [3] Farabi, M.S.A., Ibrahim, M.L., Rashid, U., Taufiq-Yap, Y.H.: Esterification of palm fatty acid distillate using sulfonated carbon- based catalyst derived from palm kernel shell and bamboo. *Energy Convers Manag.* 181, 562–570 (2019).
- [4] Syazwani, O.N., Rashid, U., Mastuli, M.S., Taufiq-Yap, Y.H.: Esterification of palm fatty acid distillate (PFAD) to biodiesel using Bi-functional catalyst synthesized from waste angel wing shell (*Cyrtopleura costata*). *Renew Energy*. 131, 187–196 (2019).
- [5] Liu, Z., Liu, Z.: Comparison of hydrochar- and pyrochar-based solid acid catalysts from cornstalk: Physiochemical properties, catalytic activity and deactivation behavior. *Bioresour Technol.* 297, (2020)

Synthesis of Hydroxyapatite from *Polymesoda expansa* (Lokan) Mollusk Shell using Room Temperature and Hydrothermal Methods

Rosnah Nawang^{1*}, Mohd Zobir Hussein²

¹*Nanomaterials Synthesis & Characterisation Laboratory, Institute of Nanoscience & Nanotechnology, Universiti Putra Malaysia
Serdang, Malaysia*

²*Faculty of Dentistry, Universitas Brawijaya, Malang, Indonesia*

**Corresponding author's phone: +603-9769 7548*

E-mail: rnawang@upm.edu.my

Abstract: Hydroxyapatite (HA), a calcium phosphate compound, is widely used in biomedical applications due to its similarity to human bone mineral. Natural materials rich in calcium, such as mollusk shells, can be utilized for HA synthesis. In this study, we synthesized HA from *Polymesoda expansa* (lokan) mollusk shells at pH 7.4 using both room temperature and hydrothermal methods. The HA samples were characterized using Fourier-transform infrared spectroscopy (FTIR) and X-ray diffraction (XRD). Results indicated that the HA phase was detectable as early as day 2 at room temperature, with its presence increasing over time. The hydrothermal method yielded a greater amount of HA compared to the room temperature method. These findings suggest that *Polymesoda expansa* (lokan) mollusk shells are a viable source of calcium for HA synthesis and that the hydrothermal method is more efficient for producing HA in significant quantities.

Keywords: *polymesoda expansa; mollusk shell; hydroxyapatite; room temperature; hydrothermal method*

INTRODUCTION

Hydroxyapatite (HA), with the chemical formula $\text{Ca}_{10}(\text{PO}_4)_6(\text{OH})_2$, is a calcium phosphate mineral used in biomedical applications such as bone grafts, dental implants, and coatings for metal implants [1], due to its biocompatibility and similarity to human bone mineral. It naturally occurs in bones and teeth and often contains trace elements like magnesium, fluoride, and carbonate. Synthetic HA can be produced in laboratories using chemical methods, allowing for customization to achieve high purity and controlled particle size.

Calcium and phosphate are the primary raw materials used in producing synthetic HA. Mollusk shells, which are predominantly composed of calcium carbonate (CaCO_3), offer a sustainable and abundant source of calcium for HA synthesis [2]. These shells, byproducts of the seafood industry, are typically discarded as waste, leading to environmental concerns [3]. By utilizing mollusk shells for HA synthesis, not only is the demand for natural calcium sources met, but waste is also reduced, contributing to a circular economy. Furthermore, mollusks are a vital food source globally, and the sustainable use of their shells ensures minimal environmental impact, reducing the need for mining calcium from other sources and lowering the carbon footprint associated with traditional HA production methods.

Among the various mollusk species used for this purpose, *Polymesoda expansa* (lokan), a bivalve mollusk commonly known as the mangrove clam, offers distinct advantages for HA synthesis. Found abundantly in tropical and subtropical regions, the shell of *Polymesoda expansa* is primarily composed of calcium carbonate in the aragonite phase [4], one of the three

polymorphs of calcium carbonate—the others being calcite and vaterite. Calcite is stable under ambient conditions, while aragonite is metastable, and vaterite is the least stable. Aragonite's lower stability compared to calcite results in higher solubility, providing a faster dissolution rate of calcium carbonate [5, 6], which enhances calcium availability during HA synthesis. This characteristic gives *Polymesoda expansa* (lokan) shells an advantage in producing higher yields in HA synthesis. Furthermore, aragonite's metastable nature may influence the nucleation and growth of HA crystals [6], potentially leading to unique structural properties that could enhance the material's bioactivity and performance in biomedical applications, such as bone tissue engineering and dental implants.

THEORY/LITERATURE REVIEW

Synthesis of HA can be conducted by various techniques such as dry, wet and the combination of dry and wet methods [7]. Dry method, such as solid-state and mechanochemical synthesis, used the precursors (calcium and phosphate source) in their dry condition to synthesize the HA. The characteristics of powders synthesized through dry methods are not significantly affected by processing parameters and do not require precise control conditions, making them well-suited for mass production [8].

Wet method such as chemical precipitation, hydrothermal and hydrolysis uses aqueous solution for synthesizing HA. This method can control the morphology and size of the HA particle. However, it gives samples with low crystallinity due to low processing temperature [8]. Chemical precipitation methods is conducted by mixing the calcium and phosphate containing reagent at certain desired pH with the temperature ranging from room temperature until the boiling point of water Whereas, hydrothermal method is conducted above the ambient pressure and temperature [7].

Based on the various synthesis methods mentioned earlier, such as dry and wet techniques, researchers have successfully applied these approaches to transform different mollusk shells into hydroxyapatite, taking advantage of their calcium content and structural properties. Vecchio et al. [9] converted small pieces of *Strombus gigas* and *Tridacna gigas* shells into HA using the hydrothermal method. The shells were added to an autoclave filled with $(\text{NH}_4)_2\text{HPO}_4$ solution, sealed, and then heated at different temperatures (180–250 °C) for varying durations (2–20 days). The study revealed that HA structures were formed from these shells in most of the samples at a relatively low temperature of 200°C. The average fracture stress ranged from 137 to 218 MPa for partially converted conch shell samples and from 70 to 150 MPa for both original and converted clam shell samples, values that are comparable to the mechanical strength of compact human bone. These findings suggest that the converted shell samples could be suitable for use as implants in load-bearing applications. Additionally, in-vivo testing demonstrated good biocompatibility and bioactivity of the converted shell implants.

Ahmad et al. [10] synthesized nano-HA from snail shells using calcination and wet chemical precipitation methods. The snail shell powder was heated at 900 °C for 3 hours to convert CaCO_3 into calcium oxide (CaO). Distilled water was then added to the CaO to produce a calcium hydroxide ($\text{Ca}(\text{OH})_2$) solution. Phosphoric acid was added to the solution at a rate of 15-20 drops per minute with continuous stirring at room temperature to produce hydroxyapatite. NH_4OH solution was then added to the mixture until the reaction was completed, maintaining the pH at 8 for 2 hours with constant stirring. A gelatinous white precipitate formed after the stirring was stopped. The solution was then left overnight. The precipitate was rinsed, dried in an oven

at 200 °C, and then sintered at 1000 °C for 4 hours. The results of their study showed that they successfully synthesized nano-HA powders with diameters ranging from 13.3 to 15.2 nm and high antimicrobial activity.

Roslan et al. [11] synthesized HA from powdered *Polymesoda expansa* (lokan) shells using calcination and precipitation methods. Initially, the *Polymesoda expansa* (lokan) shells were calcined at 900°C for 4 hours to convert them into CaO. Subsequently, 2.4 g of the obtained CaO was dissolved in 100 ml of distilled water under constant stirring to form Ca(OH)₂. Phosphoric acid was then added dropwise at a rate of 5.5 ml/min while maintaining continuous stirring. Concentrated ammonia solution (NH₄OH) was also added dropwise to adjust the pH to values of 9 and 13. The resulting solution was allowed to age for 24 hours, after which it was rinsed and filtered. The precipitates were then dried in a hot air oven for 6 hours at 110°C. Finally, the hardened HA was ground into a powdered form using a mortar and pestle. This study demonstrated that the researchers successfully converted the mollusk shells into HA, achieving calcium-to-phosphorus (Ca/P) ratios of 1.78 and 1.97 at pH values of 9 and 13, respectively.

Ni and Ratner [12] converted the nacreous shells of the red abalone gastropod directly into HA using a simple method that did not involve converting them into calcium oxide (CaO) or calcium hydroxide (Ca(OH)₂). In this method, the chips and powdered gastropod nacre shells were soaked in citric-phosphate buffered saline solution at pH 7.4 for periods of 5, 7, and 14 days at room temperature. The researchers found that the shells were successfully converted into HA, and the amount of HA produced increased with the soaking time.

In this study, local *Polymesoda expansa* (lokan) mollusk shells were used to synthesize HA using a phosphate-citrate buffer solution at pH 7.4 and at room temperature. For comparison, the reaction was also conducted hydrothermally in an autoclave under different time and temperature conditions. This method offers a simple procedure that does not involve calcination or the preparation of a calcium hydroxide (Ca(OH)₂) solution. To the best of our knowledge, there are no reports in the literature regarding the conversion of *Polymesoda expansa* (lokan) shells into HA using a citric-phosphate buffer solution.

MATERIALS

Polymesoda expansa (lokan) was obtained from a local market in Marang, Terengganu. Na₂HPO₄ (ACS grade) and citric acid (synthesis grade) were purchased from Merck (Germany).

EXPERIMENTAL

Preparation of *Polymesoda expansa* (lokan) shell powder

Polymesoda expansa (lokan) shells were thoroughly cleaned with tap water, rinsed with RO water, and left to dry at room temperature. The dried shells were then crushed using a mortar and pestle, followed by grinding in a planetary monomill at 600 rpm for 1 hour. The resulting shell powder was used as the calcium source for HA synthesis.

Conversion of *Polymesoda expansa* (lokan) shell into HA

A 200 ml citrate-phosphate buffer solution at pH 7.4 was prepared by mixing 177.8 ml of 0.2 M Na₂HPO₄ solution with 22.2 ml of 0.1 M citric acid. A specific amount of *Polymesoda expansa* (lokan) shell powder was then added to the buffer solution, maintaining a Ca/P ratio of 1.67.

For the room temperature reaction, the mixture was left to react for 2, 4, 10, and 20 days (hereafter referred to as 2D, 4D, 10D, and 20D) to study the effect of different reaction time on the production of HA. For the hydrothermal reaction, the mixture was heated at 100°C and 120°C for 1 to 2 days in a hydrothermal rotating oven. After the reactions were completed, the supernatant was removed, and the precipitate was rinsed with deionized water by centrifuging at 1500 rpm for 5 minutes. This rinsing process was repeated three times, after which the powder was dried in an oven at 60°C for 24 hours.

SAMPLES CHARACTERIZATION

FTIR analysis was performed on a Thermo Nicolet Nexus (UK) spectrophotometer with a resolution of 4 cm⁻¹ in the range of 400–4000 cm⁻¹. The XRD analysis of the powder samples was carried out on Ital Structure APD 2000 X-Ray diffractometer instrument in the 2 θ range of 20–60°, using CuK α radiation (λ = 1.5418 Å) at 40 kV and 30 mA. The relative peak height at the specific peak of XRD diffractogram and FTIR spectra was measured to estimate the crystallinity and percentage conversion of *Polymesoda expansa* (lokan) mollusk shell into HA.

RESULTS AND DISCUSSION

Analysis of raw *Polymesoda expansa* (lokan) shell

FTIR spectrum of raw *Polymesoda expansa* (lokan) shell in Fig. 1 shows bands at around 3435, 2922, 2522, 1787, 1477, 1082, 860 and 713-700 cm⁻¹. The broad band around 3435 cm⁻¹ is assigned to the stretching mode of adsorbed water in the shell [13]. The band at 2922 cm⁻¹ is attributed to the stretching of C-H bonds in proteins, 2522 cm⁻¹ to the OH group in HCO₃⁻, and 1787 cm⁻¹ to the stretching of the carbonyl group in acidic proteins [13]. The bands at 1477 cm⁻¹ corresponds to carbonate ion [14,15]. The bands at 1082 cm⁻¹, 860 cm⁻¹, and 713-700 cm⁻¹ are the characteristic of aragonite carbonate [16, 17].

The XRD pattern of raw *Polymesoda expansa* (lokan) shell in Fig. 2 shows that the shell is composed of calcium carbonate in the aragonite form (Ref code: 98-001-6937), which further confirm the results from FTIR.

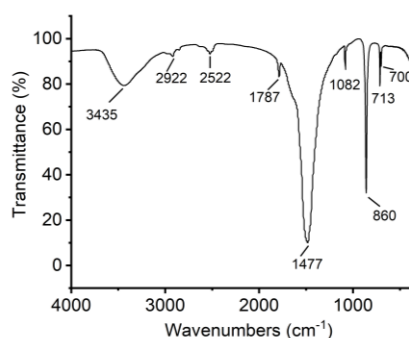


Fig. 1: XRD of raw lokan shell.

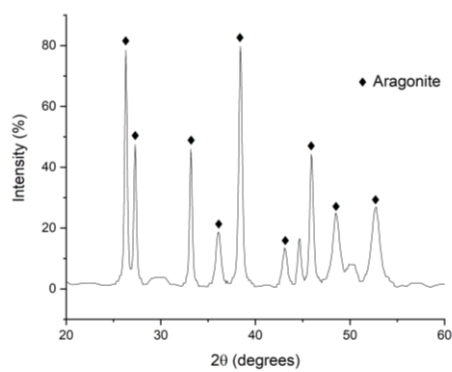


Fig. 2: XRD pattern of raw lokan shell.

FTIR analysis of hydroxyapatite powder

Fig. 3 shows the FTIR spectra of samples synthesized at room temperature. After 2 days of soaking, the sample exhibits bands at 1636, 1029, 962, 603, and 564 cm^{-1} . The band at 1636 cm^{-1} can be attributed to the adsorbed water in HA [18]. The bands at 1029, 962, 603, and 564 cm^{-1} correspond to the PO_4^{3-} group in HA [19]. Meanwhile, the bands assigned to the carbonate ions at 1477, 860 and 713-700 cm^{-1} become less intense, and the band at 1082 cm^{-1} disappears. These observations indicate that HA has formed during the reaction.

HA formation occurs through a dissolution-precipitation mechanism. In this process, Ca^{2+} ions are released from the *Polymesoda expansa* (lokan) shell and react with PO_4^{3-} ions in the solution to form HA, as shown in Eq. 1. As seen in Figure 3, the characteristic HA peak becomes more intense with increased soaking time, while the carbonate ion peaks diminish, indicating that more HA is formed as reaction time increases. At room temperature, the nucleation and growth of HA crystals proceed gradually. Over longer reaction times, more nucleation sites form, allowing the crystals to grow. However, due to the limited kinetic energy at room temperature, this process is slow, leading to the gradual development of HA.

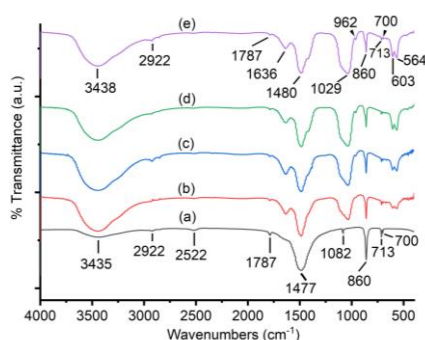
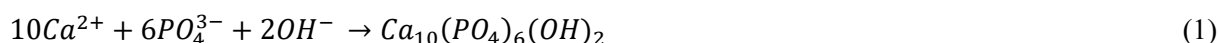


Fig. 3: FTIR spectra of (a) raw lokan shell; and samples synthesized at room temperature for (b) 2 days (c) 4 days (d) 10 days (e) 20 days.

In contrast, the FTIR spectra of samples synthesized using the hydrothermal method (Fig. 4) show a more intense HA peak and weaker carbonate ion bands compared to those synthesized at room temperature. This suggests that the hydrothermal method enhances the formation of more crystalline and purer hydroxyapatite. The elevated temperature and pressure during hydrothermal synthesis accelerate the nucleation and growth of HA crystals [6], resulting in a

more stable and well-defined structure. Additionally, these conditions improve calcium solubility, ensuring a more complete reaction and higher yield. As a result, the hydrothermal process is more effective in producing high-quality HA.

To quantify these findings, a detailed analysis of the FTIR spectra provides insights into the degree of HA formation and purity, as shown in Tables 1 and 2. By examining the relative peak intensities, we can assess the extent of crystallinity [19], HA formation, and the reduction of carbonate content in the samples.

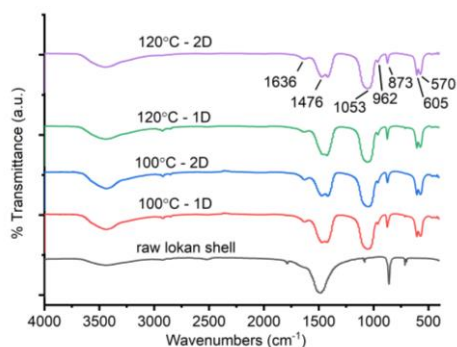


Fig. 4: FTIR spectra of raw lokan shell and samples synthesized at 100 and 120 °C for 1 and 2 days using hydrothermal method.

Table 1 shows that the relative peak heights for the PO_4^{3-} group at 1029, 962, 603, and 564 cm^{-1} increase with reaction time at room temperature (from 2D to 20D) and under hydrothermal conditions (100°C to 120°C for 1D and 2D). The increasing phosphate peak intensities indicate the formation and crystallization of HA as the reaction progresses. For the room temperature reactions, the data demonstrate that longer reaction durations enhance HA crystallinity, as seen in the increasing peak heights of the PO_4^{3-} group. For example, the peak at 1029 cm^{-1} rises from 35.24 (2D) to 70.22 (20D). Similar trends are observed for the other phosphate-related peaks (962, 603, and 564 cm^{-1}), reflecting the gradual formation of HA over time.

In contrast, the hydrothermal reactions exhibit a significant increase in relative peak heights, even over shorter reaction durations (1 to 2 days). The sample treated at 120°C for 1 day (120°C 1D) shows the highest relative peak height at 1029 cm^{-1} (79.99). This suggests that hydrothermal conditions promote faster HA formation compared to room temperature reactions, where 20 days are needed to achieve similar results.

Table 2: Relative peak height for bands assigned to PO_4^{3-} group in HA

Samples	Relative peak height for bands assigned to PO_4^{3-} group			
	1029 cm^{-1}	962 cm^{-1}	603 cm^{-1}	564 cm^{-1}
Lokan raw	-	-	-	-
2D	35.24	1.44	5.73	8.92
4D	62.49	2.01	10.46	12.67
10D	65.86	5.28	16.75	15.05
20D	70.22	4.82	18.12	17.23
100°C 1D	64.84	6.06	20.22	20.43
100°C 2D	62.23	5.80	17.62	20.97

120°C 1D	79.99	5.25	20.56	18.77
120°C 2D	78.12	4.56	16.87	20.51

Table 2 shows that the relative peak heights for the carbonate group (CO_3^{2-}) at 1082, 860, 713, and 700 cm^{-1} diminish as the reaction progresses. This reduction in carbonate peaks reflects successful decarbonation, a key process in transforming calcium carbonate (CaCO_3) from mollusk shells into HA. For samples prepared at room temperature, there is a noticeable decrease in carbonate peaks with increasing reaction duration. For example, the peak at 860 cm^{-1} decreases from 41.27 (2D) to 37.87 (20D), indicating the ongoing removal of carbonate species, which is essential for forming pure HA. However, reactions at room temperature require extended durations (up to 20 days) to achieve significant decarbonation. In contrast, for samples prepared under hydrothermal conditions, the carbonate peaks decrease more rapidly. For instance, the relative peak height at 860 cm^{-1} drops to 29.58 for the 100°C 1D sample and further to 23.40 for the 120°C 2D sample, confirming that higher temperatures expedite decarbonation and lead to the formation of purer HA with fewer carbonate impurities.

Table 3: Relative peak height for bands assigned to CO_3^{2-} group in calcium carbonate

Samples	Relative peak height for bands assigned to CO_3^{2-} group			
	1082 cm^{-1}	860 cm^{-1}	713 cm^{-1}	700 cm^{-1}
Lokan raw	4.66	65.98	15.39	6.50
2D	-	41.27	7.28	3.21
4D	-	38.33	6.55	2.50
10D	-	37.66	5.44	2.37
20D	-	37.87	5.19	2.58
100°C 1D	-	29.58	3.16	-
100°C 2D	-	27.39	-	-
120°C 1D	-	31.64	2.79	-
120°C 2D	-	23.40	-	-

XRD analysis of hydroxyapatite powder

Fig. 5 shows the XRD patterns of samples synthesized at room temperature. After 2 days of soaking, the peaks assigned to aragonite at $2\theta = 26.28$, 27.27 , and 38.40 become less intense, while the peak at $2\theta = 33.16$ disappears. Notably, a new peak at around $2\theta = 31.78$, corresponding to hydroxyapatite (HA), appears. These observations indicate the formation of the HA phase in the samples. After 10 and 20 days of soaking, the peak at $2\theta = 27.27$ disappears, and the intensity of the peak at $2\theta = 31.78$ increases. This reveals that the amount of the HA phase increases while the amount of calcium carbonate decreases as reaction time extends.

Fig. 6 presents the XRD patterns of samples synthesized using the hydrothermal method. After 1 day of reaction at 100 °C, the aragonite peaks at $2\theta = 26.28$, 27.27 , 33.16 , 36.07 , 38.40 , 45.90 , and 48.5 disappear, while new peaks corresponding to HA at $2\theta = 25.58$, 31.8 , 39.9 , 42.12 , 46.66 , and 49.28 emerge. The intensity of the HA peak at $2\theta = 31.78$ increases with rising temperature and reaction time. Compared to the reaction at room temperature, the hydrothermal method

produces XRD peaks of higher intensity, indicating a greater formation of the HA phase through this method.

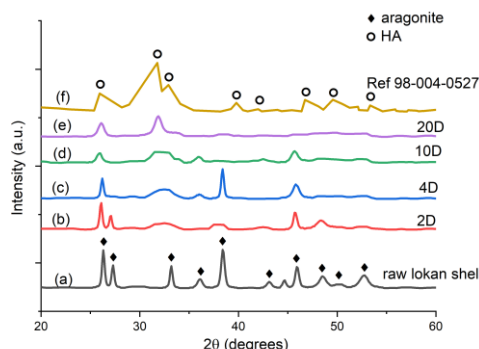


Fig. 5: XRD patterns of (a) raw lokan shell; (b-e) samples synthesized at room temperature for 2, 4, 10 and 20 days respectively; and (f) standard HA with Ref. No 96-004-0527.

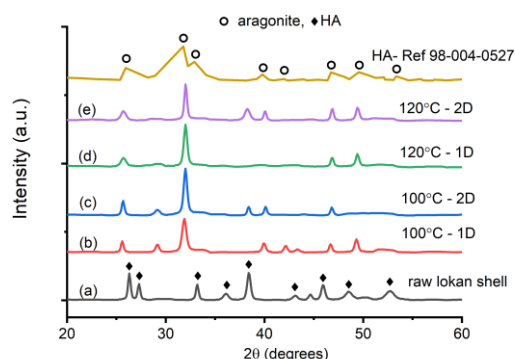


Fig. 6: XRD patterns of raw lokan shell and samples synthesized at 100 and 120 °C for 1 and 2 days using hydrothermal method.

To further elucidate these findings, a quantitative analysis of the XRD data was performed. By measuring the relative peak heights [19], we can obtain information regarding the phase composition and crystallinity of HA in the synthesized samples. Table 3 presents the relative peak heights from XRD diffractograms at various 2θ values (25.58° , 31.78° , 46.66° , and 49.28°), which correspond to key diffraction peaks associated with the HA phase under different synthesis conditions.

The gradual increase in peak intensities with reaction time (from 2D to 20D) indicates that prolonged exposure at room temperature promotes the slow crystallization of HA. However, the absence of certain peaks (46.66° and 49.28°) under these conditions suggests that the HA structure remains incomplete, with fewer crystallographic orientations formed.

On the contrary, hydrothermal treatments at 100°C and 120°C result in much sharper and more intense peaks, indicating rapid and complete crystallization of HA. The presence of peaks at 46.66° and 49.28° confirms that hydrothermal conditions allow the formation of more fully developed HA crystals with multiple orientations, leading to a purer and more crystalline HA structure. While both 100°C and 120°C conditions produce strong HA peaks, the 100°C samples tend to have higher peak intensities at certain angles (e.g., 31.78° for 100°C 2D). This suggests that 100°C may be the optimal temperature for promoting crystallization in a shorter reaction time. However, the overall trend suggests that temperature results in highly crystalline HA, with minor differences in peak intensities.

Table 4: Relative height for peak assigned to HA phase

Samples	Relative height of peak assigned to HA phase			
	2 θ 25.58	2 θ 31.78	2 θ 46.66	2 θ 49.28
2D	-	13.55	-	-
4D	-	18.74	-	-
10D	18.67	17.92	-	-
20D	26.35	33.13	-	-
100°C 1D	32.00	89.88	22.42	35.96
100°C 2D	41.57	126.44	23.19	2.09
120°C 1D	23.93	116.43	24.10	33.46
120°C 2D	23.83	97.83	31.89	34.55

CONCLUSION

The FTIR and XRD analyses confirmed the successful formation of hydroxyapatite (HA), with FTIR revealing characteristic phosphate bands and diminishing carbonate peaks, and XRD showing the disappearance of aragonite and the emergence of HA peaks. Hydrothermal synthesis was found to produce higher crystallinity and purer HA more rapidly than room temperature methods, where HA forms more gradually. Limitations include the longer reaction times required for room temperature synthesis, incomplete crystallization, and the need for additional characterization techniques. Future work should focus on optimizing hydrothermal conditions, advanced material characterization such as SEM and BET, investigating biocompatibility, and exploring scalable production methods for HA.

ACKNOWLEDGEMENTS: We are very grateful to Universiti Putra Malaysia for supporting us by providing Research University Grant Scheme [RUGS; vot No. 9199619].

REFERENCES

- [1] Prameetha George Ittycheria, Thomas George, Mathew John, G. Meenu, Vimal Thomas, S. Aswathy, R. K. and J. T. Application of Hydroxyapatite in Regenerative Dentistry. In *Novel Biomaterials for Tissue Engineering*; Petrica Vizureanu and Madalina Simona Baltatu, Ed.; IntechOpen, 2024.
- [2] Zuliantoni, Z.; Suprpto, W.; Setyarini, P. H.; Gapsari, F. Extraction and Characterization of Snail Shell Waste Hydroxyapatite. *Results Eng.* 2022, 14 (February), 100390. <https://doi.org/10.1016/j.rineng.2022.100390>.
- [3] Topić Popović, N.; Lorencin, V.; Strunjak-Perović, I.; Čož-Rakovac, R. Shell Waste Management and Utilization: Mitigating Organic Pollution and Enhancing Sustainability. *Appl. Sci.* 2023, 13 (623). <https://doi.org/10.3390/app13010623>.
- [4] Abdullah, N. H.; Xian, O. J.; Yi, C. Z.; Yuan, N. S.; Yaacob, M. S. S.; Salim, N. A. A.; Ahmad, N.; Lazim, Z. M.; Nuid, M.; Abdullah, F. Removal of Phosphate from Synthetic Wastewater by Using Marsh Clam (*Polymesoda Expansa*) Shell as an Adsorbent. *Biointerface Res. Appl. Chem.* 2023, 13 (1), 1–12. <https://doi.org/10.33263/BRIAC131.056>.
- [5] Park, W.; Kamitakahara, M.; Nagamori, T.; Ioku, K. Effect of Synthetic Conditions on Morphology and Composition of Carbonate-Containing Hydroxyapatite Hydrothermally

- Synthesized From Calcium Carbonate. *Phosphorus Res. Bull.* 2011, 25, 72–77. <https://doi.org/10.3363/prb.25.72>.
- [6] Kamitakahara, M.; Nagamori, T.; Yokoi, T.; Ioku, K. Carbonate-Containing Hydroxyapatite Synthesized by the Hydrothermal Treatment of Different Calcium Carbonates in a Phosphate-Containing Solution. *J. Asian Ceram. Soc.* 2015, 3 (3), 287–291.
- [7] Mohd Pu'ad, N. A. S.; Abdul Haq, R. H.; Mohd Noh, H.; Abdullah, H. Z.; Idris, M. I.; Lee, T. C. Synthesis Method of Hydroxyapatite: A Review. *Mater. Today Proc.* 2020, 29 (November 2018), 233–239.
- [8] Sadat-Shojai, M.; Khorasani, M. T.; Dinpanah-Khoshdargi, E.; Jamshidi, A. Synthesis Methods for Nanosized Hydroxyapatite with Diverse Structures. *Acta Biomater.* 2013, 9 (8), 7591–7621.
- [9] Vecchio, K. S.; Zhang, X.; Massie, J. B.; Wang, M.; Kim, C. W. Conversion of Bulk Seashells to Biocompatible Hydroxyapatite for Bone Implants. *Acta Biomater.* 2007, 3 (6), 910–918.
- [10] Ahmed, H. Y.; Safwat, N.; Shehata, R.; Althubaiti, E. H.; Kareem, S.; Atef, A.; Qari, S. H.; Aljahani, A. H.; Al-Meshal, A. S.; Youssef, M.; Sami, R. Synthesis of Natural Nano-Hydroxyapatite from Snail Shells and Its Biological Activity: Antimicrobial, Antibiofilm, and Biocompatibility. *Membranes* (Basel). 2022, 12 (4). <https://doi.org/10.3390/membranes12040408>.
- [11] Roslan, M. R.; Nasir, N. F. M.; Gilani, M. A.; Mohammad, N. F.; Cheng, E. M.; Khalid, M. F. A.; Zoolfakar, A. S.; Amin, N. A. M.; Khan, S. F. Preliminary Study of the Polymesoda Expansa Based Hydroxyapatite for Medical Devices Coating Application. *AIP Conf. Proc.* 2020, 2306 (December). <https://doi.org/10.1063/5.0032391>.
- [12] Ni, M.; Ratner, B. D. Nacre Surface Transformation to Hydroxyapatite in a Phosphate Buffer Solution. *Biomaterials* 2003, 24 (23), 4323–4331. [https://doi.org/10.1016/S0142-9612\(03\)00236-9](https://doi.org/10.1016/S0142-9612(03)00236-9).
- [13] Verma, D.; Katti, K.; Katti, D. Photoacoustic FTIR Spectroscopic Study of Undisturbed Nacre from Red Abalone. *Spectrochim. Acta. A. Mol. Biomol. Spectrosc.* 2006, 64 (4), 1051–1057. <https://doi.org/10.1016/j.saa.2005.09.014>.
- [14] Balmain, J.; Hannoyer, B.; Lopez, E. Fourier Transform Infrared Spectroscopy (FTIR) and X-Ray Diffraction Analyses of Mineral and Organic Matrix during Heating of Mother of Pearl (Nacre) from the Shell of the Mollusc Pinctada Maxima. *J. Biomed. Mater. Res.* 1999, 48 (5), 749–754.
- [15] Florek, M.; Fornal, E.; Gómez-Romero, P.; Zieba, E.; Paszkowicz, W.; Lekki, J.; Nowak, J.; Kuczumow, A. Complementary Microstructural and Chemical Analyses of Sepia Officinalis Endoskeleton. *Mater. Sci. Eng. C* 2009, 29 (4), 1220–1226.
- [16] Chakrabarty, D.; Mahapatra, S. Aragonite Crystals with Unconventional Morphologies. *J. Mater. Chem.* 1999, 9 (11), 2953–2957.
- [17] Singh, K. S.; Sawant, S. G. Identification of CaCO₃ Polymorphs of Shellfish by FTIR Spectroscopy and Evaluation of Metals Adsorption by Powdered Exoskeleton Shell. *Indian J. Geo-Marine Sci.* 2022, 51 (4), 304–309.
- [18] Abifarín, J. K.; Obada, D. O.; Dauda, E. T.; Dodoo-Arhin, D. Experimental Data on the Characterization of Hydroxyapatite Synthesized from Biowastes. *Data Br.* 2019, 26, 104485.
- [19] Sahadat Hossain, M.; Ahmed, S. FTIR Spectrum Analysis to Predict the Crystalline and Amorphous Phases of Hydroxyapatite: A Comparison of Vibrational Motion to Reflection. *RSC Adv.* 2023, 13 (21), 14625–14630.

Thermogravimetric analysis (TGA) of biochar and the paste made from Prosopis Africana biomass Material

Suleiman Babani^{1,3*}, Mohd Nizar Hamidon^{1,2*}, Alyani Ismail², Haslina Jaafar², Intan Helina Hasan¹, Zainab Yunusa^{3,4}, Jamila Lamido^{1,3}, Ismail Lawal¹, Muhammad Aliyu¹

¹ Institute of Nanoscience & Nanotechnology (ION2), Universiti Putra Malaysia, 43400 UPM Serdang, Selangor, Malaysia

² Faculty of Engineering, Universiti Putra Malaysia, 43400 UPM Serdang, Selangor, Malaysia

³ Department of Electrical Engineering, Faculty of Engineering, Bayero Universiti Kano, PMB 3011 Kano, Nigeria.

⁴Department of Electrical Engineering University of Hafr Al Batin, 39524 Kingdom of Saudi Arabia KSA.

*Corresponding author's phone: +60196648600 / +60104260737

E-mail: mnh@upm.edu.my / sbabani.ele@buk.edu.ng

Abstract: This study aimed to investigate the thermal stability of biochar and paste made from Prosopis Africana biomass material using Thermogravimetric Analysis (TGA). The study was conducted using a Mettler Toledo TGA/DSC1 instrument, with samples heated from 25 °C to 800 °C at a rate of 10 °C/min with and without airflow atmosphere. The temperature was reported to influence weight loss. The TGA results showed better thermal stability of biochar without airflow up to 700 °C as compared to that of the stability with airflow. On the other hand, the onset decomposition for the paste in both conditions did not show any significant difference until 500 oC. This study highlights the potential of Prosopis Africana biomass as a sustainable source of biochar and paste materials and the importance of TGA in the study of the thermal stability of materials.

Keywords: Prosopis Africana, Biomass, Thermogravimetric analysis (TGA), linseed stand oil, m-xylene, α - terpineol.

INTRODUCTION

Thermogravimetric Analysis (TGA) is a technique used to analyze the thermal behavior of materials. It is widely used in the study of biochar, which is a type of charcoal made from biomass. Prosopis Africana is a tree species that is common in Africa and has been used for fuel and other purposes for centuries. The combustion of this biomass produces biochar as a fuel and a paste that can also be used as an electronic application. In this study, the TGA analysis of both biochar and the paste made from Prosopis Africana biomass combustion can provide insights into the thermal behavior of these materials, which can help in optimizing their production processes and identifying potential applications.

Biochar has gained increasing attention in recent years as a promising material for a variety of applications. Its properties, such as high carbon content, porosity, and stability, make it an attractive candidate for soil amendment, carbon sequestration, and energy production. TGA has been widely used to study the thermal behavior of biochar, which can provide valuable information about its thermal stability and decomposition behavior.

Carbonaceous materials, such as graphite, carbon nanotubes, nanodiamonds, carbon alloys, and activated carbon, are widely recognized for their substantial surface area, excellent electrical

conductivity, and cost-effectiveness [1]. Recently, porous carbon has been extensively investigated for its thermal behavior as a material.

For the last few years, carbon nanomaterials have been widely used in the electronics industry. It has been demonstrated that carbon nanomaterials have electrical and mechanical properties that are comparable to metals [2]. Among these carbon materials, CNT [3], graphene, [4], carbon black [5] e.t.c have gained significant attention due to their exceptional electrical and mechanical properties and low cost. These carbon materials have numerous applications, including RFID tag antennas, sensors, and photonics. In the present work, to the best of my knowledge does not report elsewhere, the combustion behaviors of P. Africana lignin in biochar and paste are investigated with thermogravimetric analysis (TGA), and the characteristics of the thermal degradation at different forms. In this study of TGA is for antenna application from the porous carbon or advantages of porous carbon that can be exploited to be used in specific applications like supercapacitors, batteries, sensors, and antennae. In this work, a new PAC biomass of powder and paste with an organic vehicle made from linseed oil is proposed and this has never been done before.

METHOD AND MATERIAL

Biochar and paste made from *Prosopis Africana* biomass material were subjected to TGA using a Mettler Toledo TGA/DSC1 instrument. The samples were obtained locally from sub-Saharan Africa in Nigeria and burned out from a warehouse locally by blacksmiths. The blacksmith's producer carbonized the *Prosopis Africana* wood to create carbon charcoal locally.

After selecting the pieces of charcoal with the least resistance to electricity to produce a higher conductivity, once chosen the most conductive pieces of charcoal, the next step is to crush them with a mortar and pestle and then sieve with an average particle size $<20\ \mu\text{m}$ to obtain the micron-sized powder used as the active material, fig. 1 shown the procesess of obtaining the biochar.

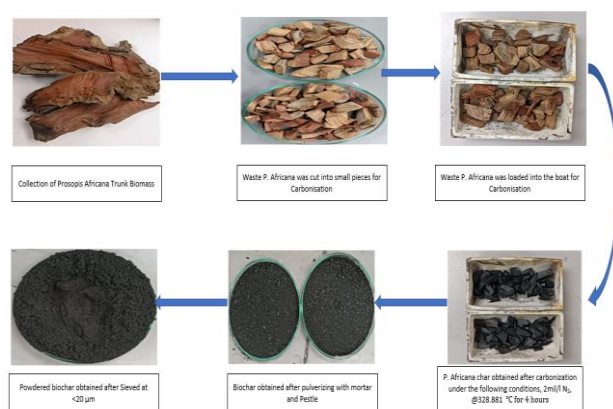


Fig. 1: Process of obtained the Biochar from Biomass Material.

The PAC biochar was weighed to the desired weight and mixed with a prepared binder composed of linseed stand oil, m-xylene, and α -terpineol. The binder was first mixed by combining 85 wt% linseed stand oil and 12.5 wt% m-xylene using a magnetic stirrer at 250 rpm for 3 hours, followed by the addition of 2.5 wt% α -terpineol and further stirring for 2 hours

while maintaining the temperature at 40°C. The weight ratio of the components of the binder was based on the previous study carried out by [6], [7].

Table I: Chemicals and Ratio Used in Binder Preparation

Binder made with linseed oil	wt (%)
Linseed stand oil	85
M- xylene	12.5
Alpha - terpineol	2.5

The weight ratio of *Prosopis africana* biochar and the binder is set with the amount of 40 wt% of char and 60 wt% of the binder. The mixture is then stirred using a magnetic stirrer with the speed of 300 rpm at 40°C for 24 hours to obtain a homogeneous paste [8], [9], [10].

RESULTS AND DISCUSSION

Thermal characteristics of *Prosopis Africana* biochar with and without airflow

The TGA of PAC powder in the absence of airflow shows an initial weight decrease caused by moisture absorption. After the weight loss of 10 % occurs at 108°C, the sample indicates considerable stability, followed by the decomposition at 740°C. A total weight loss of 15% was observed in the PAC biomass due to the thermal decomposition of the carbon content. The finding is similar to the work reported [11], [12].

Meanwhile, the TGA of *P. Africana* powder with airflow represents two weight loss stages. The first stage indicates the decomposition of moisture content in the biomass with 10% weight loss at 109 °C. The next stage is the combustion of the complex and thermally stable structure that takes place from 450 °C. The major weight loss of 97 % was observed at 750 °C which describes the oxidation of the carbon content in biochar. Both the TGA plots have been popularly applied to determine the composition of water, volatile compounds, combustible carbon, and impurities in PAC and its related materials [13].

The thermal degradation behavior of *P. juliflora* char, an invasive species, was investigated in a TG furnace over a temperature range of normal to 800°C [14]. The thermal degradation process was found to occur in three distinct stages. The first stage corresponds to the drying process, followed by a devolatilization stage, and finally, the third stage indicates the formation of carbonaceous residue. *P. juliflora* demonstrated a greater weight loss percentage when subjected to pyrolysis temperatures ranging between 200°C and 500°C. Fig. 2 shown the TGA of *prosopis africana* biomass power with and without airflow.

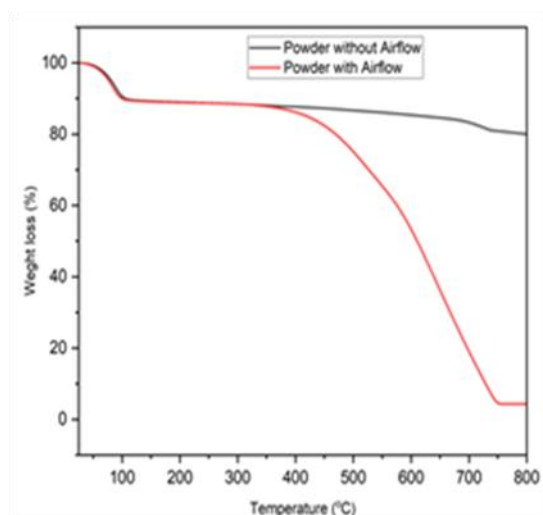


Fig. 2: TGA of Prosopis Africana of Biomass Powder with and without airflow.

Thermal characteristics of Prosopis Africana Paste with and without airflow

The TGA profile in fig. 3, shows that the paste of PAC without air flow oxidized in two stages, The first stage shows the decomposition of volatile matters which comprised m-xylene and alpha-terpineol at 100oC with 5 % weight loss, and whereas the second stage of decomposition could be attributed to the non-volatile matters which is the linseed stand oil. The carbon residue from biochar observed from 490 to 800 oC signifies the major decomposition contributed by the organic binder. This is in accordance to the finding from a similar work with graphite [9].

On the other hand, the heating of the paste of PAC in airflow shows the oxidation in three stages, Similar to the sample without airflow, the first and second stages of decomposition was due to the evaporation of volatile and non-volatile matters in linseed stand oil binder. However, the degradation in airflow was further occurred up to 660°C, leaving only 0.7% of residue. This finding could be related to the decomposition of the carbon content in biochar as the higher concentration of oxygen could accelerate the oxidation and therefore the decomposition. It is similar to values reported for the TGA of CNT [15]. Fig 3 shown the TGA of Prosopis africana paste with and without airflow.

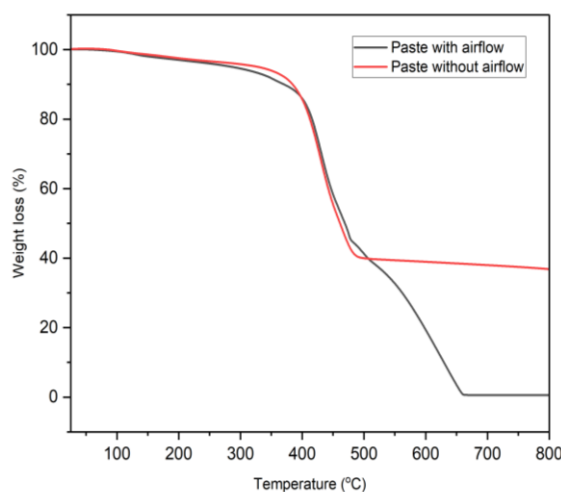


Fig. 3: TGA of Prosopis Africana of Paste with and without airflow.

CONCLUSION

This study shows the potential of PAC biomass as a sustainable source of biochar and paste material. The TGA results showed that biochar prepared from PAC has good thermal stability with minimal weight loss up to 800 °C without airflow whereas the degradation is accelerated with the increase in the oxygen concentration. This indicates that these materials can withstand high temperatures and have potential applications at high-temperatures in ambient. The thermal stability of biochar and paste made from *Prosopis Africana* biomass combustion is an important factor in their potential applications, such as soil improvement and carbon sequestration. with airflow the oxidation process happens when exposed to air and is not stable at open airflow also, its combustion reaction occurs. It broke the carbon bonding due to the air it turned to ash at 0% loss at 600°C no carbon residue left. More degradation happens with airflow and its consumed more energy and heat. While without airflow It terminates at a low temperature means no oxygen in the process the degradation of decomposition is stable at temperatures around 490°C and terminates carbon residue. Further research is needed to investigate the properties and applications of these materials in detail.

ACKNOWLEDGEMENTS: This work was funded by the Petroleum Technology Development Fund (PTDF), Nigeria, for financial support, and the Institute of Nanoscience and Nanotechnology (ION2), Universiti Putra Malaysia (UPM), Malaysia.

REFERENCES

- [1] M. N. Hamidon et al., “Morphology and Electrical Properties of Pristine and Composite rice husk ash Nano / Microparticles thick films for Gas Sensing Applications,” pp. 4–7, 2023.
- [2] N. H. A. Aziz, H. Jaafar, R. M. Sidek, S. Shafie, and M. N. Hamidon, “Raman Study on Dispersion of Carbon Nanotube in Organic Solvent as The Preparation of Conductive Nano-Ink,” *Proceedings of the 2019 IEEE Regional Symposium on Micro and Nanoelectronics, RSM 2019*, pp. 53–56, 2019.
- [3] K. P. Gopinath, D.-V. N. Vo, D. Gnana Prakash, A. Adithya Joseph, S. Viswanathan, and J. Arun, “Environmental applications of carbon-based materials: a review,” *Environmental Chemistry Letters*, vol. 19, no. 1, pp. 557–582, 2021.
- [4] M. Asnawi, S. Azhari, M. N. Hamidon, I. Ismail, and I. Helina, “Synthesis of Carbon Nanomaterials from Rice Husk via Microwave Oven,” *Journal of Nanomaterials*, vol. 2018, p. 2898326, 2018.
- [5] F. Ruiz-Perez, S. M. López-Estrada, R. V Tolentino-Hernández, and F. Caballero-Briones, “Carbon-based radar absorbing materials: A critical review,” *Journal of Science: Advanced Materials and Devices*, vol. 7, no. 3, p. 100454, 2022.
- [6] S. Babani, M. Nizar, H. Alyani, I. Haslina, J. Intan, and H. Hassan, “Development and characterization of screen - printed *Prosopis Africana* Char thick film for electronic applications,” *Journal of the Australian Ceramic Society*, no. 0123456789, 2024.
- [7] I. H. Hasan et al., “YIG Thick Film as Substrate Overlay for Bandwidth Enhancement of Microstrip Patch Antenna,” *IEEE Access*, vol. 6, pp. 32601–32611, 2018.
- [8] S. Babani, M. N. Hamidon, A. Ismail, H. Jaafar, A. A. Bakar, and I. Lawal, “Impact of Micrometer and Nanometer-Sized Particles on the Electrical Properties of *Prosopis Africana* Biochar Thick Films,” vol. 2023, pp. 97–100, 2023.
- [9] I. H. Hassan, “PREPARATION AND CHARACTERIZATION OF NANOSIZED GRAPHITE BASED THICK FILM FOR FLEXIBLE ELECTRONICS Intan,” *Solid State Science and Technology*, vol. 26, no. 2, pp. 50–56, 2018.
- [10] F. N. Shafiee, “Effect of nanometric and micronic particles size on physical and electrical properties of graphite thick film Mohd Nizar Hamidon * Mohd Haniff Wahid Abdul Halim

- Shaari Mehmet Ertugrul Nor Hapishah Abdullah and Mohd Asnawi Mohd Kusaimi Muhammad Syazwan Mus,” vol. 17, pp. 825–839, 2020.
- [11] F. A. Ahangar, U. Rashid, J. Ahmad, T. Tsubota, and A. Alsalmeh, “Conversion of waste polyethylene terephthalate (Pet) polymer into activated carbon and its feasibility to produce green fuel,” *Polymers*, vol. 13, no. 22, 2021.
- [12] D. Zhang, X. Lin, Q. Zhang, X. Ren, W. Yu, and H. Cai, “Catalytic pyrolysis of wood-plastic composite waste over activated carbon catalyst for aromatics production: Effect of preparation process of activated carbon,” *Energy*, vol. 212, p. 118983, 2020.
- [13] I. G. Shitu et al., “Effects of irradiation time on the structural, elastic, and optical properties of hexagonal (wurtzite) zinc oxide nanoparticle synthesised via microwave-assisted hydrothermal route,” *Optical and Quantum Electronics*, vol. 56, no. 2, p. 266, 2023.
- [14] Z. Kiflie, M. Solomon, and S. K. Kassahun, “Statistically optimized charcoal production from *Prosopis juliflora* for use as alternative fuel in cement factories,” *Biomass Conversion and Biorefinery*, vol. 13, no. 3, pp. 1539–1552, 2023.
- [15] V. D. Phadtare, V. G. Parale, G. K. Kulkarni, N. B. Velhal, H. H. Park, and V. R. Puri, “Screen printed carbon nanotube thick film on alumina substrate,” *Ceramics International*, vol. 43, no. 5, pp. 4612–4617, 2017.

ENERGY HARVESTING/ ENERGY STORAGE

One-Pot Functionalisation of Hydrothermally Reduced Graphene Oxide using *Garcinia mangostana* Peel Extract for Supercapacitors

Mohamad Aliff Bin Ali Rahman¹, Omar Faruqi Bin Marzuki^{1,2}, Alvin Lim Teik Zheng^{1,2}, Kwok Feng Chong^{3,4}, and Ellie Yi Lih Teo^{1,2*}

¹Institute of Ecosystem Science Borneo, Universiti Putra Malaysia, 98007 Bintulu, Sarawak, Malaysia

²Department of Science and Technology, Faculty of Humanities, Management, and Science, Universiti Putra Malaysia 97008 Bintulu, Sarawak, Malaysia

³Faculty of Industrial Sciences and Technology, Universiti Malaysia Pahang Al-Sultan Abdullah, 26300 Kuantan Pahang Darul Makmur, Malaysia

⁴Centre for Advanced Intelligent Materials, Universiti Malaysia Pahang Al-Sultan Abdullah, 26300, Kuantan, Pahang Darul Makmur, Malaysia

*Corresponding author's phone: +6086-855849

E-mail: ellie_teo@upm.edu.my

Abstract: The fabrication of high-quality graphene has long been sought, leading to the development of various synthesis pathways. One popular route is the chemical synthesis of graphene oxide (GO) followed by hydrothermal reduction to produce highly reduced graphene oxide (rGO) with good electrochemical activity. In order to avoid harsh conditions and toxic reagents, a green approach using *Garcinia mangostana* peel extract as an additive for hydrothermal reduction has been proposed. The GO precursor was synthesised *via* a modified Hummers' method and reduced hydrothermally at 180 °C for six hours. The UV-Vis, FTIR, and Raman analyses were used to characterise the effects of adding the peel extract on the reduction of GO. It was revealed that the modified rGO had a higher oxygen content and fewer structural defects than the unmodified rGO. This resulted in a significant increase in specific capacitance (C_{sp}) from 75.98 F g⁻¹ to 175.48 F g⁻¹ at 20 mV s⁻¹, showing a two-fold improvement from the unmodified product. This study demonstrates that *G. mangostana* peel extract can enhance the synthesis of hydrothermal rGO, offering a scalable and non-toxic reagent to fabricate an electroactive rGO material for supercapacitor applications.

Keywords: Mangosteen peel; hydro-thermal, reduced graphene oxide; highly oxidised; supercapacitor

INTRODUCTION

The fabrication of high-quality graphene and its derivatives has rapidly matured ever since its discovery. In particular, chemical synthesis via oxidation and reduction has been widely used to synthesise GO and rGO. Hydrazine hydrate and sodium borohydride are some of the commonly used reducing agents for the chemical reduction of GO [1]. However, the toxic nature of these popular reductants became a concern which resulted in growing interest towards the adoption of environmentally friendly methodologies as alternatives.

LITERATURE REVIEW

Hydrothermal reduction has been a go-to technique because of its low cost and scalability in producing rGO. However, it is difficult to precisely tune graphene's microstructures such as structural defects and its morphology [2]. Previously, different hydrothermal parameters have been studied to improve the quality of the hydrothermal rGO products [3]. However, little effects were reported in mitigating the defect formation and layer aggregation. Recently,

chemical-aided reactions have been introduced to resolve such limitations. Previously, Zhou et al. reported the use of glucose during the reduction of NiO-graphene nanosheet to produce a high surface area material with low defects with little observable particle agglomeration [4]. Other green additives have also been proposed such as metal salts as templates to synthesise 3D-porous graphene with stable and rigid microstructures as well as fewer defect levels [5].

Inspired by Gopalakrishnan et al. [6], the peel extract of *G. mangostana* shows potential in reducing GO into high-quality graphene using the hydrothermal method. The fruit is rich in metabolites such as phenolic acid, terpenoids, tannic acid, and flavonoids with previous successes in reducing metal nanoparticles [7]. To the best of our knowledge, the study on the application of *G. mangostana* peel extract as a green additive for the chemical reduction of GO is still limited. Therefore, the objective of this study was to investigate the utilisation of *G. mangostana* peel extract in the hydrothermal reduction of GO and its effects on the electrochemical performance of supercapacitors.

MATERIALS

All chemicals except graphite, commercially purchased from Merck, Sigma-Aldrich, Bendosen Chemicals, and HmbG Chemicals, were used without purification. Deionised water and distilled water are referred to as DI water and water in this study. Mature mangosteen fruit was sourced from a local fruit market in Puchong, Selangor (Malaysia).

EXPERIMENTAL

Preparation of Mangosteen Peel Extract

The mangosteen fruit was washed with water and wiped dry to remove any dirt or foreign materials. The fruit was processed by separating the flesh and peel wastes before the extraction. Next, the fruit peels were cut and dried under indirect sunlight for three hours, followed by oven-drying overnight at 55 °C. The dried peels were ground, packed into zip-lock bags, and stored in a -14 °C freezer with aluminium foils to prevent freeze burns. Prior to use, the powder was thawed to remove any ice formed during the storage.

A fresh peel extract was prepared using a modified reflux extraction method [8]. 6.00 g of the peel powder was weighed and transferred into a 500-mL boiling flask with 200 mL DI water. The mixture was refluxed at 60 °C for an hour and cooled before the liquid was decanted into centrifuge tubes and centrifuged at 4000 rpm for 10 minutes to separate any sediments. The supernatant was filtered and stored at 0 °C for a maximum of two weeks.

Synthesis of Modified Reduced Graphene Oxide

Graphene oxide was prepared *via* the modified Hummers' method described by Lee *et al.* [9]. The dried GO product was ground using an agate mortar pestle to form GO powder. Hydrothermal reduction of GO was carried out using a modified method from Johra and Jung [10]. The methodology was applied using the peel extract to produce the modified rGO, classified as 6HT-MWrGO and 6HT-rGO (unmodified) respectively.

Material Characterisation

The optical property was analysed using the Scinco S-3100 UV-visible spectrophotometer in a wavelength region of 200 to 800 nm. A quantitative Fourier-transform infrared (FTIR) analysis was measured using the Perkin Elmer Spectrum 100 spectrometer in a wavenumber region of

400 to 4000 cm^{-1} , prepared by the KBr pellet technique with a fixed ratio between GO and KBr of 1:74. Defect analysis was investigated *via* Raman analysis using the Witec Alpha 300R with an excitation laser of 531.94 nm, analysed in the wavenumber range of 0 to 4000 cm^{-1} .

Electrochemical Analysis

The electrodes used to evaluate the electrochemical performance of 6HT-rGO and 6HT-MWrGO are prepared based on [11]. Their performance was assessed using a three-electrode system consisting of the working electrode (rGO-coated Ni-foam), counter (Pt wire), and reference (Ag/AgCl in 1M KCl) electrodes connected to Gamry Interface 5000E. The cyclic voltammetry (CV) measurements were made in 1 M Na_2SO_4 electrolyte.

RESULTS AND DISCUSSION

Physicochemical Analysis

The UV-Vis spectra of GO, 6HT-rGO, and 6HT-MWrGO are shown in Fig. 1. GO shows a strong peak at 231 nm (triangle label) and the shoulder peak at 303 nm corresponds to the π - π^* peak of the aromatic C-C bond and the n - π^* transition peak of C=O respectively [12]. After the hydrothermal reduction, the observed strong peak red-shifted from 231 nm to 298 nm and 252 nm for 6HT-rGO and 6HT-MWrGO respectively corresponding to the restoration of C=C conjugations through rehybridization of carbon atoms from sp^3 to sp^2 . The difference in red-shifting observed between 6HT-rGO and 6HT-MWrGO suggests a variation in the degree of reduction of the two reduced products [11]. Hence, 6HT-MWrGO experienced a lower degree of reduction compared to 6HT-rGO when the *G. mangostana* peel extract was used during the hydrothermal process.

The GO curve from the quantitative FTIR analysis revealed various oxygen functional groups such as hydroxyl (O-H), carbonyl/carboxyl (C=O), and epoxy (C-O) groups (see Fig. 2), deriving from graphite oxidation [13]. Next, carbon functional groups were also observed in the spectra, belonging to the sp^3 -C-H stretching and the sp^2 -C=C stretching at 2918 cm^{-1} and 1622 cm^{-1} respectively. The calculated peak area (%) for C=C stretching increased from 5.89% (GO) to 15.33% and 15.76% for the 6HT-rGO and 6HT-MWrGO respectively,

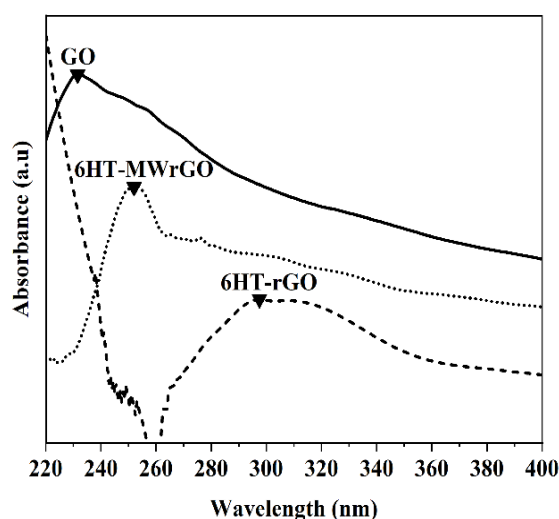


Fig. 1: The UV-Vis spectra of GO, 6HT-MW_rGO, and 6HT-rGO.

confirming the complete reduction of GO. Subsequently, a decreasing trend in the amounts of oxygen functional groups is observed: 89.98% (GO) > 81.69% (6HT-MW_rGO) > 78.11% (6HT-rGO), which correlates with the observed lower degree of reduction from the UV-Vis analysis.

These findings of 6HT-MW_rGO show the possible simultaneous functionalisation and reduction when using the peel extract during the hydrothermal process. This is based on the insignificant difference in the peak area (%) of C=C stretching yet visible distinctions were recorded in the existing peak areas (%) of oxygen functional groups between 6HT-MW_rGO and 6HT-rGO.

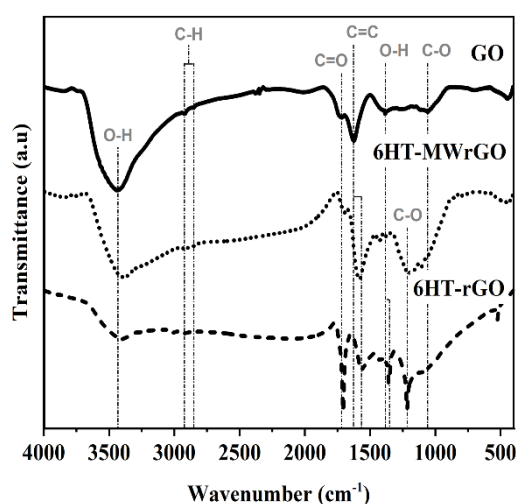


Fig. 2: The FTIR spectra of GO and the synthesised hydrothermal rGO products.

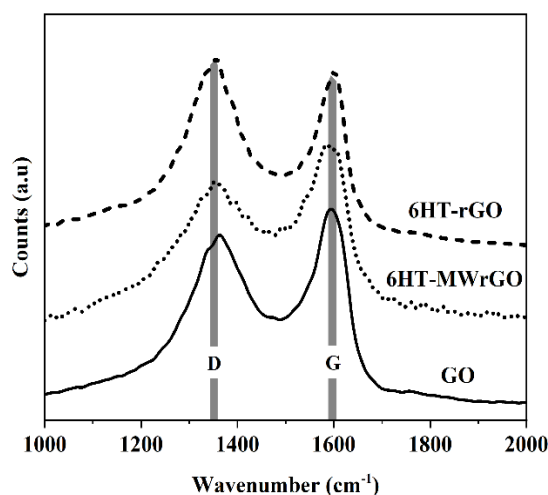


Fig. 3: The D-mode and G-mode peaks of GO, 6HT-MW_rGO, and 6HT-rGO.

The metabolites in *G. mangostana* peel extract may be the main factor responsible for preventing the complete removal of oxygen functional groups or even by functionalising onto the graphene layer [14]. This claim is supported by the rich presence of oxygen functional groups in the highly oxidised 6HT-MW_rGO.

Fig. 3 shows the Raman spectra of GO and rGO which highlights the presence of two strong peaks: D-mode and G-mode vibrations at 1350-1370 cm⁻¹ and 1580–1610 cm⁻¹ wavenumber range respectively. The D-mode peak shows the defects arising from the C=C bond deformation and heteroatom introduction while the G-mode peak forms from the in-plane E_{2g} stretching between C=C bonds in the planar graphene which are indicators of structural defects and disorders in carbon domains, quantified as the I_D/I_G ratio [13]. Table 1 summarises the I_D/I_G ratio and the mean crystallite size, L_a values of GO, 6HT-rGO, and 6HT-MWrGO calculated using the following formula [15]:

$$I_D/I_G \text{ ratio} = \frac{\text{Peak intensity of D-mode peak}}{\text{Peak intensity of G-mode peak}} \quad (1)$$

$$L_a(\text{nm}) = \frac{2.4 \times 10^{-10} \times \lambda^4}{I_D/I_G} \quad (2)$$

Where λ = the excitation laser wavelength (nm). The trend in the degree of defect in the samples is as follows: **6HT-MWrGO < GO < 6HT-rGO**. The increase in defects of

TABLE 1. The Raman peak analysis of GO, 6HT-MWrGO, and 6HT-rGO samples

Sample	Wavenumber (cm ⁻¹)		I_D/I_G ratio	L_a value (nm)
	D-mode	G-mode		
GO	1363.8	1591.9	0.92	20.93
6HT-MW rGO	1351.5	1584.7	0.88	21.91
6HT-rGO	1356.6	1601.8	1.06	18.11

6HT-rGO is due to the removal of oxygen functional groups, generating vacancies and defect regions [2]. Surprisingly, the 6HT-MWrGO has a lower defect with a larger L_a value than GO and 6HT-rGO. This finding corroborates the proposed functionalisation of *G. mangostana* to aid in the restoration and repair of the sp²-carbon network.

Electrochemical Analysis

The CV analysis was measured from 0.0 to 0.6 V at different scan rates (5 - 100 mV s⁻¹) to study the electrode mechanisms of the two samples. Fig. 4 shows the CV curves of the two rGO samples at the scan rate of 20 mV s⁻¹, where a clear difference in their curve shapes can be observed. The 6HT-rGO sample exhibited a quasi-rectangular shape often associated with an EDLC-dominant mechanism while the 6HT-MWrGO displays an irregular rectangle curve, demonstrating a mixture of EDLC and pseudo-capacitance. The performance analysis from the CV analysis is calculated using the following equations [9]:

$$C_{sp@CV} \text{ (F g}^{-1}\text{)} = \frac{\int_{V_1}^{V_2} I \, dv}{m \times v \times \Delta V} \quad (3)$$

$$q_v = \alpha v^{-1/2} + q_o \quad (4)$$

$$\frac{1}{q_v} = \alpha v^{1/2} + \frac{1}{q_t} \quad (5)$$

$$q_i = q_t - q_o \quad (6)$$

where V_1 = initial potential (V), V_2 = final potential (V), I = current (A), m = mass of active material (g), v = scan rate ($V s^{-1}$), ΔV

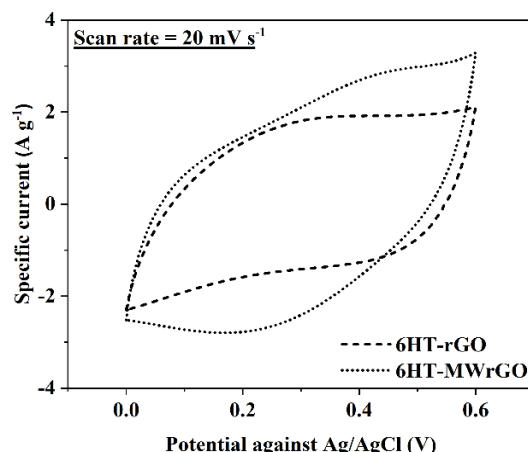


Fig. 4: The CV analysis of 6HT-MW rGO and 6HT-rGO in 1 M Na₂SO₄ electrolyte.

= the potential window (V), q_v = stored charge at a scan rate, q_o = stored charge at the outer surface, and q_i = stored charge at the inner surface. The C_{sp} values of each sample can be calculated using (3) where the samples recorded C_{sp} values of 175.48 F g⁻¹ and 75.98 F g⁻¹ for 6HT-MW rGO and 6HT-rGO respectively. This is accredited to the oxygen-rich nature of 6HT-MW rGO for pseudo-capacitance towards the improved storage capacity over 6HT-rGO [16].

Next, Trasatti's analysis of the CV curves at different scan rates elucidated the percentage contributions of EDLC and pseudo-capacitance for the hydrothermal products (see Fig. 5). The capacitance contributions were calculated using (4) – (6) and tabulated in Table 2. The improved performance of 6HT-MW rGO can again be attributed to the richer presence of oxygen, in comparison to the unmodified 6HT-rGO. Additionally, the EDLC value in 6HT-MW rGO is more than double the EDLC value of 6HT-rGO which can be a result of the lower surface defect and larger carbon domain to allow more ion adsorption on the graphene material [17].

CONCLUSION

An oxygen-rich rGO material was successfully synthesised *via* hydrothermal reduction of GO with *G. mangostana* peel extract. It was shown that 6HT-MW rGO underwent a lower degree of reduction as compared to 6HT-rGO based on the UV-

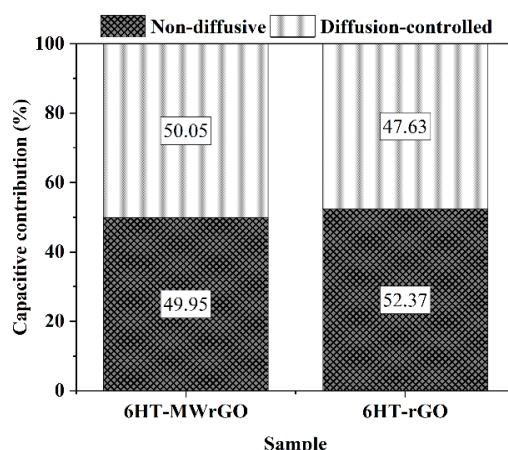


Fig. 5: The breakdown of contributions from the different types of capacitance mechanisms determined from Trasatti's analysis.

TABLE 3. The calculated capacitive distribution of 6HT-MWGO and 6HT-rGO samples

Type of capacitances	Capacitance value (F g ⁻¹)	
	6HT-MWGO	6HT-rGO
C (outer), q _o	128.08	52.90
C (inner), q _i	128.33	48.11
C (total), q _t	256.41	101.01

Vis and FTIR analyses. This resulted in the synthesis of an electroactive carbon product without needing harmful or toxic reagents. The modified rGO displayed enhanced storage capability with a recorded C_{sp} value of 175.48 F g⁻¹ which more than doubled the capacitance of unmodified rGO. Hence, the natural plant extract can be considered a beneficial additive to the hydrothermal process to synthesise an active electrode material with boosted electrochemical performance for supercapacitors.

ACKNOWLEDGEMENTS: The authors wish to thank the Ministry of Higher Education for the Fundamental Research Grant Scheme (FRGS/1/2020/STG05/UPM/02/3) and Geran Putra-IPM (GP-IPM/2020/9683600) for providing financial support for this research.

REFERENCES

- [1] V. Agarwal and P. B. Zetterlund, "Strategies for reduction of graphene oxide – A comprehensive review," *Chemical Engineering Journal*, vol. 405, pp. 1-29, 2021.
- [2] H. H. Huang, K. K. H. De Silva, G. R. A. Kumara, and M. Yoshimura, "Structural Evolution of Hydrothermally Derived Reduced Graphene Oxide," *Sci Rep*, vol. 8, no. 1, pp. 1-9, 2018.
- [3] E. T. Mombeshora, E. Muchuweni, M. L. Davies, B. S. Martincigh, and V. O. Nyamori, "Nitrogen-doped reduced graphene oxide-polyaniline composite materials: hydrothermal treatment, characterisation and supercapacitive properties," *New Journal of Chemistry*, vol. 47, no. 7, pp. 3502–3515, 2023.

- [4] M. Zhou, H. Chai, D. Jia, and W. Zhou, "The glucose-assisted synthesis of a graphene nanosheet–NiO composite for high-performance supercapacitors," *New Journal of Chemistry*, vol. 38, no. 6, pp. 2320–2326, 2014.
- [5] J. Pang et al., "From crumple conformation to gel configuration of reduced graphene oxide: The cation induction engineering," *Ceram Int*, vol. 49, no. 3, pp. 4531–4540, 2023.
- [6] A. Gopalakrishnan, P. Sahatiya, and S. Badhulika, "Low temperature, one-pot green synthesis of tailored carbon nanostructures/reduced graphene oxide composites and its investigation for supercapacitor application," *Mater Lett*, vol. 198, pp. 46–49, 2017.
- [7] E.-Y. Ahn, S.-W. Shin, K. Kim, and Y. Park, "Facile Green Synthesis of Titanium Dioxide Nanoparticles by Upcycling Mangosteen (*Garcinia mangostana*) Pericarp Extract," *Nanoscale Res Lett*, vol. 17, no. 1, pp. 1-12, 2022.
- [8] H. J. Chu, C. Y. Lee, and N. H. Tai, "Green reduction of graphene oxide by *Hibiscus sabdariffa* L. to fabricate flexible graphene electrode," *Carbon*, vol. 80, no. 1, pp. 725–733, 2014.
- [9] S. P. Lee, G. A. M. Ali, H. H. Hegazy, H. N. Lim, and K. F. Chong, "Optimizing Reduced Graphene Oxide Aerogel for a Supercapacitor," *Energy and Fuels*, vol. 35, no. 5, pp. 4559–4569, 2021.
- [10] F. T. Johra and W. G. Jung, "Hydrothermally reduced graphene oxide as a supercapacitor," *Appl Surf Sci*, vol. 357, pp. 1911–1914, 2015.
- [11] C. Bing, Y. Jiahao, L. Xiaoying, J. Qi, W. Guoping, and J. Linghua, "Effects of reduction method on reduced graphene oxide and its electrochemical energy storage performance," *Diam Relat Mater*, vol. 114, pp. 1-9, 2021.
- [12] N. H. Aminuddin Rosli, K. S. Lau, T. Winie, S. X. Chin, and C. H. Chia, "Microwave-assisted reduction of graphene oxide for an electrochemical supercapacitor: Structural and capacitance behavior," *Mater Chem Phys*, vol. 262, pp. 1-7, 2021.
- [13] M. Karbak, O. Boujibar, S. Lahmar, C. Autret-Lambert, T. Chafik, and F. Ghamouss, "Chemical Production of Graphene Oxide with High Surface Energy for Supercapacitor Applications," *C (Basel)*, vol. 8, no. 2, pp. 1-12, 2022.
- [14] Sainz-Urruela, S. Vera-López, M. Paz San Andrés, and A. M. Díez-Pascual, "Surface functionalization of graphene oxide with tannic acid: Covalent vs non-covalent approaches," *J Mol Liq*, vol. 357, pp. 1-13, 2022.
- [15] F. Tuinstra and J. L. Koenig, "Characterization of graphite fiber surfaces with Raman spectroscopy," *J Compos Mater*, vol. 4, pp. 492–497, 1970.
- [16] Z. Li et al., "Three-dimensional oxygen-doped porous graphene: Sodium chloride-template preparation, structural characterization and supercapacitor performances," *Chin J Chem Eng*, vol. 40, pp. 304–314, 2021.
- [17] H. J. Kil, K. Yun, M. E. Yoo, S. Kim, and J. W. Park, "Solution-processed graphene oxide electrode for supercapacitors fabricated using low temperature thermal reduction," *RSC Adv*, vol. 10, no. 37, pp. 22102–22111, 2020.

Nuclear Power Plants Safety- A Preliminary Review

Arunagiri Szeyuan Lam and Siti Amira Othman

Faculty of Applied Sciences and Technology, Universiti Tun Hussein Onn Malaysia, 84600, Pagoh, Johor.

sitiamira@uthm.edu.my

Abstract: Becquerel's discovery of radioactivity would gradually pave the way for nuclear physics developments over the next 87 years, leading to the harnessing of nuclear energy in power plants, a process that stands at the forefront of modern technological marvels. The International Atomic Energy Agency (IAEA), formulated guidelines upon which general reactor designs and operation procedures would be based. There are several components where radiation exposure is expected due to the containment or/and transfer of radioactive material. Designs should be constructed on the basis of a layout that is logical and divided into different zones, each housing a sector providing specific functions that are accessible for delegated personnel to conduct operations, assessments and safety inspections. Radioactive fission products and corrosion products also escape from the core, which can be minimised by pre-selecting proper materials that, upon identifying their compatible properties, could reduce corrosion and erosion rates of the circuit materials. This review looks at safety aspects in various components such as the Spent Nuclear Fuel (SNF) storage pool, ion exchange resins, fuel materials, shielding, ventilation systems and waste management. It also looks at a study on the Thorium-based Molten-Salt Reactor (TMSR) as a potential alternative to commercial power plant designs.

Keywords: Radiation, Nuclear, Nuclear Power Plants, radioactivity, exposure

INTRODUCTION

This article reviews the meticulous domain of nuclear reactor management, where precision and innovation converge to unlock the immense potential within atomic nuclei. Built on decades of dedicated research, various reactor designs, be it commercial, breeding or research alike, have undergone revolutionary enhancements in several crucial aspects, namely their energetics. From its the lethal cautionary application by the Americans on the Japanese populace during the second World War, although denounced by Oppenheimer and Einstein [1, 36], to the establishing of atomic energy organisations for its safeguarding based on the principles of seeking safer alternatives to nuclear energy exploitation for civil purposes, emphasis on the safety aspect of harnessing such energy has become more evident

In time to come, the promise of pure energy would inspire attempts to gradually reduce pollution-inducing fuel reliance (i.e. oil and gas), as nuclear fuel proved to be "clean, safe, efficient and economical". The first functioning reactor was birthed in December 1942 at the University of Chicago [2, 23]. Primarily designed as a research prototype, the Chicago Pile-1 underwent several evolutionary stages – a continuous process of testing its limitations. Despite its small electrical output, large radioactive fuel consumption, lack of shielding and a team of experts only in nuclear theory to test it out for the first time, its ability to operate at 200W paved the way for further research in the mechanisms surrounding reactor operations. It also meant that advancing into higher energy capacities required stringent safety measures, as concerns about this energy's effects on not only operating personnel but the surrounding environment also were raised.

Subsequently, steering nuclear power in the direction of commercial electricity resulted in the world's first commercial Nuclear Power Plant (NPP) in 1942 at Obninsk, Russia [29]. Other

countries, which had the means to follow suit, were namely Calder Hall of the United Kingdom in 1956 and Shippingport of the United States in 1958. These NPPs were actively connected and supplied megawatts (MW) worth of electricity to a power grid. Unfortunately, the series of events took a horrific turn when later constructed NPPs experienced fatal failures. The Three-Mile Island (TMI), Chernobyl Reactor, and Fukushima Daiichi accidents are the three most notable accidents [34] that, though further perpetuated a generally negative perception over nuclear energy dependence, drove more diligent analysis into radiation protection measures before, during and after NPP operations, hence a generation of improved power plants globally.

Therefore, one ought to recognize that nuclear reactors involve unstable, high-energy nuclei, which have spontaneous and ionising properties. In our pursuit of energy excellence, we must also navigate the complex landscape of risks associated with nuclear reactors, acknowledging the dual nature of this powerful force – one that holds promise for a sustainable future, yet demands vigilant consideration of potential hazards. As part of managing power plant operations, this review considers the principles and effects of radiation, as well as safety elements in reactor designs.

LITERATURE

Reactor Safety Specifications

The agency, which involves an IAEA Secretariat and 4 safety standards committee, prepares and reviews the safety standards in 4 main areas. They include radioactive waste safety, the safe transport of radioactive material, nuclear and radiation safety. In a 2005 report detailing radiation protection aspects of NPP designs, IAEA emphasised on provision compliance of any design with objectives under two main areas – radiation protection and technical safety [14]. As learned in the past, ensuring “radiation exposure within an installation” or resulting from intended “release of radioactive material” is well below the prescribed dose, as well as “taking all reasonably practicable measures” [13] to mitigate the consequences from these incidents are of the utmost importance for all operating personnel undertaking the task.

When planning the layout of the facility, the design target should follow an appropriate fraction of the dose limits [14] specified by the National Council on Radiation Protection and Measurements (NCRP) to reduce the effects to a level as low as reasonably achievable (ALARA). A team of experts in reactor physics including radiochemistry, material specialisation, nuclear engineering, computational physics and radiation protection are crucial in the setting of dose limits and regulations through which the welfare of every individual takes precedence above all else. Additionally, nuclear professionals are equipped with comprehensive knowledge (through competency training) that earn themselves the responsibility of NPP management from its preliminary stage of planning and construction to its decommissioning and permanent shutdown.

Part of the procedure involves developing a means of controlling exposure in the working environment. Initially, designers consult with Radiation Protection Officers (RPO) on assessing radiation exposure possibilities. This is in order to engineer technological systems that cater to the decontamination and containment of radioactivity in NPPs. Using MORET6 codes, a study on patchy nuclear chain reactions showed with the Reactor Critical Facility of Rensselaer Polytechnic Institute, a relatively higher but uneven neutron flux distribution at the mid-section of the reactor column [5].

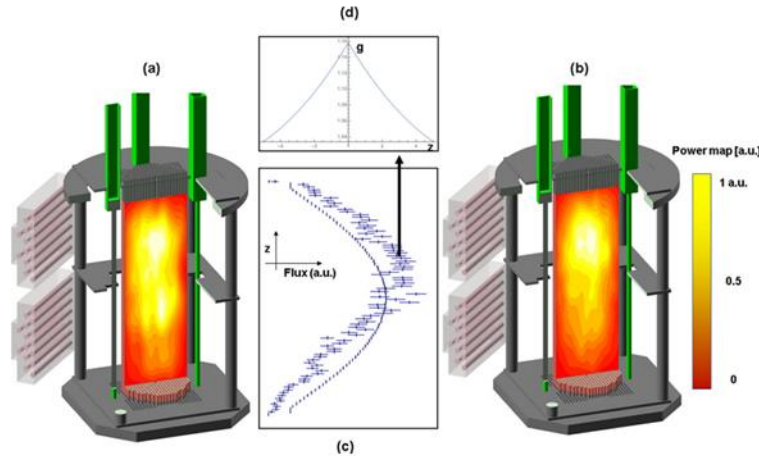


Figure 1: Power spatial distribution within the RCF.

The 2D simulated power map is projected onto a 3D cut of the 1.2 mW RCF experiment. a – power map averaged over 100s acquisition time. b – power map averaged over 1ms acquisition time. The corresponding axial power profiles are superimposed in c [5]

The MCNP6 model image, based on Figure 1, which was numerically designed using actual RCF data, is indicative of the gradual change in interaction frequency between neutron source and surrounding fuel pins throughout the reactor column. Assessing its maximum power output is an essential parameter in determining other properties of the core such as the thickness of the shielding and the capacity of the coolant in retaining operable core temperatures. Reactor benchmarking, as it is also known is a useful method of assessing NPP performance using computer-simulated experiments. However, it is worth noting that such simulations are approximations and based on assumptions made about the possible behaviour of radiation in the reactor that is physically impossible to see.

Secondly, the design of NPPs is followed up with the development and documentation of general pre-requisites. This involves diligent research on the fuel type, materials and geometry of each individual component. These three key aspects, when combined, influence the manner in which the nuclear reactions and their resulting energy output will transpire. Each NPP is generally divided into 7 distinct areas where radiation exposure certainly occurs: the Core and Vessel, Coolant and Fluid Moderator systems, Steam and Turbine systems, Waste Treatment System, Irradiated fuel, Storage of new fuel and finally Decontamination Facilities [14]. Taking these sources into consideration, the NPP design should be constructed on the basis of a layout that is logical and divided into different zones, each housing a sector providing specific functions that are accessible for delegated personnel to conduct operations, assessments and safety inspections.

Upon identifying these precursors, the reactor safety committee formulates a maintenance programme and operational tasks for trained personnel in order to execute periodically. From these actions, Radiation Protection Officers (RPO) determine radiation risks and protection measures to be carried out by operators according to their area of work as can be seen in Figure 2 below.

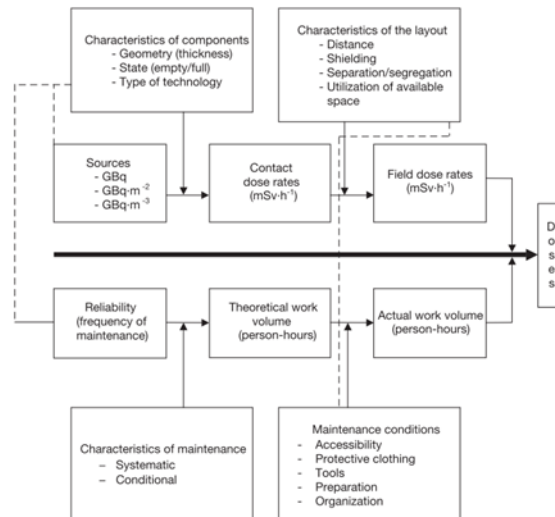


Figure 2: Schematic flow chart of the origin of doses at a plant (dashed lines indicate the possible impact of certain blocks on others) [14]

In an inspection, RPOs correlate the layout, operating procedures and a valid database to evaluate collective and individual doses. This way, a schematic flowchart of factors that determine such doses can be presented before establishing preventive measures to manage those factors. In retrospect, NPP operators have the necessary information to conduct optimisation studies where options are viable.

What is of concern for NPP operators is the source of radiation. NPPs commonly use materials that spontaneously and passively decay which, while although requires no continuous triggering to initiate energy production, will only stop emitting strong ionising radiation when they have decayed to their stable forms. The main source of radiation is radioactive fission products – high energy atomic fragments remnant from the fission chain reactions inside the reactor core. Along with fast neutrons, these materials can be located in almost any component of the power plant including the fuel elements, systems and equipment from which they originate [14].

Corrosion products also escape from the core through reactor coolant and moderator, in a Liquid-Moderated Reactor (LMR) for example. Corrosion products like hematite and magnetite [35, 41] cause damage to metallic reactor components, gradually reducing their structural integrity. This can be minimised by pre-selecting proper materials that, upon identifying their compatible properties, could reduce corrosion and erosion rates of the circuit materials. Since nuclides are also a major source of radiation, it is preferred if low-nuclide-concentration based materials were selected. Typically, commercial NPPs use lower and natural grades of fuel such as Low-Enriched Uranium (LEU) [4], depleted Uranium, natural Uranium and Mixed Oxides (MOX) as their low nuclide concentrations aid in balancing neutron economy and hence prevent reactors from achieving supercriticality.

Various zones occupied by NPP personnel require proper ventilation systems as a means of controlling the contamination in human-occupied working environments. As such, NPP operators and related professionals are prone to radiation exposure anywhere within close proximity of the reactor core. No exceptions are made for the rooms in which they work. For safety reasons, these spaces typically have ventilation systems integrated with specialised

particulate filters like High-Efficiency Particulate Air (HEPA) to prevent radioactive aerosol leakage into the environment [21]. However, such air filters come with limitations such as their inability to remove particles of certain sizes and gradual decrease in reusage efficiency. Another study in 1990 by Ruedinger discussed the obvious pros and cons of such filters, which at the time were being tested in many aspects [33].

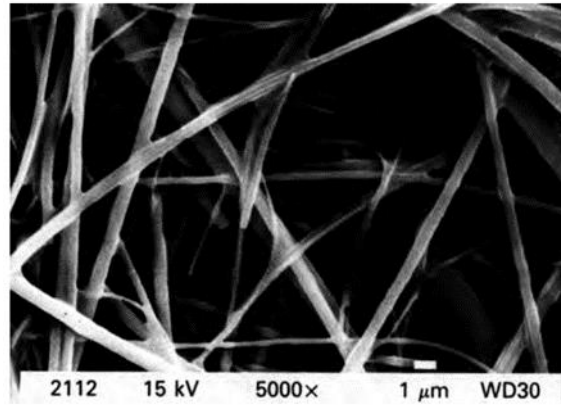


Figure 3: SEM image of fine structures in a clean HEPA particulate filter [33]

These filters, for instance as shown in Figure 3 were made from glass fibres which were “impregnated” with silicon to compensate for their high sensitivity to the effects of water. Since particulate filter efficiency has a strong correlation with radiological safety of the workers, this system requires regular maintenance.

Storage pools are another component of certain NPPs that regulate SNF activity and fuel temperatures. They are a zone adjacent to the reactor, found in plants that use fuel assemblies. During reactor operations, fuel assemblies are irradiated with a neutron source, causing them to emit heat from the energy generated via fission. The assemblies are limited to a burnup threshold to ensure criticality is maintained under a safe level. When fuels are exhausted and require replacement or repositioning with fresher fuels, they are transferred to storage pools to cool down, after which safety committees determine the age of SNF assemblies [37]. Thermohydraulic calculations are necessary in this respect, to run estimates of time-based water evaporation conditions when high-temperature assemblies are immersed.

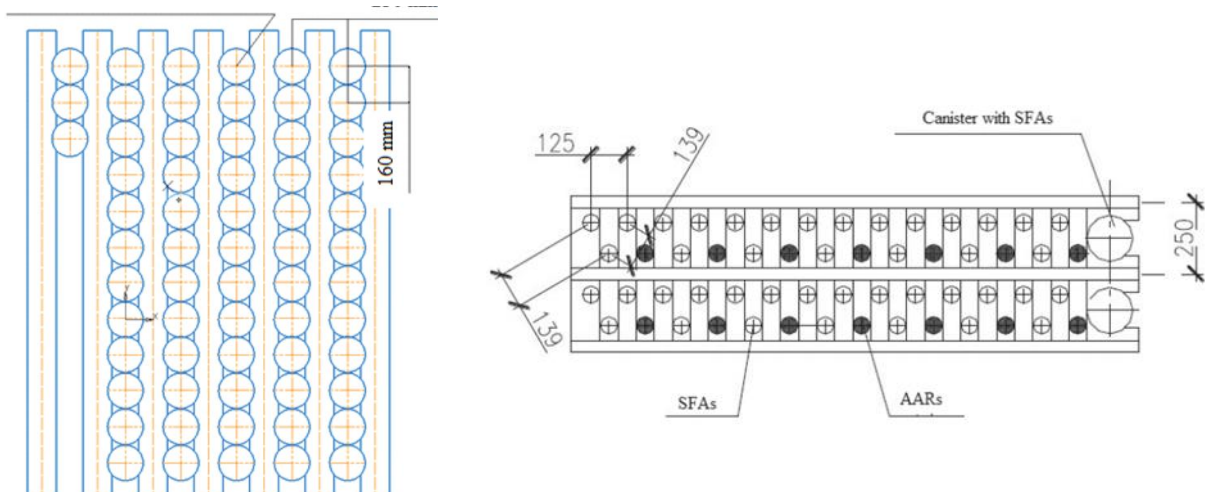


Figure 4: Layouts of Spent fuel assemblies arranged in a spent fuel pool (SFP) (right) and emergency assembly discharging compartment (left) [11].

The layouts in figure 4, are pools designed for the RBMK-100 reactor with which simulations were run to provide a correlation between cooling time, temperature and water levels for SNF [11]. This, according to the study, served as an indicator of the approximate time operators have to restore pool water levels as the complete termination of radio-thermal emissions is crucial in preparing SNF for future storage.

Ion exchange resins (IER) are utilised to reduce corrosion of reactor components and systems. They are employed in process water systems and are typically effective in transferring radioactive material from large volumes of liquid into a small solid [12]. Entailing a complex process, the use of ion exchange resins also requires detailed assessment with respect to an integrated waste management system. They primarily remove dissolved contaminants contained or streamed in systems to create ultrapure water that will be recycled. Cationic resins and anionic resins are general forms that NPP process water systems incorporate to produce reusable ultrapure water [7]. Flores does not, however, recommend that spent exchange resins being regenerated considering these substances eventually contain high activity from process water radio-filtration.

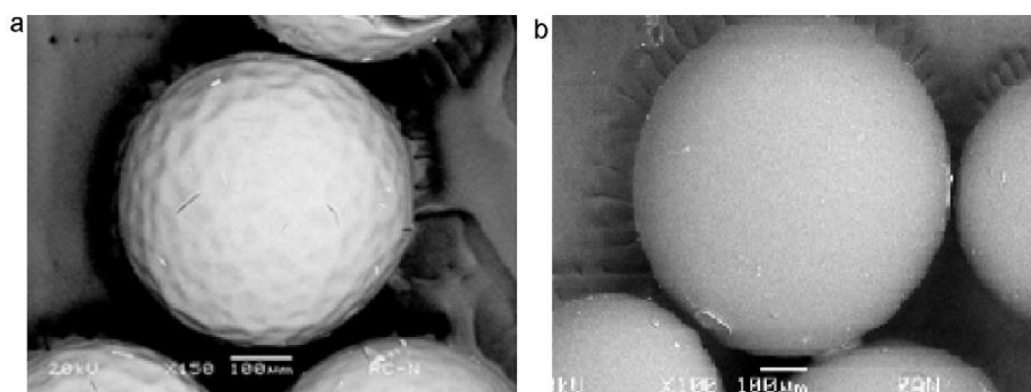


Figure 4: a) cationic resin (CR) b) anionic resin (AR) isolated by fluidization from mixed-bed nuclear-grade resins (LM)[7].

Cationic resins (CR) and anionic resins (AR) include strong and weak acid or basic functional groups which play crucial roles in demineralisation and radionuclide removal processes. In figure 4, the CR is of IRN-77 (strong acid) and the AR is of IRN-78 (strong base), both of which are polystyrene composites. Ion exchange has a special feature whereby the reversible process between solid does not permanently alter the structure of the solid itself. In practice, resins that typically come in spherical or granule shapes retain their structural integrity to carry out repetitive radio-purification. Additionally, such resins gradually lose their functional properties due to deterioration and therefore are rinsed and stored in hold-up tanks as “spent resins” [10].

Shielding Material

It is known that different types of radiation are each inhibited by a certain type and thickness of material. That is due to the properties of the radiation and its interaction with target material. For instance, α -radiation is carried by a heavy particle carrying a proton pair and a neutron pair,

which makes it easily stoppable with a thin sheet of paper. β -radiation is energy carried by a fast-travelling electron no further beyond a piece of clothing. γ rays, in spite of their low ionising power relative to the former two, is capable of penetrating thin layers of metal but is inhibited by a thick layer of Lead and other Lead-based composite variations. In nuclear reactor physics, the mechanical build of the core revolves around its material properties and their scattering nature with products of reactor fission reactions. Elastic and inelastic collisions between neutrons and fuel nuclides transpire from either scattering, absorption or fission-inducing collisions, each of which vary in probability. Overall, the collective outcome is a bulk generation of thermal energy that carries radiation in all directions.

The design of reactor shielding as outlined by the IAEA [14] should account for its durability and shear resistance. Principally, durable shielding prolongs radiation protection; coupling it with high resistance to shear pressure makes it an impenetrable core layer capable of containing a thermally energetic reactor. Additionally, shielding preferably should be of high-density elements. Such elements are typically stable and have high neutron-absorption cross-sections. That makes them favourable materials in limiting the perpetual fission chain reactions as well as the complete blocking of penetrating radiation. Considering nuclear fuels generate high thermal energy in a reactor, it is safer for personnel to operate outside the reactor core with thermally-insulating shielding. Moreover, reactor shielding is integrated together with other components and materials, with which, when finalising the design, it is to be compatible. Some examples of shielding material include concrete, and lead

A core issue is that penetrations through shielding will bring about pathways through which neutrons and gamma radiation can propagate. High-energy neutron and gamma ray exposure would result in radiation defects in the structure and thus component failure [31]. IAEA proposed modifications in the design of shielding to alleviate this issue. These included fabricating internal zigzag and curved pathways, integrating grouting into the shielding gaps as well as adding shieling plugs for the reactor vessel, like that of the Pressurised Water Reactor (PWR). This, in theory, would also hinder the straight-through penetration of fission products.

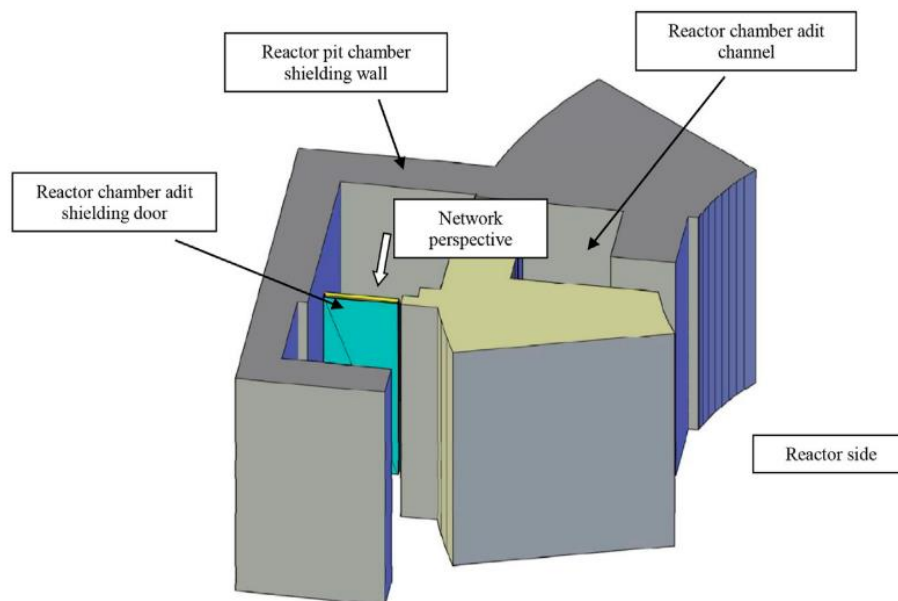


Figure 4: Simplified MCNP model of the Hualong One Reactor shielding door outside the

reactor chamber[38].

One study to analyse the heat-resistant properties of shielding materials of the reactor door inside the Hualong One Reactor (HOR) [38] discussed Lead-boron (PbB) polyethylene, Boron steel, and Epoxy resin as usual shielding materials [24, 39, 9, 22]. In figure 4, the shielding door is in close proximity to the reactor core, exposed to higher temperature, humidity and irradiation. In this test, PbB polyethylene composite possessed useful qualities for a Loss of Coolant Accident (LOCA) – high temperature resistance, and processing performance with proportions between 30% and 50%. Additionally, it exhibited satisfactory mechanical strength and shield performance [38].

Taking from Li's 1982 book, Xiao stated Iron, Lead and other high-atomic number materials [38], which are good absorbers and scatterers of gamma rays, serve as effective attenuating layers surrounding fission radiation. Considering its molecular property as a retarding factor of fast neutrons, Boron-10 in Boron Carbide became a much sought after material for moderators. To potentially obtain the best shielding, according to Xiao-Ling, was to combine the aforementioned materials in polyethylene form. However, this reduced the composite's heat deformation temperature to 85°C and melting temperature to 130°C, which proved ineffective for high temperature radiation environments. Instead, as an improvement measure, Ling proposed optimising the components including developing lead-boron polyethylene and modifying the raw materials.

Another study, which aimed to show the use of thermo-shielded structural concretes in a Nuclear Safety vessel, discussed its findings on thermal conductivity measurements [3]. Concrete is a major core material used as the final barricade against high temperature heat waves and other fission products from inside the reactor. Its attenuation ability is influenced by the aggregate, water-cement proportions, element composition, moisture content and finally density [30]. Computationally, an effective way of identifying its suitability in a reactor is by measuring its thermal conductivity – a key parameter influencing thermal trapping efficiency which, when low enough, can prevent fission products including ionising radiation from dispersing into the surrounding environment. This study demonstrated also, that well thermally insulated materials are possible with the addition of lightweight aggregates (LWA) such as pumice, coconut shell and volcanic rock [3]. This enhancement also did not compromise on the mechanical qualities of the concrete while an increase in moisture in the structure did show a correlation. Lightweight Aggregate Concrete (LWAC) would be used for its thermal diffusivity and low unit weight, which comes with porosity that reduces thermal conductivity [3]. Irregularities in material structure were also a design feature found to disrupt radiation paths and heat dispersion. This is further supported by the fact that thermal conductivity lessens in the presence of concrete cracking while its specific heat capacity is still maintained. The use of LWAs in place of conventional aggregates showed to improve thermal insulation. Significant improvements in concrete are partly due to when incorporated with hydrogen-rich polymer fibres [31]. Moreover, its "gamma- and neutron-shielding ability" improves greatly with high-density iron and lead aggregates, further lessening the weight of concrete. Despite this composition, these substances are not completely compatible with concrete, and thus contribute to structural defects that diminish concrete's resilience against external pressure and radiation.

2.3 Initiatives for The Thorium fuel-based Molten Salt Reactor

Researchers have explored other sources of fuel to tackle safety issues related to performance. NPP operators stand a better chance at sustaining chain reactions with a fuel material that has lower probability of proliferation and higher radiation resistance. Jam Emblemståg (2022) proposed the alternative implementation of Thorium-based Molten Salt Reactors (TMSR), weighing the potential advantages in Thorium's inherent properties against Uranium's as a source of fuel [6]. Not much research on the TMSR apart from its commencement in the 1960s has been done but its use as a "safe, clean, proliferation-resistant and cost-effective" power plant has garnered more analysis over the years. Thorium's chemical properties serve more as a counterintuitive component to the fission process in an NPP. The IAEA described ²³²Th to be a "better fertile material than ²³⁸U in thermal reactors due to its relatively higher neutron absorption cross-section, rendering it a more efficient substance for conversion into fissile fuel for sustaining the chain reactions [15]. Rubbia further supported this by stating that 1 tonne of Thorium produced the same amount of electrical energy as 200 tonnes of natural uranium and 3 million tonnes of coal [32].

However, the safety of operating personnel observing and monitoring the fuel energy yields is one of 4 key issues that, if guaranteed, will encourage a better acceptance of nuclear power and a more positive perception among people who 'observe from a distance' [26]. Emblemståg compared the use of a TMSR with LWR to demonstrate its potential advantages. The TMSR has the advantage of passive safety, which means they will not "fuel meltdown" [6], owing to the fact that metal fluorides are stable to reactor irradiation and that these ionic fluids experience no intense reactions when exposed to air or water [8,18,20].

In light of this, TMSRs can achieve the desired state of criticality without the concern for either excess buildup in energy from a high fission-to-absorption ratio (supercriticality) or shutdown due to insufficient fission-inducing neutrons (subcriticality). With only a small excess reactivity of 2% [27] this means that energy production is controllable. With respect to its subcriticality, the latter condition is a result of reactor poisons that accumulate in the fission chain reaction. Poisons resulting from the fission of Uranium, such as Xe-135, that have extremely high neutron absorption cross-sections, negatively impact the reactor's ability to sustain the energy generation by limiting fission-inducing interactions itself. While power plants circumvent on reactor poisoning to maintain safe fission levels, the Thorium-based reactor's safety mechanism eliminates the risk of arriving to an operational standstill. This is due to the fact that the TMSR, compared to reactors like the LWR, require no increase in fission generation (increasing neutron population) that would gradually overcome the naturally short-lived poisons. Emblemståg, 2022 further substantiated this by stating it needs "no Xenon override" that meant no large power surges as well [6].

The active replacement of molten carrier salt as the reactor still operates complements the reactor's zero reliance on an energetic override as well. For sustainability of the produced energy, salt fuels irradiated to their burnup limit are channelled and recycled at a processing plant before being reactivated at the reactor. Other nuclear power plants that incorporate online refuelling regulate thermal load more efficiently than others. This technique is combined with a continuous process of matter removal to alleviate the risk of radioactive gas emissions even under an accidental circumstance and to remove fission products within the salt during a leak or volatile substances [8, 20, 27]. Generally, such reactors like the MSR design include a failsafe solution – under the circumstance that an electrical outage may occur, a freeze plug in the reactor melts, allowing the fuel to cool down in a passive drain tank filled with borated water, hence ensuring the reactor automatically shuts down.

Radioactive Waste Management and Decontamination Systems

Achieving a conducive environment for NPPs to operate efficiently is paramount. This collective goal is to guarantee two vital aspects to reactor operations – the safety of operating personnel working within the area of potential radiation exposure, and that the functioning of the power plant can sustain an efficient cycle of fuel-to-energy production. Both aspects can be analysed in terms of the plant's radioactive waste management system whereby every process is a contributor to a potential accident that may disrupt the process. The manual for research reactor designs documented by the IAEA [17], includes a waste management programme that requires designers to maintain a minimum practicable yield of radioactive waste in terms of both activity and volume. Technological designs that facilitate radioactive waste should be resistant to radiation exposure which would allow waste management departments time to make crucial decisions such as consider the possible reuse of materials or collect, characterize and store radioactive waste safely.

NPPs, based on their design type can produce solid, liquid and gaseous forms of nuclear waste. To distinguish these forms from one another, systems both managerial and mechanical are to be developed. At a research reactor, for instance, safety officials assess dose amounts of waste that have been collected before labelling their packaging with placards that indicate the level or lethality of the substance. Uranium ores, fuel assemblies and SNF are bulk items which require special care when transporting them from operating spaces that utilise them actively to a storage unit that protects the surroundings from any remaining radiation leakage. A balanced exchange rate between fresh fuel material and expended material would ensure calculated and maintained amounts of stored waste. An example of ideal solid waste is when critical mass is too low that fission reactions cannot be contained and quickly die out. Some reactors encounter otherwise, due to compact, integrated designs and relatively quick high burnup which requires more fuel replacement and thus increased nuclear waste. An example of this is the Small Modular Reactor (SMR) which, according to Krall et al., attributed its excess waste to the use of chemically reactive fuels among other components [19]. One of the 3 SMRs studied used 5% enriched UO₂. The critical mass of water-moderated UO₂ exponentially reduces when enriched from 1% to 5% [28] which, in this case, 1) only makes the SNF more easily fissile and 2) is unfavourable for waste storage or reprocessing. SNFs should be stored and disposed of in subcritical configuration to inhibit them from sustaining any further fission chain reactions. Even the configurations of the containers capacity and distancing should allow heat to dissipate from the SNF.

Liquid effluents originate usually from the reprocessing of SNFs, otherwise known as High level waste (HLW). The procedure involves the dissolution of the fuel for further treatment. As part of separating fissile remnants from the fission and activation products, the main stream that carries high radioactivity and actinides is the nitric acid waste stream [16]. In other such cases, liquid waste can come from the maintenance of reactor coolants and other radioactive systems. The way to treat such waste is through the use of evaporators, filters and demineralisers [40]. A reactor safety committee takes Radiation Protection Standards that “prescribe charge limits” for gaseous and liquid radioactive waste into account. The data is set as a yardstick for RPOs and RP personnel to base their assessments on, in the case of monitoring this form of waste.

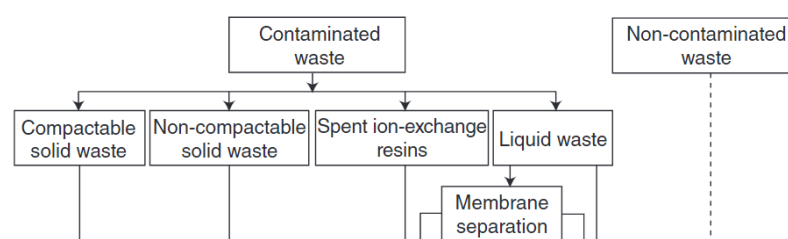


Figure 5: Contaminated waste treatment procedure for decommissioning sites [40]

Figure 5 shows an example of a waste management system implemented by South Korea during the Decommissioning and Decontamination (D&D) of their first Korean Research Reactors, KRR 1 (est. 1962) and KRR 2 (est. 1972). Liquid waste would either be naturally evaporated if it had significantly low doses and radioactive nuclide concentrations or channelled through a membrane for fission material filtration and demineralisation before being compacted into solid waste for long-term storage.

Gaseous radioactive waste would require more specialised technology as volatile particles in this case may carry radiation undetectable by smell or visibility. The main source of gaseous waste effluents is off-gas – released from the SNF during reprocessing dissolution containing fission products and rare gases. Elaborating further on the related discussion in subtopic 2.1, NPP ventilation systems have well-arranged airflow pathways, strategical discharge points and detachable filters that minimise contamination resuspension and enable the safe removal of airborne nuclear waste. In research reactors, for instance, a ventilation system is located above the reactor to ideally minimise activation products like ^{41}Ar and fission products such as Xe gas. Carbon filters are also integrated into these systems as they are chemically inert yet effective particulate trapping materials [17]. It is important to note that radioactive gases are filtered and retained till complete decay to stable products is achieved before being expelled. Further improvements to the ventilation system have also been put forth, one of which was an off-gas scrubber made of hydroxide base for MSRs. The study, by Medina A. S., focused on the capturing capacity of the molten hydroxide scrubber on iodine radionuclides when an off-gas waste stream travels through it [25]. With promising results, Medina further added that such scrubbers were capable of isolating aerosols and particulates as well as neutralising acidic species [25].

Conclusion

NPPs stemmed from a short history of discoveries in nuclear physics combined with the atrocities of war that led to international consensus on the redirection of their energy source. In the years to come pure energy would come to generate electricity for power grids, allowing homes to be run and industries to thrive. Reactor operation requires vigilant observation and control, given the nature of radioactive sources. In the interest of long spans of sustainable fission energy, various mechanisms were developed. However, this comes with the consequence of radiation exposure from radionuclides such as uranium, plutonium and their constituent isotopes decaying to more stable forms over extremely long periods. The development of an NPP requires detailed planning and scrutiny in its phase of drafting a layout and specific function, its operations by personnel and finally its decommissioning and the

management of nuclear waste. Among all this is the aspect of radiation protection, which takes into account the safety of all operating personnel based on stipulated dose limits, and technical safety. The IAEA publishes regularly revised guidelines upon which NPPs around the world refer to for the design of a reactor. These guidelines consider the possible presence of radiation in zones within the power plant compound that should be safely and properly contained from the environment and operating personnel. NPPs consist of safety elements such as storage pools, shielding, freeze plugs, moderators, and ion exchange resins which, all, control the emission of thermal energy and radioactivity to a significant degree respectively. Much research over time has helped reactors improve conventional methods and material applications including reinforcement initiatives of shielding material and nuclear waste management procedures. In all areas of reactor safety, studies in this paper demonstrated that almost all materials and procedures had pros and cons, most notably in maintaining balance between energy sustainability and exposure risk management. The operation of a reactor eventually raises the question of waste management and decontamination, whereby the proper disposal of spent fuel and other radioactive sources takes precedence over anything else.

REFERENCES

- [1] Andren, M. (2022). Atomic War or World Peace Order? Karl Jaspers, Denis de Rougemont, Bertrand Russell. *Global Intellectual History*, 7(4). <https://doi.org/10.1080/23801883.2020.1830494>.
- [2] Allardice C., & Trapnell E. R. (1982). *The First Reactor*. United States Department of Energy.
- [3] Anish, M., Arunkumar, T., Jayaprabakar, J., Al Obaid, S., Alfarraj, S., Raj, M. M., & Belay, A. (2022). Thermal Conductivity of Thermally Insulated Concretes in a Nuclear Safety Vessel of Reactor Vault: Experimental Interpretation. *Advances in Materials Science and Engineering*, 2022. <https://doi.org/10.1155/2022/4493910>.
- [4] Brown, N. R., Worrall, A., & Todosow, M. (2017). Impact of thermal spectrum small modular reactors on performance of once-through nuclear fuel cycles with low-enriched uranium. *Annals of Nuclear Energy*, 101, 166–173. <https://doi.org/10.1016/j.anucene.2016.11.003>.
- [5] Dumonteil, E., Bahran, R., Cutler, T., Dechenaux, B., Grove, T., Hutchinson, J., McKenzie, G., McSpaden, A., Monange, W., Nelson, M., Thompson, N., & Zoia, A. (2021). Patchy nuclear chain reactions. *Communications Physics*, 4(1). <https://doi.org/10.1038/s42005-021-00654-9>.
- [6] Emblemsvåg, J. (2022). Safe, clean, proliferation resistant and cost-effective Thorium-based Molten Salt Reactors for sustainable development. *International Journal of Sustainable Energy*, 41(6). <https://doi.org/10.1080/14786451.2021.1928130>.
- [7] Flores-Espinosa, R., Ortiz-Oliveros, H. B., Olguín, M. T., Perusquia-Cueto, M. R., & Gallardo-San-Vicente, R. (2012). Separation and treatment of ion-exchange resins used in cleaning systems of a research nuclear reactor. *Chemical Engineering Journal*, 188, 71–76. <https://doi.org/10.1016/j.cej.2012.02.011>.
- [8] Furukawa, K., Arakawa, K., Erbay, L. B., Ito, Y., Kato, Y., Kiyavitskaya, H., Lecocq, A., Mitachi, K., Moir, R., Numata, H., Pleasant, J. P., Sato, Y., Shimazu, Y., Simonenco, V. A., Sood, D. D., Urban, C., & Yoshioka, R. (2008). A road map for the realization of global-scale thorium breeding fuel cycle by single molten-fluoride flow. *Energy Conversion and Management*, 49(7), 1832–1848. <https://doi.org/10.1016/j.enconman.2007.09.027>.
- [9] Guo, P., Dong, L., Wang, C., et al. (2010). Preparation of boron Carbide or Ultra-High Molecular Weight Polyethylene Composites for Neutron Shielding[J]. *J. Mater. Eng.* Z2, 337–340.
- [10] Hafeez, M. A., Singh, B. K., Yang, S. H., Kim, J., Kim, B., Shin, Y., & Um, W. (2023). Recent advances in Fenton-like treatment of radioactive ion exchange resins. *Chemical Engineering Journal Advances*, 14. <https://doi.org/10.1016/j.cej.2023.100461>.
- [11] Hakobyan, D. A., & Slobodchuk, V. I. (2021). Temperature conditions in the RBMK spent fuel pool in the event of disturbances in its cooling mode. *Nuclear Energy and Technology*, 7(1). <https://doi.org/10.3897/nucet.7.64363>.
- [12] Hussain, A., & Al-Othmany, D. (2013). Treatment and Conditioning of Spent Ion Exchange Resin from Nuclear Power Plant (Vol. 15). Online. www.iiste.org.
- [13] IAEA (2016). Safety of nuclear power plants: Design. Specific Safety Requirements No. SSR-2/1 (Rev. 1). IAEA Safety Standards, 1.

- [14] International Atomic Energy Agency (2005). Radiation Protection Aspects of Design for Nuclear Power Plants for protecting people and the environment Safety Guide. <http://www-ns.iaea.org/standards/>
- [15] International Atomic Energy Agency (2005). Thorium fuel cycle: potential benefits and challenges. International Atomic Energy Agency.
- [16] International Atomic Energy Agency (2009). IAEA Safety Standards Classification of Radioactive Waste for protecting people and the environment No. GSG-1 General Safety Guide. <http://www-ns.iaea.org/standards/> retrieved 21 November 2023.
- [17] International Atomic Energy Agency (2023). Radiation Protection and Radioactive Waste Management in the Design and Operation of Research Reactors. <https://www.iaea.org/resources/safety-standards> retrieved 21 November 2023
- [18] Juhasz, A. J., Rarick, R. A., & Rangarajan, R. (2009). High Efficiency Nuclear Power Plants Using Liquid Fluoride Thorium Reactor Technology. <http://www.sti.nasa.gov> retrieved 21 November 2023.
- [19] Krall, L. M., Macfarlane, A. M., & Ewing, R. C. (2022). Nuclear waste from small modular reactors. *Proceedings of the National Academy of Sciences of the United States of America*, 119(23). <https://doi.org/10.1073/pnas.2111833119> retrieved 21 November 2023.
- [20] LeBlanc, D. (2010). Molten salt reactors: A new beginning for an old idea. *Nuclear Engineering and Design*, 240(6), 1644–1656. <https://doi.org/10.1016/j.nucengdes.2009.12.033>.
- [21] Lee, M. H., Yang, W., Chae, N., & Choi, S. (2020). Performance assessment of HEPA filter against radioactive aerosols from metal cutting during nuclear decommissioning. *Nuclear Engineering and Technology*, 52(5), 1043–1050. <https://doi.org/10.1016/j.net.2019.10.017>.
- [22] Li, X., Yu, F., Sun, L., et al. (2015). Multi-objective Optimization Design of lead-boron Polyethylene Shielding Composite [J]. *Ship Sci. Technol.* 37 (12), 148–154. (in Chinese).
- [23] Li, Z., Sha, H., Yang, N., Yuan, Y., & Zhu, G. (2019). Phosphoric Acid Based Porous Aromatic Framework for Uranium Extraction. *Acta Chimica Sinica*, 77(5). <https://doi.org/10.6023/A19010028>.
- [24] Lu, J., and Chen, J. (1994). High Effective Shielding Material lead-boron Polyethylene[J]. *Nucl. Power Eng.* 15 (4), 370–374. (in Chinese).
- [25] Medina, A. S., Felmy, H. M., Vitale-Sullivan, M. E., Lackey, H. E., Branch, S. D., Bryan, S. A., & Lines, A. M. (2022). Iodine and Carbonate Species Monitoring in Molten NaOH-KOH Eutectic Scrubber via Dual-Phase in Situ Raman Spectroscopy. *ACS Omega*, 7(44). <https://doi.org/10.1021/acsomega.2c05522>.
- [26] MIT (2018), *The Future of Nuclear Energy in a Carbon-Constrained World – An Interdisciplinary MIT Study*. Boston, MA: Massachusetts Institute of Technology. retrieved 21 November 2023
- [27] Moir & Teller (2005), Thorium-fueled Underground Power Plant Based on Molten Salt Technology, *Nuclear Technology* 151 (September): 334–340.
- [28] Paxton, H. C., & Pruvost, N. L. (1986). Critical Dimensions of Systems Containing 235 U, 239 Pu, and 233 U 1986 Revision. retrieved 21 November 2023
- [29] Petros'yants, A. M. (1984.). A Pioneer of Nuclear Power Plants. *IAEA Bulletin*, Vol. 26, No.4, retrieved 21 November 2023
- [30] Prochon, P., & Piotrowski, T. (2020). The effect of cement and aggregate type and w/c ratio on the bound water content and neutron shielding efficiency of concretes. *Construction and Building Materials*, 264. <https://doi.org/10.1016/j.conbuildmat.2020.120210>.
- [31] Qi, Z., Yang, Z., Li, J., Guo, Y., Yang, G., Yu, Y., & Zhang, J. (2022). The Advancement of Neutron-Shielding Materials for the Transportation and Storage of Spent Nuclear Fuel. *Materials*, 15(9). <https://doi.org/10.3390/ma15093255>.
- [32] Rubbia, C., et al. (2016). “A Future for Thorium Power? Thorium Energy for the World: Proceedings of the ThEC13 Conference.” In *CERN, Globe of Science and Innovation*, Geneva, edited by J.-P. Revol and M. Bourquin, 9–25. Geneva: Springer.
- [33] Ruedinger, V., Ricketts, C. I., & Wilhelm, J. G. (1990). High-strength high-efficiency particulate air filters for nuclear applications. *Nuclear Technology*, 92(1), 11–29. <https://doi.org/10.13182/nt90-a34483>.
- [34] Schöbel, M., Silla, I., Teperi, A. M., Gustafsson, R., Piirto, A., Rollenhagen, C., & Wahlström, B. (2022). Human and organizational factors in European nuclear safety: A fifty-year perspective on insights, implementations, and ways forward. *Energy Research and Social Science*, 85. <https://doi.org/10.1016/j.erss.2021.102378>.
- [35] Turner, C. W., & Chi, L. (2012). Formation Of Corrosion Products Of Carbon Steel Under Condenser Operating Conditions. retrieved 21 November 2023
- [36] Turner, J. E. (2007). About Atomic Physics and Radiation. In *Atoms, Radiation, and Radiation Protection* (2nd ed., pp. 1–13). John Wiley & Sons, Ltd. <https://doi.org/10.1002/9783527616978.ch1>.

- [37] Veinović, Ž., Uroić, G., Domitrović, D., & Kegel, L. (2020). Thermo-hydro-mechanical effects on host rock for a generic spent nuclear fuel repository. *Rudarsko Geolosko Naftni Zbornik*, 35(1). <https://doi.org/10.17794/rgn.2020.1.6>.
- [38] Xiao-ling, L. I., Rong-jun, W., Xiao-hui, X., Duo-fei, Z., & Ming, Y. U. (2021). Study of a High Temperature–Resistant Shielding Material for the Shielding Doors of Nuclear Power Plants. *Frontiers in Energy Research*, 9. <https://doi.org/10.3389/fenrg.2021.751654>
- [39] Yasin, T., & Khan, M. N. (2008). High density polyethylene/boron carbide composites for neutron shielding. 059. <http://www.e-polymers.org> retrieved 21 November 2023.
- [40] Yun, J. Il, Jeong, Y. H., & Kim, J. H. (2013). Republic of Korea: Experience of radioactive waste (RAW) management and contaminated site clean-up. In *Radioactive Waste Management and Contaminated Site Clean-Up: Processes, Technologies and International Experience* (pp. 673–696). Elsevier Inc. <https://doi.org/10.1533/9780857097446.2.673>
- [41] Zeman, A., Slugen, V., & Lipka, J. (n.d.). Study Of Corrosion Products From Nuclear Power Plant V-1 Bohunice. retrieved 21 November 2023.

A Review on Shape Stabilized Phase Change Material for Thermal Energy Storage Applications

Anas Islam^{1*}, A.K. Pandey¹, R. Saidur^{1,2}, Aman Yadav³, Kamal Sharma⁴

¹Research Centre for Nanomaterials and Energy Technology (RCNMET), School of Engineering and Technology, Sunway University, No. 5, Jalan Universiti, Bandar Sunway, Petaling Jaya, 47500 Selangor Darul Ehsan, Malaysia

²School of Engineering, Lancaster University, Lancaster, LA1 4YW UK

³College of Engineering, University Malaysia Pahang, Lebuhraya Tun Razak, Gambang, Kuantan 26300, Pahang, Malaysia

⁴Institute of Engineering and Technology, GLA University, Mathura, U.P. 281406, India

*Corresponding author's E-mail: drew4635@gmail.com

Abstract: Thermal energy storage (TES) using solar energy is one of the most prominent techniques to store the energy and reduce to gap between energy demand and supply. There are many useful applications that can be fuelled by TES. Phase change materials (PCM) as TES materials are of great importance as far as the energy storage applications are concerned. However, there are various bottleneck problems with pure PCM like liquid phase leakage, low thermal conductivity, supercooling etc. To overcome this deficit, highly porous foam is used to improve the leakage problem of PCMs during phase transition. Additionally, nanoparticles and nucleating agent are the most commonly employed in-practice approaches to get rid of the issue of low thermal conductivity and supercooling, respectively. In addition, even after being subjected to multiple heat cycles, foam-stabilized PCM composites showed remarkable stability without being degraded. This paper discusses the major foams that has been incorporated with different PCMs along with their critical outcomes. This paper also discusses the significant uses of foam stable PCMs reported by several researchers. As a result of its high latent heat, good thermal conductivity, balanced chemical compatibility, and high thermal stability, the foam-stable PCM composite is a viable choice for thermal-energy management systems.

Keywords: FSPCM, porous materials, foam stabilization, thermal management, TES

INTRODUCTION

Nowadays the whole world is witnessing the technical advancement at an exponential rate, with such a huge jump in the demand of energy especially from the last decade and growing greenhouse concern has prompted the scientist to look for some alternate sources of energy [1]. The other prominent reason to look for the alternate energy resources is the fast depletion of conventional energy sources such as natural gas, oil, coal, or nuclear [2]. Among the available alternate energy resources, the renewable resources of energy are the most promising ones since it is capable enough to meet global energy demand as well as a perfect answer to attain a low-carbon future [3]. Solar energy holds a dominating position as far as thermal energy storage is concerned compared to other sources of renewable energy like biomass and wind. In current era, TES is the need of the hour for the continuous energy supply in a vast number of applications like buildings, power generation etc [4]. Fig. 1 shows the potential application areas where TES is being used.

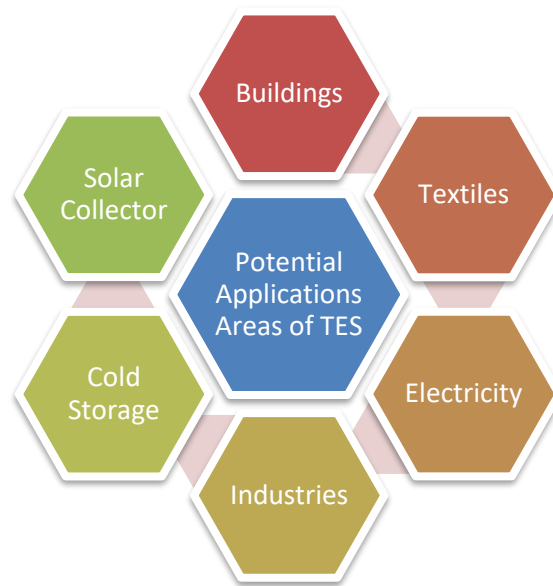


Fig. 1: Major applications of TES.

Phase change materials (PCM) are extensively used in TES, latent heat from melting and freezing can be stored in a quantity far greater than that of sensible thermal storage alone [5]. Since pristine PCMs witness several types of problems such as the leakage of liquid phase, low thermal conductivity, supercooling etc therefore it is recommended to enhance the property of PCM prior to its use [6]. There are various methods to resolve these issues with the PCM e.g., addition of nano particles and nucleating agents to improve its heat transfer rate and avoid supercooling respectively, encapsulation to protect the PCM from external environment pure PCMs, use of FSPCM to improve the thermal conductivity of PCM [7]. This article will summarize the recent advancements and challenges of foam stable phase change materials (FSPCM).

Overview of FSPCM

In order to overcome the problem of low thermal conductivity in PCM, porous materials and metallic foams are used [8]. The liquid PCMs are poured over or embedded into the foams and allowed to solidify, thereby the surface area gets increased as a result of which the heat transfer rate will also get enhanced. The rate at which heat transfers through foam depends on its PPI i.e., the number of pores per linear inch, fibre length, porosity (the ratio between total volume vs actual volume occupied by the foam), relative density, fibre thickness, surface area per unit of volume and pore density [9]. Fig. 2 shows the various types of foams that are commonly used by researchers.

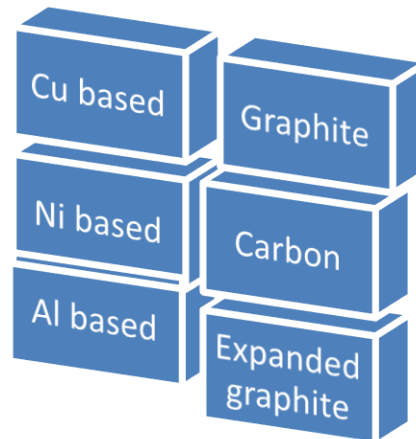


Fig. 2: Various types of foams/porous material

RECENT PROGRESS AND CHALLENGES IN FSPCM

Impregnation of PCM into a foam/ metal foam (MF) is a commonly adapted technique for preparing the FSPCM. It might not be convenient to immerse the MF into the liquid PCM directly without impregnation due to the presence of trapped air molecules in the porous structure, thus it would lead to creation of voids hence the strength of FOCM might get reduced. Finally, these air bubble trapped inside the micro-pores of a composite PCM will lead poor heat transfer and a lower PCM loading ratio. To avoid the formation of air bubbles the process of vacuum impregnation is carried out. The air bubble in the PCM are be removed with the use of a vacuum [10]. Fig. 3 depicts method of making FSPCM with the use of a vacuum, metal foam, and paraffin.

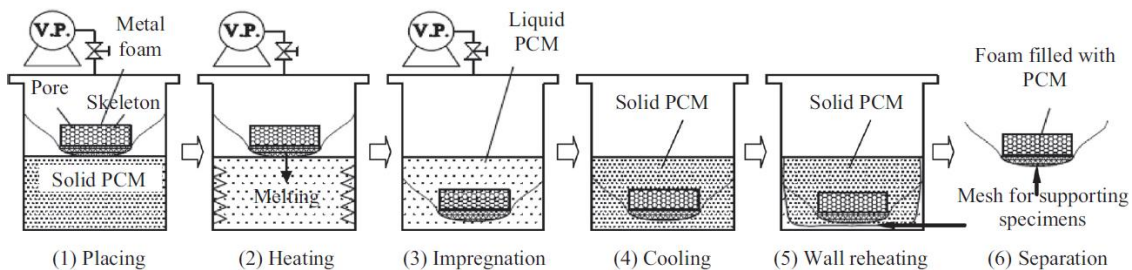


Fig. 3. Vacuum impregnation for the preparation of FPCM [8]

In the course of making shape stabilized PCM composite Warzoha et al. [11] compared vacuum impregnation to direct submersion infiltration by measuring the impregnation ratio (mass of impregnated PCM to mass of the perfectly impregnated case). The results showed that vacuum impregnation was far more effective than simple submersion, resulting in an almost 100% impregnation ratio for composite PCMs of paraffin and carbon foam. It has also been shown to be particularly successful in creating FSPCM [8]– [11].

Due to the porous structure, Cu foams have a large surface area relative to their volume. Among metals, copper has high thermal conductivity stands out as a top option for use in heat transmission. For the best heat conduction, PCMs are being combined with copper foam of

varied pore sizes and densities [12]. In order to increase heat transfer, [13] employed paraffin wax RT58 as PCM, which contains metal foams imbedded within it. Bottom surfaces of the test samples have been heated at a constant flux of heat. The authors discovered that by incorporating metal foam, the overall heat transfer rate can be increased by a factor of three to ten [14]. The thermal characteristics of a copper foam/paraffin composite were examined experimentally by the authors. It was shown that PCM temperatures could be lowered by using copper foam/paraffin composites as they considerably improved the heat transfer rate. Fig. 4 shows the aluminum foam that was prepared by [15] and copper foam prepared by [16] along with the geometrical dimensions of both foam and their respective plates. He came out with the results that copper foam, while similar in morphology to aluminium foam, has superior thermal performance.

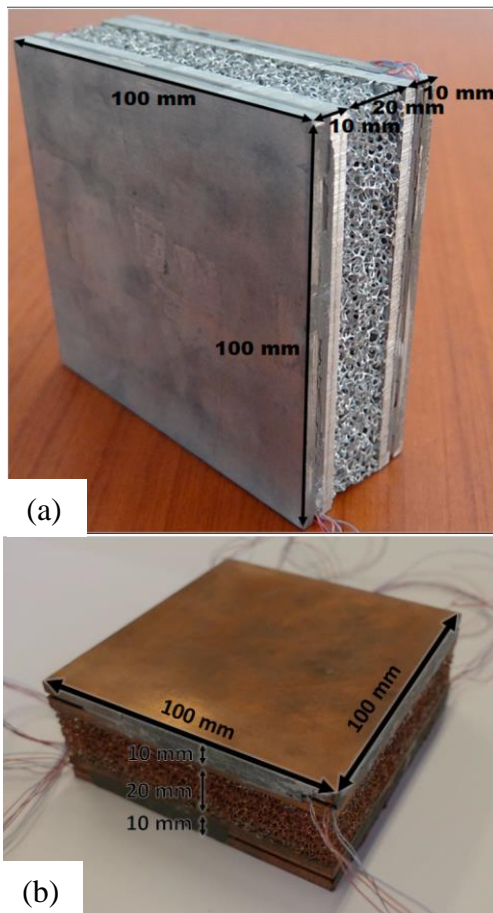


Fig. 4. Prepared samples of (a) Al-foam and (b) Cu-foam

Using numerical methods, [17] compared two PCM-based cold thermal energy storage systems. Comparing two units, one with a bio-PCM and while the other with aluminium foam, concluded that the one with Al foam shows minimal free convection in both the cooling charging and discharging processes.

Despite of low thermal conductivity (89 W/m-K) of Nickel, its relatively higher melting point (1455 °C) makes nickel foam a good candidate to be employed to acquire heat transmission rate. A significant improvement by almost three times higher than pure paraffin in the heat transfer of the paraffin/nickel foam composite was observed. Deviations in the peak melting temperatures by 0.55 °C and 0.40 °C of Paraffin/nickel foam composite and paraffin/copper

foam composite respectively with a pore size of 25PPI were also recorded as compared to pure paraffin due to the presence of the porous metal foam [8]. In order to enhance the properties of the nickel foam (NF) skeletons, [18] employed reduced graphene oxide (rGO) nanosheets adorned with Ni nanoparticles (Ni@rGO) impregnated with acidic graphene oxide solution and then thermally reduced. NF/Ni@rGO supported CPCMs are superior to their bare Ni-Foam supported counterparts in terms of form stability, heat storage density, and recycling potential.

Expanded graphite is among the most popular carbon - containing foam for heat transfer because of its lower density. Relatively minimal density and exceptionally conductive expanded graphite is used to improve the thermal conductivity and heat transfer of phase change materials (PCMs). Expanded graphite (EG) has a low density because it is extremely porous (porosity >99%) [19]. Chriaa et al. (20) used Hexadecane as PCM, and expanded graphite (EG) was added to analyze the performance of expanded graphite on the phase change materials composites [20]. This composite consists of 75% PCM, and 15% expanded graphene rest were the supporting materials. He claimed that EG has a positive impact on the thermal conductivity (TC) of PCM composite thereby increasing the TC 1.24 W/m. Some of the important studies related to FSPCM are summarized in Table 1.

Table 1: Some crucial findings on different foam stable PCM

Ref No.	Foam used	Method	Application Focused	Findings
[8]	Ni, Cu	Vacuum impregnation	Thermal charecterization	Thermal Conductivity (TC) of the FSPCM were enhanced
[21]	PW/HGF composite PCM	chemical vapor deposition (CVD)	Solar/thermal energy conversion	TC of PW/HGF is 87% higher than PW/GF and 744% higher than pure PW
[22]	Salts binaly/EGF	solution impregnation (SI) method	---	TC was enhanced by 4.9–6.9 time
[23]	Bi-Sn-In alloy/Ag/copper foam	---	Thermal management electronic device	FSPCM demonstrated excellent endothermic and exothermic properties

[24]	GNF/PCM	---	transient thermal response of PCM	base temperature of GNF/PCM enhanced 1.6 times
------	---------	-----	-----------------------------------	--

As a result of the improved thermal conductivity of PCM, the rate of heat transfer is improved. However, in most cases the specific heat of FSPCM gets lower thus it might not suitable for applications that need heat storage. When FSPCMs are employed for electronic cooling, they lower the base temperature, this limits FSPCM potential usefulness over longer cycles by decreasing its latent heat.

The rate of charging and discharging of thermal energy gets enhanced in FPCMs, the larger surface area aids in the passage of heat by conduction. Within PCM, temperature distributions become more even, because liquid PCM mobility is impeded, hence free convection heat transmission is reduced.

CONCLUSIONS

The current article reviewed the recent progress in foam stable phase change materials. Commonly used metallic (Al, Cu and Ni) and carbon based (C, Gr and Ex. Gr) foams were summarized to show their effect on the overall characteristics of PCM including the thermophysical properties. The following conclusions could be drawn based on the current study:

- The most important use of foam-stable PCMs is to enhance the thermal conductivity and heat transfer rate (k).
- In terms of thermal distribution, composite PCMs showed the most consistency.
- The time required to store and retrieve energy was reduced by a significant ratio due to the increment in the thermal charging and discharging speeds.
- FSPCMs are used to reduce the interface temperatures of electronic devices and Li-ion batteries therefore they are preferred to use in electronic devices.

References

- [1] S. Ali and S. P. Deshmukh, "An overview: Applications of thermal energy storage using phase change materials," in *Materials Today: Proceedings*, 2019, vol. 26, pp. 1231–1237. doi: 10.1016/j.matpr.2020.02.247.
- [2] A. Islam, S. P. Dwivedi, and V. K. Dwivedi, "Effect of friction stir process parameters on tensile strength of eggshell and SiC-reinforced aluminium-based composite," *World Journal of Engineering*, vol. 18, no. 1, pp. 157–166, Jan. 2021, doi: 10.1108/WJE-08-2020-0387.
- [3] M. R. M. Cruz, D. Z. Fitiwi, S. F. Santos, and J. P. S. Catalão, "A comprehensive survey of flexibility options for supporting the low-carbon energy future," *Renewable and Sustainable Energy Reviews*, vol. 97, pp. 338–353, Dec. 2018, doi: 10.1016/j.rser.2018.08.028.
- [4] C. A. Ikutegbe and M. M. Farid, "Application of phase change material foam composites in the built environment: A critical review," *Renewable and Sustainable Energy Reviews*, vol. 131. Elsevier Ltd, Oct. 01, 2020. doi: 10.1016/j.rser.2020.110008.
- [5] S. Zhang *et al.*, "A review of phase change heat transfer in shape-stabilized phase change materials (ss-PCMs) based on porous supports for thermal energy storage," *Renewable and Sustainable Energy Reviews*, vol. 135, p. 110127, Jan. 2021, doi: 10.1016/j.rser.2020.110127.

- [6] V. v. Tyagi *et al.*, "A comprehensive review on phase change materials for heat storage applications: Development, characterization, thermal and chemical stability," *Solar Energy Materials and Solar Cells*, vol. 234. Elsevier B.V., Jan. 01, 2022. doi: 10.1016/j.solmat.2021.111392.
- [7] Md. H. Zahir, S. A. Mohamed, R. Saidur, and F. A. Al-Sulaiman, "Supercooling of phase-change materials and the techniques used to mitigate the phenomenon," *Appl Energy*, vol. 240, pp. 793–817, Apr. 2019, doi: 10.1016/j.apenergy.2019.02.045.
- [8] X. Xiao, P. Zhang, and M. Li, "Preparation and thermal characterization of paraffin/metal foam composite phase change material," *Appl Energy*, vol. 112, pp. 1357–1366, Dec. 2013, doi: 10.1016/J.APENERGY.2013.04.050.
- [9] W. Cui *et al.*, "Heat transfer enhancement of phase change materials embedded with metal foam for thermal energy storage: A review," *Renewable and Sustainable Energy Reviews*, vol. 169, p. 112912, Nov. 2022, doi: 10.1016/j.rser.2022.112912.
- [10] P. Zhang, X. Xiao, and Z. W. Ma, "A review of the composite phase change materials: Fabrication, characterization, mathematical modeling and application to performance enhancement," *Appl Energy*, vol. 165, pp. 472–510, Mar. 2016, doi: 10.1016/j.apenergy.2015.12.043.
- [11] R. Warzoha, O. Sanusi, B. McManus, and A. S. Fleischer, "Development of Methods to Fully Saturate Carbon Foam With Paraffin Wax Phase Change Material for Energy Storage," *J Sol Energy Eng*, vol. 135, no. 2, May 2013, doi: 10.1115/1.4007934.
- [12] T. ur Rehman, H. M. Ali, M. M. Janjua, U. Sajjad, and W. M. Yan, "A critical review on heat transfer augmentation of phase change materials embedded with porous materials/foams," *International Journal of Heat and Mass Transfer*, vol. 135. Elsevier Ltd, pp. 649–673, Jun. 01, 2019. doi: 10.1016/j.ijheatmasstransfer.2019.02.001.
- [13] W. Zhao, D. M. France, W. Yu, T. Kim, and D. Singh, "Phase change material with graphite foam for applications in high-temperature latent heat storage systems of concentrated solar power plants," *Renew Energy*, vol. 69, pp. 134–146, Sep. 2014, doi: 10.1016/j.renene.2014.03.031.
- [14] J. Zhao, Y. Guo, F. Feng, Q. Tong, W. Qv, and H. Wang, "Microstructure and thermal properties of a paraffin/expanded graphite phase-change composite for thermal storage," *Renew Energy*, vol. 36, no. 5, pp. 1339–1342, May 2011, doi: 10.1016/j.renene.2010.11.028.
- [15] A. Diani and M. Campanale, "Transient melting of paraffin waxes embedded in aluminum foams: Experimental results and modeling," *International Journal of Thermal Sciences*, vol. 144, pp. 119–128, Oct. 2019, doi: 10.1016/j.ijthermalsci.2019.06.004.
- [16] A. Diani and L. Rossetto, "Melting of pcms embedded in copper foams: An experimental study," *Materials*, vol. 14, no. 5, pp. 1–13, Mar. 2021, doi: 10.3390/ma14051195.
- [17] M. Caliano, N. Bianco, G. Graditi, and L. Mongibello, "Analysis of a phase change material-based unit and of an aluminum foam/phase change material composite-based unit for cold thermal energy storage by numerical simulation," *Appl Energy*, vol. 256, p. 113921, Dec. 2019, doi: 10.1016/J.APENERGY.2019.113921.
- [18] R. Yang, X. Huang, G. Zhao, Z. Liu, and G. Wang, "Ni@rGO into nickel foam for composite polyethylene glycol and erythritol phase change materials," *Chemical Engineering Journal*, vol. 451, Jan. 2023, doi: 10.1016/j.cej.2022.138900.
- [19] J. Lopez, Z. Acem, and E. Palomo Del Barrio, "KNO₃/NaNO₃ - Graphite materials for thermal energy storage at high temperature: Part II. - Phase transition properties," *Appl Therm Eng*, vol. 30, no. 13, pp. 1586–1593, Sep. 2010, doi: 10.1016/J.APPLTHERMALENG.2010.03.014.

- [20] I. Chriaa, M. Karkri, A. Trigui, I. Jedidi, M. Abdelmouleh, and C. Boudaya, "The performances of expanded graphite on the phase change materials composites for thermal energy storage," *Polymer (Guildf)*, vol. 212, p. 123128, Jan. 2021, doi: 10.1016/J.POLYMER.2020.123128.
- [21] J. Yang *et al.*, "Hybrid graphene aerogels/phase change material composites: Thermal conductivity, shape-stabilization and light-to-thermal energy storage," *Carbon N Y*, vol. 100, pp. 693–702, Apr. 2016, doi: 10.1016/j.carbon.2016.01.063.
- [22] L. Zhong, X. Zhang, Y. Luan, G. Wang, Y. Feng, and D. Feng, "Preparation and thermal properties of porous heterogeneous composite phase change materials based on molten salts/expanded graphite," *Solar Energy*, vol. 107, pp. 63–73, Sep. 2014, doi: 10.1016/j.solener.2014.05.019.
- [23] K. Chen, J. Ding, W. Wang, and J. Lu, "Shape-stable Bi-Sn-In alloy/Ag/copper foam composite phase change material for thermal storage and management," *Chemical Engineering Journal*, vol. 454, p. 140087, Feb. 2023, doi: 10.1016/J.CEJ.2022.140087.
- [24] K. Chintakrinda, R. D. Weinstein, and A. S. Fleischer, "A direct comparison of three different material enhancement methods on the transient thermal response of paraffin phase change material exposed to high heat fluxes," *International Journal of Thermal Sciences*, vol. 50, no. 9, pp. 1639–1647, Sep. 2011, doi: 10.1016/j.ijthermalsci.2011.04.005.
- [25] T. Kim, D. M. France, W. Yu, W. Zhao, and D. Singh, "Heat transfer analysis of a latent heat thermal energy storage system using graphite foam for concentrated solar power," *Solar Energy*, vol. 103, pp. 438–447, May 2014, doi: 10.1016/j.solener.2014.02.038.
- [26] X. Huang, Y. Lin, G. Alva, and G. Fang, "Thermal properties and thermal conductivity enhancement of composite phase change materials using myristyl alcohol/metal foam for solar thermal storage," *Solar Energy Materials and Solar Cells*, vol. 170, pp. 68–76, Oct. 2017, doi: 10.1016/j.solmat.2017.05.059.
- [27] A. Hussain, I. H. Abidi, C. Y. Tso, K. C. Chan, Z. Luo, and C. Y. H. Chao, "Thermal management of lithium ion batteries using graphene coated nickel foam saturated with phase change materials," *International Journal of Thermal Sciences*, vol. 124, pp. 23–35, Feb. 2018, doi: 10.1016/j.ijthermalsci.2017.09.019.
- [28] A. Hussain, C. Y. Tso, and C. Y. H. Chao, "Experimental investigation of a passive thermal management system for high-powered lithium ion batteries using nickel foam-paraffin composite," *Energy*, vol. 115, pp. 209–218, Nov. 2016, doi: 10.1016/j.energy.2016.09.008.
- [29] Z. Wang, Z. Zhang, L. Jia, and L. Yang, "Paraffin and paraffin/aluminum foam composite phase change material heat storage experimental study based on thermal management of Li-ion battery," *Appl Therm Eng*, vol. 78, pp. 428–436, Mar. 2015, doi: 10.1016/j.applthermaleng.2015.01.009.
- [30] S. Feng, Y. Zhang, M. Shi, T. Wen, and T. J. Lu, "Unidirectional freezing of phase change materials saturated in open-cell metal foams," *Appl Therm Eng*, vol. 88, pp. 315–321, Sep. 2015, doi: 10.1016/j.applthermaleng.2014.09.055.

MODELLING

Spinodal Transformations in Thin Films

Rahul Basu^{1*}

(Emeritus Professor):¹EngineeringDept. JNTU, Bangalore, India

E-mail: *raulbasu@gmail.com

Abstract: The Spinodal Decomposition equations, as proposed by Cahn and Hilliard, are described by a fourth-order partial differential equation (PDE) that remains unsolved analytically up to the present time. This article delves into an exploration of these equations in their various forms, investigating solutions for both steady-state and transient scenarios using a variety of methodologies. Furthermore, the study addresses the moving boundary associated with the transformation through the lens of heat transfer principles. An attempt is made to solve this boundary using a combination of series and similarity transformation approaches. The equation under consideration is believed to consist of two components: one stemming from the conventional Laplacian and Fickian contributions, for which Stefan solutions are well-established, and another involving a Double Laplacian term that has yet to be thoroughly investigated. To facilitate the analysis, the thin film approximation is employed to simplify certain aspects and to facilitate the derivation of a numerical solution.

Keywords: Cahn Hilliard (CH) ; Spinodal Alloys ; Nanomaterials ; Thin Films, Perturbation

INTRODUCTION

The Cahn-Hilliard equation describes the process of phase separation in binary mixtures, alloys and polymer blends. This study focuses on the perturbation solutions of the one-dimensional Cahn- Hilliard equation with a double-well free energy potential, specifically applied to thin films. While many studies have described abstract approaches to the formulation and basis of the equations, few have attempted thin film perturbation analysis to understand time evolution and thin film aspects near the initiation of spinodal transformation. Such materials are now being applied towards sustainable metal processing because of the outstanding properties and reusable features exhibited. The micro-structure of these alloys creates these outstanding qualities. These alloys can be recycled without much reheating or re-working to retain such microstructures. Thus, it would contribute to sustainable manufacture and processing

THEORY

The Cahn-Hilliard equation in one dimension with a constant mobility M and a double-well free energy potential is given by:

$$\partial u / \partial t = M \nabla^2 (\varepsilon^2 \nabla^2 u + f'(u)) \quad (1)$$

where u is the order parameter, ε is a parameter related to the interfacial width, and $f(u)$ is the free energy density with a double-well given by:

$$f(u) = 1/4 u^4 - 1/2 u^2 \quad (2)$$

Linearization and Fourier Transform:

Starting with a uniform state and introducing a small perturbation, let:

$$u(\xi, t) = u_0 + u_1(\xi, t) \quad (3)$$

Assuming $u_0 = 0$ (a solution of the unperturbed system), the equation becomes:

$$\partial u_1 / \partial t = -M \partial^2 (\partial^2 u_1 + u_1) \quad (4)$$

Applying the Fourier transform: $\hat{u}_1(k, \tau) = \hat{u}_1(k, 0) \exp(-Mk^2(\varepsilon^2 k^2 + 1)\tau) \quad (5)$

(note t becomes τ x transforms to k on transforming. We use t and τ interchangeably in places as the transform in x does not affect t).

Thin Films and Fourier Series Expansion

For thin films with no-flux, or non zero boundary conditions at $\xi = 0$ and $\xi = L$, we use a sine or cosine series expansion:

$$u_1(\xi, \tau) = \sum_{n=0}^{\infty} a_n(\tau) \cos\left(\frac{n\pi\xi}{L}\right) \quad (6)$$

Substituting this into the linearized equation, we obtain after some simplifications, and solving the ODE for the coefficients:

$$a_n(\tau) = a_n(0) \exp\left(-M\left(\varepsilon^2 \frac{(n\pi)^4}{L^4} + \left(\frac{n\pi}{L}\right)^2\right)\tau\right) \quad (7)$$

The final solution for u_1 in a thin film is on retransforming:

$$u(\xi, t) = \sum_{n=0}^{\infty} a_n(0) \cos\left(\frac{n\pi\xi}{L}\right) \exp\left(-M\left(\varepsilon^2 \left(\frac{n\pi}{L}\right)^4 + \left(\frac{n\pi}{L}\right)^2\right)t\right) \quad (8)$$

Evaluation of the first few terms

For very small times t , the term $\varepsilon^2(n\pi/L)^4$ becomes negligible compared to $(n\pi/L)^2$. The first few terms are:

$$u(x, t) \approx \sum_{n=0}^{\infty} [a_n(0) \cos\left(\frac{n\pi\xi}{L}\right) \exp\left(\frac{-M(n\pi)^2 t}{L^2}\right)] \quad (9)$$

Since $u(x, \xi) = u_0 + u_1(\xi) = u_a + a_0(\xi) + a_1(\xi) \cos\left(\frac{\pi\xi}{L}\right)$,

$$u(x, \xi) = u_0 + u_1(\xi) = u_0 + a_0(\xi) + a_1(\xi) \cos\left(\frac{\pi\xi}{L}\right) \quad (9.1)$$

$$u(\xi, 0) = u_0 + u_1(\xi, 0) = u_0 + a_0(0) + a_1(0) \cos\left(\frac{\pi\xi}{L}\right) \quad (9.2)$$

with boundary conditions

$u(0, t) = a$ and $u(L, t) = b$, we get:

From (3) $a = u_0 + u_1(0, t) = u_0 + a_0(0) + a_1(0)$

$b = u_0 + a_0(0) - a_1(0)$ (10)

Since $u_0 = 0$ (by condition)

$$u(\xi, t) = \frac{a+b}{2} + \frac{a-b}{2} \cos\left(\frac{\pi\xi}{L}\right) \exp\left(-M\left(\frac{\pi}{L}\right)^2 t\right) \quad (11)$$

For small ξ , the approximation gives:

$$u_1 \approx a_0(0) + a_1(0) \left(1 - M\left(\frac{\pi}{L}\right)^2 t\right)$$

$$\sim (a+b)/2 + (a-b)/2 (1 - M(\pi/L)^2 t) \quad (12)$$

Examining the growth of the two regimes (small time and small distance), take the ratio of the quantities:

$$\frac{1 - (\pi \cdot \xi / L)^2 / 2}{1 - M \cdot (\xi / L)^2 \cdot t} \quad (13)$$

If L is large compared to ξ and Mt , the expression can be expanded by the binomial theorem:

$$\left(1 - \left(\frac{\pi\xi}{L}\right)^2 / 2\right) \times \left(1 + M\left(\frac{\xi}{L}\right)^2 \tau\right) \approx 1 + M\left(\frac{\xi}{L}\right)^2 t \quad (14)$$

Boundary Layer Thickness

Given the function, need to estimate the thickness of the boundary layer where the variable u changes rapidly. Using the definition of boundary layer as that where the variable drops to $1/e$ of its original value:

$$k=1/\pi\sqrt{[2L(1-1/e)]}$$

$$(\text{approx } 0.3578 \sqrt{L}) \quad (16)$$

Perturbation Analysis

In the context of the Cahn-Hilliard equation with a double-well potential, the equation takes the form:

$$\partial\phi/\partial t = \nabla \cdot (M \nabla (-\varepsilon^2 \nabla^2 \phi + \partial f / \partial \phi)) \quad (17)$$

where f is the order parameter, M is the mobility, and ε (epsilon) is a small parameter related to the interface width.

A singular perturbation approach involves re-scaling the spatial and/or temporal variables to exploit the small parameter epsilon. The idea is to separate the solution into an inner region, where rapid changes occur (like at an interface), and an outer region where the solution varies slowly.

Step 1: Inner and Outer Expansions

We expect different behavior in the inner region (near the interface) and the outer region (away from the interface).

Inner Region (Interface)

In the inner region, we introduce the scaled coordinate $\xi = x/\varepsilon$. The order parameter ϕ is expanded as:
 $\phi = \phi_0(\xi) + \varepsilon \phi_1(\xi) + \varepsilon^2 \phi_2(\xi) + \dots$

Substituting into the CH equation and considering leading-order terms, we get

$$\partial^2 \phi_0 / \partial \xi^2 = \partial f / \partial \phi \big|_{\phi=\phi_0} \quad (19)$$

$$\text{This simplifies to: } d^2 \phi_0 / d \xi^2 = \phi_0 (\phi_0^2 - 1) \quad (20)$$

This is a well-known equation describing the profile across the interface. The solution is:

$$\phi_0(\xi) = \tanh\left(\frac{\xi}{\sqrt{2}}\right) \quad (21)$$

This represents the smooth transition layer between the two phases.

Outer Region (Bulk)

In the outer region, where variations are slow, the small parameter (epsilon, ε) does not play a significant role in the leading order. Thus, the equation simplifies to

$$\partial\phi/\partial t = M \nabla^2 (\partial f / \partial \phi) \quad (22)$$

where we take $\phi = \phi_0(x) + \varepsilon \phi_1(x) + \dots$, and $\varepsilon \rightarrow 0$

Step 2: Matching Conditions

The inner and outer solutions must match in the overlap region. For the leading-order terms, we require that: $\lim_{\epsilon \rightarrow 0} \phi_0(\xi) = \phi_{\text{outer}}(x)$ (23)

This implies that far from the interface, the inner solution matches the outer solution.

Step 3: Composite Solution

The composite solution combines the inner and outer solutions to provide a uniform approximation across the entire domain. It is given by

$$\phi \approx \phi_{\text{outer}}(x) + [\phi_0(\frac{x-x_0}{\epsilon})] - \phi_{\text{outer}}(x_0) \quad (24)$$

where x_0 is the location of the interface. The expansion of $\tanh(x/\epsilon\sqrt{2})$ is given from Wolfram as $\tanh(x/\epsilon\sqrt{2}) \approx x/\epsilon\sqrt{2} - (x^3/6\epsilon^3 2^{1/2}) + \dots$ (25)

$$\frac{x}{\sqrt{2}\epsilon} - \frac{x^3}{6(\sqrt{2}\epsilon^3)} + \frac{x^5}{30\sqrt{2}\epsilon^5} - \frac{17x^7}{2520(\sqrt{2}\epsilon^7)} + \frac{31x^9}{22680\sqrt{2}\epsilon^9} - \frac{691x^{11}}{2494800(\sqrt{2}\epsilon^{11})} + O(x^{12})$$

Fig.1 Expansion (from WOLFRAM)

(It may be noted that this is an odd series and in fact $\tanh(x) \sim \sinh(x)$ for small x)

RESULTS

The singular perturbation approach for the CH equation with epsilon ϵ as a small parameter reveals that:

3.1 Inner Region (Interface): The order parameter ϕ transitions smoothly across the interface according to: $\phi_0(\xi) = \tanh\left(\frac{\xi}{\sqrt{2}}\right)$

3.1.1 The solution near the inner boundary varies as $\exp(-\xi)\cos(x)$ Outer Region (Bulk): Away from the interface, the order parameter satisfies the simpler diffusion equation (22). The solution is the well known erf(x) error function.

3.1.2 Composite Solution: Combines inner and outer solutions to provide a uniform approximation. This is done by applying the boundary conditions at each interface and adjusting constants. This approach highlights how singular perturbation methods can effectively capture the behavior of the order parameter near the interface and in the bulk, providing a comprehensive understanding of the solution to the Cahn-Hilliard equation.

LITERATURE REVIEW

The perturbation solutions for thin films has rarely been attempted. The references provide a comprehensive overview of the development and expansion of the Cahn-Hilliard equation, which is pivotal in modeling phase separation and microstructural evolution in materials science.

Cahn and Hilliard [1] introduced the Cahn-Hilliard equation, focusing on interfacial free energy and concentration gradients, establishing a cornerstone for phase transition studies. Voorhees [2] extended this by developing the theory of Ostwald ripening, explaining the coarsening process during phase separation, a crucial phenomenon for understanding microstructural evolution in materials. Novick-Cohen [3] emphasized mathematical rigor in studying phase separation, offering new insights into the equation's forms and applications.

Glasner [4] improved numerical simulations of phase separation by introducing a boundary integral method that handles complex boundary conditions more effectively. Allen and Cahn [5] applied the equation to ordered binary alloys, broadening its utility in modeling complex material systems. Chen [6] reviewed phase- field models, positioning the equation as central to understanding dynamic microstructural changes across various materials.

In recent advancements, Wu [7] reviewed the Cahn-Hilliard equation with dynamic boundary conditions, providing a more comprehensive understanding of its behavior in realistic settings. Bonfoh, Grasselli, and Miranville [8] introduced new analytical techniques for the one- dimensional equation with singular perturbations, aiding in better modeling of interface behavior. Miranville and Zelik [9,10,11] explored the equation with logarithmic potentials, enhancing its applicability to systems with complex energy landscapes, and focused on handling singularities in potentials and dynamic boundary conditions.

Finally, Londen and Petzeltová [12] contributed a detailed analysis of solution regularity near potential barriers in the equation with singular potentials, crucial for model stability. Linearising and applying perturbations give a good approximation of the solution, especially for small times " t ". The authors [12] investigate the regularity properties of solutions and explore how these solutions behave near potential barriers. Specifically, they examine the conditions under which solutions stay separated from these barriers, an important consideration in ensuring the stability and physical relevance of the model. This study is significant in understanding phase separation processes in materials science, particularly when the potential involved has singularities, which can represent more realistic physical situations.

MATERIALS

This study being computational, no experimental materials or equipment were used, apart from online simulators like WOLFRAM.

DISCUSSION

Graphs showing the variation of solutions for different regions are attached. Fig.2 shows the three curves for the inner, transition and outer solutions separately.

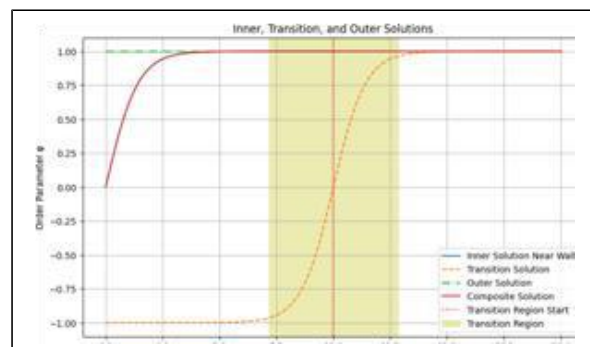


Fig. 2: The inner, transition and outer solution curves

Fig 2 shows the inner, transition and outer solutions in different colours. The transition is a sigmoid curve due to the tanh form, the inner a trig function(1-cos) which can satisfy both nonflux and dirichlet conditions, and the outer solution approaching a constant (erf at large arguments). (Fig 4 shows the curves marked with symbols also)

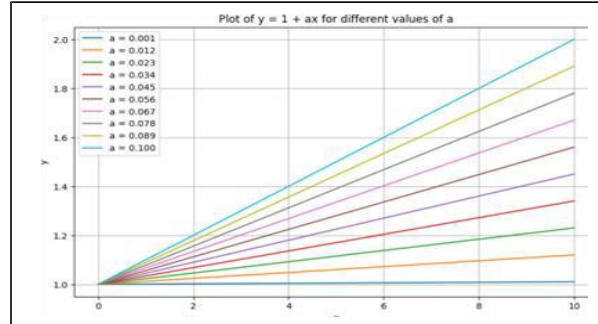


Fig. 3: Ratio of the x and t solutions for small values

Fig.3 shows the linear approximation to the ratios of the small x and t expansions given by eqn. 13. Matching of the inner and transition regions at present depends on the functions $\cos(x)$ and $\sinh(x)$ for small x. It will be easier if the inner solution is chosen as a sine function, however our choice of non zero B.C's has facilitated the application of a cos function. For zero boundary conditions, a sine function is preferable and matching may be easier. The matching is not done here for space reasons.

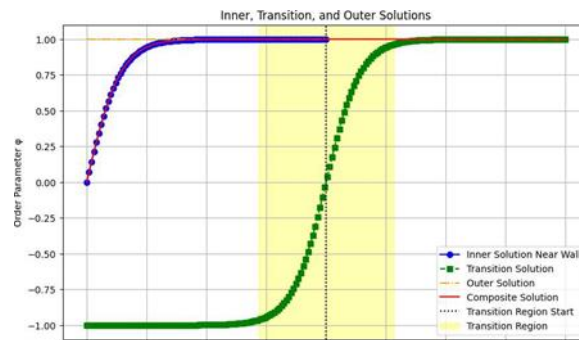


Fig 4. Transition curves highlighted with different symbols

The results of the study highlight the complex dynamics of spinodal decomposition in thin films, particularly through the application of the Cahn-Hilliard equation. By employing a singular perturbation approach, the study successfully captures the distinct behaviors in different regions of the thin film. The inner region, near the interface, exhibits a smooth transition described by a hyperbolic tangent (tanh) function, while the outer region, representing the bulk material, follows a simpler diffusion equation modeled by an error function (erf). The combination of these solutions into a composite model provides a comprehensive understanding of the phase separation process, emphasizing the critical role of boundary conditions in thin film geometries. Additionally, the exploration of boundary layer thickness offers valuable insights into the spatial extent of phase boundaries, which is crucial for determining the material properties. Overall, the results underscore the importance of considering both inner and outer regions to accurately model the early stages of spinodal transformations in confined systems.

The results presented in the paper show that the inner solution, characterized by a hyperbolic tangent (\tanh) profile, and the outer solution, described by an error function (erf), can be successfully combined to model phase separation in thin films. This composite solution provides a uniform approximation that captures the essential physics of spinodal decomposition in confined geometries.

The discussion of boundary layer thickness further enhances our understanding of how the order parameter varies near the interface. By estimating where the order parameter drops to a fraction ($1/e$) of its original value, (where e is the euler constant). The paper elaborates on the spatial extent of phase boundaries in thin films, a factor in determining material properties.

One of the contributions of the paper is its application of singular perturbation techniques to the CH equation in thin films. This approach separates the problem into inner and outer regions, corresponding to areas near the interface and the bulk material, respectively. The inner region experiences rapid changes in the order parameter, which is modeled using a scaled coordinate system. The solution in this region reveals a smooth transition layer, a hallmark of spinodal decomposition.

In contrast, the outer region experiences slower variations, allowing the equation to simplify to a more classical diffusion equation. The combination of these solutions via matching conditions gives a comprehensive view of the phase separation process across the entire film. The use of a thin film approximation simplifies the analysis, making it easier to derive solutions that can be compared with experimental or numerical data. In the context of the Cahn-Hilliard equation with fourth-order terms, the small parameter ϵ represents the interfacial width. The equation includes both second-order diffusion terms and higher-order fourth-order terms, which introduce the complexity in describing phase separation processes, particularly near interfaces.

Neglecting the Fourth-Order Terms

For small (ϵ), the fourth-order term, which is proportional to (ϵ^2) , becomes negligible compared to the second-order term. This situation often arises when analyzing behavior far from interfaces or at longer timescales, where the rapid changes in concentration occur over much larger spatial scales. In such cases, the second-order terms dominate, and the fourth-order contributions can be omitted, reducing the equation to something akin to a standard diffusion equation.

In thin film scenarios, as in this analysis, for early stages or regions where time (t) is small, the fourth-order term $\epsilon^2(\nabla^4 c)$ becomes negligible compared to the second-order term $(\nabla^2 c)^2$, as expressed in equation (9).

Stretching Parameter and Fourth- Order Effects

The stretching parameter involves scaling spatial or temporal coordinates with ϵ (epsilon), which is important in separating inner and outer regions in singular perturbation methods. In the inner region (near the interface), the scaled variable magnifies the region where the fourth-order term is significant. Here, the rapid variations across the interface are described by the hyperbolic tangent profile that incorporates (ϵ) , making the fourth-order term essential to capture the smooth transition. As we scale space and time, the small parameter (ϵ) balances the fourth-order effect, allowing the analysis to retain the critical information about the phase boundaries and interfacial movement. In contrast, in the outer region (bulk),

where ε tends to zero, the fourth- order term vanishes, and the simpler diffusion dynamics (second-order) dominate.

In summary, the fourth-order terms can be neglected when (ε) is small, and far from the interface, but they are critical in regions where rapid transitions (interface regions) occur, especially when stretched coordinates are applied to focus on such transitions.

FUTURE WORK

Future research could extend this perturbation approach to two and three- dimensional systems, consider the effects of varying mobility M , and more complex free energy potentials. Numerical simulations could also validate the analytical predictions and explore the nonlinear regime of the Cahn-Hilliard equation.

CONCLUSION

The simulation given in the paper shows the characteristics of the start of the phase development process. It is emphasized that due to the 4th order terms in the CH equation., it is an extension of the regular Stefan or diffusion problem, where the 4th order terms appear as a small perturbation due to the parameter ε . After using transformations, this obvious feature is recognizable, and further analysis is much simpler.

REFERENCES

- [1] J. W. Cahn and J. E. Hilliard, "Free Energy of a Nonuniform System. I. Interfacial Free Energy," J. Chem. Phys., vol. 28, no. 2, pp. 258–267, 1958.
- [2] P. W. Voorhees, "The theory of Ostwald ripening," J. Stat. Phys., vol. 38, pp. 231– 252, 1985.
- [3] A. Novick-Cohen, "The Cahn-Hilliard Equation: Mathematical and Modeling Perspectives," Adv. Math. Sci. Appl., vol. 8, pp. 965–985, 1998.
- [4] K. Glasner, "A boundary integral method for the Cahn-Hilliard equation," J. Comp. Phys., vol. 174, pp. 695–711, 2001.
- [5] S. M. Allen and J. W. Cahn, "Ground State Structures in Ordered Binary Alloys with Second Neighbor Interactions," Acta Metall., vol. 20, pp. 423–433, 1972.
- [6] L. Q. Chen, "Phase-field models for microstructure evolution," Annu. Rev. Mater. Res., vol. 32, pp. 113–140, 2002.
- [7] H. Wu, "A review on the Cahn–Hilliard equation: classical results and recent advances in dynamic boundary conditions," *Electronic Research Archive*, vol. 30, no. 8, pp. 2788-2832, 2022.
- [8] A. Bonfoh, M. Grasselli, and A. Miranville, "Singularly perturbed 1D Cahn– Hilliard equation revisited," *Nonlinear Differ. Equ. Appl.*, vol. 17, pp. 663-695, 2010. doi: 10.1007/s00030-010-0075-0.
- [9] A. Miranville and S. Zelik, "The Cahn- Hilliard Equation with Logarithmic Potentials," *Milan J. Math.*, vol. 79, pp. 561- 596, 2011. doi: 10.1007/s00032-011-0165-4.
- [10] A. Miranville and S. Zelik, "The Cahn- Hilliard Equation with Singular Potentials and Dynamic Boundary Conditions," arXiv:0904.4023, 2009.
- [11] A. Miranville, *The Cahn–Hilliard Equation: Recent Advances and Applications* (CBMS-NSF Regional Conference Series in Applied Mathematics).
- [12] S. O. Londen and H. Petzeltová, "Regularity and separation from potential barriers for the Cahn–Hilliard equation with singular potential," *J. Evol. Equ.*, vol. 18, pp. 1381-1393, 2018.

Heat Transfer and Crust Formation of Japanese Glutinous Rice During Deep-Frying Process

M. Nazli Naim^{1,2*}, Nadira Syahira Solehan¹, Mohd Afandi P. Mohammed¹, Siti Hajar Othman^{1,2}, Noor Fitrah Abu Bakar³.

¹*Department of Process and Food Engineering, Faculty of Engineering, 43400, Universiti Putra Malaysia, Serdang, Selangor, Malaysia*

²*Nanomaterials Processing and Technology Laboratory, Institute of Nanoscience and Nanotechnology, 43400, Universiti Putra Malaysia, Serdang, Selangor, Malaysia*

³*School of Chemical Engineering, College of Engineering, 40450, Universiti Teknologi MARA, Shah Alam, Malaysia*

**Corresponding author's phone: +603-9769 6359*

E-mail: mohdnazli@upm.edu.my

Abstract: A glutinous rice dough, Japanese Mochi, was subjected to a deep-frying process at various temperatures. Three thermocouples were inserted into the cooking oil, dough surface, and dough core using a data logger to record the in-situ temperature profile. The heat transfer coefficient was calculated according to the temperature profile and was compared to the crust formation along the frying process. During frying, the maximum convective heat transfer coefficient occurs at 50 s with values between 156.83 to 398.32 W/m²K when the temperature was varied from 170-190 °C. It was found that the crust formation was proportional to water removal until the end of the falling rate. At this phase, water migration occurs from the dough's core into the oil phase, eventually degrading the cooking oil by hydrolysis. This observation suggests that the frying time should not exceed the maximum heat transfer coefficient values to avoid large amounts of water migration into the cooking oil and shorten its cycles.

Keywords: Heat transfer coefficient, crust formation, glutinous rice flour, mochi, deep-frying kinetics.

INTRODUCTION

The increase in food prices since mid-2020 has been driven by factors such as the recovery in demand following the Covid-19 crisis, adverse weather impacts on supply, a growing number of trade restrictions on food products, and rapidly soaring input costs, notably energy and fertilisers [1]. To minimise the impact, optimisation in food processing needs to be further investigated by referring to the food processing principles and fundamentals. This work focuses on fried food products due to their wide application worldwide. The frying process comprises physicochemical reactions and transformations, such as starch gelatinisation, water vaporisation, protein denaturation, and crust formation [2-4]. Improper heat transfer in the frying process may ruin the fried food product and increase the cooking oil degradation rate. Uncontrollable heat transfer may also affect the cooking lifecycles as the oil hydrolysis oxidation and polymerisation contribute to total polar material (TPM) and other organoleptic compounds [10], which shortens the cooking oil life cycle and eventually contributes to the cooking oil wastage. Many countries already recognize the relationship between TPM and cooking oil life cycles, and in fact, it has been adopted by most national standards and laws [11]. Although the relationship of TPM with hydrolysis, oxidation and polymerisation was established by many workers [1-4], the impact of leftover debris by crust with repeatedly used frying oil is not well studied because of enormous food formulation around the globe, plus

the requirement of the samples to be in a prolonged in repeatedly heated cooking oil which can be only demonstrated in commercial frying process. Therefore, a significant study relating this unique food formulation is essential and should not depend on degraded cooking oil caused by hydrolysis, oxidation, and polymerization, as mentioned by many workers.

THEORY/LITERATURE REVIEW

The heat transfer during the frying process is governed by convection from the heat source to cooking oil, followed by conduction inside the fried food. The heat transfer profile can be illustrated in Fig. 1, which consists of several continuous phases: A: Initial heating, B: Surface boiling, C: Falling rate and D: End of bubble point. The crust formation of stray fried food typically develops from phase B to phase D. During phase B, the fry's surface temperature reaches the water's evaporation temperature. This phenomenon can be described according to Eq. (1)- Eq. (3),

Phase A:

$$\dot{Q}_{conv}(W) = hA(T_o - T_s) \quad (1)$$

$$hA(T_o - T_s) = \frac{dm}{dt} \Delta H_{vap} + MC_p \frac{dT}{dt} \quad (2)$$

Phase B:

$$hA(T_o - T_s) = \frac{dm}{dt} \Delta H_{vap} + MC_p \frac{dT}{dt} \quad (3)$$

Where,

h = heat transfer coefficient

T_s = surface temperature

T_o = oil temperature

C_p = specific heat capacity

ΔH_{vap} = heat of water vaporization

A = area

dm/dt = rate of mass

Starting from phase B, water evaporation is greater than the internal heat of the fried food, so the latent heat of evaporation initiates the drying of the food moisture from the outmost layer to the inner core. A significant crust thickness is developed as the drying progresses from the outer layer to the core. Thus, the basis for frying is connected to heat transfer coefficient, and allows an accurate description of the kinetics of water loss during frying can be developed to optimize the frying process [4-5].

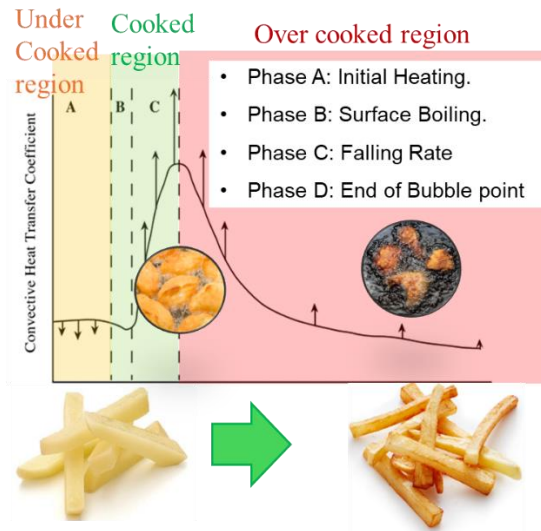


Fig. 1 The heat transfer profile along the frying process according to the phases. The crust formation is developed from phase B to phase D.

The microstructure of the crust region formed during the first moments of frying and the moving boundary at the crust/core interface determines the texture, crispness, oil-uptake, and outer appearance of the food. Frying time, capillary pressure, thickness and microstructure of the crust (inclusive of leftover debris), and permeability of fried food products to oil seem to be decisive for the oil degradation level. After the frying process, total mass of fried product is used to calculate the heat transfer coefficient according to Eq. 3

The heat transfer coefficient were have been used to predict the water loss that eventually contributes to cooking oil hydrolysis in post-frying [12] as well as for other cooking method [13-15]. The migrated water along the frying process is hypothesized to cause dramatic changes in TPM value as cooking oils are non-polar in nature. Therefore, in this work the increment in TPM value is postulated to be caused by the polar compounds acting as emulsifying agents that can lower the interfacial tension and make the crust prone to rupture. The rupture is later identified as leftover debris that occurred after the frying process.

MATERIALS

A series of mochi dough formulations were developed with various water contents while the compositions of other ingredient were fixed to verify the water migration with the function of heat transfer coefficient. The formulations of fried mochi are shown in Table 1.

EXPERIMENTAL

The heat transfer coefficient h of fried mochi was calculated using the Eq. (4) [5-6].

$$h = \frac{dm_w}{dt} \left(\frac{\Delta H_{vap}}{A(T_0 - T_s)} \right) \quad (4)$$

The oil temperature and the mochi surface temperature will be measured in this study using a thermocouple and data logger. Additionally, the heat of water evaporation was obtained from the saturated water (liquid-vapour) table. The temperature changes in this study were recorded using a data logger, GL240, Graphtec Corporation, Japan, throughout the deep-frying process. The temperature of the fried mochi's surface and core and the oil temperature are the control variables in this system.

To measure the cooking oil TPM during frying. The mochi samples were fried at different frying temperatures, 70 °C, 120 °C, 150 °C and 180 °C at 5 minutes per batch. The same frying oil will be used to deep-fry the same mochi batch samples until it reaches 25% of the TPM value. The oil degradation was measured using Testo 270, Testo SE & Co. KGaA, Germany. After completion of the TPM measurement, the moisture content of each sample was measured using a Moisture Analyzer.

Table 1: Dough formulations of deep-fried mochi.

Formulation of Fried Mochi	Ingredient Composition			
	30.43 wt.%	36.96 wt.%	43.48 wt.%	50.00 wt.%
	Amount (g)			
Glutinous rice flour	70	85	100	115
Water	130	115	100	85
Sugar	30	30	30	30

RESULTS AND DISCUSSION

From Fig. 2, the maximum values of heat transfer coefficient for 30.43 wt.% dough composition were found to be 225.043, 276.575, and 398.323 W/m²K at temperatures of 170°C, 180°C, and 190°C, respectively. The maximum values occurred at 50 s of frying time, whereby the highest rate of water loss is noticed.

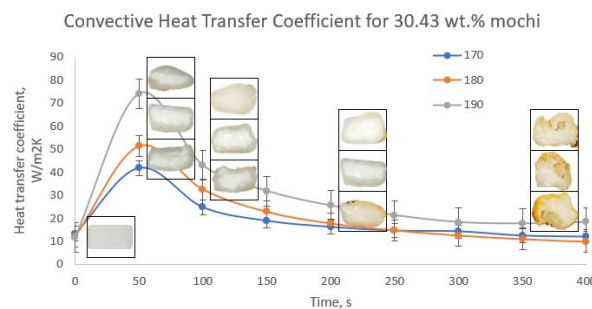


Fig. 2: Heat transfer coefficient of various dough compositions at 170, 180 and 190 °C together with crust picture along the frying process.

Furthermore, to obtain a good cooked product, the core of the fried food needs to reach a pure water boiling point so that starch gelatinization occurs, whereby a high heat value greater

than core temperature is required to obtain sufficient water loss [7]. Besides that, this figure clearly shows that the maximum heat transfer coefficient at 190°C is much higher than 180°C and 170°C. This is because as the oil temperature increases, the oil and mochi temperature gradient's driving force also increases, resulting in a higher value of the maximum heat transfer coefficient [8].

Refer to Fig. 3, the crust thickness for all dough compositions increases as frying time and oil temperature increase. After the falling rate phase, the surface layer becomes completely dry, and heat transfer increases the core of the dough to boiling point temperature. Referring to the given formulation in Eq. (3)- Eq. (4), it was found that greater mass contributes to higher crust thickness as less water is used in the formulation. This means that the 50.00 wt.% dough has greater crust thickness than the dough composition of 30.43, 36.96, and 43.48 wt.%. Interestingly, the crust formation was proportional to water removal until the end of the falling rate. After the falling rate, the crust formation rate was exponentially developed, caused by water migration from the dough's core into the oil phase, which degraded the cooking oil. The observation was valid for all dough formulations.

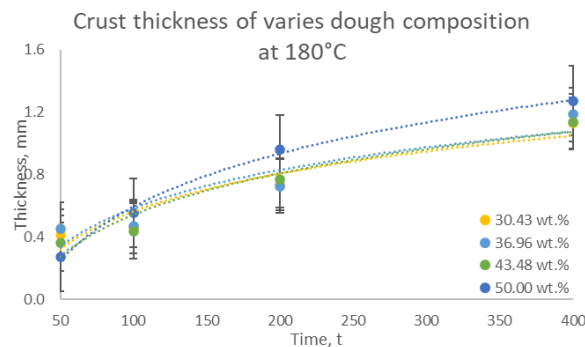


Fig. 3: Crust thickness of varies dough composition fried at 170, 180 and 190 °C.

For precise observation, several selected sample formulations were subjected to a frying procedure followed by TPM measurement. From Fig. 4, the TPM rate /cycles for both 150 °C and 180 °C increased from 2.7 ± 0.1 , 3.1 ± 0.01 and 3.2 ± 0.5 when the moisture content of the dough formulation was reduced from 36.96 wt%, 43.48 wt% and 50 wt% respectively. Only temperatures greater than 150 °C are considered, as these are the typical frying temperature standards when referring to EU standards. The allowable TPM value is <25%. Temperature lower than 150 °C are considered as the reference in this work. Referring to the TPM rate/cycles, shorter frying cycles were noticed when dough with low water concentration was subjected to frying. This phenomenon showed that the TPM value was not only contributed by cooking oil polymerization and oxidation but also depending on water hydrolysis caused by migrated water that eventually contributed to crust formation left after a series of frying cycles.

The increment of TPM value in Fig. 4 was significant to the increment of crust thickness in Fig. 3. Therefore, we presumed that the dramatic changes in the microstructure of the crust region thickness have also caused a reduction of surface tension by the degraded cooking oil by hydrolysis. As a result, a large amount of leftover crust was found in the bottom of the fryer after the completion of the frying cycles when exceeding the TPM value.

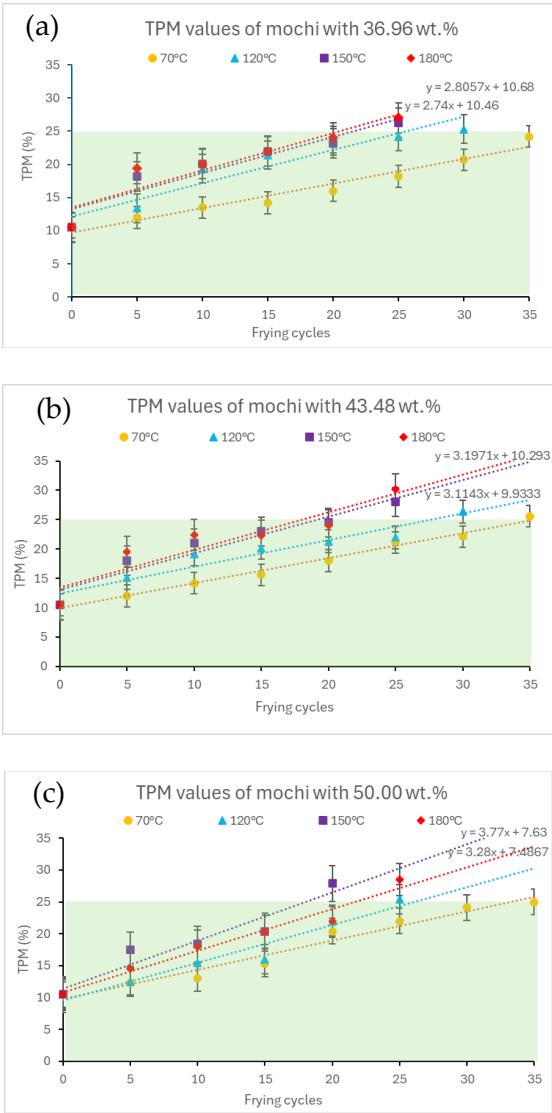


Fig. 4 TPM vs Frying cycle of mochi dough (36.7-50.0 wt%) at different frying temperatures.

A picture of leftover debris after the completion of the cycles is shown in Fig. 5. All debris were expected to develop from crust left over especially with samples with low water concentration, as mentioned in Fig. 3 earlier.

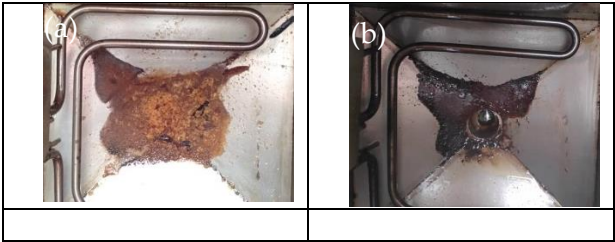


Fig.5 Leftover debris of 36.7 wt% dough formulation after TPM >25% of 150 °C and 180 °C with densier and darker colour of left over debris is noticed in (b) compared to (a). Cooking oil was drained with a filter at the bottom of the fryer after the completion of the cooking oil cycles.

CONCLUSION

This study confirms the importance of heat and mass transfer measurement relation to crust formation. Optimal heat transfer produces minimal water migration into the cooking oil and thin crust formation. The whole process contributing to more significant cooking oil cycles with less cooking oil wastage. This information is essential not only to reduce carbon footprint cause by the discarded cooking oil waste but also to produce healthy fried food. Exceeding the TPM value not only abused the cooking procedure but also increase the leftover crust inside the used cooking oil caused by increase thickness of microstructure of the crust region and reducing surface tension between the degraded cooking oil.

ACKNOWLEDGEMENTS: This work was supported by the Fundamental Research Grant Scheme, FRGS/1/2019/TK02/UPM/02/11 (554098), Ministry of Higher Education (MOHE) Malaysia. The work facilities were provided by the Faculty of Engineering, Universiti Putra Malaysia, Serdang, Malaysia, and Universiti Teknologi MARA, Shah Alam, Malaysia.

REFERENCES

- [1] International energy agency <https://www.iea.org>. <https://www.iea.org/commentaries/how-the-energy-crisis-is-exacerbating-the-food-crisis>.
- [2] B. E. Farkas, & L. J. Hubbard, "Analysis of convective heat transfer during immersion frying," *Drying Technology*, 18(6), 1269–1285, 2000. <https://doi.org/10.1080/07373930008917776>.
- [3] A. Alvis, C. Vélez, M. Rada-Mendoza, M. Villamiel, & H. S. Villada, "Heat transfer coefficient during deep-fat frying," In *Food Control*, Vol. 20, Issue 4, pp. 321–325, 2009. <https://doi.org/10.1016/j.foodcont.2008.05.016>
- [4] S. Budžaki, & B. Šeruga, "Determination of convective heat transfer coefficient during frying of potato dough," *Journal of Food Engineering*, 66(3), 307–314, 2005. <https://doi.org/10.1016/j.jfoodeng.2004.03.023>
- [5] A. Safari, R. Salamat, & O. D. Baik, "A review on heat and mass transfer coefficients during deep-fat frying: Determination methods and influencing factors," *Journal of Food Engineering*, Vol. 230, pp. 114–123, 2018. <https://doi.org/10.1016/j.jfoodeng.2018.01.022>
- [6] J. S. Lioumbas, M. Kostoglou, T. D. Karapantsios, "On the capacity of a crust–core model to describe potato deep-fat frying," *Food research international*, Volume 46, Issue 1,185-193, 2012. <https://doi.org/10.1016/j.foodres.2011.12.012>
- [7] K. N. van Koerten, M. A. I. Schutyser, D. Somsen, & R. M. Boom, "Crust morphology and crispness development during deep-fat frying of potato," *Food Research International*, 78, 336–342, 2015. <https://doi.org/10.1016/j.foodres.2015.09.022>
- [8] K. N. van Koerten, D. Somsen, R. M. Boom, & M. A. I. Schutyser, "Modelling water evaporation during frying with an evaporation dependent heat transfer coefficient,"

- Journal of Food Engineering, 197, 60–67, 2017.
<https://doi.org/10.1016/j.jfoodeng.2016.11.007>
- [9] 10.F.D. Gunstone, Modifying lipids for use in food. Woodhead Publishing Limited and CRC Press LLC. 2006.
- [10] 11.C. Gertz, “Fundamentals of the frying process,” Eur. J. Lipid Sci. Technol., 116, 0000–0000. 2014.
- [11] <https://doi.org/10.1002/ejlt.201400015>
- [12] 12. Q. Hu, J. Zhang, L. He, L. Wei, R. Xing, N. Yu, W. Huang & Y. Chen, “Revealing oxidative degradation of lipids and screening potential markers of four vegetable oils during thermal processing by pseudotargeted oxidative lipidomics,” Food Research International 175, 113725, 2024. <https://doi.org/10.1016/j.foodres.2023.113725>
- [13] 13.R. M. Costa, F. A. R. Oliveira, O. Delaney, V. Gekas, “Analysis of the heat transfer coefficient during potato frying,” Journal of Food Engineering, 39 293-299, 1999 .
[https://doi.org/10.1016/S0260-8774\(98\)00169-1](https://doi.org/10.1016/S0260-8774(98)00169-1)
- [14] 14.S. Shan & D. R. Heldman, “The Influence of Operation Parameters and Product Properties on Time-to-Temper for Frozen Raw Meat Based on Simulation,” Food Engineering Reviews 13:225–235, 2021. <https://doi.org/10.1007/s12393-020-09247-8>
- [15] 15.O. D. Baik, S. Grabowski, M. Trigui, M. Marcotte, F. Castaigne, “Heat Transfer Coefficients on Cakes Baked in a Tunnel Type Industrial Oven”, Journal of Food Science, 64(4):688 – 694, 1999. <https://doi.org/10.1111/j.1365-2621.1999.tb15111.x>

Silicon carbide-adsorbed halogen groups: A case for applying DFT

Nguyen Thanh Tung^{1,2*}, Tran Cong Phong^{2,3}, Hoang Van Ngoc⁴

¹ *Institute for Advanced Study in Technology, Ton Duc Thang University, Ho Chi Minh City, Vietnam*

² *Faculty of Electrical and Electronics Engineering, Ton Duc Thang University, Ho Chi Minh City, Vietnam*

³ *Atomic Molecular and Optical physics Research Group, Institute for Advanced Study in Technology,*

Ton Duc Thang University, Ho Chi Minh City, Vietnam

⁴ *Institute for Southeast Regional Development Studies, Thu Dau Mot University, Binh Duong Province, Vietnam*

*Corresponding author's phone: +84917919864

* Email authors corresponding: nguyenthanhtung.st@tdtu.edu.vn

Abstract: In this article, we present the process of studying halogen group atoms adsorbed with Si-C and the results obtained by the DFT calculation method. This shows that, due to its high electronegativity, the adsorbed adsorption is very strong in the F(p) electronic orbitals. This contribution makes the compound form a metal. Similarly for Cl(p) and Br(p), especially for I(p), these orbitals are weaker so the band gap still exists although with a relatively small value. Research results show that doping with halogen elements has fundamentally changed the band gap of pristine Si-C, providing application orientation for future electronic devices and sensors.

Keywords: silicon carbide, halogens adsorbed SiC, SiC applied

INTRODUCTION

Two-dimensional (2D) graphene has been synthesized in recent decades [1-3]. The performance of many traditional devices can be significantly enhanced by the unique properties of these materials, many studies have focused on graphene [4-6]. Silicene is also recognised as a two-dimensional material of graphene, which exists as a symmetrical structure with insignificant elasticity [7-8]. Many abnormal properties of graphene, including such as the Dirac hooks formed by the π bands at the symmetrical bonding point of the first Brillouin region, along with the total dominance of the π ranges at low energy, and the separation of the σ and π strips at deep energy, have been found in silicone [9]. Furthermore, silicene exhibits a number of special characteristics, including a large boundary width resulting from the combination of orbits at the Dirac point [10], the appearance of a polarized metal phase in the valley area with an abnormal quantum Hall effect [11], a study of the Hall rotation effect of the quantum at low temperatures [12], and the transformation of the topological insulator into a phase of insulation in response to external electrical fields [13]. Since silicon atoms are the main component of silicone [14], which is the main element in the field of silicon electronics [15], silicone is also more likely to be compatible in electronic devices than graphene. Since silicon has the advantage of being easy to integrate with Si-based electrical devices, it has become the main subject of many recent studies [16,17]. However, the small bandwidth of silicene limits its enormous potential for useful nanoelectronic field applications [18]. Therefore, in order to extend the beneficial properties of silicon to envisaged

nanoelectronics applications, it is necessary to expand the area of prohibition [19]. Several techniques, including atomic absorption [20], substitution [21], chemical function [22], mechanical capture [23], stacking configuration [24], application of external fields [25], and finite quantum limitation [26], have been used to expand the silicone capture area.

With the results achieved after doping SiNRs and C in a 1:1 ratio, we get a SiC compound with a significantly increased band gap from 0.26 eV to 2.37 eV. On the other hand, the initial SNRs structure had a warping of 0.75 Å, after doping with SiC the warping decreased to zero. This proves that the doping of C into SiNRs with different ratios is very important, it changes the Si-Si and Si-C bonds strictly based on the electromagnetic force of orbital electrons [27].

Following this result, we tried to dope halogen elements into the substrate to obtain SiC through DFT simulation, to investigate the changes in structural properties, electromagnetics and band gap energy

COMPUTATIONAL METHOD

The Vienna ab initio package simulation (VASP) incorporates the first principle density function theory (DFT), The computed VASP takes into account the distribution and concentration of adatoms. Exchange and correlation energy, which are obtained from numerous Coulomb interactions, are calculated using the Perdew-Burke-Ernzerhof function (PBE) in accordance with the gradient approximation. Projector amplified wave simulations are used to characterise electron-ion interactions. Building on a flat wave basis with a maximum power cut of 400 eV, functional wave and state energy are constructed. The Monkhorst-Pack diagram's k-point grids of $12 \times 1 \times 1$ and $100 \times 1 \times 1$ are used to further compute the structure's electronics and optimise the structure, respectively. The upper bound on the Hellmann-Feynman forces is less than 0.01 eV^{-1} . The energy convergence between the two closest ion stages is set at 10^{-5} eV .

RESULTS AND DISCUSSION

The atomic structure of pristine SiC is presented in Fig 1(b) consisting of six Si atoms and six C atoms, of which four H atoms are located on the edge where Si and C are aligned on an Armchair structure with six lines or Dimer index $N = 6$. The binding length of Si-C atoms is about 1.77 Å [27] and the flexibility is zero, similar to the structure of Graphene. The halogen groups F, Cl, Br, and I are fused at top (T), valley (V), bridge (B), and hollow (H) locations. Fig 1(a) represents the top-position fusion of the X halogen atoms including F, Cl, Br, and I. Fig 1(a) represents the top-position fusion of the X halogen atoms including F, Cl, Br, and I. By applying the DFT method, using the VASP software, we calculated the forming energy values, the parameters for link length, magnetic moment and forbidden area width for each of the different cases presented in Table 1.

Considering the electron zone structure and the density of the DOS state of the SiC substrate in Fig 2, we see the wine-colored Si(s) electron orbits primarily located at the bottom of the chemical region of about -8 eV to -4 eV and the most active at -7.5 eV; the Si(p_x) green color electron orbit operating at the top of the chemical region, from fermi to -2eV, and the base of the conductive region of 2 eV to 3 eV. For C alone, the dark-cyan colored C(s) electron orbit extends from the chemistry to the conductive region, but the energy is very weak; for the C (p_x) orbital electron, the cyan carries from -3 eV to the top of the chemistry and from the bottom

of the region to 5 eV, with the strongest energy being -1 eV up to the fermi level with three very strong peaks at -1.2 eV, -0.8 eV, and -0.2 eV. For the C(p_z) electron orbit, the blue works from -1.4 eV to -8 eV but is strongest at -1.5 eV, -2.6 eV, and -3.2 eV. The remaining C(p_y) navy-colored electron orbits operate with weak energy but range from -1 eV to -7 eV.

In general, the orbital electrons that contribute to the formation of fermi levels are primarily C (p_x) and Si (p_x).

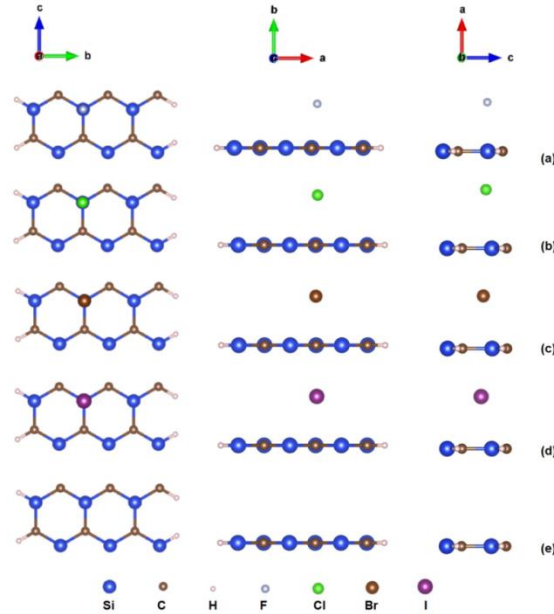


Fig 1 . (a) Structural of SiC-F(T), (b) SiC-Cl(T), (c) SiC-Br(T), and (d) SiC-I(T) and (e) pristine SiC

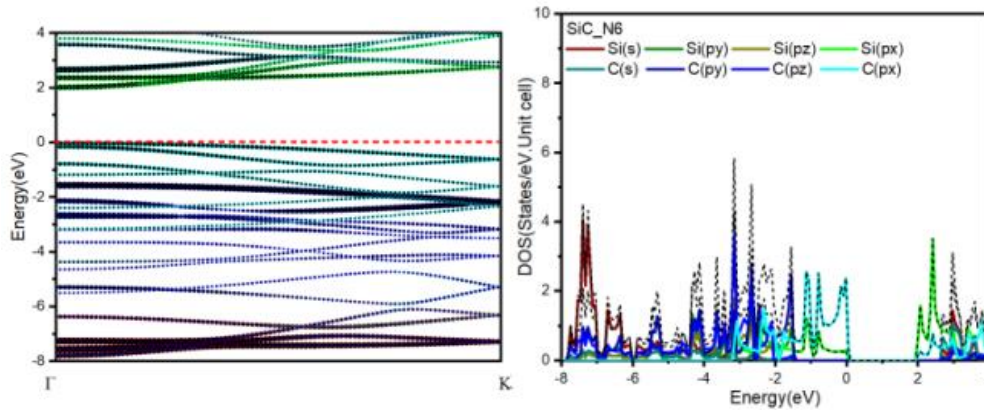


Fig 2 . The BAND and PDOS structure of SiC

We look at the structure of the electron zone and the density of the DOS state of the compound after fitting from Fig 3 to Fig 6 of each of the atoms in the halogen group with the SiC substrate, we generally use for the fitting electronic orbits of the Halogen group as F, Cl, Br, I with the symbol X, namely the corresponding electronic orbit X(s) orange, X(p_x) red, X (p_y) yellow, and X(p_z) magenta.

First, we investigate the case of the F-atom fusion with the SiC substrate at the three positions of the bridge, hollow, and top of the red orbital F(p_x) electron with very strong energy, with

two characteristic peaks of -0.2 eV and -0.7 eV approximately the same, specifically with the position of the valley of this orbit $F(p_x)$ moving around -2.2 eV and -3.2 eV. In the hollow and top positions, the purple $F(p_z)$ orbit is perpendicular to the fermi and -1.9 eV, but for the bridge position, it is replaced by $F(p_y)$, and the electron orbits $F(p_z)$ coincide with $F(p_x)$. For the valley position alone, the $F(p_z)$ orbit has a very strong peak, but it moves towards -4.8 eV, and a peak is at -1.9 eV. This suggests that the orbital electrons of the F atom, including $F(p_x)$, $F(p_y)$, and $F(p_z)$, have significantly contributed to reducing the Eg band area energy width to zero, making the fissile material metal. We call ΔE the absorbed energy after doping, E_{SiC} the energy of the SiC substrate before doping, E_X the energy of the halogen atom and E_{SiC-X} the energy of the system after doping, we apply the following formula:

$$\Delta E = E_{SiC-X} - E_X - E_{SiC} \quad (1)$$

In terms of initial charge density, the pristine orbital charge density has the form $SiC(s^{12.03}, p^{16.69}, d^{0.0}, tot^{28.73})$ and halogen atoms also have similar orbital charge density. respectively, considering the case of top position (T) which we present in Fig 4, $F(s^{1.72}, p^{3.98}, d^{0.0}, tot^{5.69})$, $Cl(s^{1.62}, p^{3.28}, d^{0.0}, tot^{4.89})$, $Br(s^{1.63}, p^{3.04}, d^{0.0}, tot^{4.67})$, and $I(s^{1.53}, p^{2.65}, d^{0.0}, tot^{4.18})$. After doping together, the results show that the orbital electrons mainly transition to the s and p orbitals. Specifically, for $SiC-F(s^{13.49}, p^{19.26}, d^{0.0}, tot^{32.76})$, $SiC-Cl(s^{13.78}, p^{18.72}, d^{0.0}, tot^{32.10})$, $SiC-Br(s^{13.39}, p^{18.43}, d^{0.0}, tot^{31.84})$, and $SiC-I(s^{13.29}, p^{17.95}, d^{0.0}, tot^{31.26})$. We apply the following formula:

$$\Delta \rho = \rho_{SiC-X} - \rho_X - \rho_{SiC} \quad (2)$$

Then ρ_{SiC-X} is the orbital charge density, ρ_X is the orbital charge density of halogen atom X, and ρ_{SiC} is the orbital SiC.

Table 1: Calculation results for halogens atoms when adsorbed with Si-C

Configuation	no (%)	ΔE (eV)	Si-C (Å)	Si-Si (Å)	Buckling (Å)	Si-C-Si (deg)	Eg (eV)	Mag (μ_B)
SiH (12Si:4H)	100	x	x	2.26	0.75	x	0.33	0
SiC	6:6	x	1.77	x	0	120.00	2.10	0
SiC-F(B)	6:6:1	-1.00	1.87	x	0.10	119.98	0	-0.53
SiC-F(H)	6:6:1	-0.98	1.87	x	0.09	119.96	0	-0.20
SiC-F(T)	6:6:1	-1.02	1.87	x	0.10	119.97	0	0.56
SiC-F(V)	6:6:1	-0.99	1.88	x	0.08	119.99	0	0.57
SiC-Cl(B)	6:6:1	-2.46	1.92	x	0.42	119.20	0	0.26
SiC-Cl(H)	6:6:1	-2.37	1.91	x	0.42	118.75	0	0.99
SiC-Cl(T)	6:6:1	-2.47	1.94	x	0.42	119.19	0	0.38
SiC-Cl(V)	6:6:1	-2.34	1.92	x	0.42	119.99	0	-0.41
SiC-Br(B)	6:6:1	-1.83	1.94	x	0.40	119.32	0	0.41
SiC-Br(H)	6:6:1	-1.82	1.94	x	0.40	119.14	0	0.41
SiC-Br(T)	6:6:1	-1.86	1.9	x	0.41	119.28	0	0.17
SiC-Br(V)	6:6:1	-1.83	1.91	x	0.33	119.97	0	0.83

SiC-I(B)	6:6:1	-1.09	1.94	x	0.36	119.85	0	0.93
SiC-I(H)	6:6:1	-1.08	1.93	x	0.37	119.26	0	0.72
SiC-I(T)	6:6:1	-1.10	1.89	x	0.37	119.42	0	0.06
SiC-I(V)	6:6:1	-1.23	1.85	x	0.37	119.87	0	0.99

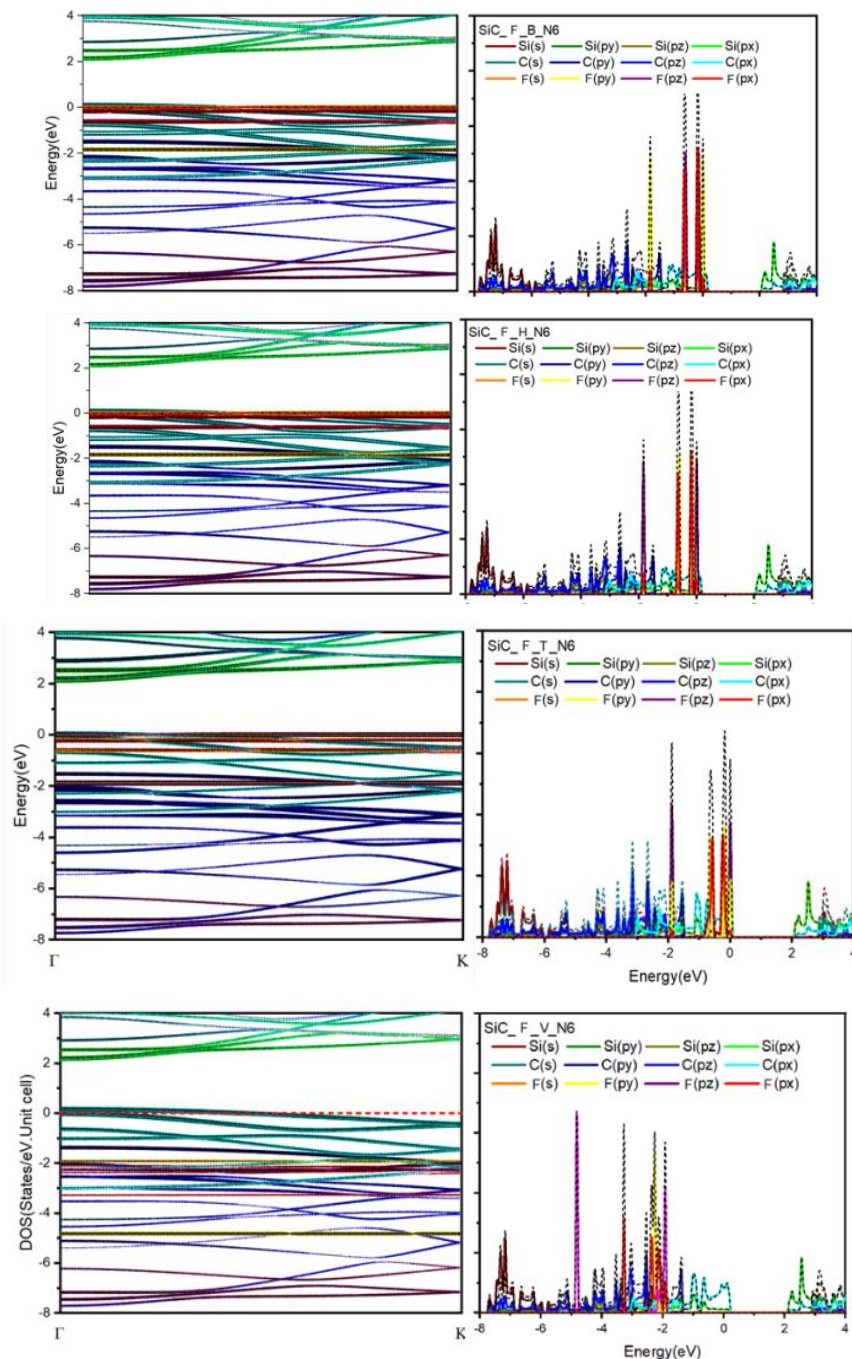


Fig 3. The BAND and PDOS of F adsorbed SiC for 4 positions

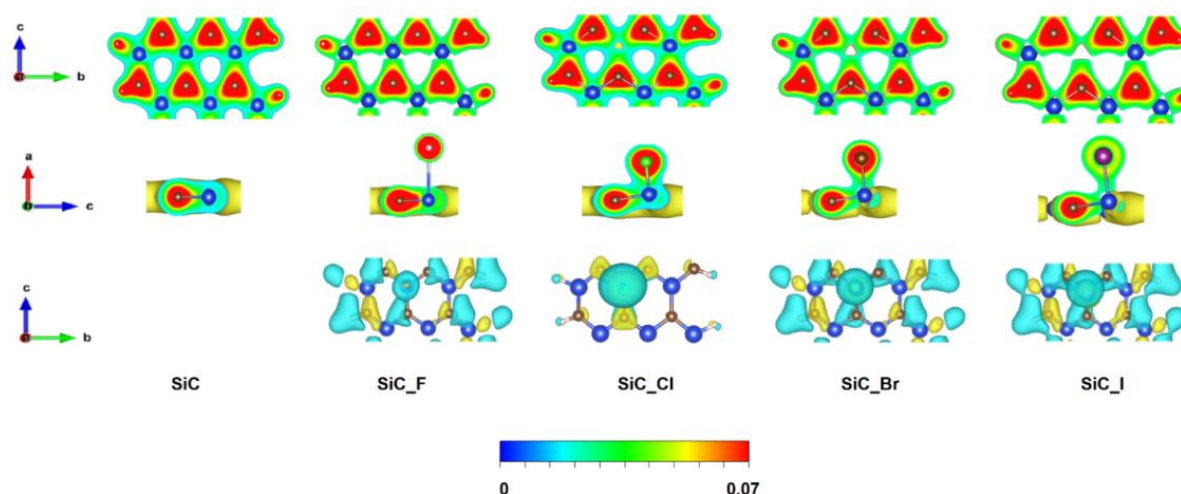


Fig 4. The CHARG of halogen adsorbed Si-C at top positions

For halogen atoms we can calculate the following results:

$$\Delta Q_F(s^{-0.26}, p^{-1.41}, d^{0.0}, tot^{1.66}),$$

$$\Delta Q_{Cl}(s^{0.13}, p^{-1.25}, d^{0.0}, tot^{1.52}),$$

$$\Delta Q_{Br}(s^{-0.27}, p^{-1.30}, d^{0.0}, tot^{1.56}),$$

$$\Delta Q_I(s^{-0.27}, p^{-1.39}, d^{0.0}, tot^{1.65}),$$

CONCLUSIONS

The results of the calculation showed that most of the halogen group atoms mixed with SiC are very small in width, almost metal-like compounds. This result can be applied to the manufacture of SiCs as sensors to detect halogen atoms in the environment; it shows very wide potential applications in practice.

ACKNOWLEDGEMENTS: This research used resources of the high-performance computer cluster (HPCC) at Thu Dau Mot University, Binh Duong Province, Vietnam.

REFERENCES

- [1] K. Novoselov, et al., "Electric field effect in atomically thin carbon films", Science, vol.306, pp. 666–669, 2004.
- [2] D.K. Nguyen, N.T.T. Tran, Y.H. Chiu, G. Gumbs, M.F. Lin, "Rich essential properties of Si-adsorbed graphene", Sci. Rep, vol.10, pp. 1–16, 2020.
3. N.T.T. Tran, D.K. Nguyen, O.E. Glukhova, M.F. Lin, "Coverage-dependent essential properties of halogenated graphene: a DFT study", Sci. Rep. vol.7, pp. 1–13, 2017.
4. N.J. Roome, J.D. Carey, "Beyond graphene: stable elemental monolayers of silicene and germanene", ACS Appl. Mater. Interfaces, vol. 6, pp. 7743–7750, 2014.
- [3] Nguyen, D.K., Tran, N.T.T., Nguyen, T.T. et al. "Diverse Electronic and Magnetic Properties of Chlorination-Related Graphene Nanoribbons". Sci Rep 8, pp. 17859 , 2018.

- [4] M. Pumera, Z. Sofer, “2D monoelemental arsenene, antimonene, and bismuthene: beyond black phosphorus”, *Adv. Mater*, vol. 29, pp. 1605299, 2017..
- [5] S. Huang, W. Kang, L. Yang, “Electronic structure and quasiparticle bandgap of silicene structures”, *Appl. Phys. Lett.* vol.102, pp. 133106, 2013.
- [6] N.T.T. Tran, G. Gumbs, D.K. Nguyen, M.F. Lin, “Fundamental properties of metaladsorbed silicene: a DFT study”, *ACS Omega*, vol.5, pp. 13760–13769, 2020.
- [7] D.K. Nguyen, N.T.T. Tran, Y.H. Chiu, M.F. Lin, “Concentration-diversified magnetic and electronic properties of halogen-adsorbed silicene”, *Sci. Rep* 9, pp. 1–15, 2019.
- [8] C.C. Liu, H. Jiang, Y. Yao, “Low-energy effective Hamiltonian involving spin-orbit coupling in silicene and two-dimensional germanium and tin”, *Phys. Rev. B*, vol.84, pp. 195430, 2011.
- [9] M. Ezawa, “Valley-polarized metals and quantum anomalous Hall effect in silicene”, *Phys. Rev. Lett*, vol.109, pp. 055502, 2012.
- [10] C.C. Liu, W. Feng, Y. Yao, “Quantum spin Hall effect in silicene and two-dimensional germanium”, *Phys. Rev. Lett.* vol.107, pp. 076802, 2011.
- [11] M. Ezawa, “A topological insulator and helical zero mode in silicene under an inhomogeneous electric field”, *New J. Phys*, vol.14, pp. 033003, 2012.
- [12] A. Molle, C. Grazianetti, L. Tao, D. Taneja, M.H. Alam, D. Akinwande, “Silicene, silicene derivatives, and their device applications”, *Chem. Soc. Rev*, vol.47, pp. 6370–6387, 2018.
- [13] L. Venema, “Silicon electronics and beyond”, *Nature*, vol.479, pp. 309-309, 2018.
- [14] N.D. Drummond, V. Zolyomi, V.I. Fal’Ko, “Electrically tunable band gap in silicene”, *Phys. Rev. B*, vol. 85, pp. 075423, 2012.
- [15] M.A. Kharadi, G.F.A. Malik, F.A. Khanday, K.A. Shah, S. Mittal, B.K. Kaushik, “Silicene: from material to device applications”, *ECS J. Solid State Sci. Technol*, vol. 9, pp 115031, 2020.
- [16] Z. Ni, et al., “Tunable bandgap in silicene and germanene”, *Nano Lett*, vol.12, pp. 113–118, 2012.
- [17] Y. Du, et al., “Tuning the bandgap in silicene by oxidation”, *ACS Nano*, vol. 8, pp. 10019–10025, 2014.
- [18] S.Y. Lin, S.L. Chang, N.T.T. Tran, P.H. Yang, M.F.H. Lin, “Si–Si bonding-induced unusual electronic properties of silicene: a method to identify hydrogen concentration”, *Phys. Chem. Chem. Phys*, vol. 17, pp. 26443–26450, 2015.
- [19] R. Quhe, et al., “Tunable and sizable band gap in silicene by surface adsorption”, *Sci. Rep*, vol. 2, pp.1–6, 2012.

- [20] B. Huang, H.J. Xiang, S.H. Wei, "Chemical functionalization of silicene: spontaneous structural transition and exotic electronic properties", *Phys. Rev. Lett*, vol. 111, pp.145502, 2013.
- [21] R. Qin, C.H. Wang, W. Zhu, Y. Zhang, "First-principles calculations of mechanical and electronic properties of silicene under strain", *AIP Adv*, vol.2, pp. 022159, 2012.
- [22] H. Fu, J. Zhang, Z. Ding, H. Li, S. Meng, "Stacking-dependent electronic structure of bilayer silicene", *Appl. Phys. Lett*, vol.104, pp. 131904, 2014.
- [23] C. Lian, J. Ni, "The effects of thermal and electric fields on the electronic structures of silicene", *Phys. Chem. Chem. Phys*, vol.17, pp.13366–13373, 2015.
- [24] Y.L. Song, Y. Zhang, J.M. Zhang, D.B. Lu, "Effects of the edge shape and the width on the structural and electronic properties of silicene nanoribbons", *Appl. Surf. Sci*, vol.256, pp. 6313–6317, 2010.
- [25] Thanh Tung Nguyen, V. N. Hoang, T. P. T. Huynh, D. K. Nguyen, V. O. Vo, "Diverse structural and electronic properties of carbon-substituted armchair silicene nanoribbons: A first-principles study", *Physica E*, vol.142, pp.115309, 2022.

NANOMATERIALS SYNTHESIS AND PROCESSING

Review on Synthesis and Evaluation Performance of Ap Based Solid Composite Propellants with GO and CNT as Burning Catalyst

Muhammad Faizridhwan **Ramle**³, Norkhairunnisa **Mazlan**^{1,2,3}

¹ Aerospace Malaysia Research Centre (AMRC), Universiti Putra Malaysia, 43400 UPM Serdang, Selangor

² Department of Aerospace Engineering, Faculty of Engineering, Universiti Putra Malaysia, UPM Serdang, Seri Kembangan 43400, Selangor Darul Ehsan, Malaysia

³ Nanomaterials Processing and Technology Laboratory, Institute of Nanoscience and Nanotechnology (ION2), Universiti Putra Malaysia, 43400 UPM Serdang, Selangor

*Corresponding author's phone: +603-9769 6403

E-mail: norkhairunnisa@upm.edu.my

Abstract: Military sources widely utilize composite solid propellant (CSP) to fabricate weapons, while aerospace industries use it for rocket propulsion. Due to its stability and high burning efficiency, AP has been a popular choice for oxidizers. However, AP needs an additive catalyst to improve CSP's thermal and mechanical performance. The first part of this review paper will explain aluminum (Al) as a metallic fuel. The researcher explores the properties of the aluminum used in CSP that can improve performance. In addition, the study highlights the synthesis of diverse burning catalysts using AP and other metallic fuels, examining their impact on the system. Finally, this paper examines the synthesis of graphene oxide (GO) and carbon nanotubes (CNT) using Al, highlighting the achieved improvements. highlighting the achieved improvements, for example, GO at 1 wt% increases the burning rate from 8.3 mm/s to 11.1 mm/s. Other than that, Al/CNT improves the burning rate from 1.18 mm/s to 2 mm/s with 1 wt% of CNT. This review aims to provide a comprehensive overview of Al/GO and Al/CNT as burning catalysts that can improve the performance of AP-based CSP since it can be applied in the military or aerospace industry for rocket improvement.

Keywords: Ammonium perchlorate (AP), Aluminum (Al), Catalyst, Carbon nanotube (CNT), Composite solid propellant (CSP), Graphene oxide (GO)

INTRODUCTION

A type of jet propulsion known as rocket propulsion uses stored matter known as propellant to produce thrust [1]. Specifically for model rockets, a motor generates thrust by ejecting burned propellant at high velocities, thereby increasing rocket velocities [2]. In addition to overcoming gravitational force, the fuel, also known as propellant, aids in accelerating against gravity to reach space [3]. The propellants typically fall into one of three categories: solid, liquid, or hybrid. The performance of a rocket relies upon the decision of fuel with proper qualities regarding weight, power, and execution boundaries [4].

Types of Rocket Propellant

In solid state, solid propellants are a mixture of fuel and oxidizer [5]. It is used in space shuttles, military weapons, and other applications as an energetic particle [6]. The propellant's simplicity, dependability, storage capacity, high thrust, mass flow during launching, and other characteristics are intriguing [7]. Simpler rockets like boosters and fireworks typically use them due to their lower efficiency and inability to throttle or restart once ignited [8].

According to researcher [9], liquid propellants are propellant products in liquid form, stored in separate tanks, and fed into the combustion chamber where they ignite. Liquid propellants offer greater efficiency and control than solid propellants but are also more complex and expensive [10].

Hybrid propellants are propellants that combine a solid fuel with a liquid or gaseous oxidizer [11]. They offer some of the advantages of both solid and liquid propellants, such as the simplicity of solid propellants and the controllability of liquid propellants [12]. However, hybrid propellants are also more complex to develop and manufacture than solid propellants [13].

Solid rocket motors have become increasingly popular as aerospace technology advances because of their many benefits. Compared to liquid propellant, solid propellant has short volume, extended storage cycle, good performance, high safety, and ease of use. Current propellants often lack precise control over burning rates, limiting performance optimization for different missions. Thus, this paper will explain on how to overcome those gaps.

Composite Solid Propellant

Composite Solid Propellant (CSP) is an essential component in the construction of any effective solid rocket motor [14]. Without CSP, achieving the necessary attitude, distance, and force for a rocket would be challenging and highly unlikely to succeed. Current CSPs have fixed burning rates once ignited, making it difficult to optimize propulsion for various stages of flight or mission profiles. To improve the performance liability, additive can be added in the propellant. CSP consists of many constituents that form a heterogeneous mixture. These elements include oxidizers (such as perchlorates, nitrates, nitramines, and nitramides), energetic fuels (in the form of fine metallic powders), binder, and other additives [15]. Oxidizers used to provide the fuel with the necessary oxygen for a self-sustaining exothermic reaction, generating the hot gases that propel the rocket. Fuels react with the oxidizer to release energy and generate hot gases while the binder holds the propellant grains together, ensures proper burning characteristics, and maintains structural integrity during storage and launch.

Rocket propellants commonly use Ammonium perchlorate (AP) as an oxidizer due to its advantageous energy properties, such as high thermal stability, specific impulse, low shock sensitivity, great compatibility, and extended shelf life. Some researcher [16] prefer AP due to its increased density and greater oxygen content. AP component constitutes about 60% of the weight of CSPs [17]. Hence, the velocity of AP breakdown is a crucial factor that directly influences the propellant's performance [18].

Other than that, hydroxyl-terminated polybutadiene (HTPB) is an example of good binder in CSP because it can bind the various propellant ingredients, such as the oxidizer, fuel, and any additive

materials, together into a stable and homogeneous mass [19]. This guarantees the uniform distribution of all components and their effective contributions during combustion.

The propellant burning rate goes up when the AP particle diameter is reduced; however, reducing the particle diameter beyond a certain point does not provide an increase in the burning rate and can result in processing issues and safety concerns during grain manufacturing. The agglomerate event can affect CSP's performance. It reacts with compounds that have a reducing effect, releasing significant amounts of energy and force [20]. Various additives, including catalysts, can modify the burning rates and ballistic properties of AP-based CSP, in addition to its dependence on particle size [21].

In order to get a consistent burning rate and a low pressure exponent, it is advisable to incorporate a burning rate catalyst into the propellant [22]. Adding a catalyst, like ferric oxide (Fe_2O_3), can change how quickly the oxidizer breaks down, which lets the burning rate of the propellant be more precisely controlled [23]. Moreover, reseracher [24] suggest using catalysts synthesized with fuel to boost the reaction rate and lower the reaction temperature.

APPLICATION OF SYNTHESIS GO AND CNT AS CATALYST IN AP BASED CSP

Rockets depend on AP-based CSP as their primary engines, although it has the potential to improve their combustion efficiency. Nevertheless, a novel technique called in-situ synthesis offers a more straightforward resolution [25]. In this case, the propellant mixture consists of metallic fuels like as aluminium or boron. During the process of burning, these fuels undergo a chemical reaction with AP oxides, resulting in the formation of metal oxides that function as catalysts [26]. An benefit of the in-situ technique is that catalyst particles are optimally sized and evenly dispersed inside the propellant, resulting in enhanced efficiency and controlled combustion [27].

Utilizing aluminium (Al) as a fuel in AP-based CSP

Aluminium (Al) is an essential component in the creation of CSP. Solid propellants sometimes use aluminium powder as a metallic fuel to improve the energy efficiency of solid rocket motors [28]. Al metal is a very promising catalyst because it has the potential to attain a high burning rate, is easy to make, uses readily available ingredients, and is inexpensive to manufacture [29]. Fig. 1 [30] indicate that the ilustration of AP, binder, and catalyst in a rocket.

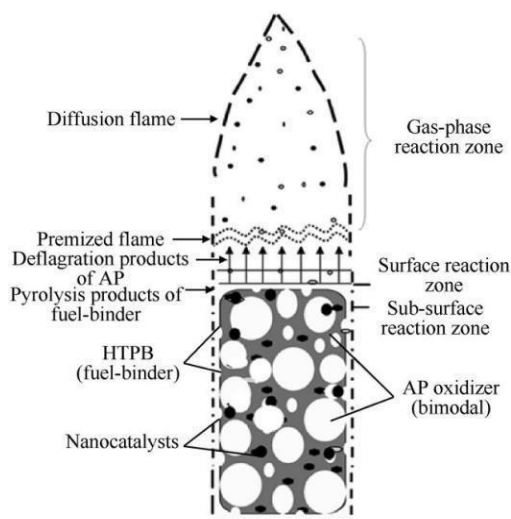


Figure 2.1: Illustration inside CSP [30].

Researchers have used boron (B) and magnesium (Mg) as alternative fuels in CSP, instead of employing Al as a metallic fuel [31]. Despite its lower weight compared to aluminium and its high energy density, magnesium is more challenging to store due to its increased reactivity with atmospheric water vapour. Moreover, boron has an exceptionally elevated energy density; nonetheless, it might be challenging to initiate combustion, resulting in the production of a hazardous residue upon burning.

The research conducted by Korotkih et al. (2018) [32] demonstrates that substituting the ASD-4 aluminium powder with boron powder results in a reduction of the ignition delay time of solid fuel samples by a factor of 2.2–2.8 as can be seen in Fig. 2. By using aluminium borides, fuels may decrease their ignition delay time by 1.7–2.2 times compared to the original composition. There was a disparity in the time it took for high-energy materials (HEM) to ignite when exposed to radiant heating. Upon analysis, it was shown that this phenomenon is correlated with the pace of the oxidation process and the heat generated during the heating and ignition of the metal additives used.

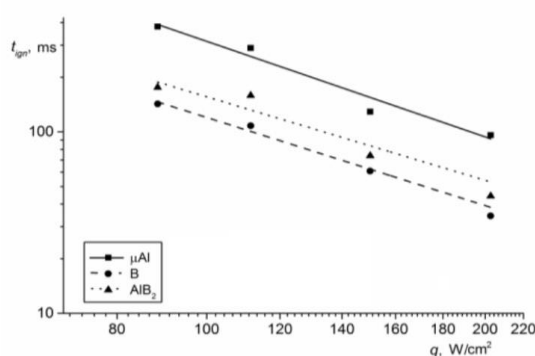


Fig. 2: Ignition delay time vs laser heat flux density [32]

Nanoaluminum and microaluminum

Within the realm of CSP applications, Al is often used in two separate manifestations: either as nanoparticles with dimensions on the nanometer scale or as particles with dimensions on the micrometre scale. The ignition temperature of nano-sized aluminium (n-Al) is lower and its reactivity is higher in comparison to micro-sized aluminium (μ -Al) [33]. However, n-Al tends to aggregate and has a greater ratio of non-reactive Al_2O_3 . For example, a nanoparticle made of aluminium (n-Al) measuring 50 nm in diameter is coated with a layer of aluminium oxide (Al_2O_3) that is about 2 nm in thickness. The shell constitutes around 30% of the overall mass of the n-Al particle. Thus, μ -Al particles [34] are still extensively used in practical applications.

The ignition delay of formulations including nAl is shorter compared to formulations containing μ Al. Fig. 3 [35] state that nAl powders have properties that make them simpler to ignite, such as smaller particle size, bigger specific surface area, thinner oxide layer thickness, and improved interaction with other propellant components. The minimal slopes of the curves that show the relationship between ignition delay time and radiant flux also indicate the chemical activity of nAl, which enhances the release of heat in the condensed phase [36].

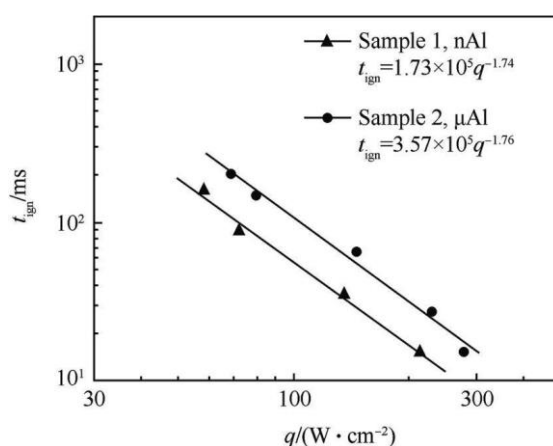


Fig. 3: Ignition delay vs radiant flux intensity at atmospheric pressure [36]

Synthesis AL with burning catalyst in AP based CSP

In order to enhance efficiency, researchers added or developed catalysts in conjunction with Al. When constructing a solid composite propellant, it is crucial to consider the burning rate, total impulse, and thrust as the primary considerations. According to researchers [37], the use of extra burning rate catalysts may improve the ballistic performance of rocket propellant. These catalysts work by reducing the activation energy needed for combustion and enhancing the thermal breakdown process. Furthermore, the use of a highly efficient combustion catalyst to improve performance is the most cost-effective method for developing rocket motors [38]. These catalysts are compatible with all propellant compositions.

Catalyst effect on burning rate performance in AP based CSP

Elbasuney and El-Sayyad (2020) [39] state that the burning rate catalyst has advantageous effects on the CSP. For example, burning rate catalysts may be readily found on the market at affordable rates. Only a tiny fraction of weight is required for fuel and CSP production, and they have the ability to enhance the performance of rocket propellant. Therefore, previous research has used several catalysts to examine the improvements achieved with different types of combustion catalysts. Table 1 demonstrates that prior research used several catalysts to augment the combustion rate of the CSP.

Table 1: Burn Rate of AP/HTPB/AL with different types of catalyst

Formulation	Catalyst	%wt	Burn Rate (mm/s)	References
AP/HTPB/AL-CATOCENE	CATOCENE	2	-	[18]
AP/HTPB/AL-HIC	HIC	5	40.3	[40]
AP/Al/HTPB- n-Fe ₂ O ₃	n-Fe ₂ O ₃	1	35.4	[41]
		2	38.2	
AP/Al/HTPB- Graphene	Graphene	1	6.4	[42]
AP/Al/HTPB- n-TiO ₂	n-TiO ₂	1	7.9	
AP/Al/HTPB-GTNC	GTNC	1	9.1	
AP/AL/HTPB	-	1	10.37	[43]
AP/AL/HTPB-G-792-Fe	G-792-Fe	1	13.36	
AP/Al/HTPB-Butane/HTPB	Butane/HTPB	0.11	12.15	[44]
		0.42	14.65	
		1	19.03	
		2.33	21.2	
AP/AL/HTPB - Fe	Fe	1	15.69	[45]

The impact of catalysts on the mechanical characteristics of CSP.

CSPs are prone to deterioration over time as a result of variables such as temperature variations and storage conditions. CSP may be evaluated for changes in mechanical properties by the use of destructive testing. The tensile strength and other mechanical qualities may degrade with time. For example, research papers state that by adding 1% of graphene as catalyst, it can improve the maximum tensile strength of AP-HTPB propellant from 1.33 to 2.01 MPa [46]. Destructive testing is used to assess the remaining operational lifespan of the propellant. Destructive testing may detect the occurrence of undesired breakdown products that may affect stability.

The normal composition of solid propellant formulations includes nanocatalysts, which are commonly included in Al powder at a mass percentage (wt%) ranging from 5% to 10% [47]. The study conducted by Cheng et al. (2020) [7] used cobalt (Co) wt% Al powder as a sample to investigate the synthesis efficiency of Co/Al composite fuels. This research demonstrates that Co/Al composite fuels with 9.1 wt% Co effectively encapsulate the Al particles and exhibit thermal stability up to 1000 °C without any breaking of the Al particles. This is because the increased concentration of cobalt (Co wt%) is unable to attain the threshold energy required for oxidation-induced rupture.

The impact of catalyst on the process of thermal decomposition

Cobalt nitrate (CoFe_2O_4) indicated as an example of a catalyst that can improve thermal decomposition., which can decrease the value of high thermal decomposition, T_{HTD} by 108.99 C. The surface of CoFe_2O_4 acts as a Lewis acid, attracting electrons from the oxidizer molecule and weakening specific bonds. This weakens the overall structure of the oxidizer, making it easier to decompose. Also, Liu et al. (2023) [48] paper says that Xiong et al. (2016) [49] used a colloidal crystal template method to make nano CoFe_2O_4 with a three-dimensional porous structure. The synthesised CoFe_2O_4 particles have a pore size of around 200 nm and a distinctive spinel structure. The material has a specific surface area of 55.646 m²/g, which is significantly greater than that of the 40 nm spherical CoFe_2O_4 . Furthermore, link between the reactant effects of permeable nano CoFe_2O_4 and circular nano CoFe_2O_4 on how well AP worked with warm corruption when using DSC were found.

Fig. 4, depicts the DSC curves. The high-temperature decomposition (HTD) of AP may be effectively reduced by up to 91.46 °C at a concentration of 6% porous nanoco Fe_2O_4 . Also, the porous CoFe_2O_4 might expand the intensity of the disintegration interaction by up to 1120.88 J/g, which is 2.3 times more prominent than unadulterated AP. Porous nanocomposite metal oxides (MOs) possess a substantial specific surface area of 55.646 m²/g, enabling them to efficiently adsorb a significant quantity of substances. Consequently, the gaseous byproducts that are generated adhere to the surface of the permeable nanocomposite CoFe_2O_4 (refer to Fig. 5). Subsequently, following electron transfer at the active site, the gaseous intermediate products are released and isolated from the surface of the pore to produce final products such as hydrogen chloride (HCl), water (H₂O), chlorine gas (Cl₂), oxygen gas (O₂), nitrogen monoxide (NO), nitrous oxide (N₂O), and nitrogen dioxide (NO₂).

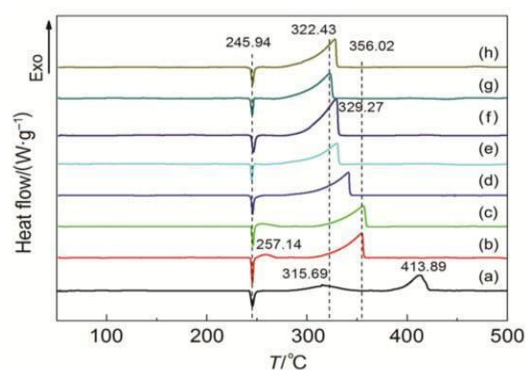


Fig. 4: DSC curves of the AP decomposition in the absence and presence of different blend ratios of nanoporous CoFe_2O_4 [48]

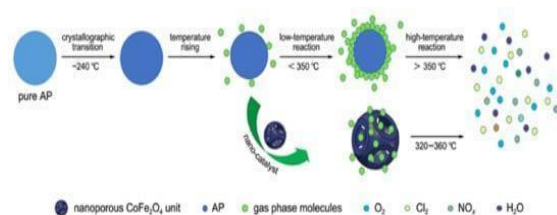


Fig. 5: Schematic diagram of the thermal AP decomposition process in the absence and presence of nanoporous CoFe_2O_4 [48]

Comparison between Al/GO and Al/CNT

Graphene oxide (GO) possesses a lattice structure that is two-dimensional, and its density is 1.8 g/cm³. Some researchers [34] propose the combination of GO and Al to preserve a substantial energy density and a significant Al mass content. The oxygen functional groups on GO could serve as attachment points for other performance-enhancing additives, allowing for more targeted modification of propellant properties. Graphene forms a connection with the surface of the metal nanoparticle, which stops the catalyst particles from coming together in a group [50]. Although nanoscale catalysts provide various advantages, their extensive surface area can adversely impact the mechanical characteristics of solid rocket propellants. Due to the catalyst's large surface area, an extra binder is required to ensure thorough coverage of all surfaces. Fig. 6 illustrates the potential placement of graphene in CSP to mitigate agglomeration between AP and Al.

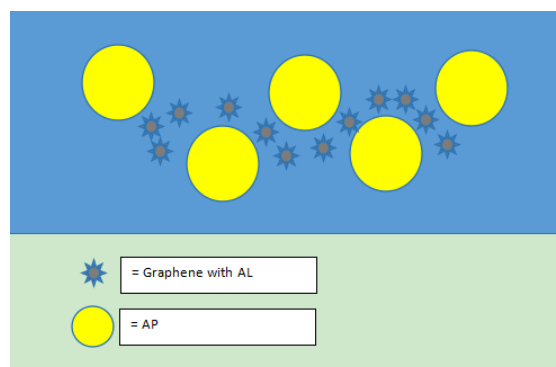


Figure 2.7: Graphene prevent agglomerate of AP in CSP

Instead of GO, carbon nanotube (CNT) has similar performance in terms of manufacturing and outcomes. Rao et al. (2016) [51] found that CNT can boost the burning rate of AP/HTPB propellants

by 10–30% compared to propellants without a catalyst. According to research [30], CNTs can lead to a burning rate enhancement of 15 to 40% compared to GO. The magnitude of the increase is dependent on variables such as the type of CNT, its concentration, and its dispersion within the propellant matrix. CNT has a high aspect ratio and a large surface area per unit mass [52]. This facilitates increased contact between the catalyst and the adjacent AP particles. The surface area of CNT can vary between 50 and 1300 m²/g, depending on the exact kind [53]. GO, like CNTs, has a large theoretical surface area of about 2600 m²/g because it is made up of a sheet that is only one atom thick [54]. The large surface area allows for a sufficient number of active sites for catalytic reactions to occur.

Method of Synthesis: Al/GO and Al/CNT

Some researchers have demonstrated the synthesis of Al/GO using Hammer's method [55]. The process began by creating a GO suspension (1.0 mg/mL) through sonication of graphite oxide powder in N-dimethylformamide (DMF) for 2 hours. An Al suspension (10 mg/mL) was prepared by dispersing Al nanoparticles in a DMF/isopropanol (1:1) solvent mixture. The GO suspension was then added to the Al suspension and ultrasonically dispersed for 1 hour. The resulting mixtures were centrifuged at 11,000 rpm for 20 minutes, and the obtained precipitants were dried in a vacuum oven at 60°C to remove any residual solvent, yielding the GO/Al nanocomposites.

However, researchers have discovered a variety of methods for synthesizing CNT with Al. For example, ball milling, ultrasonication, cold press, sinetering, and hot extrusion. In order to create a composite material, aluminum powder and carbon nanotubes (CNTs) are mixed together using the powder metallurgy method. To equally distribute the CNTs throughout the aluminum matrix, mechanical mixing—often accomplished by ball milling—is the first step in the process. To produce a solid preform, the powder is combined and then cold-compacted under high pressure. After that, this preform is sintered at temperatures lower than the melting point of aluminum, which permits the bonding of the metal particles while preserving the CNTs' structural integrity [56].

Furthermore, align the CNTs for better characteristics and further densify the material, further procedures like hot pressing or extrusion may be used. According to research [57], multiwall carbon nanotubes (MWCNTs) can produce Al/MWCNT composites via ball milling and hot extrusion. For grain sizes less than 70 nm, the efficiency of reinforcing with carbon nanotubes follows the discontinuous fiber volume fraction rule. The study said that using a normal powder metallurgy method, it is possible to make large-scale Al/CNT composites with CNT that are aligned in a single direction.

Hammer's method requires special equipment and expertise to handle the process. Compared to ball milling, it can be less complex equipment and also allows for precise control over the final properties of the propellant. However, it is not suitable for large scale production, and it is difficult to achieve high purity of the propellant.

Characterize catalyst

There are some characterizations can be made in order to evaluate the performance of the synthesized for example, Scanning Electron Microscopy (SEM), X-ray Diffraction (XRD), Thermogravimetric Analysis (TGA), and Differential Scanning Calorimetry (DSC). A Scanning Electron Microscope (SEM) was used to examine the morphology of the synthesis. Thermogravimetric Analysis (TGA) and Differential Scanning Calorimetry (DSC) were carried out to measure the thermal analysis in which

samples were heated from 25 to 1000°C at a rate of 10 K min⁻¹. To analyze the crystalline phase of the synthesis for both elements, X-ray Diffractometer (XRD) will be use.

In terms of DSC performance, graphene reduces both the high temperature decomposition (HTD) and low temperature decomposition (LTD) but has no effect on the crystallographic transition process of AP when compared to pure AP. The LTD drops by 0.7 °C until 28.9 °C, and the HTD decreases by 0.7 °C until 68.3 °C, respectively, after adding 0.5 wt.%, 1 wt.%, 2 wt.%, and 3 wt.% graphene [58]. Other than that, according to the research [58,59], graphene and CNT can reduce the particles size of agglomeration by using SEM detector.

The Impact of GO on Thermal Decomposition.

According to research [60], the use of GO as a catalyst can enhance the heat of reaction for oxidizers like polyvinylidene fluoride (PVDF). This paper proved the statement by doping 0.5% GO into PVDF/CuO/Al samples. The results indicate that adding 0.5 wt% of GO to PVDF increases its reaction heat to 3809.1 J/g, which is 1.1% higher than that of pure PVDF, due to GO's catalytic effect. However, higher concentrations of GO are detrimental to energy enhancement. At 1 wt% and 3 wt% GO, the reaction heats for PVDF decrease to 3491.0 J/g and 3244.0 J/g, respectively, which are both lower than the reaction heat of pure PVDF. Thus, it shows that only 0.5 wt% of GO are needed to improve reaction of heat of PVDF/CuO/Al and the excess GO will decrease the performance of the samples.

Zhu et al. (2021) [61] demonstrated that incorporating 10 wt.% fluorinated graphene (FG) reduces the maximum flame time (t') while increasing the stable burning time (t''), thus enhancing time of combustion stability. However, when the FG content increases from 15 to 25 wt.%, t' increases and t'' decreases, attributed to the rise in combustion intensity and energy release rate. These findings indicate that FG improves fuel combustion stability and energy release.

The impact of carbon nanotubes on thermal decomposition

The exact decomposition temperature is influenced by factors such as the type (single-walled vs. multi-walled) of carbon nanotubes (CNTs), their purity, and the surrounding atmosphere. Other than that, agglomeration of CNT hinder the Uniform dispersion of CNTs within the TNP/TNR matrix is crucial for maximizing the heat transfer and catalytic effects. However, research indicates that additives have a much smaller effect on the burning rate of picric acid (TNP) compared to styphnic acid (TNR). For instance, at a pressure of 2 MPa, adding 1% CNT increases the burning rate of TNP by approximately 1.4 times and TNR by about 2 times [62].

Al/GO can be seen to improve the burning rate of the composite from Graphene at 1 wt% increases the burning rate from 8.3 mm/s to 11.1 mm/s. Other than that, Al/CNT improves the burning rate from 1.18 mm/s to 2 mm/s with 1 wt% of CNT. Both shows an improvement but GO takes the slight lead. Moreover, GO lowers the activation energy required for the decomposition of other materials in a composite compared to CNT, impact on overall decomposition temperature depends on the specific type and interaction with the other material.

CONCLUSION

This can conclude from reviewing most past research papers that CSP is an essential component in the construction of any effective solid rocket motor. The performance of CSP depends on many constituents that form a heterogeneous mixture, including oxidizers, energetic fuels, burning rate regulators, and other additives. Since AP is considered widely used due to its exceptional mix of

features, it enables the rocket motor to sustain highly efficient burning. However, the propellant's performance may suffer due to the easy absorption of AP. Therefore, adding a catalyst can prevent the agglomerate event.

In this review, many researchers have mixed their own oxidizer with various types of burning catalysts in order to achieve their own objective, which is to improve the propellant's properties. Furthermore, the size of the materials used significantly influences their performance. It is evident that the propellant mechanism benefits greatly from the reduction of Al's size from micro to nanosized, as it reduces the propellant's ignition delay time. Other than that, nanocatalysts such as nanoferric oxide (nFe₂O₃) can influence the pace at which the oxidizer decomposes and allow for more accurate regulation of the propellant's burning rate.

In addition, this review has explained various methods for synthesizing GO and CNT with Al. Synthesis Al/GO using the Hammers method, ultrasonic method, or electrospinning [57]. Given the variety of methods available for Al/CNT synthesis, one can combine two methods to synthesize it and compare the resulting value with other methods. This can be observed that the small amount of addition of GO and CNT to produce Al/CNT and Al/GO enhances the propellant's properties such as burning rate and thermal decomposition without significantly increasing the weight of the materials.

RECOMMENDATION

The use of dangerous chemicals like sulfuric acid in its synthesis raises worries for the environment and public safety, and the expensive cost of raw materials exacerbates challenges with economic viability. These are the constraints of using GO and CNT in industrial processes. Post-synthesis processing problems with both compounds include challenging dispersion and intricate purification. Significant obstacles also include the health concerns of inhaling nanoparticles and the environmental effects of disposing of trash. Ultimately, large-scale adoption is complicated by the need for scalability, which calls for tackling murky legislative frameworks, dependable supply networks, and interoperability with current industrial processes.

However due to GO's strong reactivity, ignition temperatures may be lowered, resulting in faster and more regulated burn rates and a lesser chance of inadvertent detonations. Because of their enormous surface area and thermal stability, CNTs may encourage more uniform energy release, enhancing the dependability and consistency of propulsion systems. Additionally, these substances could lessen the requirement for pricey metallic catalysts, which would cut production prices all around. On the other hand, using them might cause environmental problems. Thus, GO and CNT are highly expectation for future years due to drastic improvement that have contribute in past research.

ACKNOWLEDGEMENTS: The authors would like to express their gratitude to Universiti Putra Malaysia (UPM) for providing the assistance and resources necessary to conduct this review study

REFERENCES

- [1] A. Y. Alemayehu and L. G. Solomon, "Design of a Solid Rocket Propulsion System," *International journal of aeronautical science & aerospace research*, pp. 224–229, Jul. 2020.
- [2] N. Achara, G. C. Japheth, W. C. Solomon, and M. Bonet, "FACTORS THAT INFLUENCE THE OPERATION OF THE ROCKET SYSTEM," *Nigerian Journal of Engineering Science and Technology Research*, vol. 8, no. 2, pp. 151–156, 2022.
- [3] J. Akhavan, *The Chemistry of Explosives 4E*. Royal Society of Chemistry, 2022. Accessed: Jun. 07, 2024.
- [4] S. K. Pradhan, V. Kedia, and P. Kour, "Review on different materials and their characterization as rocket propellant," *Materials Today: Proceedings*, vol. 33, no. 8, Mar. 2020.

- [5] J. P. Lichthardt *et al.*, “Novel Segregated Solid Propulsion System with Separately Stored Fuel and Oxidizer,” *Propellants, Explosives, Pyrotechnics*, vol. 47, no. 11, Jul. 2022.
- [6] T. M. Klapötke, *Chemistry of High-Energy Materials*. Walter de Gruyter GmbH & Co KG, 2022.
- [7] B. P. and C. M. Roland, “SOLID PROPELLANTS,” *Rubber Chemistry and Technology*, vol. 92, no. 1, pp. 1–24, Jan. 2019.
- [8] R. J. Rocha, “Accelerated Aging Tests of HTPB-Based Propellants,” *Advances in chemical and materials engineering book series*, pp. 246–271, Jan. 2018.
- [9] N. Ringas, “Propellant Feed Assembly Design for a Pressure-Fed 1 kN Liquid Propellant Rocket Engine Test Platform,” *Southern space studies*, pp. 25–45, Jan. 2022.
- [10] S. Pérez-Roca *et al.*, “A survey of automatic control methods for liquid-propellant rocket engines,” *Progress in Aerospace Sciences*, vol. 107, pp. 63–84, May 2019.
- [11] G. Risha, E. Boyer, R. Wehrman, and K. Kuo, “Performance Comparison of HTPB-Based Solid Fuels Containing Nano-Sized Energetic Powder in a Cylindrical Hybrid Rocket Motor,” *38th AIAA/ASME/SAE/ASEE Joint Propulsion Conference & Exhibit*, Jul. 2002.
- [12] A. Okninski, W. Kopacz, D. Kaniewski, and K. Sobczak, “Hybrid rocket propulsion technology for space transportation revisited - propellant solutions and challenges,” *FirePhysChem*, vol. 1, no. 4, pp. 260–271, Dec. 2021.
- [13] A. Karabeyoglu, “CHALLENGES IN THE DEVELOPMENT OF LARGE-SCALE HYBRID ROCKETS,” *International journal of energetic materials and chemical propulsion*, vol. 16, no. 3, pp. 243–261, Jan. 2017.
- [14] Y. Liu *et al.*, “Application of 3D energetic metal-organic frameworks containing Cu as the combustion catalyst to composite solid propellant,” *Combustion and Flame*, vol. 225, pp. 57–64, Mar. 2021.
- [15] F.-M. Dîrloman, A.-N. Rotariu, T. Rotariu, G.-F. Noja, R.-E. Ginghină, and N.-D. Zvîncu, “Ballistic and thermal characterisation of greener composite solid propellants based on phase stabilized ammonium nitrate,” *Case studies in thermal engineering*, vol. 54, pp. 103987–103987, Feb. 2024.
- [16] H. Naseem, J. Yerra, H. Murthy, and P. A. Ramakrishna, “Ageing studies on AP/HTPB based composites solid propellants,” *Energetic Materials Frontiers*, vol. 2, no. 2, pp. 111–124, Jun. 2021.
- [17] J. Ashish, G. Swaroop, and B. Kandasubramanian, “Effect of Ammonium Perchlorate Particle Size on Flow, Ballistic, and Mechanical Properties of Composite Propellant,” *Nanomaterials in Rocket Propulsion Systems*, pp. 299–362, Jan. 2019.
- [18] J. Liu, L. Wang, L. Wang, S. Z. Vatsadze, Z. Huang, and B. U. Amin, “A review on synthesis of Fe-based compounds and their properties as the burning rate catalysts for propellants,” *Journal of Organometallic Chemistry*, vol. 980–981, pp. 122514–122514, Sep. 2022.
- [19] J. A. Vara, P. N. Dave, and V. R. Ram, “Nanomaterials as modifier for composite solid propellants,” *Nano-structures & nano-objects*, vol. 20, pp. 100372–100372, Oct. 2019.
- [20] S. Isert, L. J. Groven, R. P. Lucht, and S. F. Son, “The effect of encapsulated nanosized catalysts on the combustion of composite solid propellants,” *Combustion and flame*, vol. 162, no. 5, pp. 1821–1828, May 2015.
- [21] A. R. Demko, “Advancements in Composite Solid Propellant Testing and Evaluation for Formulations Containing Novel Nano-Additives,” *oaktrust.library.tamu.edu*, May 02, 2017.
- [22] M. Zhang *et al.*, “Novel graphene iron organic nanocomposites for enhancing combustion and safety properties of AP-HTPB propellant,” *Combustion and flame*, vol. 263, pp. 113420–113420, May 2024.
- [23] Z. Ma, F. Li, and H. Bai, “Effect of Fe₂O₃ in Fe₂O₃/AP Composite Particles on Thermal Decomposition of AP and on Burning Rate of the Composite Propellant,” *Propellants, Explosives, Pyrotechnics*, vol. 31, no. 6, pp. 447–451, Dec. 2006.

- [24] J. Gao, L. Wang, H. Yu, A. Xiao, and W. Ding, "Recent Research Progress in Burning Rate Catalysts," *Propellants, Explosives, Pyrotechnics*, vol. 36, no. 5, pp. 404–409, Sep. 2011.
- [25] A. R. Demko *et al.*, "Temperature Sensitivity of Composite Propellants Containing Novel Nano-Additive Catalysts," *Journal of Propulsion and Power*, vol. 34, no. 3, pp. 795–807, Dec. 2017.
- [26] A. R. Demko, J. A. Lajoie, A. R. Thomas, D. J. Ramirez, and T. R. Sippel, "Impacts of Metal Oxide Crystalline Structure on The Decomposition of Solid Propellants Under Combustion Heating Rates," *Fuel communications*, vol. 19, pp. 100112–100112, Jun. 2024.
- [27] L. Jie-Yao, Y. Su-Lan, W. Shixi, T. Gen, Y. Wenming, and Y. Qi-Long, "Burning rate modulation for composite propellants by interfacial control of Al@AP with precise catalysis of CuO," *Combustion and Flame*, vol. 240, p. 112029, Jun. 2022.
- [28] M. Abd-Elghany, A. Elbeih, and T. M. Klapötke, "Thermo-analytical study of 2,2,2-trinitroethyl-formate as a new oxidizer and its propellant based on a GAP matrix in comparison with ammonium dinitramide," *Journal of analytical and applied pyrolysis*, vol. 133, pp. 30–38, Aug. 2018.
- [29] S. Chaturvedi and P. N. Dave, "Solid propellants: AP/HTPB composite propellants," *Arabian Journal of Chemistry*, vol. 12, no. 8, pp. 2061–2068, Dec. 2019.
- [30] N. S. Yadav, P. P. Srivastava, and M. Varma, "Recent advances in catalytic combustion of AP-based composite solid propellants," *Defence Technology*, vol. 17, no. 3, pp. 1013–1031, Jun. 2021.
- [31] T. Xue *et al.*, "Ignition and combustion of metal fuels under microgravity: a short review," *FirePhysChem*, vol. 2, no. 4, pp. 340–356, Dec. 2022.
- [32] A. Korotkikh, I. Sorokin, and E. Selikhova, "Ignition and combustion of high-energy materials containing aluminum, boron and aluminum diboride," *MATEC Web of Conferences*, vol. 194, p. 01055, 2018.
- [33] A. Sossi *et al.*, "Non-isothermal oxidation of aluminum nanopowder coated by hydrocarbons and fluorohydrocarbons," *Applied surface science*, vol. 271, no. 2, pp. 337–343, Apr. 2013.
- [34] Y. Jiang *et al.*, "Energetic Performance of Optically Activated Aluminum/Graphene Oxide Composites," *ACS Nano*, vol. 12, no. 11, pp. 11366–11375, Oct. 2018.
- [35] Y. Huang, G. A. Risha, V. Yang, and R. A. Yetter, "Effect of particle size on combustion of aluminum particle dust in air," *Combustion and Flame*, vol. 156, no. 1, pp. 5–13, Jan. 2009.
- [36] L. T. DeLuca and W. Pang, "Transient Burning of nAl-Loaded Solid Rocket Propellants," *Springer eBooks*, pp. 111–156, Jan. 2020.
- [37] S. Elbasuney and M. Yehia, "Ferric Oxide Colloid: A Novel Nano-catalyst for Solid Propellants," *Journal of inorganic and organometallic polymers and materials*, vol. 30, no. 3, pp. 706–713, Nov. 2019.
- [38] Z. Cheng *et al.*, "Formation of composite fuels by coating aluminum powder with a cobalt nanocatalyst: Enhanced heat release and catalytic performance," *Chemical engineering journal*, vol. 385, pp. 123859–123859, Apr. 2020.
- [39] S. Elbasuney and G. S. El-Sayyad, "The potentials of TiO₂ nanocatalyst on HMX thermolysis," *Journal of Materials Science: Materials in Electronics*, vol. 31, no. 17, pp. 14930–14940, Jul. 2020.
- [40] W.-Q. Pang *et al.*, "Combustion behavior of AP/HTPB/Al composite propellant containing hydroborate iron compound," *Combustion and Flame*, vol. 220, pp. 157–167, Oct. 2020.
- [41] K.-T. Lu, T.-M. Yang, J.-S. Li, and T.-F. Yeh, "Study on the Burning Characteristics of AP/Al/HTPB Composite Solid Propellant Containing Nano-Sized Ferric Oxide Powder," *Combustion Science and Technology*, vol. 184, no. 12, pp. 2100–2116, Dec. 2012.
- [42] A. Dey *et al.*, "A graphene titanium dioxide nanocomposite (GTNC): one pot green synthesis and its application in a solid rocket propellant," *RSC Advances*, vol. 5, no. 78, pp. 63777–63785, 2015.

- [43] M. Zhang *et al.*, “Evaluation of graphene-ferrocene nanocomposite as multifunctional combustion catalyst in AP-HTPB propellant,” *Fuel*, vol. 302, pp. 121229–121229, Oct. 2021.
- [44] K. Ghosh *et al.*, “Studies on Aluminized, High Burning Rate, Butacene® Based, Composite Propellants,” *Central European Journal of Energetic Materials*, vol. 11, no. 3, Jan. 2014.
- [45] J. A. Styborski, M. J. Scorza, M. N. Smith, and M. A. Oehlschlaeger, “Iron Nanoparticle Additives as Burning Rate Enhancers in AP/HTPB Composite Propellants,” *Propellants, Explosives, Pyrotechnics*, vol. 40, no. 2, pp. 253–259, Oct. 2014.
- [46] M. Zhang *et al.*, “Evaluation of graphene-ferrocene nanocomposite as multifunctional combustion catalyst in AP-HTPB propellant,” *Fuel*, vol. 302, pp. 121229–121229, Oct. 2021.
- [47] L. Liu, J. Li, L. Zhang, and S. Tian, “Effects of magnesium-based hydrogen storage materials on the thermal decomposition, burning rate, and explosive heat of ammonium perchlorate-based composite solid propellant,” *Journal of Hazardous Materials*, vol. 342, pp. 477–481, Jan. 2018.
- [48] Y. Liu, J. Dang, Y. Ma, and H. Ma, “Hematite: A Good Catalyst for the Thermal Decomposition of Energetic Materials and the Application in Nano-Thermite,” *Molecules*, vol. 28, no. 5, pp. 2035–2035, Feb. 2023.
- [49] W.-H. XIONG *et al.*, “Preparation of Nanoporous CoFe₂O₄ and Its Catalytic Performance during the Thermal Decomposition of Ammonium Perchlorate,” *Wuli huaxue xuebao*, vol. 32, no. 8, pp. 2093–2100, Jan. 2016.
- [50] F. Maggi, L. T. DeLuca, and A. Bandera, “Pocket Model for Aluminum Agglomeration Based on Propellant Microstructure,” *AIAA Journal*, vol. 53, no. 11, pp. 3395–3403, Nov. 2015.
- [51] D. C. K. Rao, N. Yadav, and P. C. Joshi, “Cu–Co–O nano-catalysts as a burn rate modifier for composite solid propellants,” *Defence Technology*, vol. 12, no. 4, pp. 297–304, Aug. 2016.
- [52] T. Wang, B. Song, K. Qiao, Y. Huang, and L. Wang, “Effect of Dimensions and Agglomerations of Carbon Nanotubes on Synchronous Enhancement of Mechanical and Damping Properties of Epoxy Nanocomposites,” *Nanomaterials*, vol. 8, no. 12, pp. 996–996, Dec. 2018.
- [53] U. Vellaisamy and S. Biswas, “Effect of metal additives on neutralization and characteristics of AP/HTPB solid propellants,” *Combustion and Flame*, vol. 221, pp. 326–337, Nov. 2020.
- [54] S. Zhang, H. Wang, J. Liu, and C. Bao, “Measuring the specific surface area of monolayer graphene oxide in water,” *Materials Letters*, vol. 261, p. 127098, Feb. 2020.
- [55] N. Yan, L. Qin, H. Hao, L. Hui, F. Zhao, and H. Feng, “Iron oxide/aluminum/graphene energetic nanocomposites synthesized by atomic layer deposition: Enhanced energy release and reduced electrostatic ignition hazard,” *Applied Surface Science*, vol. 408, pp. 51–59, Jun. 2017.
- [56] S. K. Tiwari, H. Sharma, A. Umamaheswararao, and S. Sharma, “Synthesis and Characterization of Aluminum Composite Reinforced by Multiwall Carbon Nanotubes,” *Lecture notes in mechanical engineering*, pp. 115–124, Jan. 2020.
- [57] H. CHOI, G. KWON, G. LEE, and D. BAE, “Reinforcement with carbon nanotubes in aluminum matrix composites,” *Scripta Materialia*, vol. 59, no. 3, pp. 360–363, Aug. 2008.
- [58] L. Liu *et al.*, “Combustion promotion and agglomeration reduction of the composite propellant using graphene,” *Aerospace Science and Technology*, vol. 118, p. 106988, Nov. 2021.
- [59] S. S. Morad, “Fabrication and characterization of aluminum-carbon nanotubes (Al-CNT) functionally graded cylinders,” *AUC Knowledge Fountain*, 2016.
- [60] J.-Y. Lyu *et al.*, “Fabrication of high-performance graphene oxide doped PVDF/CuO/Al nanocomposites via electrospinning,” *Chemical Engineering Journal*, vol. 368, pp. 129–137, Jul. 2019.
- [61] B. Zhu, S. Zhang, Y. Sun, Y. Ji, and J. Wang, “Fluorinated graphene improving thermal reaction and combustion characteristics of nano-aluminum powder,” *Thermochimica acta*, vol. 705, pp. 179038–179038, Nov. 2021.
- [62] A. P. Denisyuk, Zar Ni Aung, and Y. G. Shepelev, “Energetic Materials Combustion Catalysis: Necessary Conditions for Implementation,” *Propellants, explosives, pyrotechnics*, vol. 46, no. 1, pp. 90–98, Oct. 2020.

CARBON CAPTURE AND STORAGE

Optimizing Steel Slag Utilization for Carbon Capture: Mechanisms and Potential in Mineral Carbonation

Umi Rukiah **Abdullah**¹, Faradiella **Mohd Kusin**^{1*},
Wan Azlina **Wan Ab Karim Ghani**²

¹*Department of Environment, Faculty of Forestry and Environment, Universiti Putra Malaysia, 43400 UPM Serdang, Selangor*

² *Department of Chemical and Environmental Engineering, Faculty of Engineering, Universiti Putra Malaysia (UPM), Serdang 43400, Malaysia*

**Corresponding author's phone: +603-97698596
E-mail: faradiella@upm.edu.my*

Abstract: Steel slag, a by-product of steel production, is increasingly recognized as a valuable resource for carbon capture and storage via mineral carbonation. This study investigates the potential of steel slag as CO₂ sequestration agent via indirect mineral carbonation process. An elution experiment was conducted to enhance the carbonation process, examining the impact of reaction time, temperature and CO₂ pressure. The mineralogical and chemical behavior of steel slag were analyzed using XRD, and XRF techniques. Results indicate varying percentages of minerals for steel slag; CaO (29.60%), Fe₂O₃ (24.5%) and SiO₂ (15.60%). Steel slag utilization demonstrated potential as viable CO₂ capture agent from steel production, thereby advancing sustainable practices. CO₂ mitigation practices through utilization of industrial wastes serve as beneficial approach for long-term carbon capture and storage.

Keywords: mineral carbonation; steel slag; alkaline industrial waste; CO₂ sequestration

INTRODUCTION

Climate change, driven by rising levels of atmospheric carbon dioxide (CO₂), presents one of the most pressing challenges of our time [1]. As industrial activities continue to elevate CO₂ emissions, finding effective and sustainable carbon sequestration methods has become imperative for mitigating global warming and its associated impacts. Among various strategies, the utilization of industrial by-products for carbon capture offers a promising avenue for reducing greenhouse gas concentrations.

Carbon mineralization is an efficient and risk-free way to transform CO₂ into stable carbonates [2,3]. Steel slag is a by-product of metallurgical procedures that remove impurities like silica, sulfur, phosphorus, and manganese from molten or scrap steel [4,5]. Steel slags with calcium-magnesium (Ca-Mg) silicate minerals, natural lime (CaO) and portlandite (Ca(OH)₂) concentrations, alkaline pH, and low chemical stability are considered a highly potential source for CO₂ sequestration [6]. Comprising various oxides and silicates, steel slag exhibits alkaline properties that enable it to react with CO₂, forming stable carbonates. Furthermore, alkaline solid wastes are much more suitable for CO₂ mineralization due to their relatively higher reactivity and intrinsic alkalinity, with ready availability near industrial sites [2]. Thus, recent studies have revealed its potential as a valuable resource for carbon sequestration.

Exploring the use of steel slag for carbon sequestration not only addresses waste management issues but also leverages its chemical composition to capture CO₂ effectively. Unlike conventional sequestration techniques, the utilization of steel slag offers dual benefits of reducing industrial waste and contributing to climate change mitigation [7]. Understanding the mechanisms and potential of steel slag in this context is crucial for developing sustainable industrial practices. Alkaline solid wastes, on the other hand, are much more suitable for CO₂ mineralization because of their relatively higher reactivity and intrinsic alkalinity, and they are readily available near industrial sites

Despite their enormous potential, the current scale-up uses of CO₂ mineral carbonation are limited. This study aims to investigate the potential of steel slag as a carbon sequestration agent by examining its chemical and physical properties, determine the potential of silicate minerals from steel slag for mineral carbonation process. By elucidating these aspects, we seek to provide a comprehensive assessment of steel slag's viability as a sustainable solution for carbon sequestration.

MATERIALS

SAMPLE PREPARATION

Industrial solid waste, i.e. steel slag (SS) was collected from Lion Titco, Megasteel Sdn.Bhd. The company was to recover iron metal from slag, which would then be reintroduced into the respective steel mills' electric arc furnaces (EAF) as scrap. SS powder was delivered uncrushed and was then grounded with a mortar and pestle. Before the experiment, sample was filtered through standard 35 µm sieves and dried overnight at 105 °C. The samples were then transferred to the laboratory for mineralogical analysis (Fig. 1).

Sample characterization and analysis

X-ray diffraction (XRD) and X-ray fluorescence (XRF) was used to determine the primary elemental composition of the of the alkaline residue. The mineral components of steel slag samples were identified by XRD analysis [8]. To begin, a few grams of samples were placed on a rectangular sample holder and compressed to ensure that no sample fell outside of the sample holder's specified area. Following that, the sample holders were piled on a sample rack. After that, the samples were examined using the Bruker AXS Germany D8 Advanced X-Ray Diffraction. The diffractogram data was analyzed with Diffract EVA software to identify the minerals present in the samples, and then with Origin Pro to label the peak of the graph with a specific label based on the type of mineral [9].



Fig. 1: Picture of steel slag sample.

XRF (X-ray fluorescence) analysis is a non-destructive analytical method for determining the elemental composition of materials. It runs by irradiating a sample with high-energy X-rays, causing the atoms to generate fluorescent X-rays specific to each element present. The generated X-rays were then detected and analyzed to determine and characterize the elements in the sample [10].

RESULTS AND DISCUSSION

Mineralogy of steel slag samples

The mineralogical composition of the steel slag is summarized in table 1. The crystalline phases were mainly comprised 6 different mineral kinds: calcite, quartz, magnesium zinc iron oxide, brucite, hydrocalumite and heulandite. Fig. 2 indicates that the highest peak of hydrocalumite ($\text{Ca}_2\text{Al}(\text{OH})_7 \cdot 3\text{H}_2\text{O}$) was present in steel slag samples because steel slag contains a high concentration of calcite [7]. Calcium oxide combines with CO_2 in the atmosphere, forming calcium carbonate (calcite) [11]. Our study also found some brucite ($\text{Mg}(\text{OH})_2$).

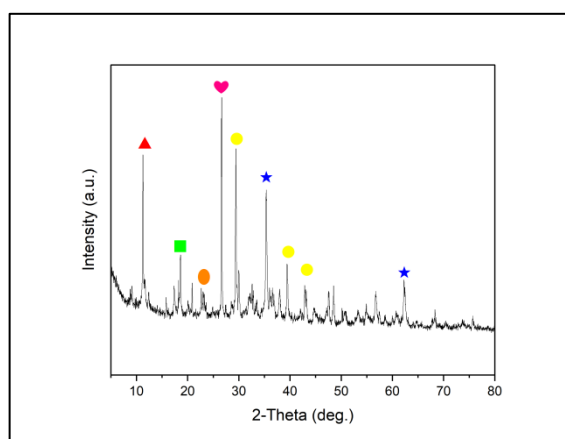


Fig. 2: Minerals from XRD analysis of the steel slag samples. The added number signify the peaks for all types of steel slag minerals: calcite (yellow circle), quartz (pink heart), magnesium zinc iron oxide (blue star), brucite (green square), hydrocalumite (red triangle) and heulandite (orange oval).

TABLE 1: . Summary of composition of minerals in steel slag samples.

Minerals	Chemical formula
<i>Primary minerals</i>	
1. Hydrocalumite ^b	$\text{Ca}_2\text{Al}(\text{OH})_7 \cdot 3\text{H}_2\text{O}$
2. Quartz ^c	SiO_2
3. Calcite ^b	$\text{Ca}(\text{CO}_3)$
<i>Secondary minerals</i>	
4. Magnesium zinc iron oxide ^a	$(\text{Mg}_{0.04} \text{Zn}_{0.46} \text{Fe}_{0.5}) (\text{Mg}_{0.46} \text{Zn}_{0.04} \text{Fe}_{1.5}) \text{O}_4$
5. Heulandite-Ca ^b	$\text{CaAl}_2 \text{Si}_7\text{O}_{18} \cdot 6\text{H}_2\text{O}$
6. Brucite ^a	$\text{Mg}(\text{OH})_2$

^aDivalent cation, ^bCarbonate minerals, ^cSilica

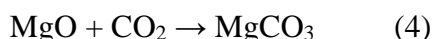
The most dominant mineral in the steel slag samples was hydrocalumite, followed by quartz (SiO₂) and calcite (CaCO₃) (Fig. 2).

The carbonation of hydrocalumite involves its reaction with CO₂ to form calcium carbonate (CaCO₃) and other compounds. Rossi et al. (2019) evaluated calcined hydrocalumite as a CO₂ adsorbent using thermogravimetric analysis. Their study demonstrated that calcined hydrocalumite effectively captures CO₂, forming stable carbonates as shown in the following equations (1,2) [12]. This reaction reflects a transition of calcium and aluminium minerals, which may contribute to carbon dioxide sequestration by creating stable carbonate minerals by reaction with CO₂ as shown in equation 1. In terms of mineral carbonation, this process involves the conversion of the calcium-aluminum hydroxide chloride compound and water into calcium oxide, calcium-aluminum oxide, additional water, and hydrogen chloride, effectively sequestering CO₂ into stable carbonate minerals as shown in equation 2.



Chemical composition of steel slag samples

The chemical composition of the steel slag determined by XRF analysis and presented in the form of CaO, Fe₂O₃, SiO₂, Al₂O₃, MgO, ZnO and SO₃ are given in Fig. 3. The sample contains a significant amount of CaO (29.6 %). Calcium oxide is the major component of mineral carbonation. CaO easily combines with CO₂ to produce calcium carbonate (CaCO₃), a stable and sustainable chemical. Carbonate minerals contain metal cations such as calcium (Ca), magnesium (Mg), and iron (Fe), which are required for mineral carbonation. These cations combine with CO₂ to generate stable carbonate minerals, such as calcite (CaCO₃), magnesite (MgCO₃), and siderite (FeCO₃) [13]. This technique forms slag into a more stable and less reactive material, in addition to sequestering CO₂ [11]. The high iron content can facilitate the formation of iron carbonates under specific conditions, although this is less common than the formation of calcium or magnesium carbonates. The presence of Fe₂O₃ (24.50%), also enhances the overall density and stability of the carbonated material. For instance, the mineral carbonation of steel slag primarily involves the creation of stable carbonate minerals from the slag's different oxides as shown in following reaction (3,4)[14]:



MgO was also found in the sample, i.e. 9.07% which is important as reactive mineral for carbonation alongside CaO and Fe₂O₃.

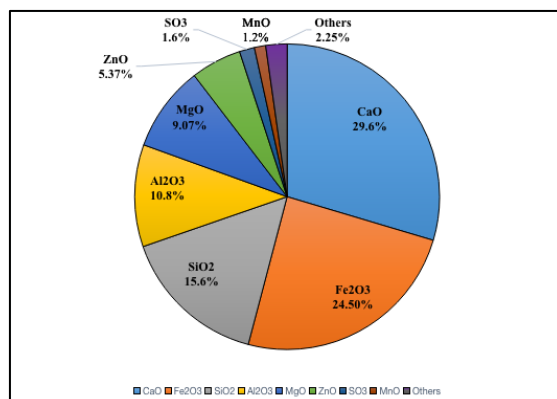


Fig. 3: Chemical composition of steel slag

Potential carbon sequestration capacity of steel slag

Based on the mineralogical and chemical composition, potential carbon sequestration capacity of the material can be estimated. It was found that the capacity of CO₂ sequestration of the steel slag is about 32.3%. Theoretically, it can be estimated that around 63.1% of CO₂ can be captured based on 1 g of CaO/MgO/Fe₂O₃ that can sequester 1 g of CO₂. The combined XRD and XRF analysis have indicated steel slag's substantial potential for carbon sequestration. Steel slag is a desirable material for capturing and storing CO₂ due to the availability of reactive oxides (e.g., CaO, MgO and Fe₂O₃) and mineral phases that promote carbonation. In this study, steel slag contained magnesium divalent cation (magnesium zinc iron oxide and brucite) and carbonate mineral (calcite) respectively, that are potential for mineral carbonation.

Factors influencing Carbonation of steel slag

Reaction of time

The time of the carbonation process greatly affects the amount of CO₂ absorbed by steel slag. Steel-making slag's potential to sequester CO₂ rises with reaction time due to calcium carbonate production [15]. Wei et al. discovered that longer carbonation times accelerate the carbonation process in steel slag-desulfurization gypsum, eventually leading to equilibrium [16].

3.4.2 Temperature

The process of steel slag carbonation is influenced by temperature. Higher temperatures affect the solubility of CO₂ and the rate at which slag dissolves in water during carbonation. Carbonation temperature also effects crystal formation and growth, as well as their microscopic structure. However, temperatures exceeding 200°C were found to delay the carbonation process.

According to [16], the optimal temperature for carbonizing steel slag is 200°C for EAF slag, where 200°C showed to be best for carbonation, as increasing the temperature boosted mineral dissolution. Dry carbonation typically requires greater temperatures than aqueous carbonation. According to research, the carbonation efficiency of suspended steel slag with high CO₂ pressure increases from 46% to 70% as the temperature rises from 50°C to 200°C. However, when steel slag is utilised as a construction material with low water-to-solid ratios and low CO₂ pressure, it is unclear if greater curing temperatures increase carbonation.

CO₂ Pressure

Multiple studies have found that CO₂ pressure plays an important role in the carbonation of steelmaking slag. While some studies show that increasing CO₂ pressure improves carbonation, others show that it has little to no effect, and in other situations, it may even slow the reaction. According to Henry's law, CO₂ solubility increases with pressure at constant temperature, implying that increasing pressure results in more CO₂ molecules involved in the carbonisation process. For example, pressures of 10, 50, 100, and 150 bar were evaluated for CO₂ uptake under identical conditions (50°C, L/S = 1). A linear link between CO₂ pressure and dissolved CO₂ is seen, which can speed up carbonation. However, if CO₂ dissolution is not a limiting factor, pressure will have no effect

on the process. On the other hand, if calcium extraction is limited, CO₂ pressure becomes more important [16].

CONCLUSION

Steel slag represents an influential potential in carbon sequestration, providing an effective way to reduce atmospheric CO₂ levels. Its significant capability for mineral carbonation, which converts CO₂ into stable carbonate minerals, places it as a key role in combating climate change. The primary minerals detected in steel slag include hydrocalumite, quartz, and calcite. Magnesium divalent cation (magnesium zinc iron oxide and brucite) and carbonate mineral (calcite) are essential for carbon capture and storage due to their stable carbonate forms. As research progresses, optimizing steel slag's efficiency as a carbon sink promises not only environmental benefits but also economic gains through the repurposing of industrial waste. Harnessing this potential requires additional research and investment, establishing the path for scalable and long-term global carbon management plans.

ACKNOWLEDGEMENTS: The authors acknowledge the financial support from the Ministry of Higher Education Malaysia through the Fundamental Research Grant Scheme, FRGS/1/2023/TK08/UPM/02/9 (5540604) and IPS Grant 9709500 from Universiti Putra Malaysia.

REFERENCES

- [1] S. Gupta, "Carbon sequestration in cementitious matrix containing pyrogenic carbon from waste biomass: A comparison of external and internal carbonation approach," *Journal of Building Engineering*, vol. 43, p. 102910, 2021.
- [2] W. Liu et al., "CO₂ mineral carbonation using industrial solid wastes: A review of recent developments," *Chemical Engineering Journal*, vol. 416, p. 129093, 2021.
- [3] S. N. M. Syed Hasan, F. Mohd Kusin, S. Jusop, and F. Mohamat Yusuff, "Potential of Soil, Sludge and Sediment for Mineral Carbonation Process in Selinsing Gold Mine, Malaysia," *Minerals*, vol. 8, no. 6, p. 257, 2018.
- [4] R. Ragipani, S. Bhattacharya, and A. K. Suresh, "A review on steel slag valorisation via mineral carbonation," *Reaction Chemistry & Engineering*, vol. 6, no. 7, pp. 1152–1178, 2021.
- [5] Z. Chen, R. Li, X. Zheng, and J. Liu, "Carbon sequestration of steel slag and carbonation for activating RO phase," *Cement and Concrete Research*, vol. 139, p. 106271, 2021.
- [6] K. R. Reddy, A. Gopakumar, and J. K. Chetri, "Critical review of applications of iron and steel slags for carbon sequestration and environmental remediation," *Reviews in Environmental Science and Bio/Technology*, vol. 18, no. 1, pp. 127–152, 2019.
- [7] L. Li, T.-C. Ling, and S.-Y. Pan, "Environmental benefit assessment of steel slag utilization and carbonation: A systematic review," *Science of The Total Environment*, vol. 806, p. 150280, 2022.
- [8] V. L. M. Molahid, F. M. Kusin, and S. N. M. Syed Hasan, "Mineralogical and chemical characterization of mining waste and utilization for carbon sequestration through mineral carbonation," *Environmental Geochemistry and Health*, vol. 45, no. 7, pp. 4439–4460, 2023.
- [9] S. N. M. S. Hasan and F. M. Kusin, "Potential of Mining Waste from Metallic Mineral Industry for Carbon Sequestration," *IOP Conference Series: Materials Science and Engineering*, vol. 458, p. 012013, 2018.
- [10] E. Marguí, I. Queralt, and E. de Almeida, "X-ray fluorescence spectrometry for environmental analysis: Basic principles, instrumentation, applications and recent trends," *Chemosphere*, vol. 303, p. 135006, 2022.

- [11] K. Elyasi Gomari, S. Rezaei Gomari, D. Hughes, and T. Ahmed, "Exploring the potential of steel slag waste for carbon sequestration through mineral carbonation: A comparative study of blast-furnace slag and ladle slag," *Journal of Environmental Management*, vol. 351, p. 119835, 2024.
- [12] T. M. Rossi, J. C. Campos, and M. M. V. M. Souza, "An evaluation of calcined hydrocalumite as carbon dioxide adsorbent using thermogravimetric analysis," *Applied Clay Science*, vol. 182, p. 105252, 2019.
- [13] I. M. Power, S. A. Wilson, and G. M. Dipple, "Serpentine Carbonation for CO₂ Sequestration," *Elements*, vol. 9, no. 2, pp. 115–121, 2013.
- [14] J.-Y. Lin, E. A. Garcia, F. C. Ballesteros, S. Garcia-Segura, and M.-C. Lu, "A review on chemical precipitation in carbon capture, utilization and storage," *Sustainable Environment Research*, vol. 32, no. 1, p. 45, 2022.
- [15] A. Baras, J. Li, W. Ni, Z. Hussain, and M. Hitch, "Evaluation of potential factors affecting steel slag carbonation," *Processes*, vol. 11, no. 9, Art. no. 2590, 2023.
- [16] X. Wei, W. Ni, S. Zhang, X. Wang, J. Li, and H. Du, "Influence of the key factors on the performance of steel slag-desulphurisation gypsum-based hydration-carbonation materials," *J. Build. Eng.*, vol. 45, Art. no. 103591, 2022.

Elution of Calcium from Marble Waste as a Preparatory Step for Indirect Aqueous Mineral Carbonation for Carbon Capture and Storage

Muhammad Hameer Soomro¹, Faradiella Mohd Kusin^{1,2*}, Ferdaus Mohamat-Yusuff¹, Nik Norsyahariati Nik Daud³

¹*Dept. of Environment, Faculty of Forestry and Environment, Universiti Putra Malaysia, UPM Serdang, Selangor, Malaysia*

² *Inst. of Tropical Forestry and Forest Products (INTROP), Universiti Putra Malaysia, UPM Serdang, Selangor, Malaysia*

³ *Dept. of Civil Engineering, Faculty of Engineering, Universiti Putra Malaysia, UPM Serdang, Selangor, Malaysia*

**Corresponding author's phone: +603-97698596
E-mail: faradiella@upm.edu.my*

Abstract: This study emphasizes on the utilization of industrial waste (marble processing waste) as a feedstock material in the preliminary step of indirect aqueous mineral carbonation for CCS. The role of calcium (Ca) was assessed in terms of elution behavior to improve carbonation uptake. The Ca elution experiment was carried out using formic acid at two concentrations (0.5 and 1.0 M) and times (up to 150 min) at ambient conditions. The physicochemical analysis confirmed the significant amount of Ca in the waste sample. The elution method at ambient temperature achieved >90% of Ca elution efficiency using 1.0 M solution at 100 min with the L/S ratio of (1:30). It was found that formic acid can elute maximum Ca from the sample at ambient conditions which would ultimately increase the carbonation efficiency. Furthermore, the carbon sequestration potential was calculated using the elution results of Ca (1.0 M and 100 min), which can sequester up to 583.72 mg CO₂/g of marble waste sample. Findings suggested that the utilization of marble waste might capture a good amount of CO₂, thus suggesting that this material has the potential for long-term CCS applications.

Keywords: calcium elution; indirect aqueous mineral carbonation; carbon capture and storage; climate change; industrial waste.

INTRODUCTION

The drastic increase in global carbon dioxide (CO₂) emissions mainly due to anthropogenic activities has caused negative impacts on both humans and the environment, as a result of climate change and global warming. According to studies, a CO₂ concentration of less than 350 parts per million (ppm) is considered safe. However, the safest level of CO₂ has already surpassed and is close to 400 ppm [1, 2]. To tackle these emissions, numerous technologies have been considered to reduce CO₂ emissions worldwide and carbon capture and storage (CCS) via mineral carbonation is one of them. CCS and particularly indirect aqueous mineral carbonation can capture significant amounts of CO₂ before releasing it into the atmosphere. In this technology, basic minerals such as calcium (Ca) and magnesium (Mg) react with CO₂ and convert to carbonates resulting in safe and long-term storage of CO₂ [3, 4]. Industrial alkaline wastes are the ideal source to be used as feedstock for the CCS via mineral carbonation. Many studies have assessed the different industrial wastes for the CCS waste/dust with varying ratios of impurities. However, this study utilized marble processing waste as feedstock material in a preparatory step for CCS via indirect aqueous mineral carbonation with

almost zero impurities in it. Therefore, it might assist in simultaneously reducing waste and CO₂ emissions.

LITERATURE REVIEW

Techniques for carbonation-based CCS involve the removal of CO₂ from industrial exhaust gases. Carbonation-based CCS is divided into two methods: (i) direct and (ii) indirect carbonation. The direct carbonation method involves - direct reaction of metal oxide (MO-Ca/Mg) with CO₂ in a controlled environment and converting it into carbonates. However, the indirect carbonation extracts the MO first by applying an extraction agent and then reacts with CO₂, hence converting it into carbonates [4]. The more Ca/Mg extracted, the more carbonation might occur. It has been suggested that the solution type (ammonium salt-based extractant and acid-based extractant) and extraction parameters (molar concentration, temperature, time, pH, particle size) have a significant impact on the total Ca/Mg extraction yields [5, 6]. Previous studies observed that acid-based extraction agents are more effective compared to salt-based extractants. Whereas, when applying temperature salt-based extractants observed good yield which suggested temperature is directly proportional to extraction yield. On the other hand, studies reported that acidic pH is more favorable for better extraction yield. Moreover, particle size is a crucial factor, the coarser the particle size, the better the extraction yield [7, 8].

Previous studies assessed different industrial waste materials with various impurities. Huang et al. [9] assessed coal fly ash as feedstock material for carbonated-based CCS, where other metals such as SiO₂ and Al₂O₃ are present along with desired elements such as Ca and Mg with the portion of 46.9% and 19.5%, 17.8% and 1.15% respectively. Kim and Jung [10] assessed cement kiln dust as feedstock material with desired and other metal proportions of CaO, K₂O, Cl, and SiO₂ of about 46.4%, 21%, 15.7%, and 6.4% respectively. In addition, the above studies show various proportions of other elements available in various feedstocks for the carbonation-based CCS approach. It has been suggested that a modification treatment be carried out before the extraction process if the Ca/Mg-bearing phases contain other elements to bring them into stable phases, which not only makes the method complex but also increases the overall cost of the process. Therefore, there is a need to evaluate other waste materials for CCS via mineral carbonation. Massive amounts of marble waste are generated worldwide in the form of dust/stone and wastewater, this can result in solid waste dumps and air pollution. Marble waste is a pure form of Ca with almost zero impurities (>80%) [11, 12], which suggests an ideal feedstock material for the carbonation-based CCS.

The primary goal of this research is to explore the possibility of marble waste as feedstock for carbonation-based CCS to reduce waste and CO₂ emissions simultaneously. Specifically, this study assessed the utilization of marble waste as feedstock material in the preparatory step of indirect aqueous mineral carbonation, and determined the leaching or elution efficiency using different concentrations of acid and different reaction times at ambient conditions to reduce overall cost.

MATERIALS

The marble waste samples were collected from GCCP Resources Limited, a marble processing company located in Simpang Pulai, Perak Malaysia. 10 kg of small fractions between 1-10 cm in size waste samples were obtained. The samples were air-dried for 48 hours at room temperature. The

samples were crushed using a crusher and sieved (<0.5 mm) to homogenize the samples for further analysis and elution experiments.

EXPERIMENTAL

Physiochemical and Mineralogical Analysis

The particle size, microstructure, and chemical composition (percentage weight) were analyzed using scanning electron microscopy attached with energy dispersive X-ray spectroscopy (SEM-EDX, Philips XL30, Netherlands-Inca Software). Four spots were randomly scanned at 2 different locations and all values were normalized. Its maximum resolution, under ideal conditions, is 3.5 nm. The mineral phases of the samples were assessed by x-ray diffraction (XRD, Bruker-AXS D8 Advanced diffractometer). The software (Diffrac AT EVA V.9.0) was used to analyze the integrated intensity of peak areas to identify the mineral phases of the samples. A portable pH meter (Thermo SCIENTIFIC Orion Star A121) was used to determine the pH of solution.

Elution/Leaching Experiment

The marble waste was subjected to an elution experiment in the laboratory as a pre-carbonation step to extract Ca. A modified version of an elution experiment for carbonation conducted by Kim and Jung [10] earlier was implemented in this study. Formic acid (analytical reagent grade) was used as an elution agent to assess their elution/leaching behavior using marble waste.

Elution Agent Concentration and Time

The elution efficiency was assessed using formic acid at two different concentrations of 0.5 M and 1.0 M. Marble waste and acid solution was mixed at a ratio of 1:30 (5g: 150 ml) in flasks and was shaken at a rate of 230 rounds per minute for 150 min on an orbital shaker at ambient conditions. To evaluate the elution efficiency according to time, samples were obtained sequentially at 20, 60, 100, and 150 minutes to assess the Ca concentration.

Analytical and Post-Elution

During the elution experiment, a 10 ml disposable plastic syringe with a connected head of 0.45 µm membrane filter was used to collect samples. The 15 ml centrifuge tubes were used to keep the samples and were analyzed to determine the Ca concentration in the solution by using an Inductively Coupled Plasma Optical Emission Spectroscopy (ICP-OES, Perkin Elmer Optima 7300 DV). Next, using the Kim and Kim [13] method, concentration results (mg/L) were calculated to determine the elution efficiency.

CO₂ Sequestration Potential

Furthermore, the sequestration potential of CO₂ using the indirect aqueous mineral carbonation approach of marble waste was calculated. Based on the Ca and CO₃²⁻ (carbonate ion), a balanced stoichiometric ratio of 1:1, the theoretical sequestration potential of Ca was calculated using Equation 1 [14].

$$PCO_2 = \frac{\left(Ce \cdot V_{sol} \cdot \frac{1 \text{ mmol Ca}}{40.08 \text{ mg Ca}} \cdot \frac{1 \text{ mmol CO}_2}{1 \text{ mmol Ca}} \cdot \frac{44.01 \text{ mg CO}_2}{1 \text{ mmol CO}_2} \right)}{Mi} \cdot \frac{\text{mg CO}_2}{\text{g sample}} \quad (1)$$

where PCO_2 refers to the sequestration potential of CO_2 in unit $mg\ CO_2/g$ waste sample, C_e refers to the elemental concentration in the solution (mg/L), V_{sol} refers to the solution volume (L), and M_i refers initial weight of the sample (g).

RESULTS AND DISCUSSION

Physiochemical and Mineralogical

The SEM images examined the morphology and particle size of the marble waste sample. The microstructure of the marble sample revealed that some particles are in agglomerated form while some are scattered (Fig. 1). The sample particles indicate irregular crystalline shapes. The average particle size was determined using the SEM images (at $5.00k\times$ magnification) by measuring two random particles. The average particle size was determined to be $<1\ \mu m$. Therefore, it turned out that the sample grinding achieved a suitable particle size for the elution and carbonation experiment [15].

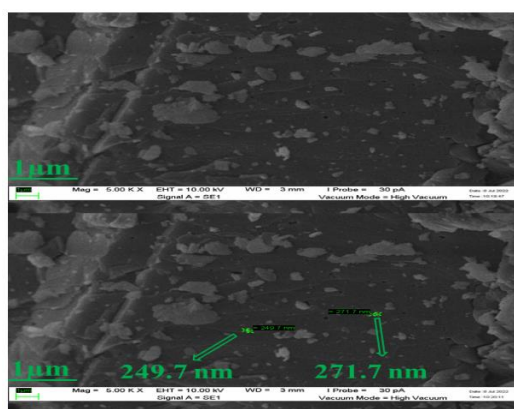


Fig. 1. SEM images of marble waste samples with their particle size.

Table 5. Chemical composition of marble waste

Chemical Formation	Concentration (wt.%)
Ca	56.17
O	35.7
C	7.21
*Other (Si, Mg, Al, Fe)	0.92

Table 1 shows the chemical composition of marble waste sample as the mass percentage of elements. The predominant element of the marble waste sample was Ca, with the maximum amount of Ca (56.17%), followed by O (35.7%), and C (7.21%). The remaining elements (Si, Mg, Al, Fe) were also in meager quantities. Therefore, it was confirmed that reactive metal oxides (Ca) were available in the marble waste sample with almost no impurities. Once the Ca bonded with CO_2 , carbonate minerals formed, as explained by equation 2.

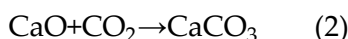


Fig. 2 represents the mineralogy of the marble waste sample and phase distribution by XRD. The XRD analysis shows that calcite ($CaCO_3$), wollastonite ($CaSiO_3$), and akermanite ($Ca_2MgSi_2O_7$) were observed in the marble sample. The mineral phase distribution shows that calcite (96.3%) was the major mineral present in the waste sample, followed by wollastonite (2.6%). The mineralogy of the sample suggested that the 100% Ca presence in the sample can react with CO_2 and turned into $CaCO_3$.

This illustrates the presence of valuable minerals in marble waste samples with almost no impurities. Thus, the chemical composition summary was corroborated by the XRD findings.

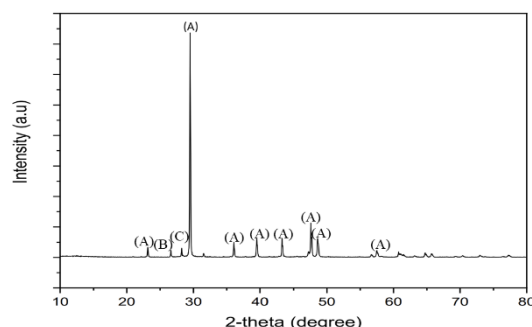


Fig. 2. XRD diffractograms of marble waste sample (A = Calcite; CaCO_3 , B = Wollastonite; CaSiO_3 , C = Akermanite; $\text{Ca}_2\text{MgSi}_2\text{O}_7$)

Ca Elution Results

The elution of Ca using formic acid resulted in the formation of calcium formate [16]. Fig. 3. represents the elution results of Ca employing formic acid using two different concentrations (0.5 M and 1.0M) solutions. The Ca elution results indicated that the higher molar concentrated solution performs better with higher elution efficiencies from start to end (up to 150 min). The maximum Ca elution efficiency of 94% was achieved using 1.0 M solution at 100 min, followed by 86% using 1.0 M solution at 60 min. The highest elution efficiency using low concentrated solution (0.5 M) was 76% in the first 20 min, followed by 74% at 60 min. However, a declining trend was observed which suggested the completion of the reaction that took place. Therefore, it can be concluded that a higher molar concentration of formic acid can extract more than 90% of Ca from the marble waste samples at ambient conditions. In comparison with a previous study conducted by Ghoorah et al. [17], where they used >80% of wollastonite mineral, it was observed that a lower elution efficiency was resulted at a lower temperature due to silica layer formation which eventually affects the dissolution process by time. Thus a higher elution efficiency (>90%) in this study justified the utilization of waste material with no impurities.

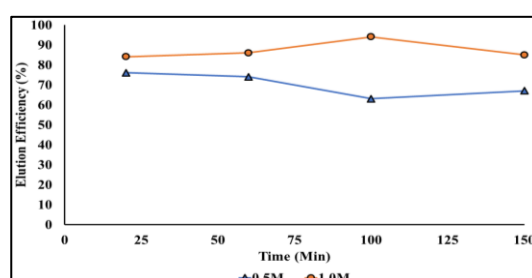


Fig. 3. Elution results of Ca as a function of reaction time using 0.5 M and 1.0 M concentrations of formic acid.

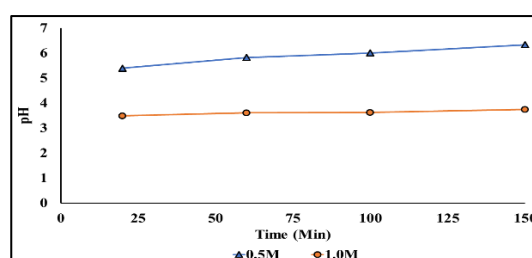


Fig. 4. pH variation of 0.5 M and 1.0 M formic acid solution as a function of time.

pH Variation

Fig. 4 shows the pH variation observed for 0.5 M and 1.0 M formic acid solution. The pH of the formic acid solution significantly affects the Ca elution process. In this study, the pH of the 1.0 M solution remains acidic (3.4-3.7), however, the 0.5 M solution pH shows an acidic to slightly acidic nature (5.3-6.3) throughout the experiment (up to 150 min). The pH results suggested that the acidic pH was more favorable to eluting Ca using formic acid at faster rates and ambient conditions. On the other hand, a slightly upward trend in pH suggested the mechanism of alkalization in the reaction mixture that raises the pH of the solution by consuming protons and releasing Ca from the sample [17].

Summary and CO₂ Sequestration Potential

The elution results with the best Ca elution efficiency employing two different formic acid concentrations at various contact times are summarized in Tab. 2. 1.0 M solution exhibited the highest elution efficiency for Ca with 94% at 100 min. Whereas, the highest elution efficiency using 0.5 M solution was 76% at 20 min. Therefore, it can be suggested that the higher molar concentration of formic acid was more effective under ambient conditions. Furthermore, the marble waste CO₂ sequestration potential was also calculated for Ca elution efficiency in this study. The CO₂ sequestration capacity of marble waste using 0.5 M (20 min) and 1.0 M (100 min) formic acid solution was estimated to be 471.72 mg CO₂/g sample and 583.72 mg CO₂/g sample (Tab. 2).

Table 6. Summary of Ca elution with highest efficiency of 0.5 M and 1.0 M formic acid solutions with respective CO₂ uptake potential.

Characteristics	0.5 M	1.0 M
Elution Efficiency	76%	94%
Reaction Time	20 Min	100 Min
L/S Ratio	1:30	1:30
CO ₂ Uptake Potential	471.72 mg CO ₂ /g	583.72 mg CO ₂ /g

CONCLUSION

The Ca elution from marble waste as the initial stage for indirect aqueous mineral carbonation was studied. The elution experiments were conducted using formic acid at two concentrations (0.5 and 1.0 M) and at different times (up to 150 min). The physiochemical analysis confirmed the essential elements/minerals and particle size for the elution and carbonation experiment with almost no impurities. The highest elution efficiency of 94% was achieved using 1.0 M formic acid solution at 100 min (ambient conditions) with the estimated CO₂ sequestration capacity of 583.72 mg CO₂/g marble waste sample. Therefore, the utilization of marble waste might be able to capture a significant quantity of CO₂, indicating that this material might be useful for CCS via indirect aqueous carbonation applications.

ACKNOWLEDGEMENTS: The authors acknowledge the financial support from the Ministry of Higher Education Malaysia through the Fundamental Research Grant Scheme, FRGS/1/2023/TK08/UPM/02/9 (5540604) and IPS Grant 9709500 from Universiti Putra Malaysia.

REFERENCES

- [1] Wennersten, R., Q. Sun, and H. Li, The future potential for Carbon Capture and Storage in climate change mitigation—an overview from perspectives of technology, economy and risk. *Journal of cleaner production*, 2015. 103: p. 724-736.
- [2] Rahman, F.A., et al., Pollution to solution: Capture and sequestration of carbon dioxide (CO₂) and its utilization as a renewable energy source for a sustainable future. *Renewable and Sustainable Energy Reviews*, 2017. 71: p. 112-126.
- [3] Markusson, N., et al., A socio-technical framework for assessing the viability of carbon capture and storage technology. *Technological Forecasting and Social Change*, 2012. 79(5): p. 903-918.
- [4] Bobicki, E.R., et al., Carbon capture and storage using alkaline industrial wastes. *Progress in Energy and Combustion Science*, 2012. 38(2): p. 302-320.
- [5] Dri, M., A. Sanna, and M.M. Maroto-Valer, Dissolution of steel slag and recycled concrete aggregate in ammonium bisulphate for CO₂ mineral carbonation. *Fuel processing technology*, 2013. 113: p. 114-122.
- [6] Cheng, C., et al., CO₂ sequestration and CaCO₃ recovery with steel slag by a novel two-step leaching and carbonation method. *Science of The Total Environment*, 2023. 891: p. 164203.
- [7] Galina, N.R., et al., Experimental study on mineral dissolution and carbonation efficiency applied to pH-swing mineral carbonation for improved CO₂ sequestration. *Energies*, 2023. 16(5): p. 2449.
- [8] Spínola, A.C., et al., Mineral carbonation of a pulp and paper industry waste for CO₂ sequestration. *Process Safety and Environmental Protection*, 2021. 148: p. 968-979.
- [9] Huang, Y., et al., Protonated amines mediated CO₂ mineralization of coal fly ash and polymorph selection of CaCO₃. *Chemical Engineering Journal*, 2022. 450: p. 138121.
- [10] Kim, M.-J. and S. Jung, Calcium elution from cement kiln dust using chelating agents, and CO₂ storage and CaCO₃ production through carbonation. *Environmental Science and Pollution Research*, 2020. 27: p. 20490-20499.
- [11] Aliabdo, A.A., M. Abd Elmoaty, and E.M. Auda, Re-use of waste marble dust in the production of cement and concrete. *Construction and building materials*, 2014. 50: p. 28-41.
- [12] Mulk, S., et al., Impact of marble industry effluents on water and sediment quality of Barandu River in Buner District, Pakistan. *Environmental monitoring and assessment*, 2015. 187: p. 1-23.
- [13] Kim, D. and M.-J. Kim, Calcium extraction from paper sludge ash using various solvents to store carbon dioxide. *KSCE Journal of Civil Engineering*, 2018. 22: p. 4799-4805.
- [14] Razote, B.J., et al., Leaching characteristics of an iron-rich siltation pond waste and its viability in indirect carbon sequestration. *International Journal of Mining, Reclamation and Environment*, 2021. 35(6): p. 435-450.
- [15] Molahid, V.L.M., et al., CO₂ sequestration through mineral carbonation: effect of different parameters on carbonation of Fe-rich mine waste materials. *Processes*, 2022. 10(2): p. 432.
- [16] Ma, H., et al., Preparation of feed grade calcium formate from calcium carbide residue. *Clean Technologies and Environmental Policy*, 2016. 18: p. 1905-1915.
- [17] Ghoorah, M., et al., Selection of acid for weak acid processing of wollastonite for mineralisation of CO₂. *Fuel*, 2014. 122: p. 277-28

BIOMEDICAL APPLICATIONS

Antibacterial Activity of Biosynthesized Silver Nanoparticles using *Clitoria ternatea* against *Cutibacterium acnes*

Khor Zhi **Xin**¹, Nik Ahmad Nizam Nik **Malek**^{1,2*}, Muhammad Hariz **Asraf**¹, Too Soon **Wei**¹

¹ Dept. of Biosciences, Faculty of Science, Universiti Teknologi Malaysia,
Johor Bahru, Malaysia

² Centre for Sustainable Nanomaterials (CSNano), Institute Ibnu Sina for Scientific and Industrial Research,
Universiti Teknologi Malaysia,
Johor Bahru, Malaysia

*Corresponding author's phone: +6013-7805466
E-mail: niknizam@utm.my

Abstract: The biosynthesized silver nanoparticles (AgNP) using plant extract are known for their sustainable approach and exceptional antibacterial properties. This study was designed to synthesize AgNP using *Clitoria ternatea* and evaluate their antibacterial activity against *Cutibacterium acnes*. The ideal synthesis conditions involved a 2% plant extract and a 2:8 ratio of plant extract to AgNO₃ over 216 hours of reaction time. The formation of AgNP was confirmed by a colour change from blue to dark brown with UV-Vis spectrum indicating surface plasmon resonance (SPR) peaks within 410 to 450 nm. Transmission electron microscopy (TEM) revealed spherical particles of AgNP (17.45 ± 7.41 nm). The antibacterial activity of the AgNP with different extract-to-precursor volume ratios (1:9, 2:8, and 9:1) showed antibacterial activity against *C. acnes* ATCC6919. The minimum inhibition concentration (MIC) assay showed dose-dependent inhibition of the colloidal AgNP against *C. acnes*, with effective antibacterial activity recorded at 12.50 ppm. These findings revealed *C. ternatea* as a sustainable source of synthesizing AgNP and uncovered their potential as an effective antibacterial agent against *C. acnes* infections.

Keywords: silver nanoparticles; *Clitoria ternatea*; *Cutibacterium acnes*

INTRODUCTION

Silver nanoparticles (AgNP) are increasingly prevalent due to their unique properties and wide-ranging applications in various fields such as food, pharmaceutical, and agriculture. The shift towards biological synthesis of nanoparticles offers a safer and more environmentally friendly approach than chemical and physical methods. Plant extracts rich in phytochemical compounds are widely utilized to synthesize AgNP. Studies have reported on the antibacterial activity of biosynthesized AgNP against various bacterial strains [1-3]. *Clitoria ternatea* has been identified as a potential candidate for the biosynthesis of AgNP due to its rich phytochemical content and recognized antimicrobial properties.

However, limited information is available on the effectiveness of the biosynthesized AgNPs against skin infections, particularly those caused by *Cutibacterium acnes*. The knowledge gap revolves around the antibacterial activities of biosynthesized AgNPs using *C. ternatea* and their potential to treat the bacteria *C. acnes*. Therefore, the rationale of this study is to bridge this gap and contribute to the development of eco-friendly approaches to produce AgNPs using *C. ternatea* while treating dermatological issues associated with *C. acnes*.

THEORY

Plant extracts play a crucial role in the biosynthesis of AgNP by acting as natural reducing and stabilizing agents. These extracts contain a variety of phytochemicals, including flavonoids, terpenoids, polyphenols, and proteins, which facilitate the reduction of Ag^+ to metallic silver (Ag^0) and stabilize the resulting nanoparticles, thus preventing their aggregation [4,5]. This eco-friendly and cost-effective method eliminates the need for harmful chemicals.

MATERIALS

C. ternatea flowers were obtained from Baker & Flavorist, Kuala Lumpur. AgNO_3 was obtained from Merck. The materials for antibacterial assay include Reinforced Clostridial Medium (RCM) agar (Oxoid, UK), NaCl (Merck), and McFarland standard (Oxoid, UK).

EXPERIMENTAL

The optimization of AgNP biosynthesis steps was performed by manipulating the plant extract concentration (1% and 2%), plant extract volume (0.2 mL to 1.0 mL), reaction times (0 to 264 hours) and volume ratio of plant extract to silver nitrate (1:9, 2:8, 3:7, 4:6, 5:5, 6:4, 7:3, 8:2, 1:9), determining their effects on the synthesis of AgNP using *C. ternatea*. The biosynthesis steps followed from the previous study [1]. The colloidal AgNP was analyzed using UV-Vis spectroscopy, and the powder of AgNP (After collection using centrifuge) was characterized using Fourier transform infrared spectroscopy (FTIR), X-ray diffraction analysis (XRD) and transmission electron microscopy (TEM). To examine the efficacy of the AgNP, their antibacterial activity against *C. acnes* (ATCC6919) was evaluated using the disc diffusion technique (DDT) and minimum inhibitory concentration (MIC) assays as qualitative and quantitative analyses, respectively, with slight modification by referring to the research by Din et al. [2].

RESULTS AND DISCUSSION

Biosynthesis of AgNP

In Fig. 1, different *C. ternatea* extract concentrations reacted with a fixed volume of AgNO_3 solution shows the SPR peaks appear within the range of 410 nm to 480 nm. The shifts in the position of SPR peaks suggest variations in the sizes of the AgNP. Generally, a shift to a longer wavelength suggests an increase in size, whereas a shift to a shorter wavelength indicates a decrease in size. AgNP synthesized using 1% and 2% *C. ternatea* extract have maximum absorption values at 423 nm and 418 nm, respectively. Notably, 2% *C. ternatea* extract resulted in higher absorption intensity than 1% *C. ternatea* extract at the same volume. This may be attributed to the role of the *C. ternatea* extract in the biosynthesis of AgNP. This result may be attributed to the role of the *C. ternatea* extract in the biosynthesis of AgNPs. *C. ternatea* contains various phytochemical compounds such as anthocyanins, flavonoids, and polyphenols [6]. These bioactive compounds are responsible for reducing Ag^+ to AgNPs and simultaneously stabilizing the AgNPs, preventing them from agglomeration.

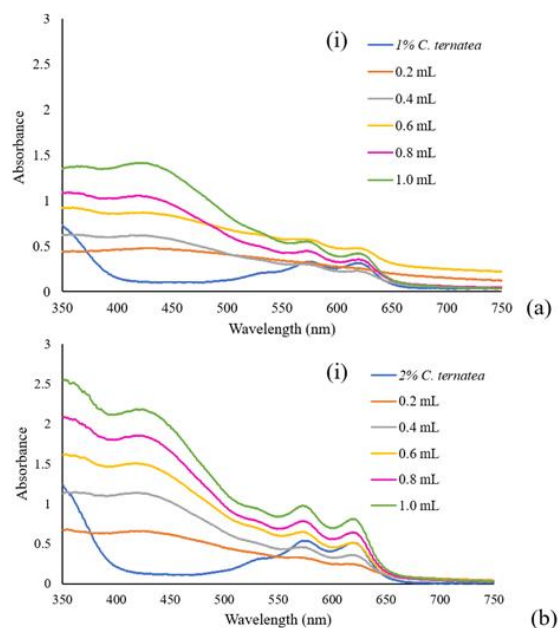


Fig. 1: UV-Vis spectra of AgNP synthesized using (a) 1% *C. ternatea* and (b) 2% *C. ternatea* extract with different volumes

Fig. 2 shows UV-Vis spectra for AgNPs formation against time. It was observed that the absorption intensities increased over time and rose gradually after 216 hours. The increase in absorption intensity over time suggests the ongoing formation of AgNPs during the synthesis reaction [1]. As the reaction progresses, increased intensity signifies the growth in the quantities and sizes of the AgNPs in the colloidal solution. Therefore, the UV-Vis spectra in Fig. 2 indicated that the synthesis reaction took almost 216 hours to complete.

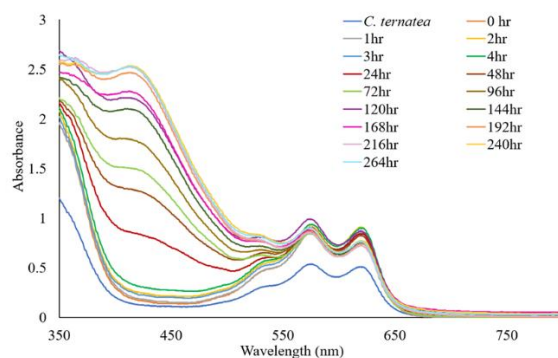


Fig. 2: UV-Vis spectra for the formation of AgNPs against time

According to Fig. 3, the highest absorption intensity was recorded at the ratio of 2:8 (*C. ternatea* extract: AgNO_3) at 430 nm, followed by 3:7, 4:6, and 1:9. In contrast, the remaining volume ratios demonstrated lower and almost similar absorption intensities. The ratio of 2:8 displayed a consistent and prominent peak at 430 nm, indicating a stable synthesis of AgNPs at this ratio. This optimal ratio signifies the availability of an ample amount of Ag^+ and bioactive compounds to reduce AgNO_3 , thus synthesizing AgNPs efficiently. Therefore, the ratio of 2:8 was considered the optimal ratio for the effective synthesis of AgNPs.

Overall, the study demonstrated that the ideal synthesis conditions involved using a 2% concentration of *C. ternatea* extract along with a 2:8 ratio of *C. ternatea* extract to AgNO₃ over 216 hours.

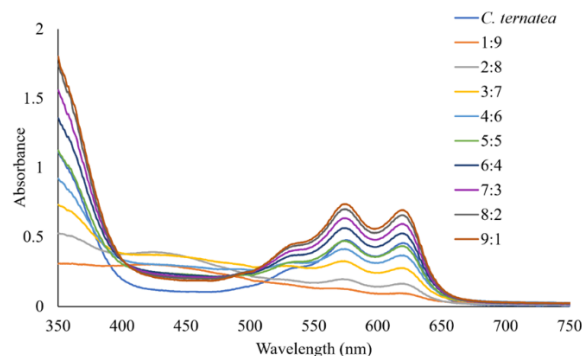


Fig. 3: UV-Vis spectra for the formation of AgNPs using varying ratios of *C. ternatea* extract to silver nitrate.

Characterization of Biosynthesized AgNP

Figs. 4, 5 and 6 show the FTIR spectrum, XRD pattern, and morphological analysis using TEM of the powder form of the biosynthesized AgNP under these optimized conditions, respectively.

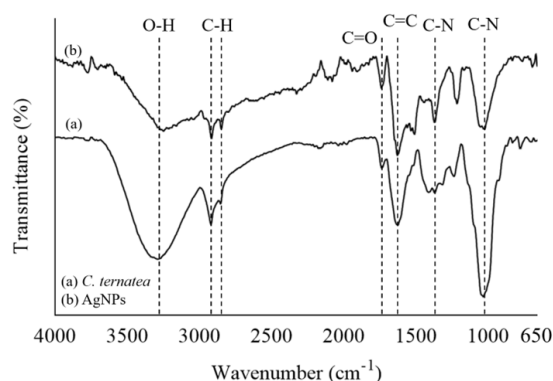


Fig. 4: FTIR spectra of (a) *C. ternatea* powder and (b) the biosynthesized AgNP

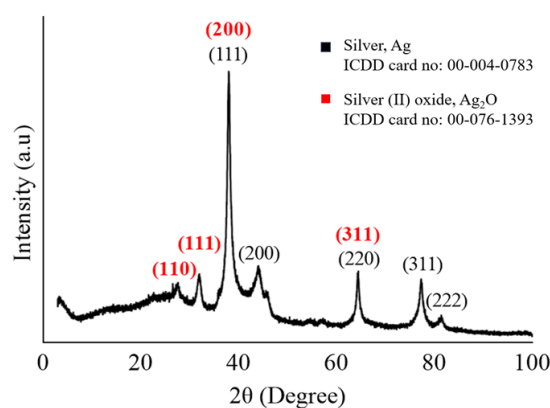


Fig. 5: XRD pattern of the biosynthesized AgNP using *C. ternatea*

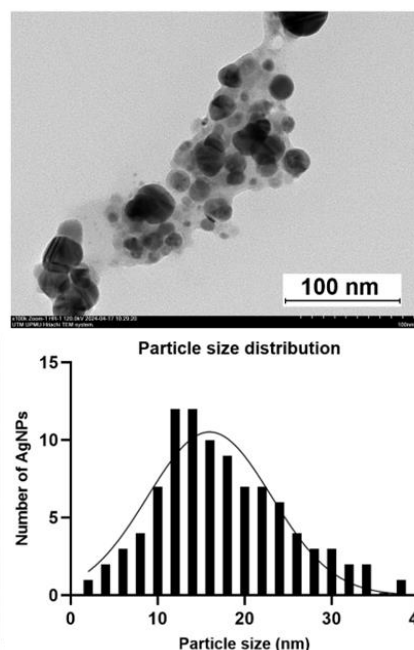


Fig. 6: TEM image and particle size distribution of biosynthesized AgNP

In the FTIR spectra (Fig. 4), the peaks observed in the *C. ternatea* powder at 2920 cm^{-1} and 2853 cm^{-1} corresponding to C-H stretching were similarly observed in the AgNP, indicating possible interactions of bioactive compounds in the formation of AgNP. The peaks at 1736 cm^{-1} in the *C. ternatea* extract and 1740 cm^{-1} in AgNP suggested the involvement of C=O-containing compounds in the biosynthesis process. The C=C stretching vibration at 1628 cm^{-1} in *C. ternatea* extract and 1627 cm^{-1} in AgNP indicated the preservation of the alkene groups that capped the AgNP surface. The peaks shifted upon biosynthesis of AgNP, suggesting the involvement of bioactive compounds derived from *C. ternatea* extract in reducing Ag^+ . This indicates that the bioactive substances derived from *C. ternatea* coexisted after biosynthesis and capped on the surface of the biosynthesized AgNP [2].

The XRD analysis (Fig. 5) revealed the presence of Ag in a face-centered cubic (fcc) structure, with diffraction peaks corresponding to (111), (200), (220), (311), and (222) reflection planes. The data were consistent with the standard reference of the International Centre for Diffraction Data (ICDD) database with DB card no. 00-004-0783. Similar findings also have been observed in other studies [1-3].

Additionally, peaks corresponding to Ag_2O were observed, indicating the oxidation of the AgNP during synthesis, possibly influenced by the biological environment. When AgNPs are exposed to oxygen or other oxidizing agents, their surface layer oxidizes and forms Ag_2O , changing the composition of the surface layer from metallic Ag to oxide or hydroxide [7]. The presence of oxygen-containing groups in plant phytochemicals, including flavonoids, phenolic acids, and terpenoids, can act as donors and coordinate with Ag^+ forming Ag_2O .

Fig. 6 reveals that the AgNP are predominantly spherical and have sizes ranging from 2 to 40 nm, with an average diameter of 17.45 ± 7.41 nm. The particle distribution histogram further confirms this size distribution.

Antibacterial Activity of Biosynthesized AgNP

The antibacterial activity of the AgNP was evaluated using the DDT (Fig. 7) and MIC (Fig. 8) against *C. acnes* ATCC6919. DDT provides a qualitative assessment based on the inhibition zones, and the MIC assay offers a quantitative measure of the lowest concentration of AgNP required to inhibit bacterial growth.

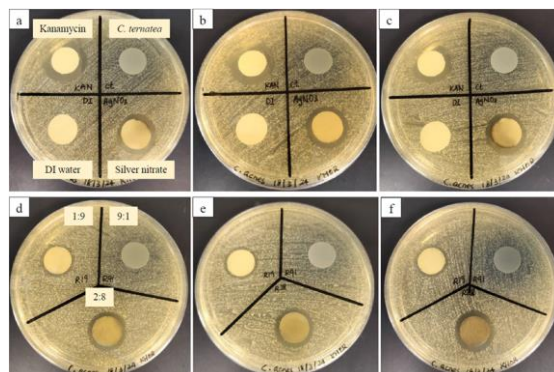


Fig. 7: DDT results show triplicate control plates (a, b, c) and triplicate sample plates (d, e, f), representing independent replicates

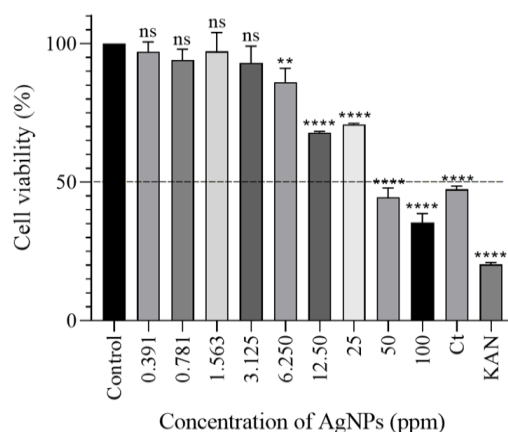


Fig. 8: The dose-dependent effect of biosynthesized AgNP on the cell viability of *C. acnes* [Asterisks (*) and "ns" denotes a statistically and not statistically significant difference ($p < 0.05$) with controls, respectively]

The antibacterial activity of biosynthesized AgNP against *C. acnes* was tested using varying volume ratios of *C. ternateia* extract to AgNO_3 (1:9, 2:8, and 1:9). The results indicated that the 2:8 ratio resulted in the largest inhibition zone (18.7 ± 0.6 mm), suggesting it may be the most effective for synthesizing AgNP with strong antibacterial properties against *C. acnes*. An inhibition zone diameter of 16.3 ± 0.6 mm was observed for the 1:9 ratio, meeting the criteria for significant antibacterial activity. However, the 9:1 ratio did not indicate a visible inhibition zone, indicating weak activity.

Fig. 8 shows the dose-dependent effects of biosynthesized AgNP on the cell viability of *C. acnes*. As the concentration of AgNP increased from 0.391 ppm to 100 ppm, there was a corresponding decrease in cell viability, indicating more significant inhibition of *C. acnes* growth at higher concentrations. The MIC value was determined to be 12.50 ppm, suggesting that concentrations below this were insufficient to prevent *C. acnes* growth, while concentrations above 12.50 ppm showed increasingly

potent inhibition. The half-maximal inhibitory concentration (IC₅₀) identified was 50 ppm, indicating that 50 ppm AgNP is required to inhibit 50% of the cell viability.

CONCLUSION

The optimal AgNP synthesis parameters involved a 2% plant extract and a 2:8 ratio of the extract to AgNO₃ over 216 hours of reaction. Characterization results confirmed the formation of spherical and crystalline AgNP with an average size of 10.22 nm. The DDT and MIC assays showed that the biosynthesized AgNP can prevent the growth of *C. acnes*. Overall, the research findings have shown the capability of synthesizing AgNP using flower extract of *C. ternatea* and their potential antibacterial activity against *C. acnes*.

ACKNOWLEDGEMENTS: Thanks to financial support by UTM and Universitas Negeri Malang under the Matching Grant (Vot No: 04M28).

REFERENCES

- [1] A. A. Hadi, N. A. N. N. Malek, J. Matmin, M. H. Asraf, H. Susanto, S. M. Din, M. Shamsuddin, "Synergistic antibacterial effect of *Persicaria odorata* synthesised silver nanoparticles with antibiotics on drug-resistant bacteria," *Inorganic Chem Comm*, vol. 159, pp. 111725, 2024.
- [2] S. M. Din, N. A. N. N. Malek, M. Shamsuddin, J. Matmin, A. A. Hadi, M. H. Asraf, "Antibacterial silver nanoparticles using different organs of *Ficus deltoidea* Jack var. *kunstleri* (King) Corner," *Biocatal Agric Biotechnol*, vol. 44, pp. 102473, 2022.
- [3] M. H. Asraf, N. A. N. N. Malek, M. R. M. Radzi, H. Susanto, "Biosynthesized *Persicaria odorata*-silver nanoparticles supported zeolite Y as biocompatible antibacterial agent against *Cutibacterium acnes*," *Particuology*, vol. 93, pp. 1-10, 2024.
- [4] A. Dhaka, S. Chand Mali, S. Sharma, R. Trivedi, "A Review on Biological Synthesis of Silver Nanoparticles and their Potential Applications," *Results Chem*, Vol. 6, pp. 101108, 2023
- [5] M. A. Dheyab, N. Oladzadabbasabadi, A. A. Aziz, P. M. Khaniabadi, M. T. S. Al-ouqaili, M. S. Jameel, F. S Braim, B. Mehrdel, M. Ghasemlou, "Recent Advances of Plant-Mediated Metal Nanoparticles: Synthesis, Properties, and Emerging Applications for Wastewater Treatment," *J Environ Chem Eng*, Vol. 12, pp. 112345, 2024.
- [6] H. Madhumitha, S. Ranjani, J. R. Karunyaa, S. Hemalatha, "*Clitoria Ternatea* Floral Mediated Synthesis, Characterization, Antioxidant, and Cytotoxicity Evaluation of Silver Nanoparticles," *Arch Breast Cancer*, vol. 10, pp. 222-231, 2023.
- [7] A. V. Blinov, A. A. Nagdalian, S. N. Povetkin, A. A. Gvozdenko, M. N. Verevkina, I. V. Rzhepakovsky, M. S. Lopteva, D. G. Maglakelidze, T. S. Kataeva, A. A. Blinova, A. Golik, G. V. Osipchuk, M. A. Shariati, "Surface-Oxidized Polymer-Stabilized Silver Nanoparticles as a Covering Component of Suture Materials," *Micromachines*, vol. 13, pp. 1105, 2022.

Development of Cellulose Nanospheres to Enhance the Antibacterial Activity of Lysozyme

Nur Khairun Atiyah **Sagee Ahmad**¹, Mohd Firdaus-**Raih**^{1,2}, Doris Huai Xia **Quay**^{1,2}, Sharifah Nabihah **Syed Jaafar**^{1,2*},

¹*Department of Applied Physics, Faculty of Science and Technology, 43000 Kajang, Universiti Kebangsaan Malaysia*

²*Bioinformatics and Molecular Simulations Research Group, Universiti Kebangsaan Malaysia, 43600 UKM Bangi, Selangor, Malaysia*

*Corresponding author's phone: +603-8921 4983
E-mail: nabihah@ukm.my

Abstract: Lysozyme-immobilized cellulose nanospheres (CNS-Lys) were synthesized and analyzed using zeta potential (ZP), Fourier transform infrared (FTIR) spectroscopy, transmission electron microscopy (TEM), and antibacterial activity against *Bacillus subtilis* (*B. subtilis*). The immobilization of lysozyme at different concentrations (0.2 mg/mL and 0.8 mg/mL) on cellulose nanospheres (CNS) surface was confirmed by the presence of amide groups, the changes of ZP values and additional layer on the CNS surface. The antibacterial activity investigation against *B. subtilis* using zone of inhibition (ZOI) assays showed that CNS-Lys possessed 25% higher antibacterial properties than free Lys.

Keywords: antibacterial; cellulose; emulsion; lysozyme; spheres; ZOI.

INTRODUCTION

In this study, we report the preparation of cellulose nanospheres (CNS) via our water-to-oil ratio (W/O) emulsion method, evaluating their physicochemical and structural properties and forming lysozyme-impregnated CNS. The CNS produced have properties that enhance the activity and stability of lysozyme, thus making them excellent potential carriers for lysozyme and other peptide or protein-based payloads.

THEORY/LITERATURE REVIEW

Lysozyme is well known for its various applications in food, medicine, and veterinary medicine because it has antimicrobial properties. However, the application of lysozyme is still limited due to its instability, low reusability [1], and short lifetime [2]. It also tends to cause aggregation caused by macromolecular crowding [3]. This can affect the quality and efficiency of lysozyme. Therefore, lysozyme has been largely immobilized on particles that act as carriers. Among them are zinc oxide (ZnO), silica [4], cellulose [5], and chitosan [6]. This enzyme immobilization technique can be divided into physical and chemical. The selection of appropriate techniques is essential to increase the interaction between lysozyme and substrate particles to increase the stability of lysozyme.

Generally, cellulose nanoparticles offer a fascinating platform in biomedicine due to their unique properties, such as high surface energy, surface-to-volume ratio, and high proportion of surface chemical groups that make them suitable as carriers. Many researchers have focused on using cellulose nanomaterial derivatives with metal nanoparticle additions as antimicrobial agents. Mwafy et al. studied the antibacterial properties of cadmium oxide in TEMPO-oxidized cellulose nanofibers

(TOCN) [7]. Besides that, carboxymethyl cellulose-based functional films prepared by incorporating curcumin and zinc oxide nanoparticles have also been reported to have antibacterial properties [8]. However, since nanometals can accumulate in many essential body organs, such as the spleen and liver, their use is prohibitive. Nanometals accumulate in the atmosphere and the human body and have significant harmful consequences [9].

MATERIALS

Cellulose from cotton linter (CL) (α -cellulose >95%) was supplied by George Weil & Sons Ltd, Guildford, United Kingdom, while liquid paraffin was from R&M Chemicals. Sorbitan monooleate (S80) (density: 0.992 g/cm³), sodium hydroxide (NaOH, 96%), urea (CH₄N₂O) (ACS reagent 99.0–100.5%), hydrochloric acid (HCl) (36%–38%), sulphuric acid (H₂SO₄) (95%–98%), acetone (99.9%), Luria Bertani (LB) agar and chicken egg white lysozyme (40,000 units/mg) were obtained from Sigma-Aldrich. The bacterial culture of the Gram-positive bacterium *B. subtilis* was obtained from the Microbial Culture Collection Laboratory, Faculty of Science and Technology, Universiti Kebangsaan Malaysia.

EXPERIMENTAL

Samples Preparations

Cellulose was treated with 40% H₂SO₄ for acid hydrolysis. 1.5g of the treated cellulose was added to the NaOH/Urea/water solution (7/12/81). The mixture was centrifuged at 10,000 rpm for 10 minutes to remove trapped air bubbles and separate dissolved and undissolved cellulose solutions.

The cellulose solution was then filled into a plastic syringe and extruded at 2.0 ml/min into a beaker containing 1.5% Span 80 and paraffin oil. The mixture was then stirred. The cellulose nanosphere solution in the lower phase was collected, filtered, and rinsed with acetone three times.

Two concentrations of lysozyme (0.2 and 0.8 mg/mL) were prepared before the cellulose solution was added to the lysozyme solution. The mixture was stirred for 15 minutes at 400 rpm and sonicated for 10 minutes at 40 kHz with 100W average ultrasonic power. After that, all this mixture was impregnated at room temperature for 12 hours. Then, the resulting suspension solution was centrifuged at 14,000 rpm for 10 minutes. Two phases were formed, and only the bottom phase, named 0.2CNS-Lys and 0.8CNS-Lys, was used further.

Samples Characterizations

A laser particle size analyser characterised the samples' zeta potential (ZP) (Malvern Zetasizer Nano ZS, Malvern, UK). All measurements for ZP were performed at 25 °C using a capillary electrophoresis cell, and the samples were suspended in an aqueous solution at pH 7. The ZP was calculated based on Smoluchowski's equation. The average of three measurements was taken to represent the measured potential. All measurements were conducted in triplicate. FTIR analysis was performed using Fourier Transform Infrared (ATR-Perkin Elmer Spectrum 400 FT-IR) to analyze the functional groups in the samples. Each sample was scanned 64 times at a resolution of 2 cm⁻¹ within the 4000 to 1000 cm⁻¹ range. The transmission electron microscope (TEM) (JEM-2100, JEO, Tokyo, Japan) was utilized to examine the morphology and microstructure of CNS, 0.2CNS-Lys and 0.8CNS-Lys. 1 mg of CNS, lysozyme and CNS-Lys samples were dried using a freeze dryer and subsequently analyzed. The free Lys and CNS-Lys' antibacterial activity was investigated using agar plate diffusion to measure zone inhibition (ZoI).

RESULTS AND DISCUSSION

The ZP values of CNS (-35.27 mV), 0.2CNS-Lys (-14.4 mV), and 0.8CNS-Lys (-9.93 mV) confirmed the successful functionalization of lysozyme onto the CNS surface via electrostatic complexation. This significant decrease in ZP is primarily driven by the steric repulsion attraction between the CNS and Lys [10].

In free lysozyme, significant peaks at 1530 cm^{-1} and 1640 cm^{-1} in the amide I and II regions indicate C=O stretching, C-N stretching, and N-H bending (Fig.1). A broad peak around 3300 cm^{-1} was also observed due to N-H stretching in the amide A region. The 3300 cm^{-1} and 2920 cm^{-1} peaks in CNS represent hydroxyl (OH) groups and C-H stretching, respectively [11]. A decrease in intensity at 2920 cm^{-1} and a clear appearance of the peak at 1643 cm^{-1} were observed after lysozyme immobilization onto CNS. Also, a slight shift at 1530 cm^{-1} indicates successful immobilization without significant alteration in lysozyme's secondary structure, which was more pronounced in 0.8CNS-Lys.

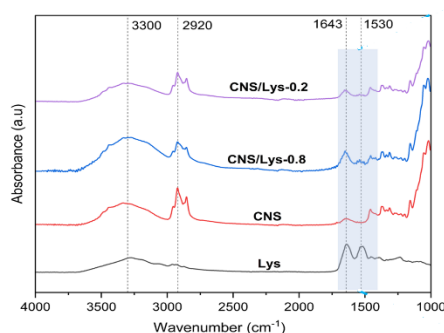


Fig. 1: FTIR spectrum of CNS, Lys and CNS-Lys

TEM imaging (Fig.2) to visualize the presence of lysozyme on the CNS revealed that the CNS exhibited a well-defined spherical shape. However, the initially perfect spherical morphology maintained by the surfactant was disrupted upon the immobilization of lysozyme around the CNS. This led to imperfect spherical morphology and increased the CNS's average size. The CNS's spherical size was 242 nm, the average size of 0.2CNS-Lys was 279, and 0.8CNS-Lys was 289 nm.

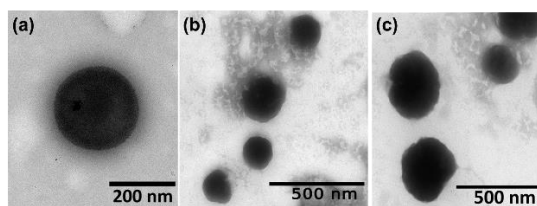


Fig. 2: TEM images of (a) CNS, (b) 0.2CNS-Lys and (c) 0.8CNS-Lys

Referring to Fig.3, the study found that 0.8CNS-Lys exhibited a larger ZoI than 0.2CNS-Lys due to its higher zeta potential (ZP) value of CNS-Lys-0.8. This value indirectly provides stability to the active sites of lysozyme, making them more exposed and effective against the *B. subtilis* membrane [12].

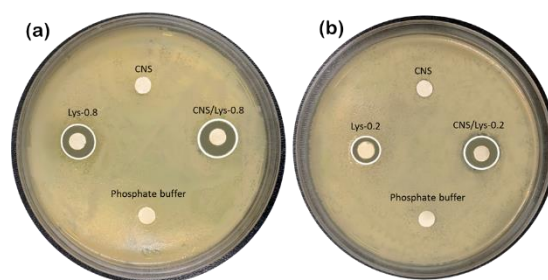


Fig. 3: ZoI of (a) 0.8CNS-Lys and (b) 0.2CNS-Lys

CONCLUSION

The CNS was confirmed to be an ideal carrier for lysozyme, other than to improve its stability. The FTIR analysis has proved the presence of lysozyme on the CNS. Diffusion assay analysis proved that CNS-Lys exhibited antibacterial properties by the presence of inhibition zones against *B. subtilis*.

ACKNOWLEDGEMENTS: The authors thank the research university grant through Geran Universiti Penyelidikan (GUP-2023-079) and the Bioresources and Biorefinery Laboratory for the financial and facilities support, respectively.

REFERENCES

- [1] H. Zhang, Q. Luan, Y. Li, J. Wang, Y. Bao, H. Tang, and F. Huang, "Fabrication of highly porous, functional cellulose-based microspheres for potential enzyme carriers," *International Journal of Biological Macromolecules*, vol. 199, pp. 61, 2022.
- [2] B. Shareghi, S. Farhadian, N. Zamani, M. Salavati N, and S. Gholamrezaei, "Stability and enzyme activity of lysozyme in the presence of Fe₃O₄ nanoparticles," *Monatshefte Für Chemie - Chemical Monthly*, vol. 147, pp. 465, 2016.
- [3] S. Venkataramani, J. Truntzer, and D. Coleman, "Thermal stability of high concentration lysozyme across varying pH: A Fourier transform infrared study," *Journal of Pharmacy & Bioallied Sciences*, vol. 5, pp. 148, 2013.
- [4] M. Du, J. Liu, F. Wang, L. Bi, C. Ma, M. Song, and G. Jiang, "A sustained-release microcarrier effectively prolongs and enhances the antibacterial activity of lysozyme," *Journal of Environmental Sciences*, vol. 129, pp. 128, 2023.
- [5] P. Ferraboschi, S. Ciceri, and P. Grisenti, "Applications of lysozyme, an innate immune defense factor, as an alternative antibiotic," *Antibiotics* vol. 10, pp. 1534, 2021.
- [6] A. Cerón, A. L. Nascife, S. Norte, S. Costa, A. J. H. Oliveira do Nascimento, F. D. P. Morisso, J. Baruque-Ramos, R. C. Oliveira, and S. M. Costa, "Synthesis of chitosan-lysozyme microspheres, physicochemical characterization, enzymatic and antimicrobial activity," *International Journal of Biological Macromolecules*, vol. 185, pp. 572, 2021.
- [7] E. A. Mwafy, M. S. Hasanin, and A. M. Mostafa, "Cadmium oxide/TEMPO-oxidized cellulose nanocomposites produced by pulsed laser ablation in liquid environment: Synthesis, characterization, and antimicrobial activity," *Optics and Laser Technology* vol. 120, pp. 105744, 2019.
- [8] S. Roy, and J. W. Rhim, "Carboxymethyl cellulose-based antioxidant and antimicrobial active packaging film incorporated with curcumin and zinc oxide," *International Journal of Biological Macromolecules*, vol. 148, pp. 666, 2022.
- [9] M. S. Hasanin, and G. O. Moustafa, "New potential green, bioactive and antimicrobial nanocomposites based on cellulose and amino acid," *International Journal of Biological Macromolecules*, vol. 144, pp. 441, 2020.

- [10] T. Wu, N. Kummer, K. J. De France, S. Campioni, Z. Zeng., G. Siqueira, J. Dong, and G. Nyström, “Nanocellulose-lysozyme colloidal gels via electrostatic complexation” *Carbohydrate Polymers*, vol. 251, pp. 1–9, 2021.
- [11] N. A. Lopes, C. M. B. Pinilla, and A. Brandelli, “Antimicrobial activity of lysozyme-nisin co-encapsulated in liposomes coated with polysaccharides,” *Food Hydrocolloids*, vol. 93, pp. 1, 2019.
- [12] F. Wu, T. Xu, G. Zhao, S. Meng, M. Wan, B. Chi, C. Mao, and J. Shen, “Mesoporous silica nanoparticles-encapsulated agarose and heparin as anticoagulant and resisting bacterial adhesion coating for biomedical silicone,” *Langmuir* vol. 33, pp. 5245–5252, 2017.

Comparative Assessment of Chemical and Green Synthesis Methods for Biomedical Applications: Crafting and Assessing Chitosan-Coated Iron Oxide Nanoparticles

Romesa Soomro¹, Muhammad Zulfadzli Bin Zainuri¹, and Che Azurahanim Che Abdullah^{1,2*}

¹*Department of Physics, Faculty of Science, Universiti Putra Malaysia, 43300, Selangor, Malaysia*

²*Nanomaterial Synthesis and Characterization Lab, Institute of Nanoscience and Nanotechnology, Universiti Putra Malaysia, 43300, Selangor, Malaysia*

Abstract: Magnetic nanoparticles (MNPs) are frequently utilised in biomedical applications such as hyperthermia, targeted drug delivery and cancer therapy. MNPs are categorised as diamagnetic, paramagnetic, ferromagnetic, ferrimagnetic, antiferromagnetic, and superparamagnetic based on their intrinsic magnetic dipoles and net magnetisation in the presence or absence of an external magnetic field. To assess the efficacy of MNPs, it is essential to modify them with biocompatible ligands and optimise their magnetic properties. Iron oxide nanoparticles (IONPs) are among the most frequently utilised metal oxide magnetic nanoparticles in biomedical applications, attributed to their biocompatibility, low toxicity, pronounced superparamagnetism, and straightforward synthesis. This study addresses these issues by comparing the physicochemical properties and toxicity of IONPs synthesized via chemical and green methods. Using a green synthesis approach, IONPs were produced and coated with chitosan (Cs) to enhance their stability and biocompatibility. The nanoparticles were characterized through X-ray diffraction (XRD), Fourier-transform infrared spectroscopy (FTIR), vibrating sample magnetometry (VSM), and thermogravimetric analysis (TGA). XRD confirmed the magnetite phase, with decreased crystallinity observed with increasing coating concentrations, while FTIR analyses verified the successful incorporation of Cs coatings. VSM showed that both green and chemically synthesized IONPs exhibited superparamagnetic behavior, with a slight reduction in saturation magnetization after chitosan coating. TGA revealed that Uncoated IONPs had improved thermal stability compared to coated ones. The brine shrimp hatching rate assay demonstrated lower cytotoxicity for Cs-coated IONPs, suggesting enhanced biocompatibility. This study highlights the effectiveness of green synthesis and chitosan coating in improving IONPs stability, magnetic properties, and safety, offering valuable insights for the development of eco-friendly and biocompatible nanomedicines.

Keywords: Magnetite nanoparticles, Iron oxide nanoparticles, Biocompatibility, Green synthesis, Chitosan coating, Brine shrimp hatching rate.

INTRODUCTION

Magnetic nanoparticles (MNP), particularly those composed of iron oxides such as magnetite (Fe_3O_4), maghemite ($\gamma\text{-Fe}_2\text{O}_3$), and hematite ($\alpha\text{-Fe}_2\text{O}_3$), exhibit superparamagnetic properties when their size is reduced to the nanoscale, typically between 10 and 100 nm. This unique behavior is crucial for various biomedical applications, including targeted drug delivery and cancer therapy [2, 3]. This unique property, along with their biocompatibility and ease of surface modification, makes Iron oxide nanoparticles (IONPs) have garnered significant attention in the field of nanotechnology due to their remarkable magnetic properties and potential biomedical applications. IONPs have been extensively studied for various therapeutic and diagnostic purposes [4, 5]. IONPs ideal candidates for applications such as targeted drug delivery [6-8], magnetic resonance imaging (MRI) contrast enhancement [9-11], hyperthermia treatment [12], and biosensing [13]. Despite their potential, the heightened toxicity of nanoparticles, particularly due to their increased surface area, ability to penetrate cellular barriers, and resistance to biodegradation, raises concerns. Nanotoxicity is often linked to oxidative stress, inflammation, apoptosis, and genotoxicity [14].

To mitigate these issues, IONPs is often coated with biocompatible materials, such as polymers, to improve their stability and reduce toxicity. Coating materials like dextran, chitosan (Cs), polyethylene glycol (PEG), and polyaniline alter the surface chemistry of IONPs, helping to disperse them into stable ferrofluids and prolong their circulation time in vivo [15-17]. Among these materials, Cs, a biodegradable and non-toxic polysaccharide derived from crustacean shells, stands out for its ability to address biological challenges, including biodegradability and biocompatibility. Precisely, it started from a process called deacetylation starting from chitin to Cs like been showed in Fig 1 [1].

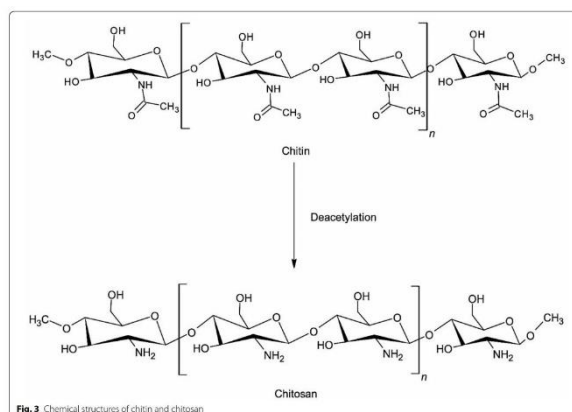


Fig. 1. Deacetylation of Chitin [1]

Goci and coworkers revealed that Cs polymers have antibacterial, biodegradability, and biocompatible potentials. They have distinct architectures, diverse features, and exceptional functionality, and find extensive use in biomedical and many industrial sectors [18]. However, the conventional chemical synthesis of IONPs often involves the use of toxic solvents and harsh conditions, raising environmental and safety concerns [19-22]. As a response to these concerns, green synthesis approaches have emerged as a promising alternative, utilizing plant extracts, microorganisms, and other biological systems to produce IONPs in a more sustainable and eco-friendly manner. Green synthesis not only reduces the use of hazardous chemicals but also enhances the biocompatibility of the nanoparticles, making them more suitable for in vivo applications [20, 21].

While green synthesis has demonstrated significant advantages, including reduced environmental impact and improved safety profiles, there is still a lack of comprehensive studies comparing the physical, chemical, and biological properties of IONPs synthesized using traditional chemical methods versus green synthesis. This gap is particularly relevant when considering the impact of synthesis methods on toxicity, a critical factor for biomedical applications. Additionally, although parameters such as pH, temperature, and stirring rate have been widely studied in the context of IONPs synthesis, less attention has been given to the role of varying concentrations of coating materials like Cs. In this study, we aim to address these gaps by comparing the physicochemical properties of IONPs synthesized through chemical and green methods and investigating the effects of different ratios of Cs coating on IONPs toxicity using the Brine Shrimp Hatching Rate (BSHR). By exploring the relationship between synthesis methods, nanoparticle properties, and cytotoxicity, this research seeks to contribute valuable insights into the development of safer and more effective MNP for biomedical applications, such as drug delivery systems [23].

MATERIAL AND METHOD

Ferric chloride ($\text{FeCl}_3 \cdot 6\text{H}_2\text{O}$, 99%), ($\text{FeCl}_2 \cdot 4\text{H}_2\text{O}$, 98%), Sodium Hydroxide, acetone, ammonium hydroxide, Chitosan, Glacial acetic acid obtained from Sigma Aldrich, and Pineapple were purchased from a local farmer in Kuala Lumpur, Malaysia. The brine shrimp cysts of *Artemia salina* were supplied by the Integrated Chemical Biophysics Research Department of the Faculty of Science, Universiti Putra Malaysia. Sea salt was procured from a local market in Malaysia. We used Milli-Q water with a resistivity of 18.2 M Ω ·cm for our study.

Synthesis of MNPs (Fe_3O_4) via Co-Precipitation Method

The first method used to synthesize MNPs is the co-precipitation method, which involves the simultaneous precipitation of salts to form a solution. FeCl_2 and FeCl_3 in a 1:2 molar ratio were mixed in 150 ml of deionized water, heated to 80°C, and stirred while nitrogen gas was bubbled through to create an oxygen-free environment [24]. This step ensures the process remains unaffected by external factors. After thorough stirring, 25 ml of ammonium hydroxide was added as a reducing agent, turning the solution black. The mixture was stirred at 800 rpm for 1 hour, then cooled, washed, and centrifuged before being dried overnight at 90°C. This process results in the formation of co-precipitated MNP (C- MNPs).



Synthesis of MNPs (Fe_3O_4) via Green Biosynthesis Method

Extraction of Pineapple peel pulp

In this process, pineapple peel pulp was prepared by thoroughly washing the peels with deionized water to remove dirt and dust. The peels were then cut into small pieces and air-dried for 10 to 12 days. After drying, 15 g of the peels were blended with 100 ml of deionized water. This mixture was refluxed at 70°C for 1 hour, producing a light-yellow solution, which was then filtered using cheesecloth. The filtrate was chilled and stored at -4°C for future use.

Green synthesis of MNPs (Fe_3O_4) using Pineapple peel pulp

An aqueous solution was synthesized by the molar combination of ferrous chloride (FeCl_2) and ferric chloride (FeCl_3) 1:2. Next, a 25 ml amount of the pineapple peel extract was slowly added to the solution while stirring continuously at a speed of 400 revolutions per minute. The pH of the solution was elevated to 11 by adding a 0.5 M NaOH solution, and the agitation was continuously sustained for 1 hour at ambient temperature. The solution progressively darkened, leading to the synthesis of MNPs. The precipitate obtained was subjected to three centrifugation cycles, and subsequently dried at 110 °C for 24 hours in the oven before being set aside for additional analysis (Fig 2). The chemical reaction of magnetite precipitation is expected to be as follows [25].

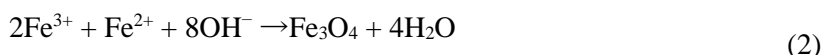




Fig. 2. Steps of green synthesis of MNPs

Coating with Chitosan to C-MNPs and G-MNPs

Preparation of Chitosan (Cs) solution

To prepare the solution, 1 g of chitosan deacetylase was mixed with 100 mL of deionized water that beforehand was added with 0.5 mL of acetic acid. The chitosan solution was stirred for 24 hours at 500 rpm at room temperature. The solution afterward was kept at room temperature [26].

Synthesis of C-MNPs-Cs and G-MNPs-Cs

First, 1g of C-MNPs and 100 mL of chitosan solution were stirred together at room temperature for 2 hours. The solutions were stirred at 800 rpm and once finished, the product was centrifuged and washed 3 times at 6000 rpm for 10 minutes. Lastly, it was dried in the oven at 90°C overnight. All the steps were being repeated for G-MNPs.

Characterization

Measurements of X-ray diffraction (XRD) was performed. Phillips, PW 3040/60 MPD X'Pert High Pro Panalytical), Fourier Transform Infrared Spectroscopy (FTIR-spectrum UATR Two, Perkin Elmer, UK), Lake Shore 7404 vibrating sample magnetometer (Lake Shore Cryotronics, Inc., Westerville, OH, USA) was used to determine the samples' magnetic properties. Additionally, Thermogravimetric analysis was performed in a N₂ atmosphere using the EXSTAR TG/DTA 7000. The samples were heated at temperature of 30 to 800°C with heating rate of 2°C/min under nitrogen atmosphere.

RESULTS AND DISCUSSION

X-ray diffraction

For the C-MNP XRD peaks, five major peaks were observed at 30.34°, 35.70°, 43.44°, 57.31°, and 62.92°, while for C-MNP-Cs, the peaks were at 30.45°, 35.90°, 43.49°, 57.48°, and 63.09°. Using the ICDD reference code (01-075-0449), these peaks were identified as corresponding to Fe₃O₄, aligning with the crystallographic planes (220), (311), (400), (511), and (440). The matching of these peaks to the magnetite diffraction data in the ICDD database confirms the successful synthesis of magnetite in both composites. This comparison with standard magnetite diffraction data ensures that the crystallinity and structure of magnetite are preserved after chitosan coating, as shown in Fig. 3 [27]. However, there is a notable difference in the intensity at the (311) crystal plane. For C-MNP-CS, the intensity is approximately less than 3500, whereas for C-MNP, the intensity exceeds 3500. This observation supports the findings of [28] who reported that coating MNPs can reduce their

crystallinity and decrease particle size. Using Scherrer's equation, the particle size (D) was calculated, and the results are presented in Table 1.

$$D = \frac{K\lambda}{\beta \cos \theta} \quad (3)$$

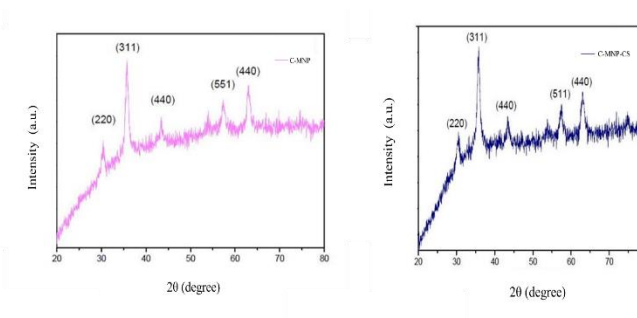


Fig. 3. XRD analysis of C-MNP and C-MNP-Cs

Table 7. The mean size for G-MNP, G-MNP-Cs, C-MNP, and C-MNP-Cs particles using Scherrer's equation

Samples	G-MNP	G-MNP-Cs	C-MNP	C-MNP-Cs
Mean crystallite size (nm)	17.48	17.84	17.45	17.44

Although the reduction in size is not much different, still it proved that coating on these particles will affect the size which depends on the type and ratio of coating. As a minor conclusion, MNP was successfully synthesized via the co-precipitation method. Fig 4 shows the XRD diffraction analysis of G-MNP and G-MNP-Cs respectively. G-MNP and G-MNP-Cs both exhibit characteristic peaks at 2θ values around 30.1°, 35.6°, 43.3°, 53.6°, 57.2°, and 62.9°, corresponding to the planes (220), (311), (400), (422), (511), and (440), respectively. These peaks are indicative of the cubic spinel structure of Fe₃O₄. The prominent (311) peak suggests that the crystallinity of the magnetite phase is retained in both samples. The XRD patterns confirm the successful synthesis of MNPs in both G-MNP and G-MNP-CS formulations, as well as the preservation of the crystalline structure after coating with CS. There is no significant shift in the peak positions after chitosan coating, indicating that the core structure of the magnetic nanoparticles remains unchanged. Using Scherrer's equation (Equation 3), D was calculated, and the results are presented in Table 1.

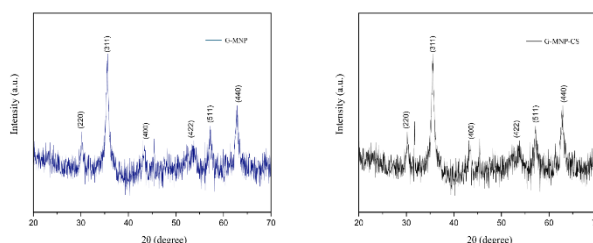


Fig. 4. XRD analysis of G-MNP and G-MNP-Cs

Fourier Transform Infrared Spectroscopy

FTIR spectroscopy provides information on the chemical composition of the nanoparticles and to better understand the coating agent's adsorption mechanism on the surface of Fe₃O₄ nanoparticles. The FTIR spectra of C-MNP, C-MNP-CS, G-MNP, and G-MNP-CS are shown in Figures 5 and 6 respectively.

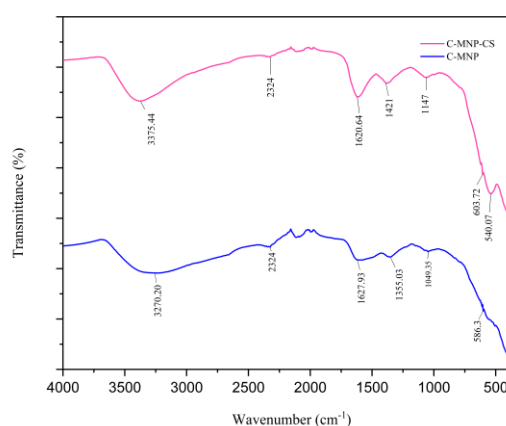


Fig. 3. FTIR analysis of C-MNP and C-MNP-Cs

The FTIR spectra of C-MNP and C-MNP-Cs, as shown in Figure 5, exhibit key functional group vibrations. For both samples, the broad band around 3270–3375 cm⁻¹ corresponds to O–H stretching vibrations, indicating the presence of hydroxyl groups. The peak at 1620 cm⁻¹ is attributed to the bending vibration of adsorbed water. The peak at 586 cm⁻¹ C-MNP and 540 cm⁻¹ C-MNP-Cs represents Fe–O stretching, confirming the presence of Fe₃O₄ nanoparticles. In the case of C-MNP-Cs, the additional peaks at 1421 cm⁻¹ and 1147 cm⁻¹ suggest the presence of C–N stretching and C–O–C vibrations, respectively, characteristic of chitosan. This indicates successful coating of the magnetic nanoparticles with chitosan, further evidenced by the shift in the Fe–O stretching peak. The overall FTIR analysis confirms the structural integrity of magnetite and the effective chitosan coating in the C-MNP-Cs sample.

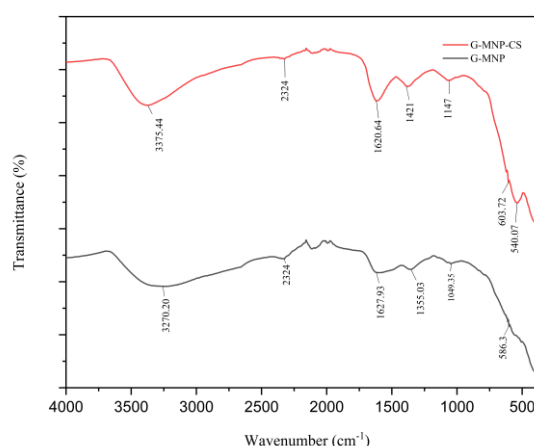
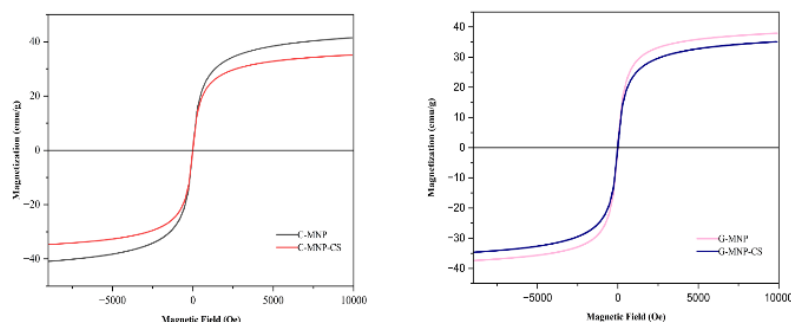


Fig. 4. FTIR analysis of G-MNP and -BMNP-Cs

The FTIR spectra of G-MNP and G-MNP-Cs in Fig 6 demonstrate the characteristic functional groups of the synthesized materials. Both samples show a broad peak around 3270–3375 cm^{-1} , indicating O–H stretching, which suggests the presence of hydroxyl groups. The absorption peak near 1620 cm^{-1} corresponds to the bending vibrations of adsorbed water. The strong peaks at 586 cm^{-1} G-MNP and 540 cm^{-1} G-MNP-Cs represent Fe–O stretching vibrations, confirming the formation of Fe_3O_4 nanoparticles. In the case of G-MNP-CS, additional peaks at 1421 cm^{-1} and 1147 cm^{-1} signify the presence of C–N stretching and C–O–C vibrations, which are typical of chitosan, verifying successful coating of the nanoparticles. The shift in the Fe–O stretching peak after chitosan coating further supports this conclusion. The FTIR analysis indicates that the core magnetite structure is retained after chitosan coating, with the added functional groups from the chitosan detected in the G-MNP-Cs spectrum [29].

Vibrating Sample Magnetometry (VSM) Analysis

VSM was used to analyze the magnetic properties of G-MNP and C-MNP, both coated and uncoated with Cs. Results are shown in Fig 7. Saturation Magnetization (M_s) of uncoated G-MNP measured 37.804 emu/g with a strong superparamagnetic response. At a coating of chitosan, M_s slightly decreased to 34.043 emu/g. This can be attributed to the fact that the chitosan coating is diamagnetic, as it provides a non-magnetic layer around the nanoparticles and therefore slightly reduces their overall magnetic properties.



For comparison, the C-MNP had a higher saturation magnetization of 41.349 emu/g, probably due to higher crystallinity and homogeneity achieved in the chemical synthesis route. After chitosan coating, these nanoparticles had an M_s value of 35.039 emu/g, following the same trend as that of the G-MNP-Cs. Despite these differences in M_s values, both green and chemically prepared MNP exhibited superparamagnetic nature having almost no coercivity and remanence. The absence of significant hysteresis further supports their suitability for biomedical applications, including targeted drug delivery and magnetic hyperthermia, where the controllable magnetic response is an essential factor. Fig 8 shows Superparamagnetic behavior of G-MNP and C-MNP.

Fig. 5. VSM curves of G-MNP and C-MNP before and after chitosan coating.

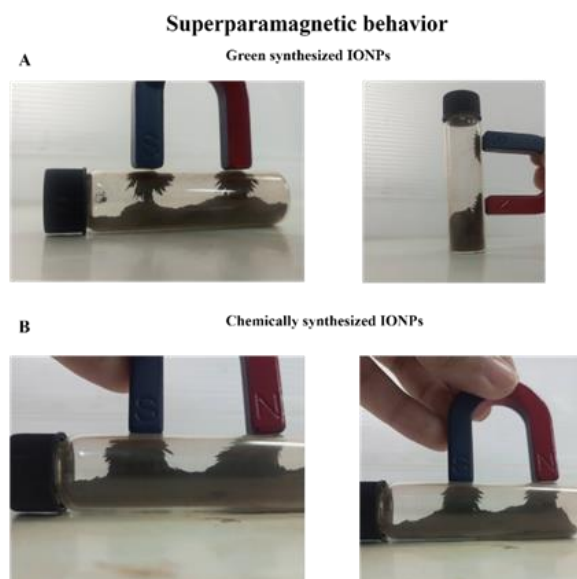


Fig. 6. Superparamagnetic behavior of green (A) and chemically synthesized (B) MNPs. Chemically synthesized MNPs show a stronger magnetic response compared to the green synthesized ones.

Thermogravimetric Analysis (TGA)

TGA of G-MNP-Cs, G-MNP, C-MNP-Cs, and C-MNP revealed distinct thermal decomposition profiles. All materials exhibited significant weight loss within the temperature range of 100°C to 800°C, indicating their vulnerability to thermal degradation. The incorporation of Cs into G-MNP and C-MNP decreased their thermal stability. This was evident in a lower onset temperature and a higher rate of weight loss, particularly between 200°C and 400°C. For example, G-MNP-Cs exhibited a 35% weight loss, while C-MNP-Cs showed a 48% weight loss within this temperature range see the Fig 9. The observed variations in decomposition patterns likely arise from differences in the chemical

composition and structural characteristics of the materials. Further studies are necessary to elucidate the specific mechanisms underlying the thermal degradation of these materials.

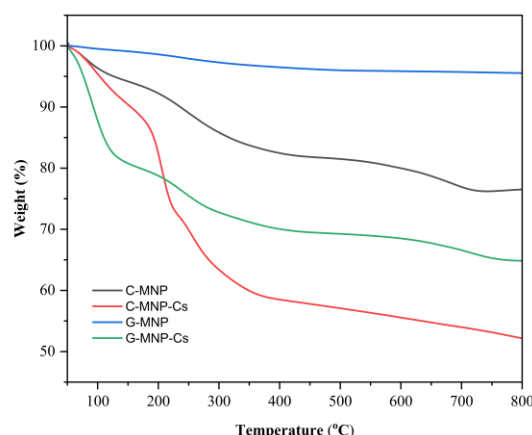


Fig. 9. TGA curves of G-MNP, C-MNP, G-MNP-Cs and C-MNP-Cs show significant weight loss between 100°C and 800°C

Brine Shrimp Hatching Rate

The brine shrimp assay was conducted solely for G-MNP, as we are concentrating on the effects of surface modification with Cs and their toxicity assessment. The Brine Shrimp Hatching Rate assay assessed the cytotoxicity of G-MNP-Cs at two distinct coating ratios, 1:1 and 1:4. The findings indicate that at a low concentration of 0.001 mg/mL, there is negligible effect on the hatching rate for both ratios, with rates remaining approximately 60%, similar to the control group. Nonetheless, as the concentration escalates, the hatching rate for the 1:1 ratio markedly declines, signifying increased toxicity. Conversely, the 1:4 ratio sustains a comparatively elevated hatching rate at lower concentrations, although it also diminishes at higher concentrations. The findings indicate that the 1:4 ratio offers superior protection against toxicity, presumably due to a more efficient Cs coating, and corroborate that nanoparticle toxicity is dose-dependent (Fig 10).

CONCLUSION

This study validated the successful synthesis of MNP through both environmentally friendly and chemical approaches. XRD analysis demonstrated distinct cubic spinel structures in all samples, with Cs-coated MNP exhibiting a slight reduction in crystallinity and an impact on particle size. FTIR validated the structural integrity of magnetite and confirmed the successful chitosan coating by the presence of distinctive chitosan peaks. VSM revealed that both green and chemically synthesised MNPs maintained superparamagnetic characteristics, with chemically synthesised MNPs exhibiting marginally enhanced magnetic responses. TGA demonstrated that without chitosan-coated MNPs exhibited superior thermal stability relative to coated samples. The Brine Shrimp Hatching Rate assay demonstrated dose-dependent cytotoxicity, with a 1:4 Cs-to-MNP ratio offering superior protection against toxicity compared to a 1:1 ratio. Although both green and chemically synthesised MNP exhibit similar properties and can be efficiently coated with Cs, the selection of method may be contingent upon particular application needs. For applications necessitating superior magnetic properties, C-MNP may be favoured. Nonetheless, green synthesis represents a more eco-friendly and sustainable

option. Additional research is required to comprehensively comprehend the long-term implications of Cs coating on the in vivo behaviour and biocompatibility of these nanoparticles.

ACKNOWLEDGEMENT: The author would like to acknowledge NANOTEDD team members for their support. The part of this work was supported by Putra Group Initiative (IPB) Research Grant financed by Universiti Putra Malaysia.

REFERENCES

- [1] M. Yadav, P. Goswami, K. Paritosh, M. Kumar, N. Pareek, and V. Vivekanand, "Seafood waste: a source for preparation of commercially employable chitin/chitosan materials," *Bioresources and Bioprocessing*, vol. 6, no. 1, p. 8, 2019/02/08 2019, doi: 10.1186/s40643-019-0243-y.
- [2] X. Feng et al., "Ultrasmall superparamagnetic iron oxide nanoparticles for enhanced tumor penetration," *Journal of Materials Chemistry B*, vol. 11, no. 15, pp. 3422-3433, 2023.
- [3] A. Hajalilou, M. Tavakoli, and E. Parvini, "Insight into Superparamagnetism in Magnetic Nanoparticles," 2023.
- [4] H. Liu, Z. Zhen, F. Chen, J. Chen, and W. Chen, "Advancements in Iron Oxide Nanoparticles for Multimodal Imaging and Tumor Theranostics," *Current Medicinal Chemistry*, 2024.
- [5] V. P. Singh, C. P. Singh, H. Ranjan, and S. K. Pandey, "Synthesis and Characterization of Iron Oxide Nanoparticles for Bio-Medical and Neuromorphic Computing Applications," in *2024 International Conference on Smart Grid and Energy (ICSGE)*, 2024: IEEE, pp. 38-42.
- [6] C. F. Chee, B. F. Leo, and C. W. Lai, "37 - Superparamagnetic iron oxide nanoparticles for drug delivery," in *Applications of Nanocomposite Materials in Drug Delivery*, Inamuddin, A. M. Asiri, and A. Mohammad Eds.: Woodhead Publishing, 2018, pp. 861-903.
- [7] S. Laurent, A. A. Saei, S. Behzadi, A. Panahifar, and M. Mahmoudi, "Superparamagnetic iron oxide nanoparticles for delivery of therapeutic agents: opportunities and challenges," *Expert opinion on drug delivery*, vol. 11, no. 9, pp. 1449-1470, 2014.
- [8] E. Alphandéry, "Iron oxide nanoparticles for therapeutic applications," *Drug discovery today*, vol. 25, no. 1, pp. 141-149, 2020.
- [9] Z. Zhao et al., "Recent advances in engineering iron oxide nanoparticles for effective magnetic resonance imaging," *Bioactive Materials*, vol. 12, pp. 214-245, 2022.
- [10] M. Salehipour, S. Rezaei, J. Mosafar, Z. Pakdin-Parizi, A. Motaharian, and M. Mogharabi-Manzari, "Recent advances in polymer-coated iron oxide nanoparticles as magnetic resonance imaging contrast agents," *Journal of Nanoparticle Research*, vol. 23, pp. 1-35, 2021.
- [11] Z. Shen, A. Wu, and X. Chen, "Iron oxide nanoparticle based contrast agents for magnetic resonance imaging," *Molecular pharmaceuticals*, vol. 14, no. 5, pp. 1352-1364, 2017.
- [12] J. Palzer, L. Eckstein, I. Slabu, O. Reisen, U. P. Neumann, and A. A. Roeth, "Iron oxide nanoparticle-based hyperthermia as a treatment option in various gastrointestinal malignancies," *Nanomaterials*, vol. 11, no. 11, p. 3013, 2021.
- [13] M. Hasanzadeh, N. Shadjou, and M. de la Guardia, "Iron and iron-oxide magnetic nanoparticles as signal-amplification elements in electrochemical biosensing," *TrAC Trends in Analytical Chemistry*, vol. 72, pp. 1-9, 2015.
- [14] V. I. Shubayev, T. R. Pisanic, and S. Jin, "Magnetic nanoparticles for theragnostics," *Advanced Drug Delivery Reviews*, vol. 61, no. 6, pp. 467-477, 2009/06/21/ 2009, doi: <https://doi.org/10.1016/j.addr.2009.03.007>.
- [15] A. Rajan, R. Chandunika, F. Raju, R. Joshi, N. K. Sahu, and R. S. Ningthoujam, "Synthesis and Processing of Magnetic-Based Nanomaterials for Biomedical Applications," *Handbook on Synthesis Strategies for Advanced Materials: Volume-II: Processing and Functionalization of Materials*, pp. 659-714, 2022.
- [16] H. Arami, Z. Stephen, O. Veisheh, and M. Zhang, "Chitosan-coated iron oxide nanoparticles for molecular imaging and drug delivery," *Chitosan for Biomaterials I*, pp. 163-184, 2011.

- [17] Z. S. Hamed Arami, O. Veisesh, and M. Zhang, "Chitosan-Coated Iron Oxide Nanoparticles for Molecular Imaging and Drug Delivery," *Chitosan for Biomaterials I*, vol. 243, pp. 163-184, 2011.
- [18] M. C. Goci, A. Leudjo Taka, L. Martin, and M. J. Klink, "Chitosan-Based Polymer Nanocomposites for Environmental Remediation of Mercury Pollution," *Polymers*, vol. 15, no. 3, p. 482, 2023. [Online]. Available: <https://www.mdpi.com/2073-4360/15/3/482>.
- [19] S. K. R. Namasivayam, "Eco friendly, green route method for the preparation of poly ethylene glycol (PEG) mediated surface modified iron oxide nanoparticles (PEG-IONps) with potential biological activities," *Environmental Quality Management*, 2024.
- [20] M. Yusefi, K. Shameli, R. R. Ali, S.-W. Pang, and S.-Y. Teow, "Evaluating Anticancer Activity of Plant-Mediated Synthesized Iron Oxide Nanoparticles Using Punica Granatum Fruit Peel Extract," *Journal of Molecular Structure*, vol. 1204, p. 127539, 2020/03/15/ 2020, doi: <https://doi.org/10.1016/j.molstruc.2019.127539>.
- [21] K. Selvam, C. Sudhakar, B. Senthilkumar, V. Sakthivel, A. Ragu Prasath, and V. Sangameshwaran, "Green Synthesis and Characterisation of Iron Oxide Nanoparticle Using Ziziphus oenoplia Fruit Extract: A Biomedical and Environmental Potential," *Waste and Biomass Valorization*, 2024/03/08 2024, doi: 10.1007/s12649-024-02445-z.
- [22] Priya, Naveen, K. Kaur, and A. K. Sidhu, "Green Synthesis: An Eco-friendly Route for the Synthesis of Iron Oxide Nanoparticles," (in English), *Frontiers in Nanotechnology*, Review vol. 3, 2021-June-15 2021, doi: 10.3389/fnano.2021.655062.
- [23] R. N. Hikmat, R. Choesrina, and S. P. Fitrianiingsih, "Cytotoxic Activity Assay of Lime Leaves (*Citrus aurantiifolia* (Christm.) Swingle) with Brine Shrimp Lethality Test (BSLT) Method on *Artemia franciscana* Kellogg," in *Bandung Conference Series: Pharmacy*, 2023, pp. 24-30.
- [24] T. Q. Bui, S. N.-C. Ton, A. T. Duong, and H. T. Tran, "Size-dependent magnetic responsiveness of magnetite nanoparticles synthesised by co-precipitation and solvothermal methods," *Journal of Science: Advanced Materials and Devices*, vol. 3, no. 1, pp. 107-112, 2018.
- [25] R. Rahmani et al., "Plant-mediated synthesis of superparamagnetic iron oxide nanoparticles (SPIONs) using aloe vera and flaxseed extracts and evaluation of their cellular toxicities," *Ceramics International*, vol. 46, no. 3, pp. 3051-3058, 2020/02/15/ 2020, doi: <https://doi.org/10.1016/j.ceramint.2019.10.005>.
- [26] A. P. M. Vieira et al., "Antibiofilm effect of chlorhexidine-carrier nanosystem based on iron oxide magnetic nanoparticles and chitosan," *Colloids and Surfaces B: Biointerfaces*, vol. 174, pp. 224-231, 2019/02/01/ 2019, doi: <https://doi.org/10.1016/j.colsurfb.2018.11.023>.
- [27] A. Fadli, A. Adnan, and A. S. Addabsi, "Synthesis of magnetite nanoparticles via co-precipitation method," in *IOP Conference Series: Materials Science and Engineering*, 2019, vol. 622, no. 1: IOP Publishing, p. 012013.
- [28] M. Khalkhali, K. Rostamizadeh, S. Sadighian, F. Khoeini, M. Naghibi, and M. Hamidi, "The impact of polymer coatings on magnetite nanoparticles performance as MRI contrast agents: a comparative study," *DARU Journal of Pharmaceutical Sciences*, vol. 23, pp. 1-12, 2015.
- [29] B. Tanhaei, A. Ayati, M. Lahtinen, and M. Sillanpää, "Preparation and characterization of a novel chitosan/Al₂O₃/magnetite nanoparticles composite adsorbent for kinetic, thermodynamic and isotherm studies of Methyl Orange adsorption," *Chemical engineering journal*, vol. 259, pp. 1-10, 2015.

Eco-Friendly Synthesis, Characterization, and Safety of Gold Nanoparticles for Targeted Colon Cancer Therapy

Siti Nadiah Zulkifli ^{1,2}, Romesa Soomro¹, Manali Haniti Zahid³, Iskandar Zulkarnain Alias³, Che Azurahanim Che Abdullah ^{1,2,*}

¹ Biophysics Laboratory, Department of Physics, Faculty of Science, Universiti Putra Malaysia, 43400 UPM Serdang, Selangor, Malaysia

² Institute of Nanoscience and Nanotechnology, Universiti Putra Malaysia, 43400 Serdang, Selangor Darul Ehsan

³ Department of Chemical Pathology, School of Medical Sciences, Health Campus, Universiti Sains Malaysia, 16150 Kubang Kerian, Kelantan

*Corresponding author's E-mail: azurahanim@upm.edu.my

Abstract: Gold nanoparticles (AuNPs) were selected for this study because of their extensive applications and the advantages they provide compared to other nanomaterials. Recent research underscores the versatility of AuNPs, primarily attributable to optimized synthesis protocols that yield nanoparticles of diverse sizes, shapes, and properties. This study modified the Turkevich method to incorporate both chemical and green synthesis approaches, highlighting the necessity for environmentally sustainable production techniques. The AuNPs were characterized via Ultraviolet-visible spectrophotometry (UV-Vis), confirming a wavelength range of 520-547 nm. Dynamic Light Scattering (DLS) was employed to ascertain the average dimensions of the nanoparticles, facilitating their appropriateness for applications. Additionally, Fourier Transform Infrared (FTIR) spectroscopy was utilized to identify possible biomolecules that facilitate nanoparticle stabilization. A brine shrimp lethality assay was performed to assess the toxicity of the synthesized nanoparticles, ensuring their safety as biocompatible carriers in colon cancer treatment. This toxicity evaluation is essential for assessing the viability of AuNPs as a secure and efficient nanocarrier for targeted colon cancer treatment.

Keywords— gold nanoparticles; chemical synthesis; green synthesis; characterization; toxicity

INTRODUCTION

Gold nanoparticles (AuNPs) have garnered significant interest due to their diverse properties conducive to prospective biomedical applications. AuNPs represent an excellent alternative owing to their synthesis capabilities, functional properties, diminished toxicity, and ease of detection. Due to their diminutive size-to-volume ratio and excellent thermal stability, AuNPs are extensively utilised in numerous biomedical applications [1-3]. Typically, AuNPs are synthesised using conventional methods, namely the Turkevich and modified Turkevich methods. These protocols produce AuNPs utilising hazardous chemicals to reduce Au (III) and stabilise Au (0) atoms on the surfaces of AuNPs. Research conducted on this reduction indicates that the reduction and capture capacity of citrate is linked to its structure, specifically the hydroxyl group bonded to the carboxyl group [4-5]. Biosynthesised green AuNPs are significantly safer and more environmentally friendly than those produced through physical and chemical methods. The biomedical applications of AuNPs are expanding daily and are not confined to drug delivery. Nanoparticles derived from plant extractions exhibit greater stability and a more rapid rate of green synthesis in comparison to chemical synthesis. This research intends to synthesise AuNPs utilising a modified Turkevich Method and examine the influence of various parameters on the produced AuNPs. This study has conducted a comparative analysis of characterisation between two methods.

THEORY/LITERATURE REVIEW

Gold nanoparticles (AuNPs) have gained prominence in biomedical research owing to their distinctive attributes, such as biocompatibility and facile functionalisation. The chemical synthesis of AuNPs, specifically the Turkevich method, is well-established and entails the reduction of gold salts utilising a chemical reductant such as citrate [6]. This technique enables regulation of nanoparticle dimensions and morphology, essential determinants affecting cellular absorption and therapeutic efficacy. Recent trends highlight green synthesis as a more sustainable alternative, employing plant extracts as reducing and stabilising agents [7]. This environmentally sustainable method reduces the utilisation of toxic chemicals, integrating biomolecules from the extracts that improve the biocompatibility of the resultant AuNPs. Literature indicates that green-synthesized AuNPs demonstrate stability comparable to or exceeding that of chemically synthesised counterparts. The brine shrimp lethality assay is commonly employed for initial toxicity evaluation, offering significant insights into the safety profile of AuNPs for potential application in colon cancer treatment [8].

MATERIALS

Gold (III) chloride hydrate ($\text{HAuCl}_4 \cdot 3\text{H}_2\text{O}$) (99.995% trace metals basis) and trisodium citrate dehydrate (ACS reagent, $\geq 99.0\%$) were procured from Sigma-Aldrich and used without additional purification. Tea polyphenol was bought from a local store in Kuala Lumpur, Malaysia. The brine shrimp cysts of *Artemia salina* were provided by a collaborator from the Integrated Chemical Biophysics Research Department at the Faculty of Science, Universiti Putra Malaysia. Sea salt was purchased from a local market in Malaysia. Milli-Q water with a resistivity of $18.2 \text{ M}\Omega\cdot\text{cm}$ was employed throughout the course of the experiment.

EXPERIMENTAL

About 10 mL of 0.1mM $\text{HAuCl}_4 \cdot 3\text{H}_2\text{O}$ was stirred at room temperature and then dropped some diluted sodium citrate as a reducing agent into the solutions for modified Turkevich's Method. The reaction started a few minutes after mixing. The color of the gold solution turns from light yellow to dark red wine which indicates the existence of AuNPs. The colloidal then continued to stir for a few minutes to make it homogenous.

Chemical Synthesis of AuNPs

About 10 mL of 0.1mM $\text{HAuCl}_4 \cdot 3\text{H}_2\text{O}$ was stirred at room temperature and then dropped some diluted sodium citrate as a reducing agent into the solutions for modified Turkevich's Method. The reaction started a few minutes after mixing. The color of the gold solution turns from light yellow to dark red wine which indicates the existence of AuNPs. The colloidal then continued to stir for a few minutes to make it homogenous.

The presence of AuNPs alters the hue of the gold solution from pale yellow to deep red wine. To achieve homogeneity, the colloidal was stirred for several additional minutes.

Green Synthesis of AuNPs

The same procedure as section 4.1 was repeated for green synthesis by replacing citrate solution with tea polyphenols. In this experiment, the volume of sodium citrate and tea polyphenols were different while the concentration of gold precursor was maintained at 0.1mM. The experiment was conducted using a different volume of extract in the range of 1-3 mL with a fixed amount of precursor at room temperature.

Toxicity testing of AuNPs

Eggs of brine shrimp were introduced into 96 well plate and the live brine shrimp calculated after 48 h. AuNPs were put into each of the 96 wells plate with different concentrations within 0–1 μL (0, 0.0625, 0.125, 0.25, 0.5, 1.0). Each concentration was repeated four times ($n = 4$). Additionally, salt water is used as a blank control. The brine shrimp cytotoxicity assay was used to determine their efficacy against AuNPs and their reducing agent, as it requires only a simple experiment and is relatively inexpensive. After 48 h, the number of live and death brine shrimp were totalled and percentage of hatching and their lethality.

RESULTS AND DISCUSSION

Due to its simplicity, the modified Turkevich's Method is the most representative and common technique to synthesize AuNPs. At first, the gold salt solution was observed as yellow until sodium citrate was added to the solution. The reduction of gold ion takes place from Au^{3+} to Au^0 . The solution turned to red wine after a few seconds indicating the formation of AuNPs. This experiment reveals the effect of the color properties to the nanoparticle formation. When the resonance of the plasmon is changed, thus the color also changes. In addition, AuNPs surface is covered with charge, which can cause repulsive forces between the nanoparticles. Hence, it can prevent aggregation since the energy barrier is too high for particles to interact (Pluchery et al., 2013).

Physicochemical Properties

The prepared samples were analyzed using X-ray diffraction (XRD), Dynamic Light Scattering (DLS), Ultraviolet-visible spectrophotometry (UV-Vis) and Fourier transform infrared (FTIR) spectroscopy. The FTIR and XRD analysis results are shown in Fig. 1 and Fig. 2, respectively.

FTIR spectroscopy detected the presence of different functional groups in the synthesized AuNPs, and the findings were shown in Fig. 1. The FTIR analysis detected functional groups in the extracts and the synthesized AuNPs. The tea polyphenols extract exhibit band approximately at 1624 cm^{-1} which is related to $\text{C}=\text{C}$ bonds that confirms the stabilizing effect of the extract. The band approximately at 3327 cm^{-1} is due to the existence of O-H band which proves the reducing property of the extract.

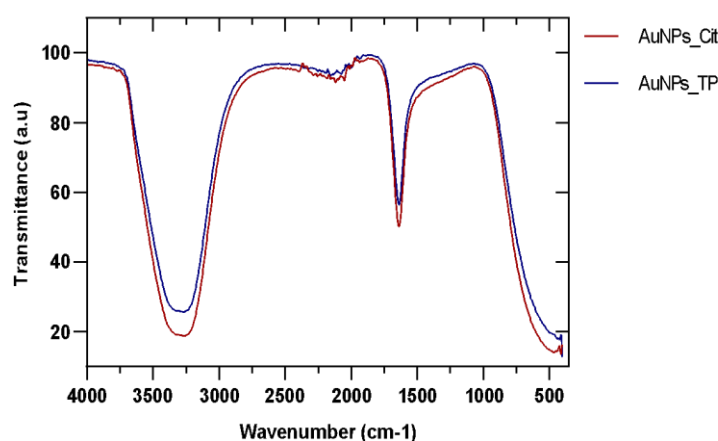


Fig. 1: The FTIR spectra of the tea polyphenols extract and the synthesized AuNPs

An XRD analysis further determined the crystalline nature structure of the AuNPs obtained. Fig. 5 Figure 2 shows the results of XRD analysis for AuNPs synthesized at 300°C . The XRD analysis

has identified four diffraction peaks of Bragg at 2θ angles: 38.27° , 44.48° , 64.73° , 77.76° and 81.93° corresponding to (111), (200), (220), and (311) planes, revealing the crystalline structure of AuNPs synthesized AuNPs in accordance with which following the relevant database file (ICDD No 96-901-2954).

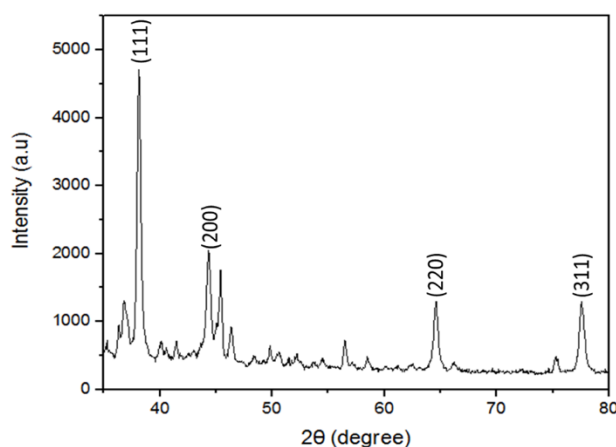


Fig. 2 : The XRD pattern of the synthesized AuNP.

Toxicity assessment of AuNPs

To assess the cytotoxicity of the synthesised AuNPs, brine shrimp were exposed to varying AuNP concentrations. The graph in Fig. 3 shows that AuNPs synthesised with tea polyphenols have a marginal increase in hatching percentage as concentration increases. As the concentration of AuNPs increased, cytotoxicity occurred, resulting in a reduction in hatching rate. AuNPs treated with citrate show significant instability, most likely due to nanoparticle aggregation, which causes the formation of a surrounding layer clump.

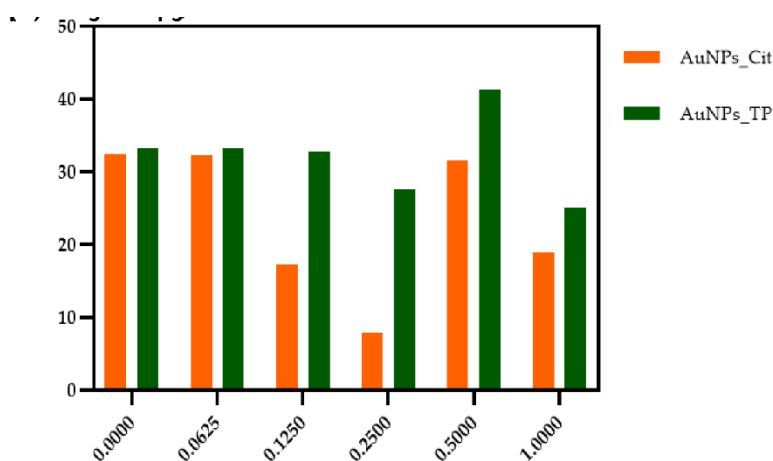


Fig. 3 : Hatching percentage of brine shrimp treated with AuNPs-Cit and AuNPs-TP

CONCLUSION

An investigation has been conducted regarding the feasibility of performing a comparative analysis of characterisation between two distinct methodologies. The modified Turkevich method successfully facilitated the synthesis of chemicals. Biogenic AuNPs are produced using green synthesis methods.

The synthesis of these AuNPs was achieved via the reduction of citrate and tea polyphenols, which serve as reducing and capping agents for the particles.

Brine shrimp have been employed in toxicity studies to investigate the potential biomedical applications of AuNPs. To ensure the safe administration of colon cancer treatment, toxicity evaluation is essential.

ACKNOWLEDGEMENTS

This work was partially supported by Universiti Sains Malaysia under Research University Grant (Project Grant No. 1001/PPSP/8012296) and Loreal for Women in Science Fellowship Grant 2023.

REFERENCES

- [1] P. M. Tiwari, K. Vig, V. A. Dennis, and S. R. Singh, "Functionalized gold nanoparticles and their biomedical applications," *Nanomaterials*, vol. 1, no. 1, pp. 31–63, 2011.
- [2] M. M. Ghobashy, S. A. Alkhursani, H. A. Alqahtani, T. K. El-damhougy, and M. Madani, "Gold nanoparticles in microelectronics advancements and biomedical applications," *Materials Science and Engineering: B*, vol. 301, p. 117191, 2024.
- [3] Ł. Niznik, M. Noga, D. Kobylarz, A. Frydrych, A. Krośniak, L. Kapka-Skrzypczak, and K. Jurowski, "Gold Nanoparticles (AuNPs)—Toxicity, Safety and Green Synthesis: A Critical Review," *International Journal of Molecular Sciences*, vol. 25, no. 7, p. 4057, 2024.
- [4] S. S. Priyadarshini, "Innovative and sustainable approaches to gold nanoparticle synthesis: beyond the Turkevich method," *J. Nanomater. Devices*, vol. 1, pp. 17–21, 2023.
- [5] W. A. A. Rosero, A. B. Barbezán, C. D. de Souza, and M. E. C. M. Rostelato, "Review of advances in coating and functionalization of gold nanoparticles: from theory to biomedical application," *Pharmaceutics*, vol. 16, no. 2, p. 255, 2024.
- [6] E. F. Oliveira, A. C. Pereira, M. A. C. Resende, and L. F. Ferreira, "Gold Nanoparticles: A Didactic Step-by-Step of the Synthesis Using the Turkevich Method, Mechanisms, and Characterizations," *Analytica*, vol. 4, no. 2, pp. 250–263, 2023.
- [7] S. K. R. Namasivayam, "Eco friendly, green route method for the preparation of polyethylene glycol (PEG) mediated surface modified iron oxide nanoparticles (PEG-IONps) with potential biological activities," *Environmental Quality Management*, 2024.
- [8] C. N. Banti and S. K. Hadjikakou, "Evaluation of Toxicity with Brine Shrimp Assay," *Bio-protocol*, vol. 11, no. 2, p. e3895, 2021.



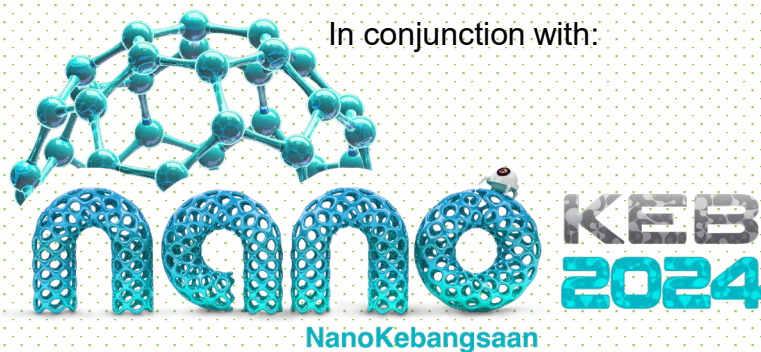
Organised by:

Institute of Nanoscience and Nanotechnology (ION2),
Universiti Putra Malaysia (UPM).

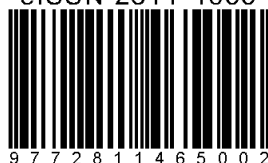
In collaboration with:

National Nanotechnology Centre (NNC),
Ministry of Science, Technology, and Innovation (MOSTI).

In conjunction with:



eISSN 2811-4655



9 7 7 2 8 1 1 4 6 5 0 0 2